

Multi-element ultra-trace detection of radionuclides in environmental samples

Faculty for Mathematics and Physics
Gottfried Wilhelm Leibniz Universität Hannover

A thesis presented for the degree of
Doktorin der Naturwissenschaften
Dr. rer. nat.

by **M.Phys. Darcy van Eerten**

2024

Examiner:

Prof. Dr. Clemens Walther
Institut für Radioökologie und Strahlenschutz
Gottfried Wilhelm Leibniz Universität Hannover

Co-examiner:

Prof. Dr. Klaus Wendt
Institut für Physik
Johannes Gutenberg Universität Mainz

Co-examiner:

Prof. Dr. Gareth Law
Department of Chemistry
University of Helsinki

Thesis Defence Date: 21.05.2024

Abstract

A ‘hot particle’ is a microscopic fragment deriving from nuclear material. The detection of these particles is in some cases the first marker of the release of nuclear material. Its history is contained in its isotopic composition, characteristic of its origin and interaction with the environment. This work focuses on environmental samples derived from the accident sites in Chernobyl and Fukushima, studied through resonant ionisation mass spectrometry, RIMS. The principle of RIMS relies on the universality of atomic structure to selectively analyse isotope ratios in a target element.

This work discusses the design and operation of different instruments. Individual hot particles were analysed in the SIRIUS RIMS instrument at the Institute for Radiation Protection and Radioecology (IRS) in Hannover, Germany. A comparison study was done on eight Chernobyl Exclusion Zone (CEZ) particles with the LION at Lawrence Livermore National Laboratory (LLNL) in Livermore, USA. Comparable results across instruments show a range of burnup dependent isotope ratios for U and Pu and Cs, characteristic of RBMK-type reactors.

Isotopic analysis therefore provides vital information about sample origin and degradation. In most mass spectrometric techniques without laser ionisation, the removal of isobaric interference requires chemical pre-treatment, thereby destroying the sample. This limits their application for isotopic analysis, necessitating a focus on one or two elements only, as allowed by small sample size. The versatility offered by multi-element RIMS makes it uniquely suited to the study of individual hot particles. In this work, isotope ratio analysis has been expanded to the actinides U, Pu, Np, and Am, and the fission products Rb, Sr, Zr, Cs and Ba. Isotope ratio analysis is interpreted in the contexts of nuclear forensics, radioecology, and reactor physics. A collection of samples can be grouped by analysing the time-dependent Sr, show how flux changes the U, Pu, and Cs composition across a reactor, and show through Ba that Cs has been lost to the environment.

Keywords— RIMS, actinides, fission products, ultra-trace analysis

Contents

Introduction	1
1 Nuclear Material in the Environment	4
1.1 Naturally occurring actinides	5
1.2 The Atomic Age	8
1.3 The Nuclear Fuel Cycle	12
1.4 Fission products	13
1.5 Reactor Accidents	17
1.5.1 Chernobyl	20
1.5.2 Fukushima	24
1.6 Summary	26
2 Hot Particle Analysis	27
2.1 Motivation for Analysis	27
2.2 Radiometric, Microscopy, and X-ray Techniques	29
2.3 Mass spectrometry	31
2.4 RIMS	33
2.4.1 Mass spectrometry	33
2.4.2 Ion production	35
2.4.3 Laser ionisation	37
2.4.4 Laser design and scheme selection	41
2.5 Summary	42
3 Sampling and Analysis	44
3.1 Sampling and Particle Isolation	44
3.1.1 Chernobyl	44
3.1.2 Fukushima	46
3.2 RIMS Analysis	52
3.2.1 SIRIUS	52
3.2.2 LION	54
3.2.3 Isobar on 238	56
3.2.4 Analysis of mass spectra	57
3.3 Summary	59

4	Advances in RIMS Capabilities	60
4.1	Ti:Sa range	60
4.2	Sr	62
4.3	Zr	64
4.4	Cs	66
4.5	Np	68
4.6	Pu	70
4.7	Ba, Am, U, and selective desorption of Rb, Cs	71
4.8	Summary	73
5	RIMS for Forensics	74
5.1	Actinide isotopic fingerprint	74
5.2	Strontium chronometry	77
5.3	Zirconium cladding	78
5.4	Instrument comparison	80
5.5	Summary	82
6	RIMS for Reactor Physics and Radioecology	84
6.1	Experimental Results vs Reactor Model	84
6.1.1	Actinides	86
6.1.2	Fission Products	90
6.2	Radioecology	93
6.2.1	Retention and loss	93
6.2.2	Fissionogenic vs environmental nuclides	95
6.3	Summary	96
	Conclusions	97
	References	102
	Appendix	121
A.1	ToF-SIMS/RIMS Settings SIRIUS	121
A.2	Mass spectra	122
A.3	Particle Isotope Ratio Data	123
	Acknowledgements	127
	CV, List of Publications	129
	Declaration of Authorship	131

Introduction

Every speck of dust is a reflection of the world around it, which can be studied at an atomic level to understand its composition and formation. When that speck is composed of nuclear material, it is evidence of a specific time and place of human activity. Microscopic fragments of nuclear material, or ‘hot particles’, can be the first indication of an accident at a facility. They can also be the last remaining remnants of an accident, left in the environment for decades.

In the nuclear weapons test sites, hot particles were formed from a combination of the bomb fuel, fission products, and the environment and infrastructure around it [1]. In April 1986, hot particles were measured in Sweden containing fission products unique to nuclear reactors, alerting the world to an accident having occurred somewhere to the east, and were determined to come from Chornobyl¹ [2]. In 2011, researchers were primed to monitor air filters for particulate matter derived from the meltdown at Fukushima Daiichi nuclear powerplant, and did indeed find hot particles [3].

The legacy of these particles is most prominent in the Chornobyl Exclusion Zone (CEZ), where an estimated 3% of the nuclear fuel was released into the environment in some form [4]. The fragments of fuel known as CEZ hot particles have remained in the environment to this day, and are the main source of contamination for non-volatile nuclear material, including the actinides U, Pu and Am. The analysis of such particles is direct evidence of the state of the reactor at the moment of the accident, and how they have reacted to weathering during the decades spent in the environment.

The following work considers how isotope ratios change, by reactor operation and interaction with the natural world. It involves two intertwining disciplines in the study of nuclear material; nuclear forensics and radioecology. In the former, we ask the question: “where did the material come from?” and in the second we ask: “how did it get here, and where will it go?”

In chapter one, we consider the ways in which nuclear material has entered the environment. The formation of hot particles specifically is limited to a number of accidents, whose circumstances affect the composition and fate of those particles. This requires knowledge

¹Upon request from Ukrainian colleagues working in the exclusion zone, the Ukrainian spelling of Chornobyl, Чорнобиль is used throughout this work. Historically the accident has been referred to by the Russian spelling Чернобыль, written variously as Chernobyl in English, Tschernobyl in German, or Czarnobyl in Polish.

of the production paths of nuclides considered to be nuclear material. This is introduced with the actinides U, Pu, and Am, whose isotopic composition depends on the probability and frequency of a handful of nuclear reactions. The reactions are the same, though they occur under different circumstances. From the rapid supernova explosions that form solar systems, and the slow formation of the Earth's crust, to the anthropogenic efforts to enrich and burn nuclear fuel, the two driving factors of nuclide production are time, and availability of neutrons.

Nuclear material constantly changes during and after irradiation, a concept known as burnup. Material can enter the environment anywhere along the nuclear fuel cycle, and it is important to consider the isotopic composition of fission products alongside the actinides. In the immediate aftermath of an accident, very short-lived radionuclides are released with half-lives in the order of seconds, days, and weeks. The most volatile, such as the noble gases $^{131m,133,135}\text{Xe}$ and $^{85,85m}\text{Kr}$, and halogens such as ^{131}I , are of direct relevance for emergency response. Longer-lived radionuclides, particularly ^{137}Cs and ^{90}Sr , are persistent markers of an accident in subsequent decades, and of significant consequence to human health and the environment.

Knowing what to look for is one thing, but measuring it is quite another. In chapter two, methods of hot particle analysis are presented, with discussion of the merits and limitations of each. The methods vary in their capability to image and map a particle, determine its chemical and physical structure, and its isotopic composition. This work looks at the capabilities of resonant ionisation mass spectrometry (RIMS). This technique allows for element selective non-destructive analysis of the isotopic composition of multiple elements in hot particles. In RIMS, positive ions are created by hitting a neutral cloud of atoms with lasers. The energy of the laser light targets a single element's unique electronic structure to excite it step-wise close to or above the ionisation potential. The theoretical principles behind resonance ionisation and mass spectrometry are discussed, and variations in the technique considered.

In chapter three, the methods of sampling, sample preparation and isolation, and analysis are laid out. Samples analysed in this work were obtained from the CEZ in 2014 and 2017, and samples from the Fukushima difficult-to-return zone were taken in 2011, 2016, 2017, 2021 and most recently by the author in 2023. The analysis of hot particles is the result of multi-disciplinary and collaborative work, in which many techniques are used along-side RIMS. The capabilities of two RIMS instruments were tested on eight of the CEZ hot particles, the LION instrument in Livermore, USA, and the SIRIUS instrument in Hannover, Germany.

Chapter four elaborates on the advances in RIMS capabilities in recent years. This includes the expansion of measurable elements in the SIRIUS instrument of Zr, Sr, Cs and Np. Each element has a unique transition width in each excitation step and corresponding saturation power. These properties of the excitation scheme have consequences for the ease of measurement on hot particles. Efficient schemes can then be applied to isotopic

mapping of samples, through which trace nuclides can be investigated in various samples. The consequences of particle morphology can then be investigated, such as with the identification of a silicate microsphere deriving from Fukushima through RIMS imaging.

Chapter five demonstrates the use of RIMS in a forensic analysis. Given no external information, what can be gained by looking purely at the isotope ratios in hot particles? The actinide isotopic fingerprint is shown to be a key marker of reactor origin. Results from particles measured in both LION and SIRIUS showed strong agreement between the two instruments, demonstrating the reliability of the RIMS method. Chronometric analyses through Sr isotope ratios are discussed, and RIMS imaging of Zr shows the isotopic heterogeneity possible in a hot particle.

Beyond identification, the many hot particles analysed in this work and elsewhere present an opportunity to compare model estimations of isotopic composition in a reactor, against what is really observed. As shown in chapter six, one can see the effects of initial composition, neutronics, and irradiation time in the resulting actinide isotope ratios. The range of burnups found in CEZ hot particles in particular shows the complexity of establishing an average across a reactor, as so many variations are seen on the microscopic scale. Such variation is difficult to capture in bulk analysis, upon which many ‘typical’ ratios of specific origin are based.

Hot particles are a product of their individual nuclear history, a history that can be probed through its isotope ratios. This work demonstrates how multi-element analysis of ultra-trace nuclides can decode the origin and weathering of nuclear material sampled in the environment. New isotope ratios in the fission products are analysed, measuring the time since irradiation and loss of Cs into the environment. The proxy term of burnup is examined, in how it can and cannot predict the isotopic composition of a material. Where burnup is insufficient, reactor models are consulted, showing how real ratios do and don’t align with predictions.

When you can measure a radioactive speck in all its complexity, establishing its source and degradation, it forms a comprehensive basis for further actions. The RIMS technique opens new opportunities for non-destructive investigation of isotopes at ultra-trace levels, with strongly suppressed molecular and isobaric interference. To achieve resonant signal on a particle is continuously awe inspiring. It works because all isotopes of a specific element contain the same number of electrons, arranged and excitable according to the laws of quantum mechanics. RIMS enables the patient researcher to return to the same particle again and again, each time with a new set of questions. The following work is an example.

Chapter 1

Nuclear Material in the Environment

Radioactivity is natural, but nuclear material is not. The term ‘nuclear material’ refers to special fissionable material and its source material [5, 6]. In essence, it is concerned with the enrichment of ^{235}U and the production of ^{239}Pu , which at scale are fundamentally human endeavours.

This chapter will discuss the origins of actinides and fission products from the nuclear reactions that form them. Uranium isotopes occur naturally in the soil, characterised by the isotopes ^{235}U and ^{238}U at a ratio $^{235}\text{U}/^{238}\text{U} = 0.007$ [7]. To form nuclear material, it must be concentrated and enriched, or irradiated to form Pu. The fallout from nuclear weapons tests is characterised by the atom/atom ratio between two isotopes of Pu, ^{240}Pu and ^{239}Pu at ratio $^{240}\text{Pu}/^{239}\text{Pu}$ of 0.18 ± 0.01 [8]. This is known as global fallout, and is measurable in soil around the world.

Global fallout must therefore always be considered when measuring nuclear material in the environment. More locally, nuclear power generation has resulted in intentional and unintentional release of nuclear material. The release can take different forms, and is composed of different nuclides. It can be released as gas (generally limited to volatile fission products), dissolved in liquid (which could itself be hazardous), or in solid form such as ‘hot particles’. Broadly speaking, hot particles are solid grains on the micrometre scale, with high concentrations of radionuclides. This may be actual nuclear fuel fragments, or nuclides incorporated into some other matrix such as silicate. The release of nuclear material depends on the different, and sometimes compounding, accidents discussed in cases such as Windscale, Mayak, and Dounreay. Measurements in this work are focused on two of the largest accidents, Chernobyl and Fukushima.

The operations of each site determine what ranges of nuclides are possible. As will be shown in this work, the measurement of the characteristic isotope ratios has often been done in isolation, with the methods available at the time and place of analysis. Through resonance ionisation mass spectrometry, a full spectrum of indicators become available which can be measured simultaneously or in quick succession. The following chapter discusses how these nuclides, particularly in hot particles, are formed, how they may enter the environment, and how their isotope ratios can be interpreted.

1.1 Naturally occurring actinides

Radioactivity describes the instability of a given nucleus, composed of neutrons and protons in some energetic configuration. Unstable nuclei must release energy in the form of radiation to become stable, making them radioactive. The abundance of elements and their isotopes is the subject of cosmochemistry and geology, though the core principles derive from nuclear physics. Nucleosynthesis can be described in terms of fusion, slow neutron capture (s-process), rapid neutron capture (r-process), proton capture (p-process), and decay [9]. These processes require a large flux of neutrons and other matter, generally only found in stars, reactors, and accelerators. The primordial nuclides are those that were present in the Earth at its formation, and decayed in the absence of large neutron fluxes to form the natural isotope composition we find today.

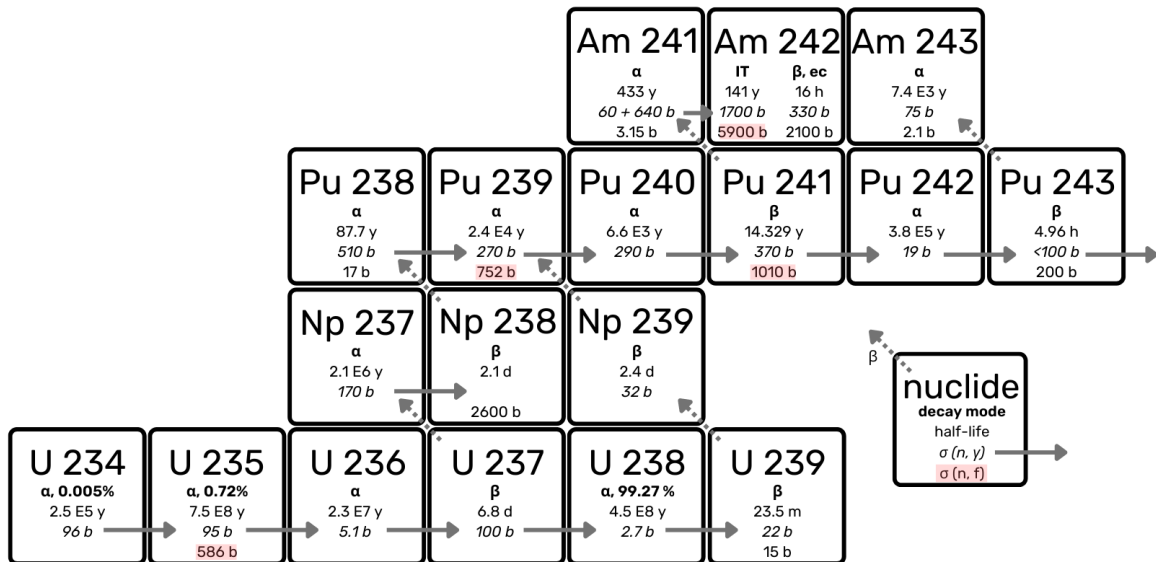


Figure 1.1: Isotope production pathways for thermal neutron capture and beta decay in U, Pu, Np, and Am. Natural abundance of U isotopes given in percent. Arrows to the right indicate thermal (n, γ) reactions, with the cross section in barns. For fissile isotopes the cross-section for $(n, fission)$ is given, where dominant fissile isotopes ^{235}U , ^{239}Pu and ^{241}Pu are highlighted in red.

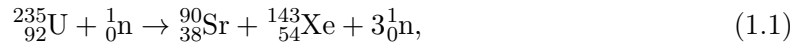
Ultimately deriving from the r-process, ^{238}U is the heaviest naturally occurring nuclide, with a half-life of 4.47×10^9 years. ^{238}U forms 99.3% of the naturally occurring uranium, with the rest made up of ^{235}U (0.07%, half-life 7.04×10^8 years) and ^{234}U (0.005%, half-life 2.46×10^5 years). The ^{238}U decay chain ends in ^{206}Pb , while ^{235}U ends in ^{207}Pb .

Isotope ratio analysis is then the study of the variation between isotopes of different origins. For example, comparisons can be made between the uranium-derived (radiogenic) Pb isotopes in natural ores (^{205}Pb , ^{206}Pb), and the primordial Pb formed absent of U

decay (^{204}Pb), as may be found in meteorites [10]. This analysis has enabled an accurate calculation of the Earth's age of 4.54×10^9 years, or slightly more than one half-life of ^{238}U [10].

Isotopes heavier than mass 238 rarely occur in nature. As shown in fig. 1.1, the isotopes of Np, Pu and Am have half-lives much shorter than the age of the Earth¹. Isotopes of these elements must be produced through neutron capture, which requires a neutron source.

Fissionable isotopes, such as ^{235}U , can fission spontaneously, or driven by a neutron. The probability of a neutron of a certain energy driving any fission reaction is determined by the cross-section $\sigma(n, f)$, measured in barn ($1 \text{ b} = 10^{-24} \text{ cm}^2$, approximately the cross-section of 1 MeV fast fission of ^{235}U [12]). The neutron energy spectrum ranges from meV to MeV, though reactions are typically characterised at thermal energy defined at 0.025 eV. An example of an (n, f) reaction could be



where ^{235}U splits into two fission products ($38 + 54 = 92$) and three neutrons ($90 + 143 + 3 = 236$). The likelihood of producing each of these nuclides, the lighter ^{90}Sr (half-life 28.91 years), and heavier ^{143}Xe (half-life 0.5 s), is determined by the independent fission yield, 0.113% and 0.182% respectively. Both nuclides decay until they reach a stable isotope, in this case ^{90}Zr and ^{143}Nd ². The cumulative yields (the sum of independent yields of parent and daughter nuclides) of $A = 90, 143$ respectively are 5.73 and 5.95%.

The cumulative yields are shown per mass number in fig. 1.2, for both ^{235}U and ^{239}Pu thermal fission. There are two peaks, referred to in this work as the 'light' (ca. mass 90) and 'heavy' (ca. mass 140) fractions. These yields must be measured empirically, and are given in nuclear libraries such as JEFF³, ENDF⁴, and JENDL⁵, which are updated regularly and can be found on websites such as Nucleonica, which uses JEFF-3.3 as its standard library [7].

In the example of ^{235}U , we see in fig. 1.1 that $\sigma(n, f) = 586 \text{ b}$ for thermal fission. A neutron could also be captured, emitting a gamma ray rather than fissioning whereby



with $\sigma(n, \gamma) = 95 \text{ b}$. The cross-section depends on the energy of the neutron, with lower energies increasing the interaction cross-section.

¹ ^{244}Pu is an exception (half-life 8.13×10^7 years), produced through the r-process and present in the Earth's crust on the order of 0.2 to 7 g [11].

²The reader is encouraged to explore the different decay chains on Nucleonica [7] or other nuclear chart. In this work, sections of the nuclear chart are discussed at thermal energy and as relevant to the isotope ratios measured in hot particles via RIMS.

³Joint Evaluated Fission and Fusion produced by the Nuclear Energy Agency (NEA) nuclear data bank

⁴Evaluated Nuclear Data File by the United States Cross Section Evaluation Working Group

⁵Japanese Evaluated Nuclear Data Library by the Japanese Nuclear Data Committee

The total number of neutron interactions N_x of type x at energy E is determined by

$$N_x = \Phi_E \sigma_x \rho_A, \quad (1.3)$$

where Φ_E is the flux of neutrons ($\text{cm}^{-2}\text{s}^{-1}$) and ρ_A is the density of target atoms. Neutrons emitted from fission are typically high energy, so-called fast neutrons at > 1 MeV. Moderation, the slowing down of neutrons through collisions, reduces the energy to the thermal (0.025 eV) and epithermal (0.025 to 0.04 eV) ranges. In this work, the importance is put on the relative probabilities of reactions: fission vs capture, capture vs decay, fast vs thermal, high flux vs low flux vs no flux. We explore how these ratios are affected by the production of nuclear materials, their use, and potential interaction with the environment.

Transuranium elements are therefore found in nature only in places with high concentrations of natural U, such as in today's uranium mines located in Kazakhstan, Canada, Namibia and Australia [13]. In these ores, spontaneous fission and (α, n) reactions can produce sufficient neutrons for (n, γ) reactions on ^{235}U and ^{238}U to form ultra-trace amounts of ^{236}U and ^{239}Pu respectively [14, 15]. Concentrations vary measurably in different ores (a ratio of 1×10^{-11} to 1×10^{-9} $^{236}\text{U}/^{238}\text{U}$, and between 1×10^8 and 1×10^{10} atoms per gram of rock for ^{239}Pu), as the neutron production and moderation depends heavily on the rock matrix [16]. The trace differences in the isotopic composition of U found in soil form the basis for understanding what was present on planet Earth in the billions of years prior to human civilisation.

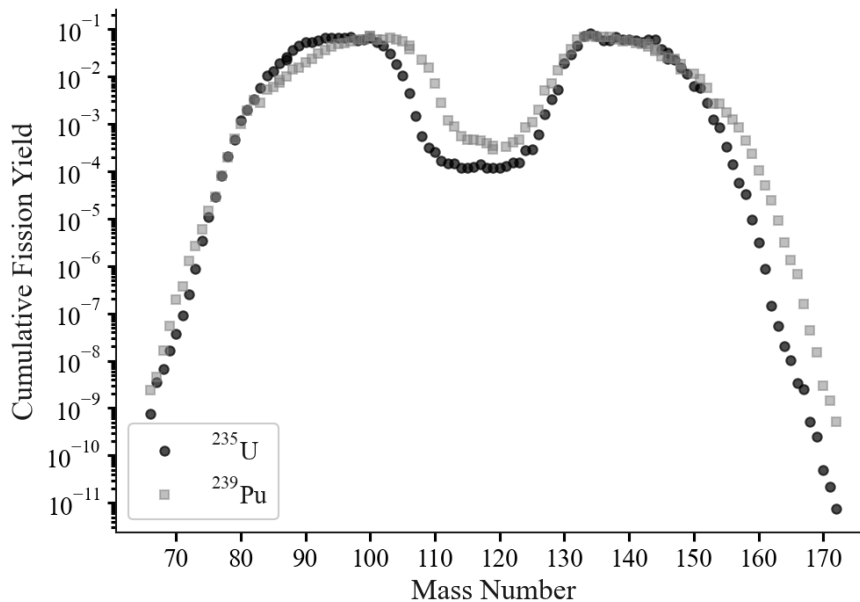


Figure 1.2: Cumulative fission yields for thermal fission from ^{235}U and ^{239}Pu , data from JENDL [7].

1.2 The Atomic Age

The development of nuclear material for the generation of energy introduced nuclides and isotope ratios vastly different from the natural world. The radioactivity of uranium was discovered in 1896 [17], and fission was demonstrated in 1938, observing the splitting of uranium into fission products and neutrons [18, 19]. The race for rapid energy generation – a bomb – began shortly after, in the backdrop of WWII. It was during this time, in the total secrecy of the Manhattan project, that plutonium was discovered as an element. Not published until after the war, ^{239}Pu was first synthesized via deuteron bombardment ($d, 2n$) of ^{238}U in 1940 [20], and the naturally occurring ^{239}Pu was extracted from pitchblende (natural uraninite ore) in 1941 [15].

Efficient energy production from fission requires the enrichment of fissile isotopes. Natural ^{235}U is typically enriched through a gas centrifuge, and ^{239}Pu must be produced through nuclear reactions. Weapons-grade U requires a $^{235}\text{U}/^{238}\text{U}$ ratio over 0.95. This high level enrichment is very energy intensive starting from a natural ratio of 0.007. As discussed earlier, ^{239}Pu is produced when ^{238}U is exposed to neutrons, and no place is better for it than a nuclear reactor. However, as shown in fig. 1.1, $\sigma(n, \gamma)$ for ^{239}Pu is high at 270 b, producing ^{240}Pu . ^{240}Pu has a very low fission cross-section, but a relatively high spontaneous fission probability ($5.7 \times 10^{-6}\%$ of decays for ^{240}Pu , vs $3.1 \times 10^{-10}\%$ for ^{239}Pu [7]), increasing the chance of premature ignition. Weapons-grade Pu must therefore be $> 90\%$ ^{239}Pu , which can be extracted from partially irradiated fuel.

Plutonium, its fission and activation products, were spread into the atmosphere on the day of the Trinity test on 16th July 1945. Since then, nuclear material has entered the environment through atmospheric explosion, and in a more limited fashion underground. It has been released in the form of leaks from improper storage or dumping, from plane crashes, and sinking ships. Waste products have entered the environment through the industrial chemistry of processing and reprocessing fuel. This work mainly considers the microscopic fuel fragments released in the form of hot particles from the Chernobyl accident. What follows is a short history of the major events that have contributed to the distribution of nuclear material into the environment, and how each can be identified by its isotopic signature.

Nuclear Weapons

Bombs released in the atmosphere can be detonated several hundred metres in the air, though only a portion of the material is fissioned. In the bombing of Nagasaki, of the 15 kg of Pu, only 1.2 kg was fissioned, while the remaining 13.8 kg was released into the atmosphere [21]. The degree to which the bomb fuel has fissioned is called ‘yield’, and is in part measured by the increase in the $^{240}\text{Pu}/^{239}\text{Pu}$ ratio. A high-yield explosion produces a high flux of neutrons, resulting in high production of ^{240}Pu , and therefore a high ratio of $^{240}\text{Pu}/^{239}\text{Pu}$.

With the end of WWII, creating more powerful and higher yield bombs was a main priority

of both the United States and the Soviet Union. In fig. 1.3, selection of $^{240}\text{Pu}/^{239}\text{Pu}$ ratios from different detonations shows the range in possible yields [22, 23, 24, 8, 25]. The lowest yields are seen in the early detonations by the Americans at Nagasaki and the Nevada test site and can still be considered weapons grade at $^{240}\text{Pu}/^{239}\text{Pu} < 0.1$. Data on the Soviet weapons program is comparatively scarce, though the $^{240}\text{Pu}/^{239}\text{Pu}$ ratios reported in samples from Semipalatinsk, Balapan, and Chernaya Bay are relatively low. The largest range is seen in the Marshall Island tests, where the islands and atolls (Bikini, Enewatak) show the effects of different detonations [25]. The heterogeneous distribution of material, or its cleanup, should therefore be considered in the analysis of such ratios.

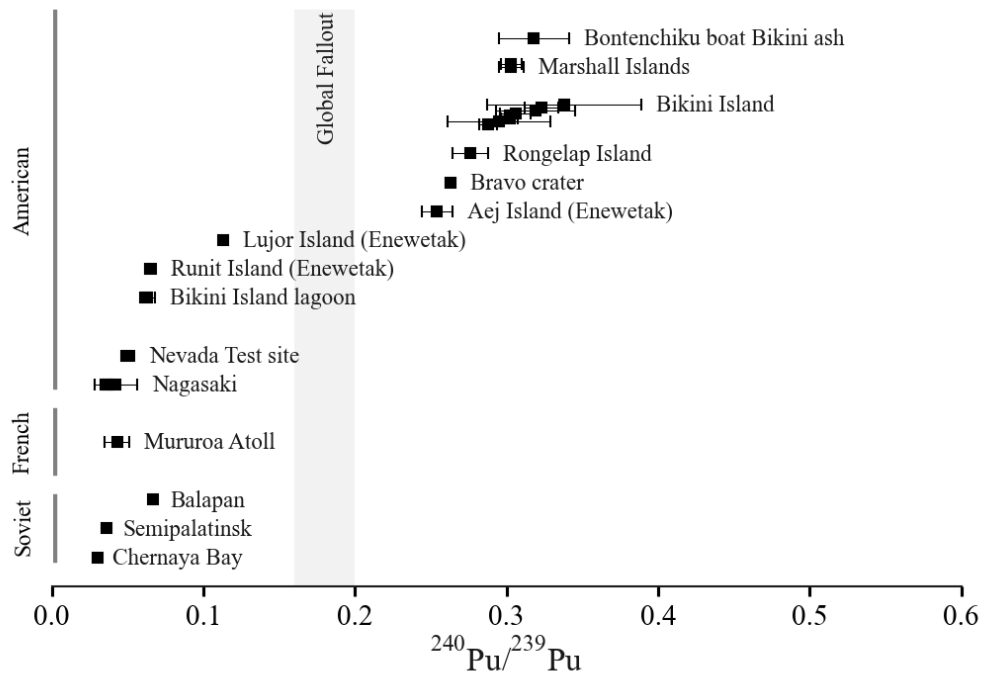


Figure 1.3: Selected $^{240}\text{Pu}/^{239}\text{Pu}$ ratios associated with Soviet, French, and American nuclear weapons programs: the Soviet test sites in Semipalatinsk, Balapan and Chernaya Bay, [23, 22], the French test site in Mururoa [22], the detonation on Nagasaki and the Nevada test site [24], and the Marshall islands tests [25, 22, 8]. The range of global fallout is marked in light grey [8].

Global Fallout

The total release of Pu from weapons testing is known as ‘global fallout’. It is characterised by a ratio of 0.18 ± 0.01 $^{240}\text{Pu}/^{239}\text{Pu}$ [8], and is the average of all the tests conducted in the northern hemisphere. The majority of the atmospheric tests were conducted in the 1950s and 1960s, after which a test ban was enforced and testing moved underground. Some 6 tons of Pu were released during these years, predominantly in the northern hemisphere [26]. The air concentration has decreased exponentially since the end of atmospheric testing in 1970, meaning that while Pu was found in trace amounts in bodies in people alive during that time (peaking in the US at 164 mBq per person in 1964), it is barely measurable

today (ca. 3 mBq) [11]. However, detectable amounts of Pu remain in soils all over the world (dominant in the northern hemisphere) in the order of Bq/kg, or pmol/kg, four orders of magnitude more than pre-atomic age concentration of Pu in soil [11]. It is for this reason that we do not consider the impact of weapons U in the environment, because it contributes so little in comparison to natural U on the order $\mu\text{mol/kg}$ in the Earth's crust.

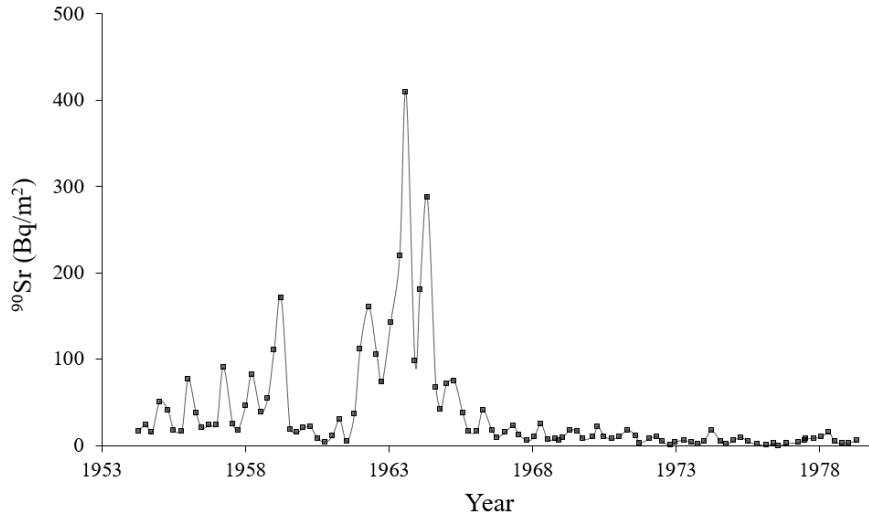


Figure 1.4: Quarterly measurements of ^{90}Sr in New York City between 1954 and 1980. Adapted from Sholkovitz [27], from data published by the Environment Measurement Laboratory [28].

Because of the sudden influx of Pu and its (radioactive) fission products, their detection in the environment is the marker of an age. Shown in fig. 1.4, the peak of the testing occurred in 1962 to 1963, where ^{90}Sr (half-life 28.91 years) on the order of 1×10^2 Bq/m² was measured in New York City [27, 28]. These measurements demonstrated the impact that atmospheric testing had far beyond the test sites, and was a factor in ending such testing. The more volatile fission product ^{137}Cs (half-life 30.08 years) has been used effectively in the study of the human impact on the environment since the 1950s [29]. However, the Cs is often tied to other major events, such as the Chernobyl accident [30], and its usefulness in the long term has been questioned by its relatively short half-life [31]. Global fallout Pu, with its longer half-life, comparative immobility, and specificity to weapons, has been used to date arctic ice cores [32], measure cyclic geochemical changes in the lake waters [27], and measure soil redistribution and erosion [29].

The exact models used to do this, and their resulting accuracy, is the subject of much debate [31, 33]. The assumption of spatial homogeneity of concentration is debated [31], though it is contended that this can be accounted for with proper sampling and statistical analysis [33]. It has been suggested that Pu data is therefore more reliable, but here the global homogeneity must be considered, whereby the French weapons program plays a role in the lower-than-global-fallout ratios of the southern hemisphere [34].

Atmospheric testing ended in the US and Soviet Union in October 1963 when they entered

into the partial test ban treaty [35], but underground testing continued (and above ground testing continued until 1974 by the French [34] and until 1980 in China [36]). With the collapse of the Soviet Union in 1991, a large amount of nuclear material was simply abandoned. As told by Harrell and Hoffman [35], in Semipalitinsk, where 116 above ground, and 340 underground tests were performed, Pu was buried into a mountainside upon the collapse of the Soviet Union. The clean up efforts were conducted in the 1990s and 2000s as a collaboration between the US, Russia, and Kazakhstan. Even then, the Pu isotope ratios were masked during the measurements as it would reveal sensitive information about the weapons program.

There have also been incidents involving accidents with weapons where they were not exploded but did contaminate the local environment. In these cases Pu really is the only marker. This is notably in Thule, Greenland, and in Palomares, Spain, where US planes crashed in the '50s with weapons on board [37, 38, 39]. Similar incidents have occurred in the former Soviet Union, where nuclear submarines are known to have sunk off the coast of Nova Zemlya [40, 41].

Hot Particles

Most of the release discussed so far has been in a finely dispersed form, dissolving into the aquatic systems, or adsorbing onto soil. The following sections will talk about the specific accidents in which so-called 'hot particles' were formed, which are broadly defined as particles $> 1 \mu\text{m}$, with high concentrations of nuclear material and/or fission products.

The formation of hot particles was immediately apparent from the Trinity test site. Named 'trinitite', these particles were made from the melted sand, (irradiated) steel infrastructure, nuclear material, and fission products that all fused into a glassy material in the heat and force of the explosion [1]. Similar materials, called 'desert glass', 'atomsite', 'Kharitonchiki' (after Soviet scientist Yuly Khariton) were found in the desert test sites of Kazakhstan, Algeria, and Australia [42]. Trinitite interestingly includes the radionuclides ^{60}Co from the activation of the steel tower from which the bomb was detonated, and ^{133}Ba from activation of BaNO_3 , which formed part of the explosive lens in the bomb. The accidents at Palomares and Thule also produced particles, containing the raw weapons fuel without fission products [39, 37].

Locally, weapons testing was devastating for the environment. The impact of these bombs wiped out most things in its radius, contaminated the environment, and increased global concentration of radiotoxic material. As seen in autopsies conducted in the '60s, continued atmospheric testing would have eventually led to harmful levels of Pu in the human body. In the following sections, we will discuss the contaminating events that occurred beyond the weapons testing era, which largely relate to the nuclear fuel cycle.

1.3 The Nuclear Fuel Cycle

From uranium ore, to enriched uranium, to (mixed) fuel, to spent fuel, each step in the nuclear fuel cycle contributes elements or removes them. Variations in the $^{235,236}\text{U}/^{238}\text{U}$ ratios in ores can be characteristic of the mine of origin [43, 16]. The enrichment of the U fuel is then characteristic of the intended reactor type, with the depleted U (0.2 to 0.4% ^{235}U) a by-product of enrichment.

A reactor design is characterised by its cooling method and moderator, which requires fuel enrichment to different levels as a result. Water is the most common coolant, which produces steam to drive a turbine to produce electricity. It is also used as a moderator and slows neutrons into thermal energies for higher interaction cross-sections. The thermal properties of water affect its ability to moderate and also absorb neutrons, the management of which is key to reactor operation. Western pressurized and boiling water (PWR, BWR) reactors are typically enriched up to 5%. Canadian reactors (CANDUs) instead use heavy water ($^2\text{H}_2\text{O}$ rather than $^1\text{H}_2\text{O}$) which has a lower absorption cross-section so that they can use natural U (0.7%) as fuel [44]. Significantly higher enriched U can be used up to 20%, as in some fast reactors, research reactors, and proposed advanced reactors, which make use of the fast neutron spectrum and require less moderation [45].

Soviet reactors are typically low enriched between 1.8% and 2.2% in RBMKs⁶ and 3 to 4% in WWERs [46]. The WWER is similar to the western PWR, whereas the RBMK uses both graphite and water as a coolant. The uranium isotope ratios can therefore be a useful starting point for identifying the reactor type. As the fuel burns, the $^{235}\text{U}/^{238}\text{U}$ falls while $^{236}\text{U}/^{238}\text{U}$ rises. Spent fuel can then be permanently stored or recycled for further use, where it gets mixed with Pu to create mixed oxide fuel, or MOX.

As fuel burns up, the isotopic composition changes, serving as a characteristic fingerprint of the design and operation history of the reactor [47, 48]. Burnup quantifies the energy produced in the reactor normalized by its fuel load, typically expressed in mega-watt days per kilogram uranium (MWd/kgU), or gigawatt days per metric ton (GWd/tU). It scales with the number of fissions that have occurred per unit mass of fuel. Burnup is therefore a proxy for the neutron fluence that drives transuranic isotope production and alters the composition of most fission products by neutron capture after they are produced.

The wide variety of ratios raises complications for assigning an origin to irradiated U [49, 14]. Referring back to fig. 1.1, the flux of the reactor affects the rate of production of Pu isotopes with respect to U isotopes. The composition also varies within the reactor itself, shown in fig. 1.5a across the length of a fuel rod, which is longer in RBMKs (7 m) than WWERs (2.5 m). Burnup is maximised in the centre of the reactor and tapers off at the edges, increasing with irradiation time. Intercomparison between Pu ratios are

⁶RBMK stands for реактор большой мощности канальный, or high powered channel reactor, and WWER is водо-водяной энергетический реактор, or water-water energy reactor, sometimes referred to as VVER

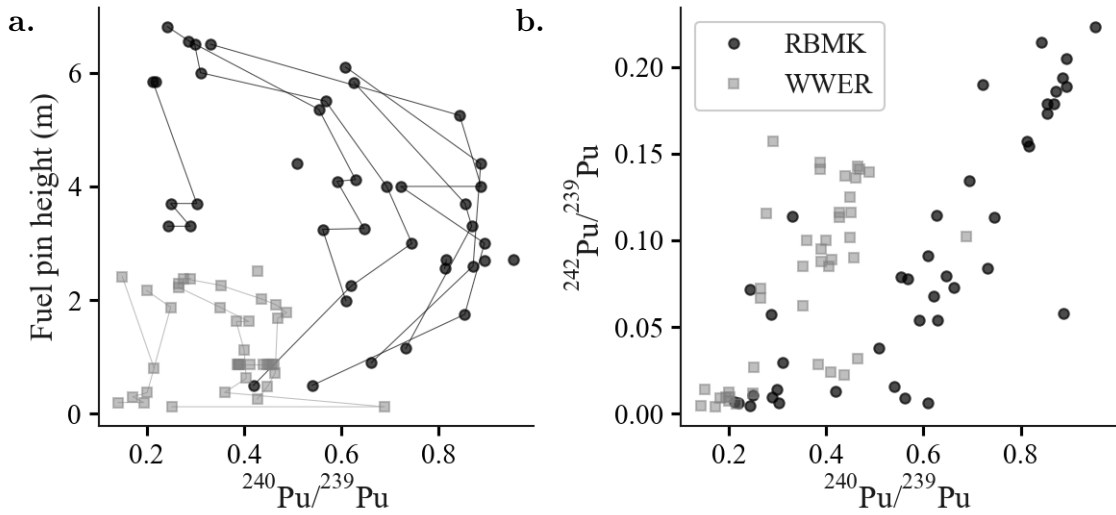


Figure 1.5: *a.* Dependence of $^{240}\text{Pu}/^{239}\text{Pu}$ on the sample origin in the fuel rod for RBMK reactors (7m tall, see Chapter 6 for further detail) and WWER reactors (2.5 m tall) in the of Makarova et al. [46]. Fuel rod sets are connected by a line. *b.* Ratios of $^{242}\text{Pu}/^{239}\text{Pu}$ vs $^{240}\text{Pu}/^{239}\text{Pu}$ in RBMK and WWER type reactors, as measured by Makarova et al. [46].

then more specific to the operation of the reactor [50], though overlaps are still possible. An example in fig. 1.5b is shown between two types of Soviet reactors: WWERs (like Zaporizhzhia in Ukraine) result in higher $^{242}\text{Pu}/^{239}\text{Pu}$ ratios with respect to $^{240}\text{Pu}/^{239}\text{Pu}$ than the RBMKs (like Chornobyl in Ukraine) [46].

1.4 Fission products

Beyond the actinides, the fission products can extend the knowledge about a material's origin and interaction with the environment. Predominantly neutron-rich, most fission products quickly beta-decay within seconds, minutes, and hours. This rapid decay is a primary source of heat in a reactor, and why a reactor must be kept cool even after fission ends. It is the volatile fission products that are most likely to be released in a reactor accident [51].

On an elemental level, the fission product decay chains go from $\text{I} \rightarrow \text{Xe} \rightarrow \text{Cs} \rightarrow \text{Ba}$, and $\text{Br} \rightarrow \text{Kr} \rightarrow \text{Rb} \rightarrow \text{Sr}$. The inert noble gases Xe and Kr are quickly dissipated into the atmosphere. Other elements such as I, Sr, and Cs, are readily incorporated into the environment. The 8 day half-life of ^{131}I is of particular concern for human health, as it can be taken up with stable iodine in the thyroid, potentially causing cancer. The calcium-mimicking ^{90}Sr can similarly accumulate in bones, and remain a far longer term source of radiation due to its 29 year half-life. The alkali metal ^{137}Cs is a primary source of radiological contamination of the environment [52, 53, 54]. With a characteristic gamma line at 662 keV and high specific activity of 3×10^{12} Bq/g, it is heavily studied in both radioecology [55] and geoscience [31].

The state of the reactor can be understood from the fission product isotope ratios. The production of these nuclides is described by the independent and cumulative fission yields, found in nuclear data libraries [7]. As discussed previously, the cumulative fission yield is a sum of the independent yields of the parent nuclides of a given isotope. Isotope ratios of fission products can be predicted based on these fission yields, and deviations from such ratios therefore give information about the state of nuclear material at the end of fission, such as burnup and chemical separation.

Heavy fission products

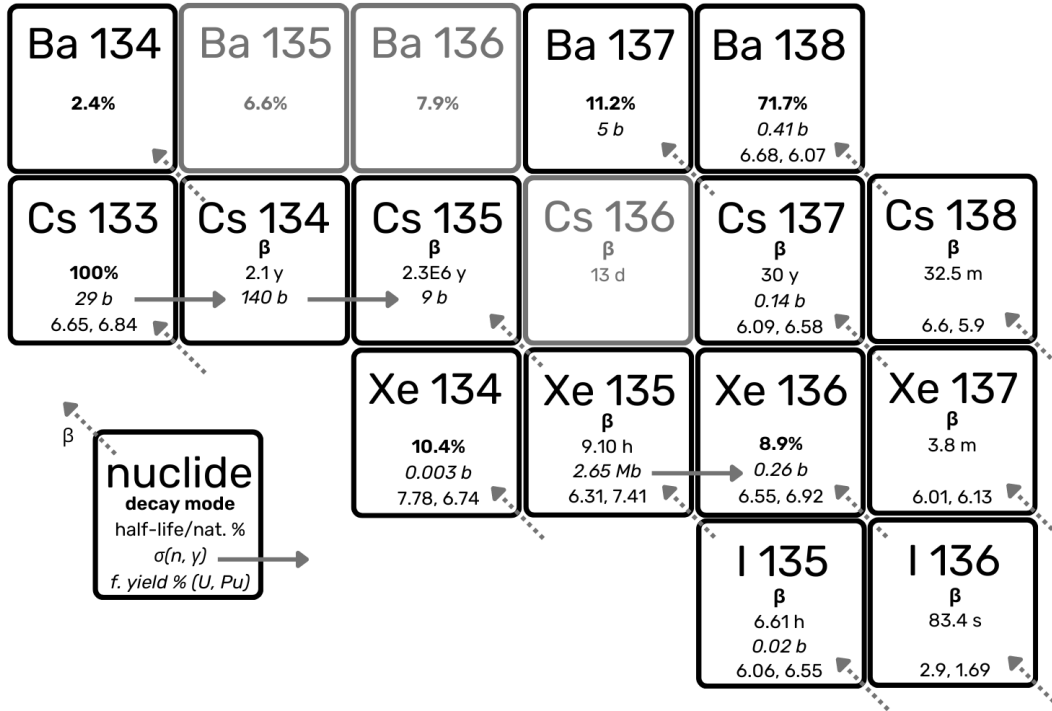


Figure 1.6: Production pathways of fission products I, Xe, Cs, Ba. Natural abundance is given in percent, and natural nuclides not produced in a reactor are shown in grey. Cumulative fission yields are given in percent for thermal fission of ^{235}U , ^{239}Pu respectively from the JEFF 3.3 library [7].

In fig. 1.6, some of the heavy fraction of fission products are shown. The nuclides ^{133}Cs , ^{137}Cs , ^{138}Ba , ^{135}Xe , are produced directly through fission (i.e., the beta-derived parents are very short-lived on the order of seconds and minutes). The rate of accumulation $\frac{d}{dt}N_{fp}$ of these nuclides is dependent on the neutron flux Φ multiplied by the cumulative fission yields (y_i) of the respective nuclide from available N_i of the fissioning isotope i so that

$$\frac{d}{dt}N_{fp} = \Phi \sum_i y_i N_i. \quad (1.4)$$

When assessing ratios between nuclides, the rate of production is less dependent on flux, and more a function of the mix of fissioning nuclides. This mix changes with fuel burnup. In low-enriched U fuel, the low burnup regime is dominated by ^{235}U fission, which shifts to ^{239}Pu with higher burnup. Simplified to only the fission yield x from ^{235}U and y from ^{239}Pu ,

if a is the time dependent fraction of ^{235}U to total fissioning isotopes and b is the fraction of ^{239}Pu , the ratio between two fission products fp_1 and fp_2 can be expressed as

$$\frac{fp_1}{fp_2} = \frac{ax_1 + by_1}{ax_2 + by_2}. \quad (1.5)$$

^{138}Ba (stable) and ^{137}Cs (half-life 30 years) are directly produced in the reactor at a similar rate, where $\sigma(n, \gamma)$ is negligible. Purely via the thermal ^{235}U fission yields, with no decay, a ratio between ^{137}Cs and ^{138}Ba of $\frac{6.09}{6.68} = 0.91$ would be expected. Purely by ^{239}Pu thermal fission, this would increase to $\frac{6.09}{6.68} = 1.08$. The measured ratio in U fuel would then range from 0.91 at 0% ^{239}Pu to 1.00 at 50% ^{239}Pu . Differences between fission libraries may add further uncertainty. The ENDF/B-VI library for example quotes different fission yields (^{138}Ba : 6.77, 6.12; ^{137}Cs : 6.19, 6.61), though the ratios stay the same at 0.91 and 1.08. ^{137}Ba has a negligible independent fission yield of $2 \times 10^{-4}\%$, and so the majority of ^{137}Ba in spent fuel will derive from decayed ^{137}Cs .

Reactor models will more accurately predict the changing fuel composition during reactor operation. Using advanced Monte Carlo based techniques, models such as ORIGEN [56, 57] take into account an initial fuel composition, reaction cross-sections at different energies, and reactor design, to model the effects of different moderators, fuel pin positions, and power output on the final isotopic composition of the spent fuel. However, algebraic estimations require only basic calculation, and in the case of $^{137}\text{Ba}/^{138}\text{Ba}$ ratios agree well with measured ratios in spent fuel. Robel et al. demonstrated this by measuring $^{137}\text{Ba}/^{138}\text{Ba}$ ratios in spent fuel that had aged for 33 years [58]. From the decay of ^{137}Cs , we would expect a ratio of

$$\frac{1}{6.68} \times 6.09 \left(1 - e^{-\ln 2 \times \frac{33}{30.08}}\right) = 0.49, \quad (1.6)$$

using the ^{235}U thermal fission yields, and the same calculation gives 0.58 for ^{239}Pu fission. The $^{137}\text{Ba}/^{138}\text{Ba}$ ratio was measured at 0.53 ± 0.02 in spent fuel samples at different sampling points in the reactor, showing only slight contribution from ^{239}Pu fission. The algebraic calculation works without the need for a reactor-specific model because the effects of neutron capture on ^{138}Ba and ^{137}Cs are minimal.

This is not the case for nuclides with high neutron capture cross-sections, or those that are only produced through neutron capture (known as activation products). ^{133}Cs is stable (the only naturally occurring Cs isotope), and has a large $\sigma(n, \gamma)$ of 100 b, resulting in ^{134}Cs . With higher burnup, more ^{133}Cs accumulates, burning into ^{134}Cs , which itself decays with a half-life of 2.1 years. Released at a given time, such as in Chernobyl or Fukushima, a narrow range of the $^{134}\text{Cs}/^{137}\text{Cs}$ ratio will be characteristic of the average burnup in the reactor at the time of the accident [2, 59, 60]. This can be easily measured through gamma spectrometry, by measuring the relative activity of ^{134}Cs , ^{137}Cs , and converting this into an atom/atom ratio by the specific activity of each nuclide in Bq/g. This method is however limited by the short decay time of ^{134}Cs .

Further capture on ^{134}Cs produces ^{135}Cs , though the vast majority of this nuclide is produced from direct decay of $^{135}\text{I} \rightarrow ^{135}\text{Xe}$, which have half-lives of 6.6 and 9.1

hours respectively. ^{135}Xe has an extremely large neutron capture cross-section of 2.7 Mb into ^{136}Xe . During reactor operation, an equilibrium is reached between burning and decaying ^{135}Xe [58]. In this way, the $^{135}\text{Cs}/^{137}\text{Cs}$ is a key distinction between reactor-derived nuclear material, and weapons material where such an equilibrium is never reached, and very little ^{135}Cs is produced [61]. With any flux-dependent marker, as shown earlier with $^{242}\text{Pu}/^{239}\text{Pu}$ in fig. 1.5a, these ratios will vary significantly depending on the position in the reactor. This is particularly notable with axial height as that sees the largest shift in moderator density, which affects the neutron flux [62, 58, 46].

Beta decay necessitates a change of element, and therefore a change in chemistry. One would be able to measure a decrease in $^{135}\text{Cs}/^{137}\text{Cs}$ ratios with distance from a weapons detonation, as the $^{135}\text{I} \rightarrow ^{135}\text{Xe}$ decay chain would be interrupted by volatilization of the gases in the atmosphere before interaction with neutrons occur [63, 61]. Chemical migration is thereby only of importance in the time-scale of the parent nuclides. A Xe-poisoning event for instance, such as occurred in Chernobyl, may be relevant to the short term production of ^{135}Cs , but not in comparison to two years of reactor operation. In the Robel case measuring spent fuel, the decay of ^{137}Cs into ^{137}Ba went as predicted. However, it has been shown in hot particles that Cs can leach out into the environment [64], which would result in a lower-than predicted ratio of $^{137}\text{Ba}/^{138}\text{Ba}$.

Light fission products

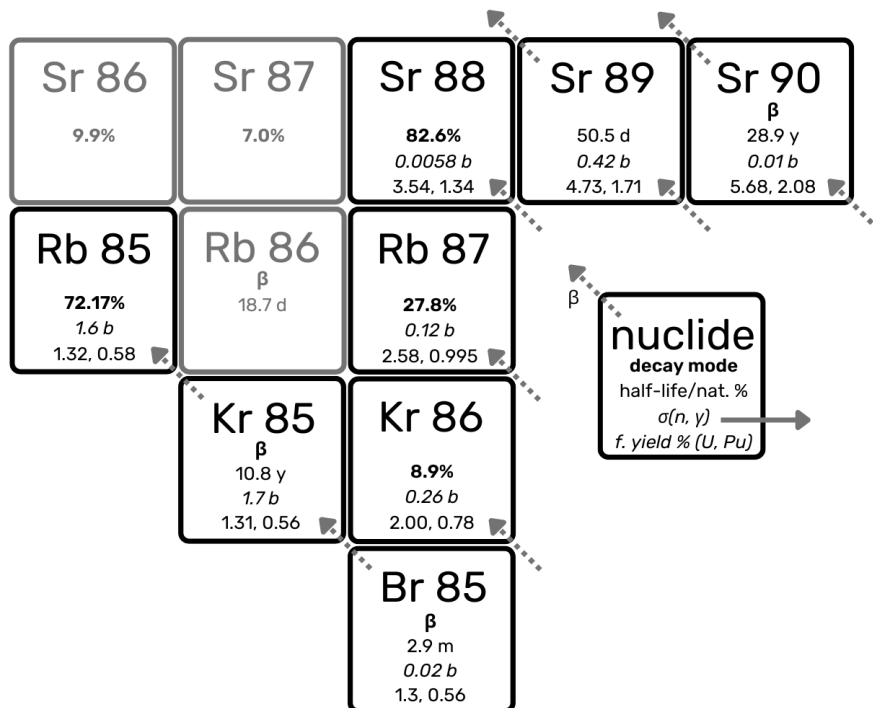


Figure 1.7: Production pathways of fission products Kr, Rb, Sr. Natural abundance is given in percent, and natural nuclides not produced in a reactor are shown in grey. Cumulative fission yields are given in percent for thermal fission of ^{235}U , ^{239}Pu respectively from the JEFF 3.3 library [7].

Lighter fission products, shown in fig. 1.7, have lower fission yields than the heavier fraction. The difference is also stronger between ^{235}U and ^{239}Pu fission, though neutron absorption cross-sections are low. As with the $^{134}\text{Cs}/^{137}\text{Cs}$ activity ratio, the $^{137}\text{Cs}/^{90}\text{Sr}$ activity ratio has also been measured as a way of determining burnup [65]. The fission yields from thermal fission of ^{235}U gives a $^{137}\text{Cs}/^{90}\text{Sr}$ activity ratio of 1.04 at the point of release, while ^{239}Pu gives 3.15. The activity ratio depends on two different elements, meaning it is only useful as a burnup marker if no chemical separation has occurred, either via fuel processing or interaction with the environment.

One suggested ratio, that is both environment and burnup independent, is the $^{90}\text{Sr}/^{88}\text{Sr}$ ratio. ^{88}Sr and ^{90}Sr are both direct fission products, with a ratio of 1.60 by ^{235}U and 1.55 ^{239}Pu thermal fission, and very low neutron absorption cross sections (0.024 b and 0.010 b respectively). The ratio is therefore, in theory, minimally sensitive to fuel composition, burnup, and chemical environment. As the $^{90}\text{Sr}/^{88}\text{Sr}$ ratio is well known, changes measured in a given sample can then be attributed solely to the decay time of ^{90}Sr . It can therefore serve as time stamp since the cessation of irradiation. This was successfully shown by Savina et al. in aged reactor samples, with an age determination within 0.6 years [66].

It has further been proposed that the $^{85}\text{Rb}/^{87}\text{Rb}$ ratios may be indicative of noble gas retention in nuclear fuel. ^{85}Br decays into ^{85}Kr , with a half-life of 10.8 years. The separation of noble gas ^{85}Kr is a key step in Pu separation, and therefore acts as a marker of fission activity when detected in the atmosphere [67, 68]. It is also assumed in source term calculations that noble gases such as Kr and Xe are (nearly) fully released into the environment in a reactor meltdown scenario [69]. There is however indication that fission gases can be retained in fuel, even in an accident scenario [70]. Evidence of this would be visible in the $^{85}\text{Rb}/^{87}\text{Rb}$ ratios, which would be depleted upon release of ^{85}Kr .

As will be shown in this work, the measurement of these isotope ratios has been done in isolation, with the methods available at the time and place of analysis. Through resonance ionisation mass spectrometry, a full spectrum of indicators become available.

1.5 Reactor Accidents

Nuclear material is heavily regulated, though there exists a risk of finding material of unknown origin [6]. Either by models [62, 71] or by measured ratios [46, 58], reference data is essential to accurately identify the origin of material [49]. This is especially relevant with regards to new reactor fleets that may arise in the coming decades⁷. By analysing how accidents in the past have released materials, and how those materials behave in the environment and differ from models and libraries, we can prepare for future events.

⁷Where a specific reactor type, such as the VVER, RBMK reactors in the Soviet Union, or the AGR/Magnox reactors of the UK were unique in the world, a mixture of reactors can be found in some countries. This is the case in China for example, which has reactors built by the French, Russians, Americans and Canadians as well as their own designs [72]

Windscale, England

While there are hundreds of nuclear powerplants operating in the world, the releases of nuclear material into the environment are very limited. The Windscale Piles (operating between 1950 and 1957 on the site that would become Sellafield) are a notable example. Cartridges of natural uranium metal, encased in aluminium to prevent oxidation, were pushed horizontally through a graphite channel, until they dropped into a water pond to be cooled and handled [73]. The burnup was then limited to maximise ^{239}Pu production and minimise ^{240}Pu , and cooled entirely by air. The air flow was so high that cartridges regularly burst from their channels, some of which were broken. Flakes typically $< 100\ \mu\text{m}$ of the oxidised U were carried up into the chimney and past the filters. It is estimated that some 20 kg of partially irradiated natural U was lost to the environment this way between 1952 and 1957 [74]. In 1957, the Windscale fire was the first major accident to occur at a powerplant, whereby neutron irradiated graphite caused a buildup of Wigner energy that burst and caught fire [73]. Fission gases, particularly ^{131}I which contaminated the food supply, were the main release into the environment. Some particulate matter is also known to have escaped.

In the two particle samples measured by McMahon et al. in 1994 [65], $^{137}\text{Cs}/^{90}\text{Sr}$ activity ratios were reported to be 0.95 and 2.6 respectively (date corrected to 1954), neither of which correspond to the expected ratio of 1.096 at 500 MWd/t as reported by the operators. Even assuming non-thermal fission, an activity ratio below 1 is an indication that leaching of Cs has occurred. McMahon concludes that it is likely that the high ratio of 2.6 would not be caused by a high percentage of Pu fission, but rather by depletion of Sr with respect to Cs through environmental exposure.

Dounreay, Scotland

In the Dounreay site, on the northeast coast of Scotland, shavings from fuel disassembly and reprocessing were washed away into the sea [76]. The first of these particles was found in 1984, and monthly inspections of the beaches near the site have regularly found particles since the early 2000s. The activity per particle is decreasing over time, as shown in fig. 1.8, faster than natural decay of Cs would suggest. The persistent occurrence of these particles is likely due to a cache of particles located near the tunnel from which they were originally washed out. This was cleaned in 2008, when a large number of particles were cleared, but they nonetheless continue to show up on the shores. The technology with which to detect the particles has also improved due to advances in remotely operated vehicle (ROV) technology [77, 76]. The Dounreay particles are some of the most active and physically large (up to mm scale) particles found in the environment, in the order of kBq to MBq per particle. The reports concluded that a particle of over 1 MBq could cause significant harm to a member of the public [78], and therefore particles over 1 MBq are classified as ‘significant’. The report then designates particles below 100 kBq as ‘minor’, and in between is classified ‘relevant’.

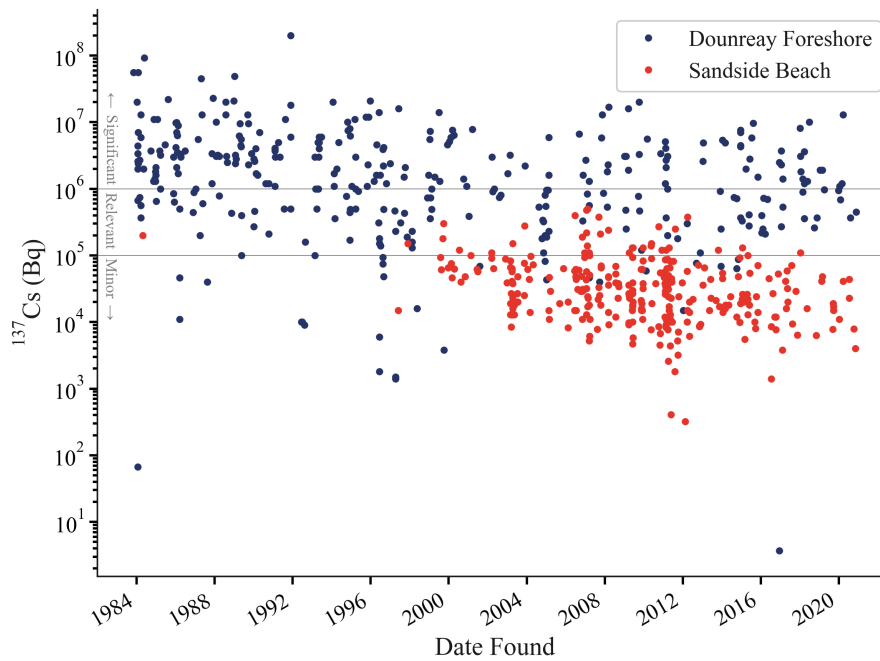


Figure 1.8: *Particles found on the Dounreay foreshore and their reported ^{137}Cs activity [75].*

Sellafield, La Hague, Savannah River

Both authorised and inadvertent releases into the environment of a substantial amount of nuclear material have derived from reprocessing facilities. Separation must happen chemically, and chemical separation produces waste. Reprocessing facilities have therefore been a consistent sources of contamination due to regular discharge of effluent. The main sites are Sellafield (northwest England, formerly Windscale), La Hague (northern France), Savannah River (South Carolina, USA), and Mayak (southern Urals, Russia).

Effluent discharge from Sellafield into the Irish Sea peaked in the mid 1970's, which dramatically decreased after new treatment methods [79]. Nonetheless, historic accumulations in patches of sediment continue to be a source of radionuclides. Activities in the sediment measured in the Esk Estuary in 2020 are in the range of 1×10^2 Bq/kg for ^{238}Pu , 1×10^3 Bq/kg for ^{137}Cs , $^{239,240}\text{Pu}$, ^{241}Am and 1×10^4 Bq/kg ^{241}Pu [80].

Releases from the Savannah River Site were largely limited to the years 1955 and 1969 when exhaust filters failed [81]. Unique to the site, ^{238}Pu was produced for the purposes of thermoelectric generation in space, comprising the majority of the yearly released Pu in the '70s and '80s [81]. As with La Hague and Sellafield, the facility operates today with closely monitored environmental regulations to keep releases to a minimum [82, 83].

Mayak, Russia

The Mayak production facility has been the site of multiple releases in its long history [84]. In the Kyshtym accident of 1957, a chemical explosion was caused by the loss of cooling in a storage facility that contained fission products in liquid [85]. The waste was largely separated from ^{137}Cs , but even so a large amount short lived ^{95}Nb (half-life 35 days), ^{95}Zr (half-life 64 days), and ^{144}Ce (half-life 285 days) were released, and ^{90}Sr was deposited in the order of kBq/m^2 , resulting in the public experiencing internal doses up to 1.5 Sv ⁸. Release of intermediate-level waste into the nearby rivers and lakes was routine in the years prior, and thousands of inhabitants of nearby villages were evacuated due to the contamination between 1953 and 1967 [84]. Today, the contamination is therefore highly mixed, between the military and civilian reactors, reprocessing activities, accidental, and intentional (retrospectively acknowledged to be ill-advised) release. As measured by Oughton et al., the $^{240}\text{Pu}/^{239}\text{Pu}$ ratios in soils and sediments of the area range from weapons grade to highly burned up fuel [84].

Arguably, in contrast to pollutants such as the harmful chemicals used in industry and agriculture, the polluting nature of the early nuclear facilities was recognised and responded to rather quickly. In the years after the war, the effects of nuclear material on humans and the environment were closely studied, in part because radionuclides are so detectable. Any deviation from the low background concentration of radionuclides is easily monitored. The recognition that nuclides were entering the environment from a specific source, in combination with the danger they could pose to human health, then prompted efforts to reduce those releases. Particularly with advances in separation chemistry, intentional releases have significantly reduced over decades [79].

1.5.1 Chernobyl

The Chernobyl accident of 1986 changed things dramatically, most prominently in the public perception of contamination from nuclear activities. As with the weapons tests, contamination spread beyond international borders. Unlike the weapons tests, the release was unintentional, and served no greater national interests. As in Kyshtym, workers and responders died and thousands of civilians were evacuated. It was, from all perspectives, an avoidable and unnecessary tragedy.

The Chernobyl nuclear powerplant is situated just southeast of the town of Pripyat, on what is now the border between Belarus and Ukraine. The events of 26th April 1986 and its aftermath are detailed in numerous reports, both from immediately after the accident [89] and in the subsequent years [90, 91]. Multiple aspects of the RBMK design, and errors made by the operators, contributed to the meltdown. The initial explosion was released into a narrow corridor called the ‘western trace’ in the direction of what is now known as the red forest, 100 km long and 1 km wide [92]. A greater release of fission gases occurred in the

⁸This is far in excess of the current German recommended limit of 1 mSv effective dose to the public not occupationally exposed to radiation [86] [85]. The subject of dose is beyond the scope of this work, however, radiation-induced effects such as vomiting and headaches begin to occur at acute exposures of 1 Sv upwards [87].

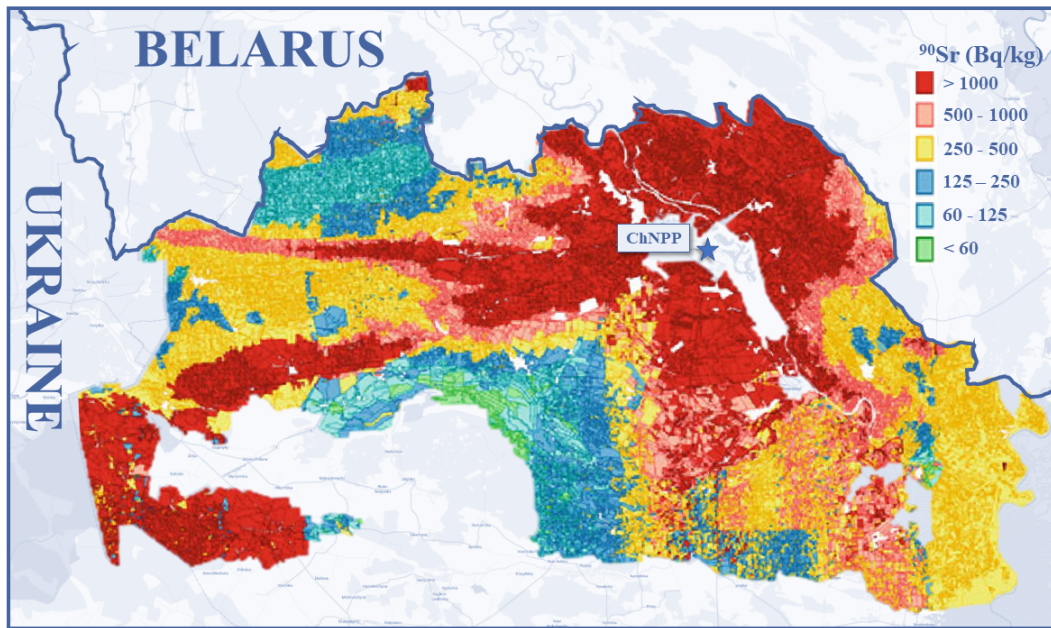


Figure 1.9: *Chornobyl exclusion zone, on the northern border between Ukraine and Belarus, adapted from the map of estimated ^{90}Sr contamination in 2020 by Yoschenko et al. [88] with data from the Ukrainian Institute of Agricultural Radiology (UIAR, 1998). Basemap is ESRI.*

following 10 days after, peaking in days 7 to 10 when the reactor fuel was hottest, forming the northern, northwestern, and southwestern traces that contaminated the majority of Europe [93, 92, 94, 91] and were detectable even in India [95]. What remains today in the Chornobyl Exclusion zone (CEZ) can be seen in fig. 1.9, showing contamination of ^{90}Sr in pine trees as estimated in 2020 by Yoschenko et al. [88]. The contamination is still severe, in some places exceeding what was reported in the Eastern Ural trace [85].

Source Term and Burnup

An estimation of the total release can be made by calculating the source term. As defined by Voilleque, the source term is a “shorthand expression that refers to the quantities and compositions of radioactive materials released, locations of the release points, and the rates of release during the times considered in the assessment” [96]. The calculation of a source term for the accident has been considered by a variety of different groups, typically by calculating an inventory from an average burnup across the reactor with results agreeing at least in order of magnitude [97, 98]. The average burnup used for such calculations range between 10 and 13 GWd/tU [97]. As reported by Begichev, the largest fraction of the fuel was between 11.3 and 14.8 GWd/tU, though fractions below 2.6 GWd/tU were found in 10% of the inventory with a minimum ^{235}U enrichment of 1.9% (See fig. 1.10a) [99].

The translation of burnup to U isotope ratios in ChNPP fuel is discussed by Mironov et al. [99] and later adapted by Raiwa [101], using an empirical relation between burnup and the $^{236}\text{U}/^{238}\text{U}$ ratio as shown in fig. 1.10b. In Mironov et al., measurements of 12 samples

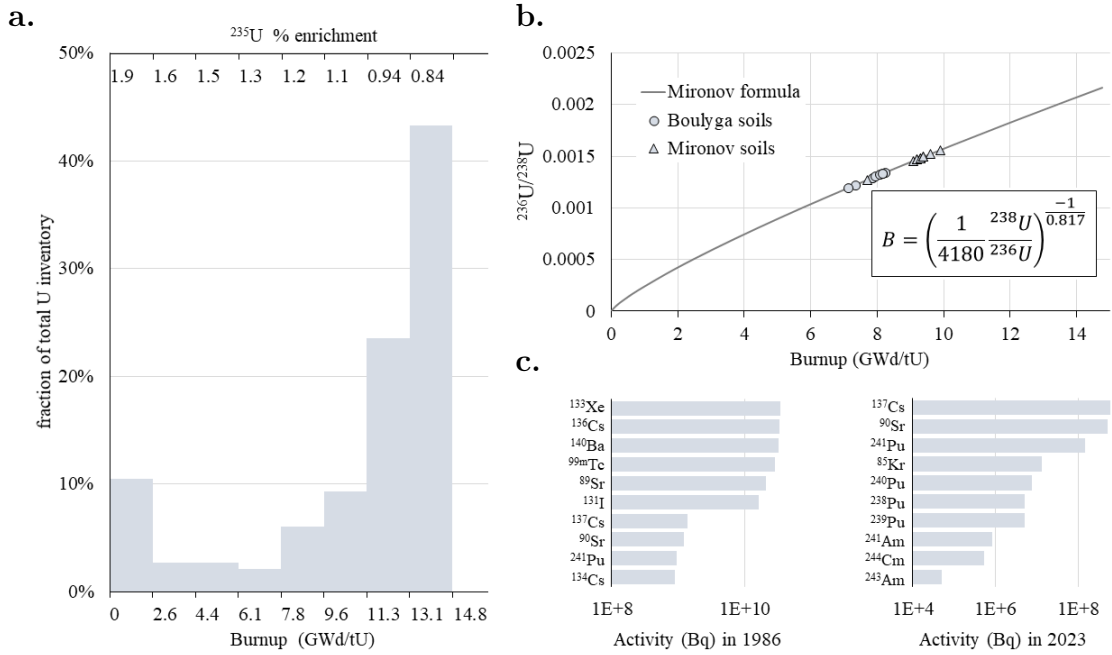


Figure 1.10: *a. Burnup distribution in fuel fractions of the ChNPP as reported by Begichev et al., adapted from Mironov et al. [99]. b. soil measurements of $^{236}\text{U}/^{238}\text{U}$ ratios in soils by Mironov et al. and Boulyga et al., with burnups as calculated by Mironov [99, 100]. c. Top ten nuclides by activity in the source term as calculated by Begichev [99], at the time of the accident and today in 2023.*

from the CEZ showed an average burnup of 9.4 ± 0.3 GWd/tU, which is a very narrow range that does not reflect the average as calculated by Begichev. Boulyga et al. similarly measured 8 soil samples with a low average burnup of 7.9 ± 0.4 GWd/tU [100]. The source terms calculated agree at least within an order of magnitude, and the results from Begichev are shown in fig. 1.10c.

For emergency management, it is important to determine the largest risk factors for exposure in both the short and long term. Figures such as the source term can be useful, but have also been misinterpreted. In a recent paper by Lopez et al. looking at sediment cores in Sweden [102], the Chernobyl $^{240}\text{Pu}/^{239}\text{Pu}$ ratios were attributed to the Kirchner and Noack source term calculations of 1988 at an exceedingly narrow range of 0.408 ± 0.003 . This is not only incorrect (the Kirchner and Noack predicted ratio is 0.563 [103]), but fails to acknowledge the far larger range of ratios measured in actual CEZ soils, from 0.3 to 0.5, though 0.4 is a reasonable average [22, 100, 103, 104]. As will be shown in this work, the variation in the reactor due to burnup results in a variation in isotope ratios in the nuclides emitted from it during the accident.

What a source term can do is give a sense of what could possibly be emitted. As seen in fig. 1.10c, the inert ^{133}Xe was the source of activity in the release. The large release of ^{131}I necessitated the limitation of milk consumption [91]. In the long-term, it is ^{137}Cs and ^{90}Sr that are of greater concern, alongside the isotopes of Pu and Am. In contrast to the Windscale and Kyshtym accidents, the full inventory of the ChNPP Unit 4 was exposed to

the environment in some degree, making it vastly more complex. Exactly how much, or in what form, is still not fully understood.

Hot Particles

The cover on the reactor was blown off in the initial explosion, and fires burned from the core. Responders initially dropped neutron absorbing boron onto the reactor core from a helicopter, though most of the material missed the actual core [91]. As noted by Guntay et al., a key characteristic of the Chernobyl accident is the amount of fuel released into the environment from the exposed core, estimated to be as much as 3.5% of the fuel [97]. Highly active (50 - 200 Bq) particles of ca. 10 μm were found in air filters in Finland, Greece, Hungary, Norway, Poland, Sweden and West Germany within days of the accident [2, 105, 106]. Two types of particles were identified: those formed from the volatile fission products that contained only beta emitters mixed with building materials, and those composed of chunks of partially irradiated fuel [107, 108]. The former were smaller, lighter, traveled further, and largely composed of short-lived fission products than the latter. These were larger, denser, and more persistent in the immediate environment. They are the focus of this work.

Most of these fuel particles are to be found in the CEZ. The preeminent authority of the topic is Valery Kashparov, who alongside Brit Salbu has written extensively on the origin and analysis of these particles [109, 110, 4, 92]. Kashparov devised the categorisation of these particles by three primary formation mechanisms:

- Fusion with the zirconium cladding in the first seconds of the accident,
- The mechanical destruction of fuel during the initial explosion,
- High temperature oxidation of nuclear fuel.

Kashparov suggests that it is the slow degradation of these particles into the environment that forms the major contamination in the wider ecosystem, particularly of ^{90}Sr . He states that 90% of the ^{90}Sr is associated with the dissolution of fuel particles, through which the Ca-like Sr can enter vegetation, surface and groundwater. In 2003 it was estimated that 0.4 to 0.5% of the inventory of Unit 4 was released in the form of particles, most concentrated in the immediate vicinity of the reactor [4]. It is contended that the U-Zr particles are found mostly in the western trace, and the highly oxidised (UO_{2+x}) particles found in the northern and southern traces. The U-Zr and non-oxidised UO_2 particles are chemically stable, with minimal leaching. The U-Zr particles are believed to be the most stable as they are less likely to be oxidized further in the environment.

These definitive categories were recently challenged by Leifermann et al. [64], whereby a blurring of these distinct categories was found, with particles displaying a mixture of characteristics. Extensive separation of particles from limited samples has shown the variety of different particle types found in the same sampling location. For instance, particles of the U-Zr type have been found outside the western trace [64]. As will also be

Class	Elements	Release assumption
1: Volatile FPs	Xe, Kr, I, Cs, Rb, Te, Cd, Ag, Sb	near total
2: Semi volatile FPs	Mo, Ba, Rh, Pd, Tc	sensitive to redox conditions, retention in vessel
3: Low volatile FPs	Ru, Ce, Sr, Y, Nb, La, Eu	weak release, increase with high burnup
4: Non-volatile FPs	Zr, Nd, Pr	limited
Actinides	U, Np, Pu, Am, Cm	limited

Table 1.1: *Release classes of elements found in irradiated nuclear fuel as described by Le Petit et al. through modelling of BWR-type reactors in the Fukushima Daiichi conditions [51].*

seen in the Fukushima accident, the categorisation of particle types is driven by what is most readily found among the samples.

1.5.2 Fukushima

In a review on the study of radioecology written in 2010, Aleksahin remarked “the ‘Chernobyl syndrome’, which seriously inhibited progress in the nuclear sector of electricity production, has been overcome to a considerable extent”. This proved to be rather over optimistic on 11th March 2011 when a 9.0 magnitude earthquake hit the east coast of Japan, shutting down the six boiling water reactors (BWRs) at the Fukushima Daiichi Nuclear Powerplant (FDNPP). The ensuing Tsunami led to a loss of cooling, causing meltdowns in units 1, 2 and 3 [51, 111], followed by hydrogen explosions in reactors 1, 3, and 4 [112]. A release classification of different elements is described by Le Petit et al., in combination with observed radionuclides in air filters in the days after the accident [51], summarized in table 1.1.

The vast majority of the release was in the form of ^{131}I (half-life 8 days), ^{132}Te (3 days), ^{134}Cs (2 years), ^{137}Cs (30 years) [113]. The shortest-lived fission products (half-lives less than a day) already decayed substantially in the reactor between shutdown and release, and noble gases ^{133}Xe (3 days) and ^{85}Kr (11 years) quickly dissipated into the atmosphere [88]. More than a decade later, it is almost exclusively ^{137}Cs , and limited ^{134}Cs , that contaminates the area, around a quarter of the release of Chornobyl [88].

From environmental analysis shortly after the accident, it was concluded that an extremely limited amount of Pu, Sr, and Nb was released in the Fukushima accident, in contrast to Chornobyl [113, 114, 88]. By ultra-trace detection, Pu derived from FDNPP has been found, though often mixed with weapons-derived Pu [113]. Work by Schneider et al. found a clear distinction between the two sources in 2 out of 20 samples: $^{240}\text{Pu}/^{239}\text{Pu}$ ratios at 0.381 ± 0.046 and 0.64 ± 0.37 . The high uncertainty reflects the trace concentration of the detected Pu, and the highly localized nature of these sources has been attributed to particulate matter [112].

The first indication of particulate matter is described in work by Adachi et al. [3], who found particles in air filters in the days after the accident. The first plume reached their institute in Tsukaba, Japan (170 km southwest of FDNPP) between 14th and 15th March, and the second plume between 20th and 22nd March. Portions of the filters were analysed using an imaging plate, and active particles were isolated through sectioning. The first particle was spherical and water insoluble, found to be 2.6 µm in diameter and 3.27 ± 0.04 Bq ¹³⁷Cs. The Cs was identifiable by X-ray analysis, alongside O, Si, Cl, Mn, Fe and Zn, suggesting the particle was mixed with building materials. Radiocesium in particles measured from the second plume had mostly attached to sulfate submicron particles, which are easily dissolved.

More such microparticles, named CsMPs, have been found since. Ikehara et al. estimated a high abundance of particles of at least 0.06 Bq in soils within the contamination plume [115, 116]. The highest abundance was found closest to FDNPP sampled in 2012, with 300 particles/g of soil, though a second sampling nearby in 2017 found less than 10 particles/g. This reduction suggests a high mobility of the particles over time, particularly due to their clay-like composition, in both size and silicate content. Indeed, the majority of writing on Fukushima hot particles is from samples taken in 2011 - 2012, and analysed in subsequent years.

Particle Types

The small spherical particles of around 2 µm that have been described by various authors [3, 117, 59, 118, 119] have been categorised as ‘type A’ particles. Assuming a particle of almost entirely silicate (> 80% as noted by Satou et al. [59]), with a density of 2.65 g/cm³, a spherical particle with a diameter of 2 µm would have a volume of $\frac{4}{3}\pi r^3 = 4.2 \times 10^{-12}$ cm³, so on the order of 1×10^{12} Bq/g. Lower activity spherical particles have also been found on the order of 10 mBq [120] with diameters in the 10 µm range, reducing the specific activity to 1×10^7 Bq/g.

These have been named ‘type E’ particles by Macsik et al., in contrast to the non-spherical particles type ‘B’ and ‘C’, which have similar or lower specific activities to type A particles [59, 60], and the glassy particles with Cs-inclusions named type ‘D’. Non-spherical particles are reported in sizes from 4 µm, 17 Bq [119] to 6 µm, 67 Bq [59], to 460 µm, 3.8 kBq [60] and the glassy particles > 500 µm, 2.5 MBq [121].

A distinction is made in between ¹³⁴Cs/¹³⁷Cs activity ratios at the time of the accident reflecting the source term of the reactor, where particles with ratios > 1.0 are attributed to reactor Unit 2 and 3, and < 1.0 are attributed to Unit 1. Particles derived from Unit 1 were released earlier, and are considered to be larger and lower in specific activity [116, 60]. Particles from Unit 2 and 3 have the higher specific activity associated with type A particles [60], and it is proposed that Unit 3 is the more likely source of particles as it was damaged to a larger extent [116].

As with the Chernobyl particles, such a categorisation is necessarily incomplete, and at

times confusing. Morphologically we can speak of spherical and non-spherical particles. The particles can be grouped by specific activity under the assumption a common formation process produced the same type of particles. We can speak of $^{134}\text{Cs}/^{137}\text{Cs}$ activity ratios, but only as long as those remain detectable with the decay of ^{134}Cs . Advanced analytical techniques have identified ^{90}Sr [60], U [117], and Pu [122] in some of the particles. In the following section we will discuss these techniques, and their ability to assess a particle's morphology, chemical form, and isotopic composition.

1.6 Summary

In this chapter, the occurrence of nuclear material in the environment was introduced. Certain isotopes from actinides are found in the environment with natural origin, while others are purely anthropogenic. Major events that released nuclear material include the atmospheric tests conducted between 1950 - 1970, which form most of the Pu measured in soil today known as global fallout, characterised by a $^{240}\text{Pu}/^{239}\text{Pu}$ ratio of 0.18.

In civil nuclear applications, a large variety of isotope ratios can be found, related to the enrichment of fuel, burnup and irradiation in the reactor, and reprocessing. The identification of a particular material coming from a specific origin is known as nuclear forensics, and requires knowledge of each step of the nuclear fuel cycle. Initial enrichment, neutronics (flux, fluence, energy), and time, are the main drivers of isotope ratio variation in the actinides and fission products.

A number of accidents with released nuclear materials were discussed. Chornobyl and Fukushima were discussed in detail, differing in their respective release of material, in the form of gas and hot particles. In Chornobyl, the hot particles are associated with fuel fragments formed in different stages of the accident. This included the initial explosion, and subsequent fires lasting many days, resulting in some particles that were highly altered in structure, and some that were simply ejected from the reactor. In Fukushima, the hot particles were formed with high concentrations of radiocesium, largely without the fuel. Multiple types of particles have been identified, though the main type are spherical microspheres made up largely of silicate, with a minimum activity of 10 mBq.

Chapter 2

Hot Particle Analysis

The analysis of hot particles depends in many cases on the aims of the investigation and the methods available. In the following chapter, the analysis methods of previous hot particle studies, deriving from Chernobyl, Fukushima, and other sources such as Dounreay, Windscale, Palomares, and Maralinga, will be presented. A combination of radiometric, microscopy, X-ray, and mass spectrometric analyses will be discussed, laying out the merits and limitations of each technique. Radiometric analysis is suited to radionuclides of the highest activity, microscopy gives insight into the size and morphology of the particle, X-ray analysis can identify elemental composition or chemical structure, and mass spectrometry can separate the analyte by atomic mass. When these techniques are spatially resolved, such as autoradiography, they are referred to as mapping or imaging techniques.

Isotope ratio analysis can be done either by specific activity of the nuclide, or by mass spectrometry. This work focuses on resonance ionisation mass spectrometry, RIMS, for element-selective isotope ratio analysis of CEZ hot particles. The theoretical principles for the technique will be presented. Different methods of mass spectrometry are discussed, as they differ both in mass separation and ion generation. Laser ionisation techniques are based on atomic spectroscopy, targeting the unique electronic structure of a given element. Resonant and non-resonant ionisation are discussed in the context of nuclear materials analysis. Isotope effects must be taken into account, such as the isotope shift, and odd-even effects deriving from hyperfine structure. The choice of excitation schemes largely depends on available lasers, and intent of the analysis. In isotope ratio analysis, an ideal scheme is efficient, accessible, and maximally suppresses isobars.

2.1 Motivation for Analysis

Human Health

The risk of hot particles to human health is primarily in the length of exposure - a particle that passes through the body is less dangerous than a particle that gets stuck. The primary exposure pathways are then ingestion and inhalation, which are affected by the solubility of a particle. The greatest risk is to the lungs, where insoluble particles are difficult to

remove. Pulmonary fibrosis, caused by the inhalation of insoluble particles of any form, is well documented as an occupation hazard among those working with fine dusts, including coal miners, construction workers, agricultural workers, and ceramicists [123, 124]. For the inhalation of hot particles, the radiation adds to the risk of fibrosis, malignant tumor growth, or both [125]. Calculations by Harrison et al. determined that a particle of 30 μm could reach the upper bronchial airways, and the smallest particles of 3 μm could access the alveolar region [78].

Cases of plutonium-induced lung fibrosis (PuLF) were observed in 188 employees (38% female) at the Mayak Production Facility [126]. As reported by Azivova et al., the majority (94%) of these workers started in the plant between 1948 and 1955, and were diagnosed with PuLF a decade later, just under a third of whom died of lung cancer [126]. Protective equipment against the aerosols they were working with was not introduced until 1957. Similar reports were made from the workers exposed to aerosolized Pu at Rocky Flats, part of the American weapons production facilities [127].

Deaths in Chernobyl were not attributed to particles in lungs, but rather to external exposure from the reactor accident. Very small ($< 1 \mu\text{m}$) particles of 5 kBq $^{239,240}\text{Pu}$ were found in autopsies by Vlasov et al. in the lungs of workers who died of acute radiation sickness from the Chernobyl accident. In that study, the lungs of deceased workers who used a respirator, or were in a location in the plant with minimal particle exposure, did not have any particles in their lungs. A couple of particles were also found in three inhabitants of villages in Belarus, who were witnesses to the accident and “died in 1990 - 1992 due to different reasons” [107]. The total intake of these persons was 13 Bq from $^{239,240}\text{Pu}$, though there was evidence of slow clearance through the alveolar region. It was concluded that the inhalation of particles should not have had health effects on those persons.

No reports of particle-related health outcomes have been reported in Fukushima, however work by Matsuya showed that DNA damage in lung tissue could be observed when intentionally exposed to Fukushima-type CsMPs [128]. The isotopic, physical and chemical composition, and mobility of a particle is therefore important to assess its risk for tissue damage. A Pu particle of mainly alpha-emitters will impart dose differently to a Cs particle of only beta/gamma emission, and depend on the equivalent dose of the affected organ. As noted in modelling by Poudel et al., self-shielding may occur in Pu particles of sufficient size, where fibrotic tissue may encapsulate it, effectively shielding the surrounding organ [125]. The damage incurred is then a function of the emitted radiation. Particles from nuclear fuel, as in the CEZ and Dounreay, will contain radionuclides of all decay modes. Fukushima-type CsMPs will contain only ^{137}Cs . Newman et al. concluded that, after controlling for the effects of age, smoking and asbestos exposure, lung fibrosis was observable at lung doses exceeding 10 Sv [127].

In the case of the Dounreay particles (made of spent MOX fuel), Harrison et al. concluded the majority were too large to even enter the lung by inhalation. Doses received through ingestion were predicted to be minimal due to the insolubility of the particles, which would

likely pass straight through the digestive tract [78]. The most likely exposure pathway was determined to be skin contact, which for a particle of 10^5 Bq ^{137}Cs , may result in ulceration after 7 hours. At the rate of one particle washing up on shore every month (see fig. 1.8), it would be very unlikely for a member of the public to be in such close contact, the most likely scenario being a particle getting lodged in someone's ear [78, 129].

Radioecology and Nuclear Forensics.

The persistence of hot particles in the environment necessitates a detailed investigation into their composition and methods of degradation. Studies on particle composition therefore focus on their chemical structure and consequences for their transfer to the ecosystem. Critical work by Byrnes et al. notes that the environmental impact assessment of the Dounreay particles should further consider smaller particles and impacts on biota [130]. They point to work on mussels intentionally exposed to Dounreay particles, which found that particles could be retained for long periods with potential for necrosis [131].

As noted earlier, the dissolution of hot particles is a primary source of ^{90}Sr and actinide contamination in the Chernobyl Exclusion Zone [4]. The mechanisms through which these particles are exposed to the environment are dependent on their chemistry. Particles can be studied through dissolution experiments which measure the conditions under which certain elements are leached out [64, 92]. As the legacy of nuclear activities continues to expand and age, analysis of particles provides information into what was released, and what may be released in the future.

As detailed in the previous chapter, nuclear forensics offers identification of the source of the material, and the nuclear processes that formed it. The microscopic nature of hot particles makes it difficult to assess these characteristic isotopes, requiring the need for advanced analytical capabilities. Structural analysis can identify major components, where cladding materials such as Zr, Nb, and Al are characteristic of the reactor design [130]. The identification of high U concentration however may be insufficient. In cases such as the smuggling of nuclear materials, radioactive materials may be incorporated into scrap metal, or natural uranium [48, 132]. The following section details the variety of techniques employed, and purpose of the analysis.

2.2 Radiometric, Microscopy, and X-ray Techniques

The initial analysis of a particle starts with finding it in the first place. The term 'hot' was initially proposed due to the bright spots left on autoradiography film, as measured after the Trinity test [1, 42]. Autoradiography is still the primary technique to identify Cs-rich particles from FDNPP [3, 115, 118, 120, 133].

In the early days of the Chernobyl accident, particles were found on air filters through autoradiography, and analysed with secondary electron microscopy (SEM) and gamma

spectrometry [2, 105, 134]. The first detection of the accident fallout was in Sweden on 28th April 1986, where the $^{137}\text{Cs}/^{134}\text{Cs}$ gamma activity ratio was measured by Devell et al. to determine that the particles were indeed deriving from a reactor and not from weapons [2]. This ratio was also used to estimate burnup [2, 95, 134]. The particles initially reported by Devell et al. were spherical 1 to 2 μm particles composed largely of fission products, though ^{239}Np , indicating fuel, was reported in one particle.

The presence of U was identified by Saari et al. by electron dispersive spectroscopy (EDS), which is typically done in tandem with SEM imaging [134]. The SEM can image the particles, and simultaneously provide an elemental composition through EDS [3, 59]. Majority components (0.1 to 1 wt%) can then be identified [134, 122]. Two of the Windscale particles were measured in 1992 by McMahon et al. with SEM, gamma and beta spectrometry [65]. Imaging is key in identifying the morphology of a particle, as in the categorisation of the CEZ particles [109, 135, 136], and Fukushima particles [60, 120]. Particles have also been identified by the sharp peak in activity seen by autoradiography or gamma spectrometry without further imaging [115, 137, 76].

Short-lived isotopes can be identified with gamma spectrometry in the immediate release of the particles [2]. Within a year, this is limited to ^{106}Ru , $^{134,137}\text{Cs}$, ^{144}Ce , $^{154,155}\text{Eu}$ and ^{241}Am . Of these, ^{144}Ce , ^{134}Cs , ^{106}Ru disappear within a decade [60, 116, 64, 2]. For analysis of Sr and Pu, beta and alpha spectrometry are required respectively [65, 136]. The activity ratios between $^{137}\text{Cs}/^{90}\text{Sr}$ has also been used as an indicator of burnup in Windscale and in Dounreay [65, 129]. This measure is complicated by chemical separation of the two elements, either by preferential leaching in the environment or, as for instance in Fukushima, a lack of Sr in the particle formation process [60]. For a more accurate source term by radiometric means, the $^{137}\text{Cs}/^{134}\text{Cs}$ activities should be used, as this is a measure of neutron flux characteristic to the reactor [60, 122]. As noted earlier, this method is time-sensitive, and is no longer possible more than a decade after the accident.

Advanced analysis: TEM, μXRF , XANES, and EXAFS

In recent years, particle analysis has focused on its microstructure. Improvements in SEM and transmission electron microscopy (TEM) techniques, alongside focused ion beam (FIB) cutting of particles have revealed the heterogeneity of such particles on the nano-scale [122, 119, 138, 139]. Micro X-ray fluorescence (μXRF) can map elements at concentrations of 10s of ppm [117, 140, 139, 121, 130], far more sensitive than EDS. Additional X-ray techniques include X-ray absorption near-edge spectroscopy (XANES) and extended X-ray absorption fine structure spectroscopy (EXAFS), which allow investigations of chemical speciation and oxidation states [141, 142, 130, 139, 122, 121, 143].

While radiometric analysis is good for identifying and characterizing a sample, especially in bulk where even the U isotope ratios can be determined [144], it is limited to the strongest emitters in very small particles. Typically, the timing and location is sufficient to assign an origin of the particle. In a recent finding of presumed hot particles in a lake sediment in

Finland, Appleby et al. concluded they “almost certainly” originated from Chernobyl [137]. The results found two particles that contained ^{137}Cs (64 ± 4 mBq and 266 ± 15 mBq) and one contained ^{241}Am (17 ± 2 mBq), meaning it might contain ^{241}Pu . Without isotope ratios however, their exact origin cannot be determined.

2.3 Mass spectrometry

The use of mass spectrometry (MS) gives access to ultra-trace nuclides regardless of activity because it is only sensitive to atomic mass. In MS, the analyte is ionised in some manner, and passed through a mass separator¹. The methods of ionisation include the use of thermal, electric, optic, plasma, and sputtering processes. The mass separators may use magnets, quadrupoles and octopoles, time-of-flight, or combinations thereof [145]. The mass resolution is determined by the separation of two masses, given by $m/\Delta m$. Because the analyte is charged, masses are noted by m/z , such that a doubly charged ion would appear at half its mass. A singly charged $^{238}\text{U}^+$ would appear at its atomic mass, $m/z = 238.05$, slightly heavier than the mass number 238 because of the effects of binding energy.

The main challenge in MS is mass interference, which can be avoided through increased mass resolution, chemical separation, or both. In the example of measuring the $^{241}\text{Pu}/^{239}\text{Pu}$ isotope ratio in nuclear fuel, there are multiple sources of possible interference. The first is environmental, deriving from molecules of organic and inorganic compounds found in soil, through which various signals could appear at $m/z = 239$ and/or $m/z = 241$.

The second is isobaric, where ^{241}Am and ^{241}Pu have the same mass number. To separate these two nuclides based on the atomic masses of the two isobaric nuclides $m_{Am,Pu}$, one would require an extremely high mass resolution of

$$\frac{m}{\Delta m} = \frac{m_{Pu}}{m_{Pu} - m_{Am}} = \frac{241.056850}{241.056850 - 241.056827} = 1 \times 10^7, \quad (2.1)$$

where most mass spectrometers are limited to the order 1×10^4 . The third source of interference is of elemental hydrides, oxides, and dioxides. In the above example, hydrides ^{240}PuH and ^{238}UH found in nuclear fuel would interfere with ^{241}Pu , and ^{239}Pu respectively. The following examples will show how MS techniques for the analysis of environmental radioactivity address these challenges.

Destructive: ICP-MS, AMS

The most accessible form of isotope ratio analysis is inductively-coupled plasma mass spectrometry (ICP-MS). The technique is ideal for liquid samples, requiring that the sample be fully dissolved [146] or extracted from the sample matrix. The sample matrix can be anything from soil [61], to fish and wild boars [30], or a single hot particle [64]. Chemical separation routines are the preferred technique to avoid isobaric interference, with protocols

¹The reader is directed Gross' excellent book on MS techniques for further reference [145].

for Pu [84, 22], U [100, 43], Cs [61, 30]. Gas reaction cells can target certain elements in adaptations such as ICP-QQQ-MS, which can further enhance isobaric suppression [61].

With ultra-trace isotopes such as ^{238}Pu , even extensive chemical separation may be insufficient to remove the isobaric ^{238}U , the ratio $^{238}\text{U}/^{238}\text{Pu}$ in RBMK fuel being on the order of 10^6 [46]. Combinations of ICP-MS techniques with radiometric techniques are therefore required, targeting the alpha-emitting ^{238}Pu [46]. ICP-MS (and variants thereof) is a destructive, but highly sensitive and versatile technique, and relies on the successful chemical separation/purification of the analyte.

The foremost technique for sensitivity is accelerator mass spectrometry (AMS), which is fully destructive and achieves its selectivity by very high mass resolution [147]. It is better suited to some elements due to their electron affinity, and has been used to great effect in studies of Pu isotope ratios in soils [104, 25]. The preciousness, smallness, and morphological complexity of hot particles make these techniques limiting. The risk of losing valuable information in destructive analysis is high, which makes non-destructive techniques preferable.

SIMS and RIMS

To combine both imaging and mass spectrometric analysis on solid samples, we therefore look to secondary ion mass spectrometry (SIMS). Not all SIMS is spatially resolved [121, 122], nor is all SIMS non-destructive (static SIMS is only destructive to the first atomic layers, while dynamic SIMS sputters through a sample in nanometre increments). Fallon et al. demonstrate the use of spatially resolved NanoSIMS on a synthetic U particle that was partly enriched, and partly depleted U [132]. Particle analysis with SIMS on Palomares particles showed homogeneous distribution of major actinide nuclides $^{235,238}\text{U}$ and $^{239,240}\text{Pu}$, but dissolution and ICP-MS was required for accurate isotope ratios without interference [39]. The isobar on 241 remains an issue in SIMS analysis, as shown by Betti et al. where conclusions could not be drawn on $^{241}\text{Pu}/^{239}\text{Pu}$ [48]. Similar results were obtained from Fukushima particles, which could show $^{135,137}\text{Cs}$, but could not resolve the interference from $^{135,137}\text{Ba}$, and so not provide accurate isotope ratios [121]. However, in work by Kurihara et al., ratios obtained this way for U and Pu showed no significant interference and matched theoretical predictions [119, 122].

The success of SIMS is dependent on the minimization of interference. This can be achieved by having a very clean sample, or else a sample of such size that environmental interference is insignificant. The aims of analysis are equally important. The $^{235}\text{U}/^{238}\text{U}$ ratios may be the only requirement, as in Fallon et al. [132]. Minor Pu interference, or hydride interference on ^{236}U , will then be insignificant. As will be shown in subsequent sections, the analysis of multiple elements simultaneously offers views into a particle that may not be possible with one element alone. With the addition of resonant laser ionisation, the inherent advantages of SIMS are further enhanced.

The principles are based on laser spectroscopy techniques for studying atomic and nuclear structure [148, 149, 150, 151], but have been extensively used in analysis of complex materials such as nuclear fuel [152]. In the context of mass spectrometry for the purpose of sample analysis, we speak generally of resonance ionisation mass spectrometry (RIMS) [153, 154, 155], or specifically (resonant laser) secondary neutral mass spectrometry, (rL-)SNMS [156, 138]. Lasers tuned to resonant transitions are directed into a cloud of neutral atoms, which target the electronic structure of a given element to step-wise excite it beyond the ionisation potential, or just below it to a highly excited Rydberg state [153, 157].

RIMS instruments differ in the method of generating neutral atoms (from quasi non-destructive to fully destructive, spatially resolved or not), the lasers and excitation schemes used to ionise elements, and the mass spectrometers used to measure them. Bulk samples have been analysed by Wendt et al., such as radiostrontium in air samples contaminated in the Chernobyl accident [158], and Pu isotopes in CEZ soils [153]. Savina et al. investigated U, Pu and Am isotopes in spent fuel segments [159], as well as fission products Sr, Mo, and Ru [66]. Radiocesium has been investigated on Fukushima particles by Sakamoto et al [138], with imaging of natural Cs distribution in biological samples made possible by RIMS [160].

Chernobyl hot particle analysis in Hannover began with the development of the rL-SNMS instrument by Franzmann et al. [156, 161, 162]. Applications of laser schemes developed by Raeder, Kneip et al. [163, 164] were applied [165, 166], and the analysis of a single isolated CEZ hot particle by Bosco et al. demonstrated the ultra-trace, isobar-free detection of ^{238}Pu and metastable ^{242m}Am [167]. Further analysis of particles was conducted by Raiwa et al., who used novel laser designs [164] for fast switching between elements [168, 101]. Building on recent work [169], the following will show how multi-element isotopic analysis on a large collection of particles demonstrates the wide-ranging capabilities of the RIMS technique for the purposes of nuclear forensics.

2.4 RIMS

RIMS has been developed in part for its advantages in the analysis of nuclear materials. It offers high efficiency, advancing the detection limits of trace isotopes, and offers high isobaric suppression through its elemental selectivity. Methods differ in the generation of neutral atoms from a sample, laser design, and mass spectrometry, each providing different strengths.

2.4.1 Mass spectrometry

The choice of mass spectrometer affects the achievable mass resolution, ranging from $m/\Delta m \sim 600$ for a quadrupole MS as used in University of Mainz [151], and up to $m/\Delta m \sim 10,000$ for ToF-SIMS as used at the University of Hannover [168], Lawrence Livermore

National Laboratory [170] and Kogakuin University [138], though it is often lower in RIMS applications. The principle of ToF-MS is demonstrated in fig. 2.1. Two positive ions of different mass $m_1 < m_2$ are extracted into the free drift path. Given the same electric energy E_{el} of the ions with charge z at potential U , their kinetic energy ($\frac{1}{2}mv^2$) will be equal to their electrical energy according to

$$E_{el} = ezU = \frac{1}{2}m_1v_1^2 = \frac{1}{2}m_2v_2^2. \quad (2.2)$$

The ions both travel the same total distance s , therefore the respective velocity v and flight time t is given by

$$v_1 = \frac{s}{t_1}, v_2 = \frac{s}{t_2}, \quad (2.3)$$

such that the difference between the two masses Δm

$$\begin{aligned} \Delta m &= 2E_{el} \left(\frac{1}{v_2^2} - \frac{1}{v_1^2} \right) \\ &= \frac{2E_{el}}{s^2} (t_2^2 - t_1^2). \end{aligned} \quad (2.4)$$

The mass resolution is therefore limited by the total travel distance, and the spread of energy upon extraction. In a reflectron ToF-MS, ions curve around as shown in fig. 2.1, both in order to double the flight path, and compensate for energy spread. The ion source could also affect the resolution. In solid sample analysis, changes in energy may derive from matrix effects, such as crystal structure with high binding energies. Topographical changes, a 20 μm crater in the sample for instance, could extend the flight path of ions and increase the time-of-flight.

Enhancements in mass resolution can be achieved through improved ion optics, gas jets, traps, and other techniques employed at beamline facilities [150, 171, 67]. Such bespoke instruments may take up a large footprint, whereas a (commercial) ToF-SIMS is quite compact. As will be shown in this work, the ToF-RIMS technique is both sufficiently sensitive while also being incredibly versatile, an asset in solid-state environmental analysis.

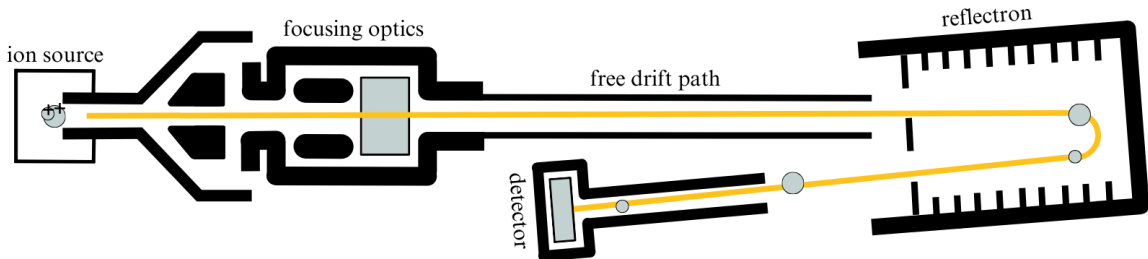


Figure 2.1: Time of flight mass spectrometry with reflectron, where two positive ions with $m_1 < m_2$ enter the ToF-MS at the same energy E , and arrive with $t_1 < t_2$.

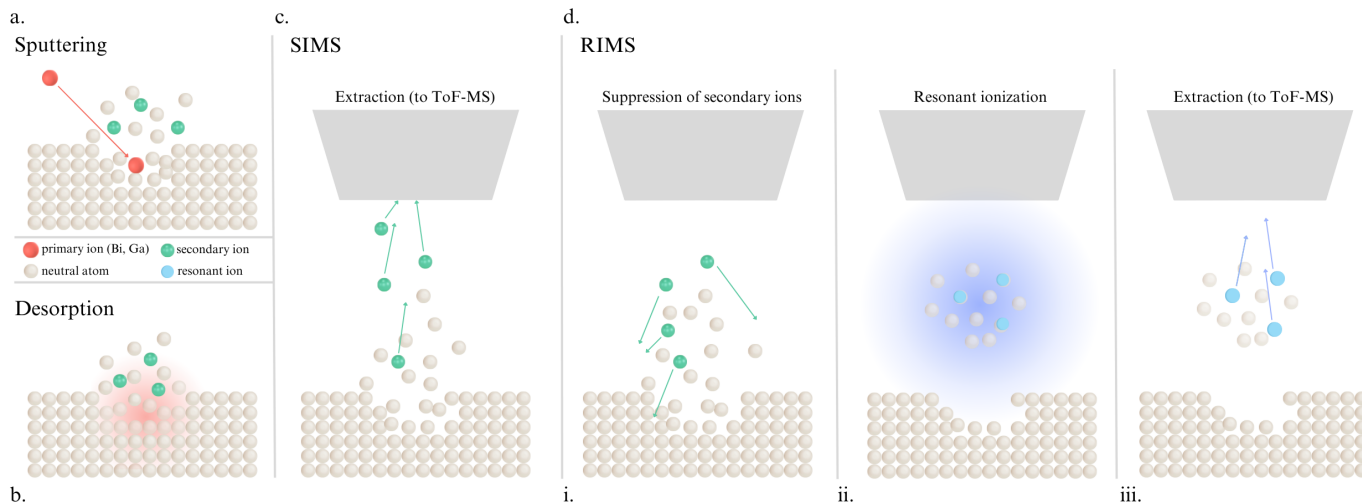


Figure 2.2: *ToF-SIMS/ToF-RIMS with sample probing via sputtering or laser desorption. a. The primary ion beam (Bi in SIRIUS, Ga in LION and Kogakuin), probes the top atomic layers of the sample surface, releasing secondary neutrals and ions. b. Laser desorption releases secondary ions and neutrals. c. SIMS mode analysis extracts all secondary ions into ToF-MS. d. RIMS mode analysis i. suppresses secondary ions, ii. resonantly ionises remaining neutrals, iii. extracts resonant ions into ToF-MS.*

2.4.2 Ion production

The ToF-SIMS/ToF-RIMS technique is demonstrated in fig. 2.2. The first atomic layers of a sample are probed to create secondary ions and neutrals either through sputtering (fig. 2.2a) or laser desorption (fig. 2.2b). In sputtering, a primary ion beam of Bi or Ga is typically used, depending on the ToF instrument. The choice and set up of the primary ion gun determines the energy imparted into the system, and the amount of analyte being sputtered. A gas-cluster ion beam (GCIB) such as Ar is frequently used to polish the sample surface, or else sputter through nano-layers of the material for depth profiling. The sample surface and composition is therefore important to the sputter yield achieved. Charging effects on the surface will deflect the primary ion beam, while matrix effects (such as crystal structure), may lead to high binding energies that decrease the effective yield.

Laser desorption with a nanosecond laser can be done in IR or UV with variable input power. The process is a mixture of light-matter interactions and heating, which are affecting, and affected by, the sample's surface chemistry. This requires a continuous adjustment of the laser power to ensure a constant signal, but is not affected by charging effects. Heat must also be fully conducted through the sample and sample holder, else risking destruction of the sample. One major advantage of this method, alongside increased signal, is the selective ionisation made possible by the heating mechanism. Analogous to thermal ionisation mass spectrometry (TIMS), elements with the lowest ionisation potential (group 1 elements Na, K, Rb, Cs), can be somewhat selectively ionised in SIMS mode at low desorption laser power.

In SIMS, the secondary ions are extracted into the ToF. In RIMS, a delay is required between the primary pulse and extraction pulse so that the secondary ions are suppressed,

the lasers are then pulsed so that the neutrals are resonantly ionised and then extracted into the ToF-MS. Approaches differ based on the cycle time and capabilities of the instrument (see fig. 2.3) for SIRIUS and LION.

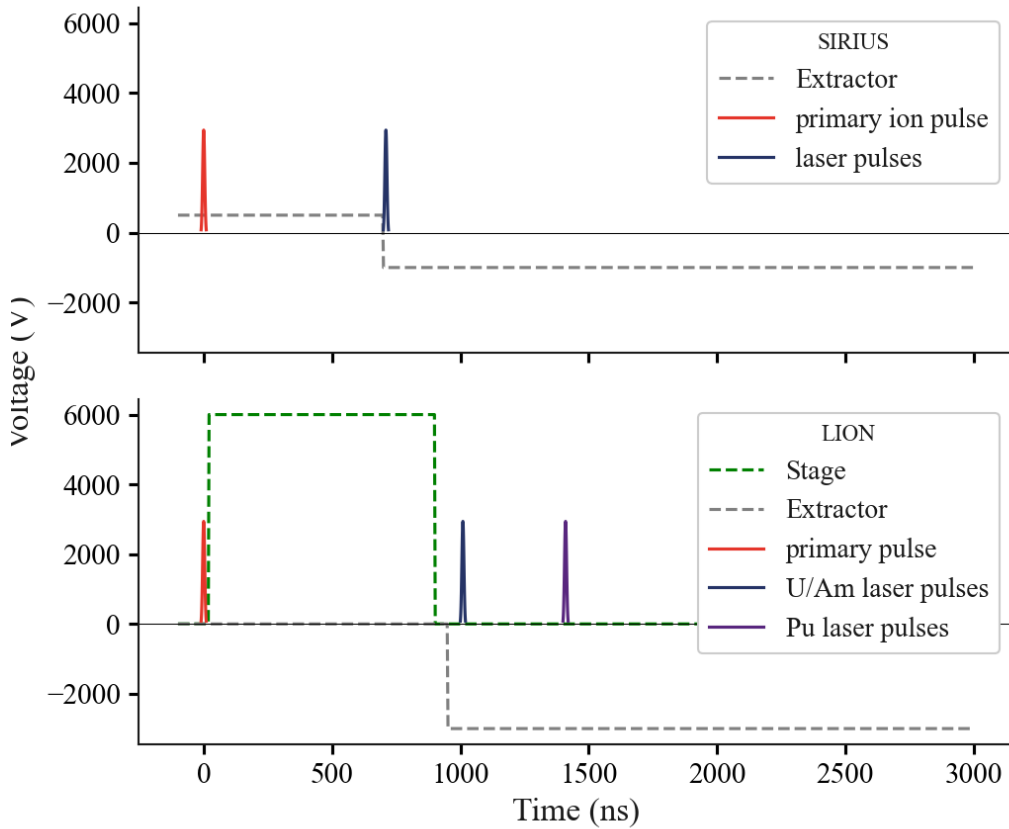


Figure 2.3: RIMS timing for the SIRIUS and LION in the first 3 μ s. LION utilizes the delay in the second set of lasers to separate U and Pu masses by 1 to 1.5 m/z [159]. The full cycle time for SIRIUS is 100 μ s (10 kHz repetition rate), and for LION 1000 μ s (1 kHz).

The SIRIUS instrument operates at 10 kHz, and LION operates at 1 kHz. In fig. 2.3, only 3 μ s of the cycle time is shown, 3% of the cycle time in SIRIUS, and 0.3% of the cycle time in LION. Where the SIRIUS instrument has a narrow window of interaction time with the neutral cloud, LION allows for temporal separation of laser pulses. Resonant lasers for elements U and Am are sent in first, and the Pu lasers sent in later. This results in a m/z shift of 1 or even 1.5, separating resonant ^{238}Pu from resonant ^{238}U [159].

Generally, the more a sample is consumed, the higher the achievable sensitivity. The desorption laser power can be increased to the point of completely destroying the sample, which may be necessary in the case of particularly small grains [172]. The RISIKO instrument in Mainz uses destructive methods to ensure high signal output for the purposes of laser spectroscopy. The sample is resistively heated in an atom beam oven to create a neutral cloud [164, 151, 152], resonantly analysed, and separated again in a QMS. In the SIRIUS instrument, the use of the GCIB for depth profiling can also eventually destroy the sample after many hours.

2.4.3 Laser ionisation

In RIMS, elements are selectively ionised from a cloud of neutral atoms by step-wise laser ionisation. Each element's electronic structure has a large number of excited energy states, typically with a lifetime on the order of 10 ns. The wavelength of the laser corresponds to the energy between one state and the next. The first laser excites an electron to the first excitation step (FES), and a second laser can excite it beyond the ionisation potential to a highly excited Rydberg state, or an auto-ionising state (AI) in the continuum. Alternatively, a less energetic (red) second laser can excite it to a second excitation step (SES), whereupon a third laser ionizes it.

Atomic structure

The principles of atom-light interactions and laser spectroscopy are described in numerous works, from which the following is adapted [173, 174, 162]. These interactions are characterized by the quantized energy levels of the individual electrons, described most essentially by the atomic number Z and quantum number n such that

$$E_n = -\frac{\mu Z^2 e^4}{8\epsilon_0^2 h^2 n^2} = -Ry \frac{Z^2}{n^2}, \quad (2.5)$$

where Ry is the Rydberg constant comprising the reduced electron mass μ , the charge e , is the permittivity of free space ϵ_0 , and Planck's constant h . The Rydberg constant is equal to the ionisation energy of the ^1H atom at 13.6 eV (i.e. ionisation potential IP). Each energy level is further described by the angular momentum quantum number l and magnetic quantum number m , and spin quantum number s . Such states can be found computationally, but are increasingly complex with the interaction between electrons (>90 in the actinides), and relativistic effects. Though advances are being made in theoretical calculations, experimental spectroscopy is still essential for finding atomic states [150].

Once a state is found, it can be driven by a laser of a wavelength equal to the energy of the transition, given by the photon energy

$$\Delta E = \hbar\omega = \frac{hc}{\lambda}, \quad (2.6)$$

where ω is the frequency, or inverse of the wavelength λ times the speed of light in vacuum c . The transition/laser energy can also be expressed by the wavenumber $\frac{1}{\lambda}$ in cm^{-1} . In RIMS, one or two of these intermediate states are excited stepwise by lasers of wavelength λ to ionise an atom beyond the ionisation potential to some auto-ionising (AI) state whereby a free electron and ion remain.

An excitation step is defined by the transition width described by the full-width half maximum a Lorentzian function. The FWHM Γ is defined by the transition's natural lifetime τ

$$\Gamma = \frac{1}{\tau}, \quad (2.7)$$

such that the Lorentzian energy distribution $P(E)$ around the transition energy E_0 becomes

$$P(E) = \frac{1}{2\pi} \frac{\Gamma}{(E - E_0)^2 + (\frac{\Gamma}{2})^2}. \quad (2.8)$$

This transition is broadened by Doppler effects due to the atoms being in motion when undergoing the transition, and power broadening effects from the laser itself. The transition measured in spectroscopy is then a Voigt profile, a convolution of the Lorentzian transition and the Gaussian broadening mechanisms.

As noted earlier, the atomic states of a given element are determined by their electronic structure. For actinides in particular, the ground state orbitals 5f, 6d, and 7p give access to a large number of states, which can overlap between elements [150]. In RIMS, a transition must therefore be sufficiently narrow to discriminate between elements, and efficient enough to produce high yields [164, 168].

An ionisation scheme is therefore a set of excitation steps that excite the target element beyond the ionisation potential. The schemes used in this work are summarized in fig. 2.4. Group one elements such as Cs have very low ionisation energy, and so less energy is required to ionise it. The actinides are all close in ionisation potential. Not every scheme is strictly resonant, as shown in the Ba and Cs schemes; while such schemes are feasible, they are inefficient.

Non-resonant ionisation

Non-resonant ionisation occurs through multiple mechanisms. Multi-photon absorption of photons is less probable than resonant ionization, though increases with atom concentration (such as ^{238}U in spent fuel) and high photon density (increased laser power). Molecules, such as oxides, have rotational and vibrational degrees of freedom. Their interaction with photons is more continuous, and can lead to ionization, dissociation, or simply absorption. Experimentally, UO_x is non-resonantly ionised more readily by higher energy (blue to UV) and more intense laser light [168, 175]. By photon-dissociation of UO_x , non-resonant U^+ is produced that contributes to the signal on $m/z = 238$ [176].

The non-resonant ionisation of ^{238}U is a limiting factor in nuclear materials analysis, as it dominates most sample matrices. Limiting photon density is an option by reducing the laser power, or increasing the interaction region of the lasers and neutrals. This however comes at the cost of resonant ion signal, and reduces the signal-to-noise ratio. As will be shown further in this work, the use of lower energy (red/IR) lasers further decreases non-resonant signal, but does not eliminate it. In the following section, experimental

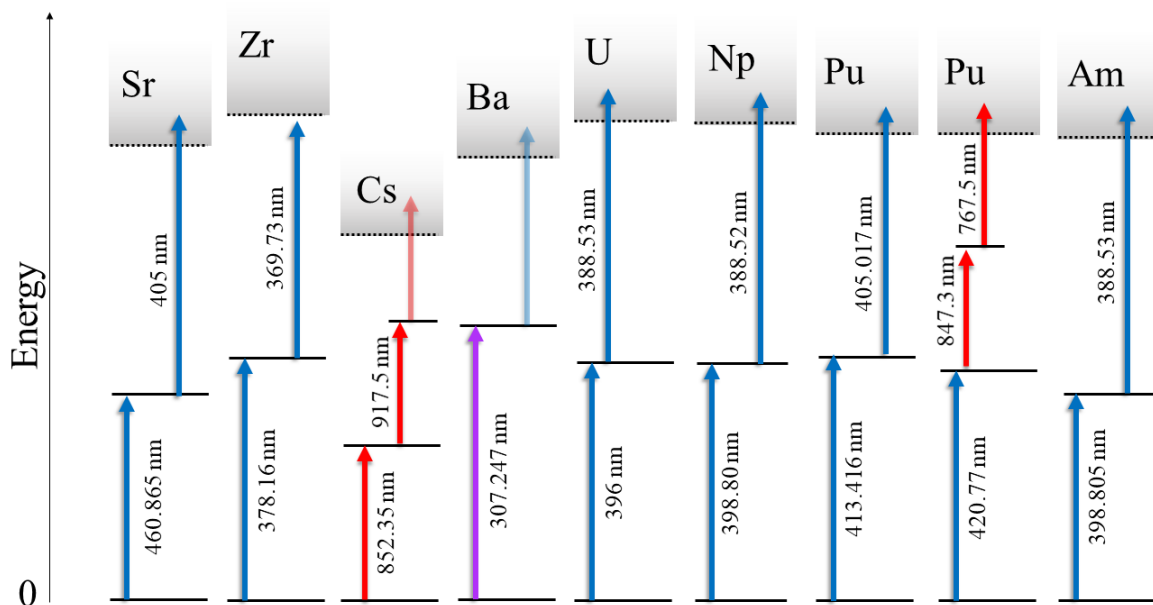


Figure 2.4: ionisation schemes used in this work for the elements Sr, Zr, Cs, Ba, U, Np, Pu, and Am. The colour of the transition indicates the colour of the laser, where purple is a UV laser.

methods will be described to accommodate for these interactions.

Isotopes: mass/field shifts and odd-even effects

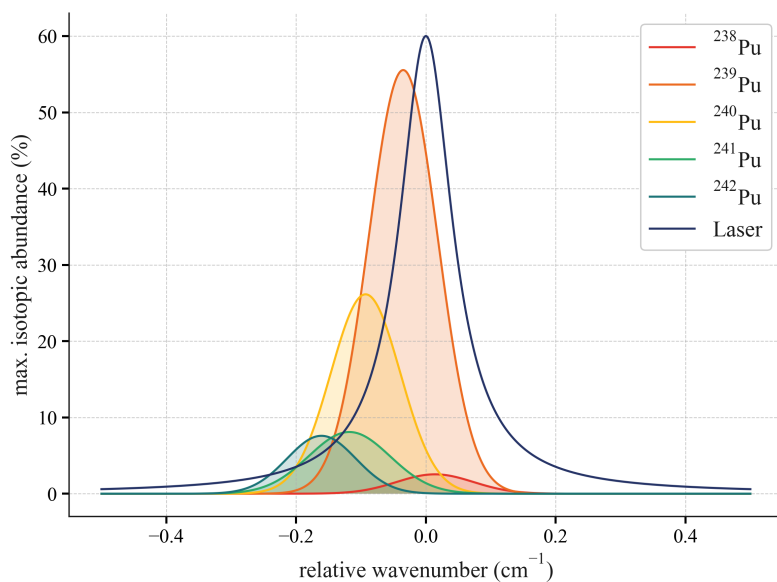


Figure 2.5: Modelled distribution of plutonium isotope abundance in the plutonium standard described in [167], with the isotope shift and transition widths (Gaussian) as measured in the FES [168]. The laser is modelled as a Lorentzian, set to a wavelength of 413.416 nm ($24188.700 \text{ cm}^{-1}$), with a laser linewidth of 0.1 cm^{-1} .

The electronic structure is not completely independent of the nucleus. Isotope shifts are introduced by changes in mass and distribution of charge in the nucleus. Mass shifts are more significant in lighter elements, caused by changes in the reduced mass of the electrons (normal mass shift) and changes in electron-electron correlations (specific mass shift). The field shift, or the spatial distribution of nuclear charge, is more significant in the heavier elements. Highly precise measurements of the isotope shifts therefore give key insights into atomic and nuclear structure [149, 150], which can be probed with extremely narrow linewidth lasers to separate each isotope.

In RIMS, by contrast, the aim is to measure all isotopes of a given element simultaneously. The isotope shift therefore presents a challenge, as shown from the Pu isotope shift measured in the SIRIUS instrument in fig. 2.5. The broad bandwidth of the laser results in broad transitions. The laser is broad enough to cover the majority of the isotope shift, but not every isotope equally, resulting in fractionation of the isotopes in mass spectrometry.

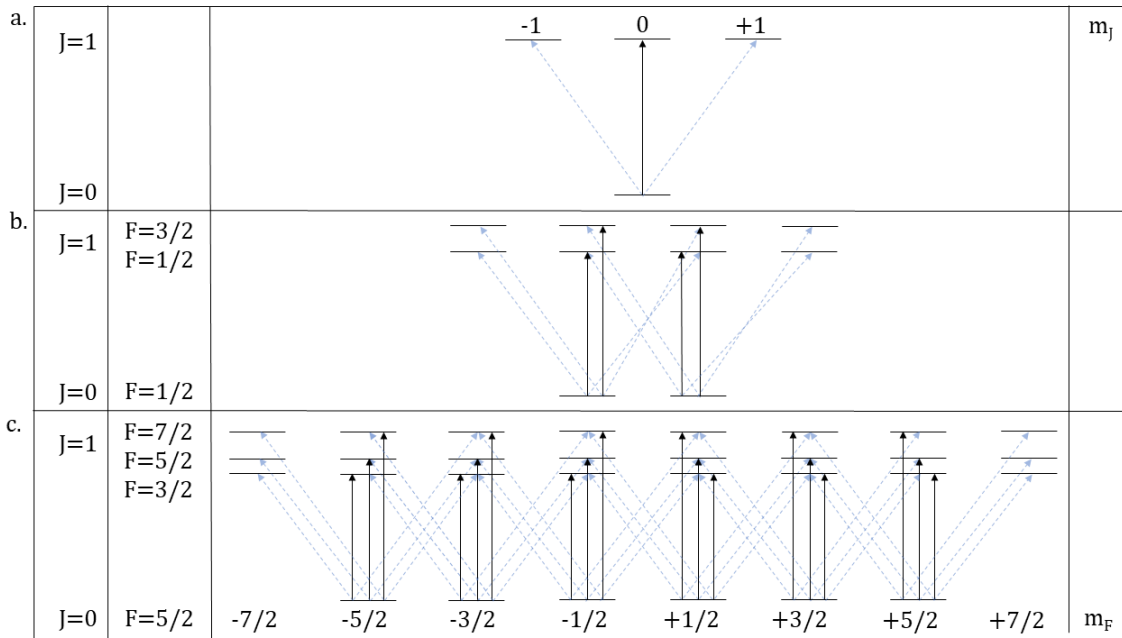


Figure 2.6: Allowed transitions under selection rules for linearly polarized light (black arrows) when $J = 0 \rightarrow 1$ and $\Delta m_{J,F} = 0$, and for non-linearly polarized light (dashed blue arrows) when $J = 0 \rightarrow 1$ and $\Delta m_{J,F} = \pm 1$. a. for even Pu isotopes $I = 0$, b. for ^{239}Pu where $I = 1/2$, c. for ^{241}Pu where $I = 5/2$.

Further fractionation is seen in the isotopes ^{239}Pu and ^{241}Pu . Even isotopes consist of pairs of nucleons, whereas odd isotopes have an unpaired nucleon, resulting in a non-zero nuclear spin I . The nuclear spin creates degeneracy in the energy state, coupled to the electron angular momentum J for a total of $(2J + 1)(2I + 1)$ magnetic substates m_J when $I = 0$, and m_F when $I \neq 0$. These substates can only be resolved with ultra-narrow bandwidth lasers, and otherwise result in a broadening as seen for ^{241}Pu in fig. 2.5.

The degeneracy of the odd isotopes further results in fractionation due to the selection

rules of electric dipole transitions. The parity must change, the orbital angular momentum may change only such that $\Delta J = 0, \pm 1$ (where $0 \leftrightarrow 0$ is not allowed), and its quantum number under linearly polarized light cannot change, such that $\Delta m_{J,F} = 0$.

As shown in fig. 2.6, in the $J = 0 \rightarrow 1$ transition (the only one allowed), fine splitting in even isotopes of Pu results in three degenerate states: $m_J = -1, 0, 1$, whereby only 1 of those 3 states, $m_J = 0$, is possible with linearly polarised light. For odd isotopes, additional transitions are made accessible with non-zero I , equal to $1/2$ for ^{239}Pu , and $5/2$ for ^{241}Pu . In linearly polarized light, $\Delta m_F = 0$. Even still, the transition probability is increased to 4 of 6 states for ^{239}Pu , and 18 of 24 for ^{241}Pu [177]. The odd-even effect is therefore a suppression of even isotopes, minimised in a transition where $\Delta J = +1$.

This odd-even effect in Pu RIMS measurement, and its dependence on polarity, is explored in more detail for the three-step transition by Bosco et al. [165]. It confirms that even isotopes are suppressed in contrast to the odd isotopes, most significantly ^{241}Pu . Naturally, $\Delta J = +1, \Delta m_{J,F} = 0$ drastically increases the allowed transitions in odd isotopes, making the odd-even effect more pronounced. This can be useful, as shown by Niki et al., where the odd isotopes of Gd were separated from the even isotopes, with the purpose of enriching the neutron poison ^{157}Gd [178].

2.4.4 Laser design and scheme selection

Author (Scheme developer)	Pu schemes (cm^{-1})			Pu schemes (nm)			IS from ^{238}Pu to ^{242}Pu (cm^{-1})			Laser linewidth (cm^{-1})
	FES	SES	AI	FES	SES	AI	FES	SES	AI	
Raiwa (Kneip)	24188.70		24690.31	413.416		405.017	0.17		0.04	0.1
Voss (Blaise)	25959.85		24572	385.210		406.97	0.09		/	0.004
Voss (Köhler)	25775.56		24162	387.965		413.87	0.24		/	0.004
Grüning (Savina))	23766.18	11802.59	13028.81	420.766	847.272	767.530	0.42	0.27	0.01	0.1 ((0.2-0.3))
Galindo-Uribarri ()	23765.98	12211.30	12613.62	420.77	818.91	792.79	/	/	/	0.1-0.2
Bosco (Raeder)	23766.11	11802.59	13329.14	420.77	847.27	750.24	0.364	0.178	0.09	0.2
Bosco (Kunz)	23766.11	12371.63	12653.67	420.77	808.3	790.28	0.364	0.102	0.087	0.2

Table 2.1: Studies done on plutonium excitation schemes and the isotope shift. Raiwa [101] and Bosco [166] measured the isotope shift on the SIRIUS instrument in Hannover based on schemes developed by Kneip [164], Raeder [163] and Kunz [179]. Voss et al. [180] performed high resolution laser spectroscopy at the IGISOL facility in Jyväskylä on only the first excitation step for plutonium, based on energy levels identified by Blaise [181] and Köhler [182]. Savina et al. at LLNL [159] use the scheme developed and characterised by Grüning [183] but with lasers of larger linewidth. Galindo-Uribarri [184] at ORNL only studied ^{242}Pu , so no isotope shifts were investigated.

A laser operates on the stimulated emission of a single wavelength λ , whose linewidth

should match the resonant transitions in atoms (0.01 to 0.1 cm^{-1} , 0.3 to 3 GHz). The Ti:Sa solid state laser has a broad emission range, typically from 700 - 950 nm , and can be frequency doubled (350 - 470) and tripled (230 - 310). In a classic design, the cavity mirrors can be changed to narrow the range of output wavelengths [162]. Alternatively, broad spectrum mirrors can be used, with a grating in place of an end mirror [101]. The angle of this grating determines output wavelength, enabling flexible and automated switching.

The frequency can be doubled internally, or externally. Internal frequency doubling has the advantage of quick switching between schemes, and significantly higher output power. However, the angle of the doubling crystal must be adjusted throughout operation. External frequency doubling has the advantage of power and wavelength stability due to the minimal changes in the cavity, at the cost of slower switching between schemes.

Each element is unique in its isotope shift, saturation power, and selectivity. For an element such as Sr, it is evident that isobaric Zr is sufficiently suppressed, and it has a broad transition that covers the full isotope shift [185]. An element such as Pu is more difficult, as seen earlier with the isotope shift and odd-even effects. Furthermore, isobaric U poses a serious barrier to the measurement of ^{238}Pu . This has led to several plutonium schemes having been found and used, collated in table 2.1. The two-step schemes require only two lasers, while the three-step schemes have advantages for selectivity.

Each scheme needs to be empirically tested on the RIMS instrument, whose laser bandwidth will affect the transition width, saturation power, isobar suppression, and final signal-to-noise ratio. The following chapters will detail the SIRIUS and LION instruments, and how different schemes were used to optimise isotope ratio analysis on hot particles.

2.5 Summary

In this chapter, methods for hot particle analysis were presented. Hot particles present a risk to human health and the environment, as they form persistent sources of radiation. Analysis methods focus on the particle structure, chemistry, and isotopic composition. The identification of particles is predominantly done through radiometric means, through autoradiography, or through isolation and gamma spectrometry. The particles are visually investigated through optical and electron microscopy, and elemental components can be identified through characteristic X-rays. Major components can be identified through EDS, while more advanced techniques such as μXRF can target trace elements as well.

Chemical analysis of hot particles can be done by investigating the particle's oxidation states through X-ray probing (EXAFS, XANES), or via its dissolution behaviour in various conditions. Isotope ratio analysis through gamma and beta spectrometry can identify sources of origin, but are limited by either time due to short half-lives, or by the chemical separation of the radionuclides.

Mass spectrometry techniques can measure both stable and unstable nuclides. ICP-MS, AMS, and TIMS are adept at isotope ratio analysis, though each element requires a tailored chemical preparation and separation method. This limits the possibility for multi-element analysis. In ToF-SIMS, static analysis is quasi non-destructive, and allows for solid sample analysis. However, since no chemical preparation is done, mass interferences from molecular compounds and isobars prevent much isotope ratio analysis.

RIMS, through its element selectivity, is uniquely suited to the challenge of analysing nuclear materials. Laser ionisation targets the electronic structure of a given element for selective ionisation. Each element presents unique challenges for RIMS analysis, including its efficiency and suppression of isobars. The concepts of isotope shift and the odd-even effect were introduced, as well as resonant and non-resonant ionisation.

Chapter 3

Sampling and Analysis

The analysis of nuclear material in the environment has two requirements, first that it be found and isolated, and the second that it be measured. The following chapter will consider the sampling methods employed in both Chernobyl and Fukushima, two very different sites. It will then focus on a technical description of the RIMS method, the SIRIUS and LION instruments, and the analytical procedure for different elements and isotope ratios.

3.1 Sampling and Particle Isolation

3.1.1 Chernobyl

Sampling in the CEZ was conducted in 2014 and 2017 [186, 187]. Locations were chosen based on their geographical interest, proximity to ChNPP, and accessibility. As seen in fig. 3.1, four locations were chosen. B, in the town of Pripyat, is so named for the drill core (Bohrkern, or BK) used to do the sampling. The location was chosen for its urban environment and being in the northern trace of the accident release. R, in the red forest (or Roter Wald, RW), is the only sample done in the western trace [4]. As the sample size was small, only a few particles were found here. C, sampled on the banks of the cooling pond (or CP), was sampled by grabbing a handful of silt. The cooling pond is slowly draining over time, as can be seen by the white outline of the pond visible in the map in fig. 3.1. This makes it an interesting sampling location to assess the particle types found in the aqueous environment, particularly as pertains to their Cs leaching behaviour. K, sampled in Kopachi (or KOP), is outside both the north and western trace, and is an open field that was formerly cultivated but has since been abandoned.

The sample preparation is described in further detail by Weiss, Leifermann, and Weissenborn in their respective works [64, 189, 190, 191]. In short, the separation method primarily uses the high density of the hot particles, which are made almost entirely of uranium oxides. Using a solution of polytungstenate, soil samples are centrifuged and subsequently bisectioned for the highest activity. The most promising soil is then stuck onto a carbon stub, which is investigated further in the SEM. Again, the density of the particles is used to its advantage as back scattered electrons (BSE) reveal the densest particles among the soil. The primary composition of U is confirmed by EDS, with a

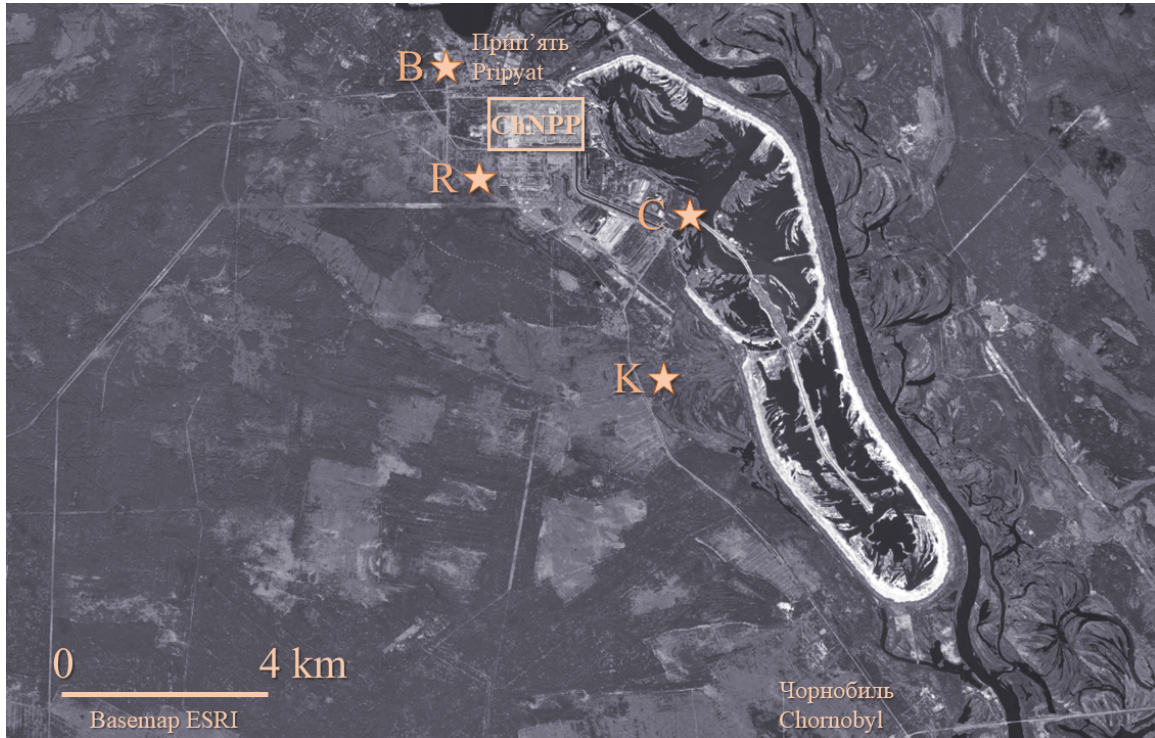


Figure 3.1: *Sampling locations by Schulz and Hamann [187, 186] in the Chornobyl Exclusion Zone, basemap ESRI [188].*

characteristic M_{α} X-ray peak for U at 3.164 keV.

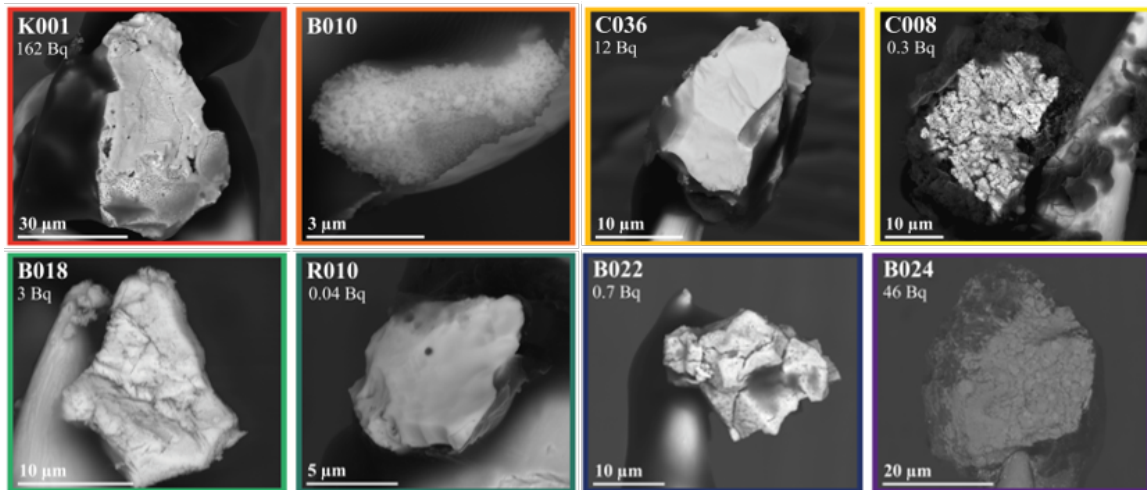


Figure 3.2: *Back scattered electron (BSE) images of eight particles from the CEZ, extracted via methods developed by Weiss and Leifermann [64], and labelled by origin (B: Pripyat, K: Kopachi, C: Cooling Pond, R: Red Forest). The total $^{137}\text{Cs} + ^{241}\text{Am}$ activity is given in Bq. For the rest of this paper, data points are colour coded to the specific particle.*

Once located, the particle is extracted from the soil matrix by a custom-made tungsten needle, with a tip diameter of $< 10 \mu\text{m}$ [64]. The tungsten needle is manoeuvred in the SEM with EDS detector (Philips XL30 and SDD-Detector, remX GmbH) by a micromanipulator (MM3A, Kleindiek Nanotechnik), and dipped into charge-sensitive glue

(SEMglu, Kleindiek Nanotechnik). This glue tipped needle is then carefully placed on top of the identified particle, and left to harden under the electron beam. Once cured, the needle is lifted, with the particle safely secured on the tip. Further EDS analysis can then reveal any major components in the particle (up to 1% in total composition), such as identifying Zr-bearing particles. Morphological analysis via SE and BSE imaging can categorize the particle based on size and ‘type’ as described by Kashparov et al., and further investigated by Leifermann et al. [64].

A selection of particles, analysed in both the SIRIUS and LION instruments, are shown in fig. 3.2. The coloured borders correspond to later work on the isotope ratios measured in each of these particles. Each particle is labelled according to its sampling location from fig. 3.1. Particles K001 and RW010 were shown by EDS to contain Zr, thus identifying them as U-Zr particles. B024 is characteristic of high burnup structure, deriving from the release of fission gases in the ceramic structure of nuclear fuel [192]. B018 and C036 are the least porous particles, though C036 is uniquely smooth on the surface. These three particles may then be categorized as unaltered fuel fragments. B022 and C036 show aggregate formations, associated with high oxidation, labelled by Kashparov as UO_{2+x} type particles [4].

Categorization is important to inform subsequent analysis of the particle, with non-destructive methods such as gamma spectrometry and RIMS. Destructive analysis is the final analytical step. The particle can be dissolved for ICP-MS analysis, or heated for thermal decomposition analysis of volatile gases [64]. In leaching experiments, the particle is sequentially suspended in solutions of various acids and combinations thereof, to determine under what conditions such particles may dissolve or disassemble [64].

3.1.2 Fukushima

The Fukushima accident was fundamentally different primarily because the release of radionuclides did not include fuel particles. Rather, volatile fission products like Cs interacted with the surrounding melted concrete. Droplets then condensed as spheres, forming Cs-MPs. These particles were found very quickly after the accident, on trees and crop coverings [118], but also in soil [133, 115]. Such particles cannot be separated by density, as they are primarily formed of silicate. Some particles contain so much Cs as to be found via EDS [3], though the most characteristic quality is their spherical shape, easily seen in a soil matrix.

Autoradiography is the most common method of identifying radioactive hotspots [133, 115, 3, 118, 120]. This has been well used in cases such as Macsik et al. where particles were identified on blades of grass [120]. Hotspots are removed and then looked at in SEM/EDS for further analysis. They can be isolated, measured with gamma spectrometry, and subsequently dissolved for mass spectral analysis. In this work, samples were analysed from previous sampling campaigns, and new sampling conducted by the author in Fukushima in 2023, shown in fig. 3.3, summarized in table 3.1.

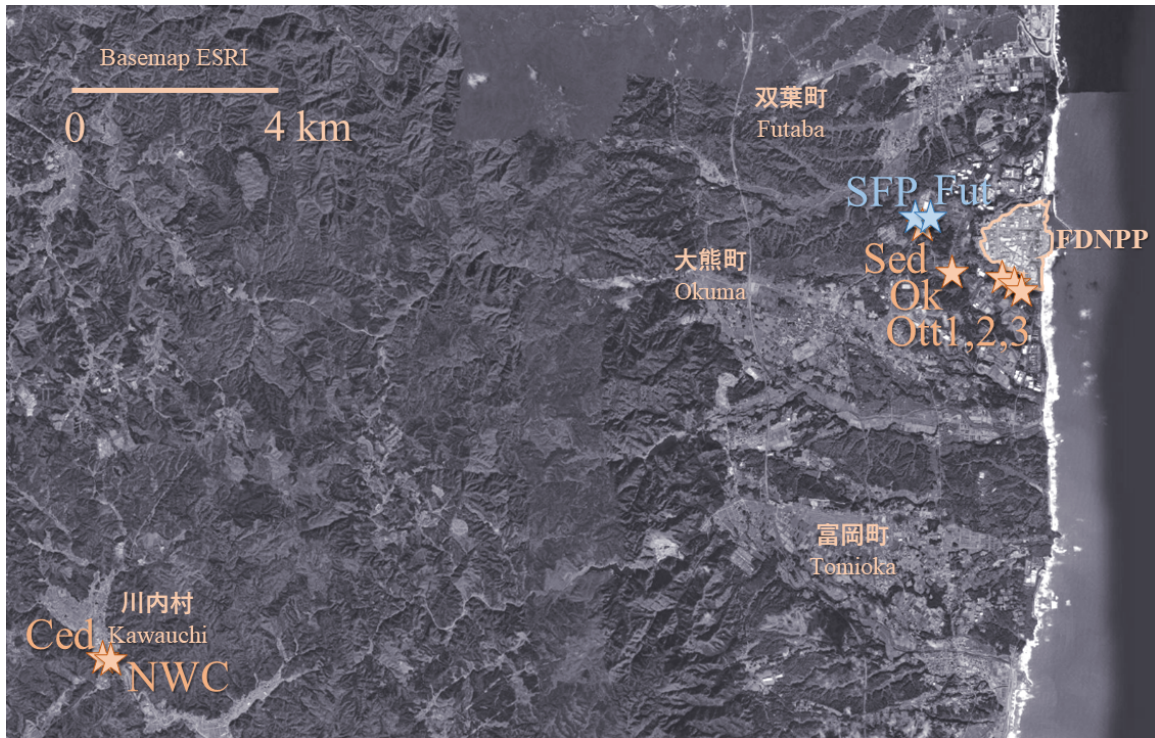


Figure 3.3: *Sampling locations near the Fukushima Daiichi Nuclear Powerplant (FDNPP), basemap ESRI [188]. Samples taken by author in blue in March 2023, see tab 3.1 for further details.*

Sample name	Description	Sampling location	Sampling date
Ott 1	Soil 630 Bq/g 0 - 2 cm	Ottazawa	Sep 2017
Ott 2	Soil 800 Bq/g 0 - 2 cm	Ottazawa	Sep 2017
Ott 3	Soil 3380 Bq/g humic substance	Ottazawa	Aug 2016
Ok	Soil 0 - 2 cm	Okuma	12 Feb 2021
Sed	Pond sediment 12 - 13 cm	Futaba	Dec 2021
SFP	Soil 0 - 10 cm	Futaba	Mar 2023
Fut	Soil 0 - 10 cm	Futaba	Mar 2023
Ced	Cedar branch	Kawauchi	Aug 2011
NWC	Non-woven cloth	Kawauchi	Aug 2011

Table 3.1: *Sampling locations and descriptions near the Fukushima Daiichi Powerplant. Ottazawa samples provided by Hirofumi Tsukada, Okuma and Shimofukuzawa Pond sediment provided by Yoshifumi Wakiyama, cedar branch and NWC samples provided by Takashi Saito (previously analysed by Yamaguchi et al. [118]), Futaba samples sampled by the author.*

A range of sampling dates and locations are represented. Active decontamination efforts are ongoing in the area around the FDNPP [193]. The primary strategy is to dig up the first 5 cm of soil. Regular sampling by Fukushima University’s Institute for Environmental Radiation has taken place in the years since the accident, some of which were made

available for hot particle search.

The Ottazawa soil samples were taken around the perimeter of FDNPP in 2017. They have a very high specific activity, in the range of 1×10^2 to 1×10^3 Bq/g. Soil samples in Okuma, and sediment samples from Shimofukuzawa pond, are regularly taken in places with low specific activity, with these samples collected in 2021. We carried out additional sampling in March 2023, which prioritized hotspots near Shimofukuzawa pond with substantially high dose rates ($> 30 \mu\text{Sv/h}$, in an area where it was typically 2 to 5 $\mu\text{Sv/h}$). The samples were separated into four sections: top (T), middle (M), bottom (B) and general (G), a mix of leftover soil. Additional samples were investigated in which particles had been found in 2011 [118]. This included a cedar branch (with auxiliary branches) ca. 20 cm in length, and a set of fibres from non-woven cloth, from Kawauchi, a town 30 km west-southwest of FDNPP.

Sample preparation

The soil samples were dried and sieved at 64 μm . A gram of the remaining sample was then dusted over a strip of carbon tape to achieve a single layer, which was measured with autoradiography overnight. As shown in fig. 3.4, hotspots in the soil can be identified with this method, which can then be cut out and placed onto an aluminium stub for subsequent analysis in the SEM, EDS, and in gamma spectrometry. The autoradiography machine used for this purpose was the GE Amersham FLA 9500, based on phosphorimaging technology. This image plating technique use a photosensitive crystal that promotes electrons to a higher energy band when exposed to radiation. A laser scanner then de-excites the electrons, producing photo-stimulated luminescence that is captured to form an image [194].

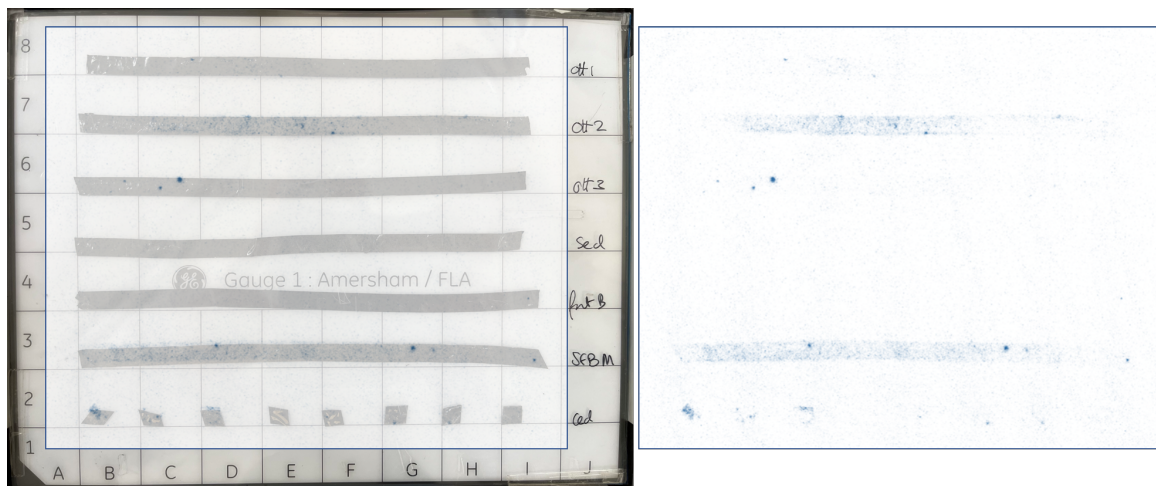


Figure 3.4: Soil samples dusted onto carbon tape and imaged with GE Amersham FLA 9500 Typhoon autoradiography imaging device. The image plate is A4 size, with each reference block (A - J, 1 - 8) being 2×2 cm.

A typical measurement requires that the plate be ‘recharged’ by exposing it to light for 20 minutes. The image plate is A4 size, and is placed on top of the samples with a layer of plastic in between, and left for a period of time. Three hours was recommended as the

minimum time for this sample type [195], though periods of two weeks are recommended for better resolution [133]. The exposure time depends on the activity of the sample and the desired resolution. The autoradiography technique is ideal for large sample areas, and can scan the images with 50 μm resolution [196]. For the best results, a point source of known activity should be used to calibrate the images. ImageJ software can analyse relative intensities of hotspots, which could then be calibrated to specific activities. However, at the time of analysis such a standard was not available.

The cut out hot spots were placed onto SEM stubs, and measured together for two weeks to assess relative activity, shown in fig. 3.5. The specific activity of the different samples is clearly visible in the intensity of the different hotspots and surrounding soil. Generally, hotspots are visible that are distinguishable from the surrounding soil. In two of the Fut T samples, the surrounding soil has a very high specific activity, in contrast to the other samples. Some hotspot extractions were unsuccessful, as in the Fut B samples and one of the Okuma samples. The analysis of the cedar leaves shows a hotspot on each leaf section.



Figure 3.5: Hotspots identified with autoradiography imaging isolated onto SEM stubs, labelled with sampling location. The stubs were exposed altogether for a week, showing the relative intensity of the hotspots.

Particle identification

The samples with identified hotspots were then analysed in the SEM, to look for characteristic spherical micro particles, and larger particles which may contain sufficient Cs to be seen in EDS. Though relatively clean-looking in the cm range of the IP analysis, in the μm range of the SEM the carbon tape is littered with soil particles of no radiological

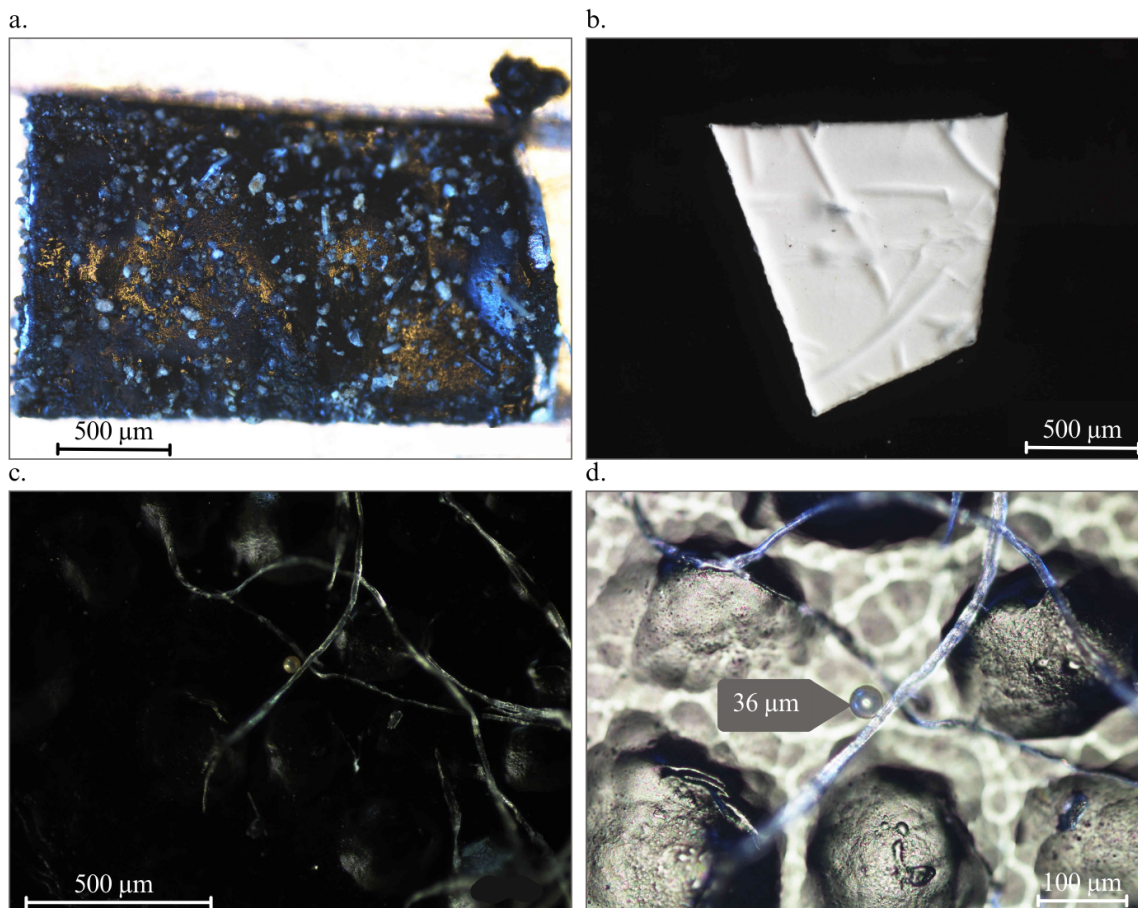


Figure 3.6: *Optical images of Fukushima samples (Eclipse LV-DAF, Nikon). a. Soil on carbon tape, sliced out of the highest activity fraction (0.9 Bq) of Fut M stub in 3.5. b. Teflon wrapping paper from sample NWC-016K, cut to smallest active piece (0.6 Bq). c. Fibres from NWC-016J, with sphere d. Sphere on fibre, measured to be 36 µm, no activity measurable upon isolation.*

interest. Many particles include steel and other iron-rich compounds, which are high in both density and disappointment. Majority silicate particles are also common, though did not contain substantial Cs. Gamma spectrometry revealed each stub to contain less than 1 Bq of ^{137}Cs activity per stub. The Fut M sample was shown to have the highest activity, and was cut into a smaller section of $< 1\text{mm}$ in length. In the optical microscope images in fig. 3.6a, it is seen how, even in a small area, there are many soil particles. No hot particles were identified through EDS or RIMS. As will be shown in the following sections, an activity of 1 Bq per particle is required for successful RIMS. In these soil samples, the contamination is distributed across all the soil in a heterogenous manner. Rather than from hot particles, the Cs contamination likely derives from wet deposition in rainfall following the accident.

The threshold activity for RIMS analysis in SIRIUS has been measured for Am as 1×10^7 atoms, based on a single particle of 20 µm. Extended to ^{137}Cs , a particle of 1 Bq would contain 1.4×10^9 atoms, and is therefore taken as a threshold value for viable analysis in RIMS. Further analysis was conducted on the NWC samples, in which ‘hot’ fibre segments

were wrapped in teflon-coated paper. The packages were of 1 to 6 Bq activity, and the fibres separated from the paper and then measured via gamma spectrometry. When measured to contain a minimum activity over 0.5 Bq, the samples were then subdivided into two parts, and measured again. This bisectioning method was continued until only a scrap of paper of $< 1 \times 1$ mm was left, as shown in fig. 3.6b. No particles were identified on this piece of paper with an activity of 0.6 Bq. The particles could be extremely small and therefore unidentifiable, or the contamination could be limited to dissolved radiocesium.

This method was successful on one single occasion, in which a spherical particle was found attached to a fibre as shown in figures 3.6b,c. The particle was subsequently imaged in SIMS, confirming it to be a silicate particle, shown in fig. 3.7. In fig. 3.7a,b, the SIMS images of the total secondary ion signal are shown in spectrometry and fast imaging mode. In fig. 3.7c, the Si ion signal is seen in spectrometry mode. In d. Cs RIMS is attempted on the particle, through which only ^{133}Cs was identified, with a large tailing obscuring other isotopes of Cs. The particle was then extracted via the method used for Chernobyl particles described above, and measured with gamma spectrometry. No Cs signal above background was measured. The activity associated with the fibres was therefore not derived from this particle. The size and shape of the particle could however be consistent with the sub 10 mBq ‘Type E’ particles described by Macsik et al., given its 36 μm diameter.

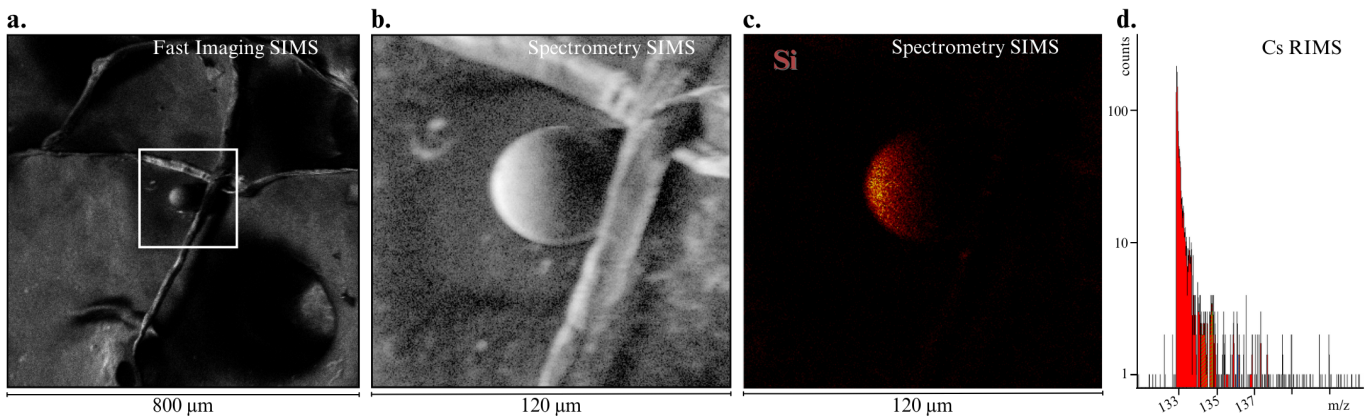


Figure 3.7: *Silicate microparticle identified from NWC-016J sample a. Total secondary ion signal in ToF-SIMS fast imaging mode, b. Spectrometry mode imaging focused on the particle at $120 \times 120 \mu\text{m}$, causing some distortion of the spherical shape c. Si^+ mapping of particle, d. Cs RIMS mass spectrum on $40 \times 40 \mu\text{m}$ window, showing resonant ^{133}Cs with large tailing.*

Cs extraction

These samples indisputably contain radiocesium as shown in the autoradiography and gamma measurements. However, in the search methods described above, no particulate form was found with sufficient concentration. It was suggested that perhaps the radiocesium could be extracted from the soil and deposited as droplet to then be analysed by RIMS in solid form.

This method requires that 1 g of soil, with 1×10^2 to 1×10^3 Bq of ^{137}Cs , be microwave digested in concentrated acid (15 ml) to dissolve all organic material. The remaining soil that is not digested is filtered out. The solution is then reduced down to a minimal volume (1 ml) at a slow pace to avoid boiling off the Cs, and is then dropped/dried onto an aluminium stub with a small-volume pipette (5 μl) for a total of 1 ml. The target volume of 1 ml was not reached because of the high concentration of minerals in the solution, resulting in a highly viscous brown liquid resembling caramel. A single droplet could be dried on a stub, 2000 μm in diameter, with < 1 Bq of activity measured by gamma spectrometry.

A new approach would be to extract the Cs from the solution before reducing it. As described by Zok and Staeger [61, 30], Cs extraction resins such as ammonium molybdophosphate (AMP) and potassium nickel ferrocyanate (KNiFC) in polyacrylnitrile (PAN) matrix are highly efficient extractors of Cs. These come in small grains (ca. 100 to 1000 μm), which are typically dissolved post extraction for analysis in ICP-MS and associated methods. While its microcrystalline structure makes it unfavourable for direct analysis in ICP-MS, it could be used in RIMS in solid state analysis, which additionally benefits from the element-selective approach to suppress interfering compounds from the resins.

Single grains of both AMP-PAN and KNiFC PAN (Triskem International) were submerged in the remaining 45 ml of solution. The 500 μm grains absorbed 1 to 2 Bq each, which in their large size is insufficient for RIMS measurement. This method shows some promise for Cs extraction, but relies on high specific concentration in the grain that could perhaps be attained by further chemical experimentation with the acidity of the solution. It may be that the natural Cs content in the soil far exceeds the radiocesium, whereby the grains are quickly saturated. To work, the grain size would have to decrease by an order of magnitude, while ^{137}Cs concentration would need to increase by an order of magnitude. Though beyond the scope of this work, it may as yet become an interesting method for the creation of solid materials out of liquid samples for the purpose of RIMS analysis.

While ultimately unsuccessful in finding hot particles in this case, the RIMS method still has a lot to offer for the ongoing decontamination and decommissioning of the FDNPP plant and surrounding area. As will be shown in the following chapters, the isotope ratios in melted fuel in particular tell a nuclear history that is comprehensive and accessible in this breadth by RIMS.

3.2 RIMS Analysis

3.2.1 SIRIUS

The SIRIUS instrument in Hannover has been previously described in various works by Franzmann, Bosco, and Raiwa [161, 167, 168, 101, 162, 166]. The instrument uses the ToF-SIMS capabilities of a commercial instrument (TOF.SIMS V from IONTOF), with

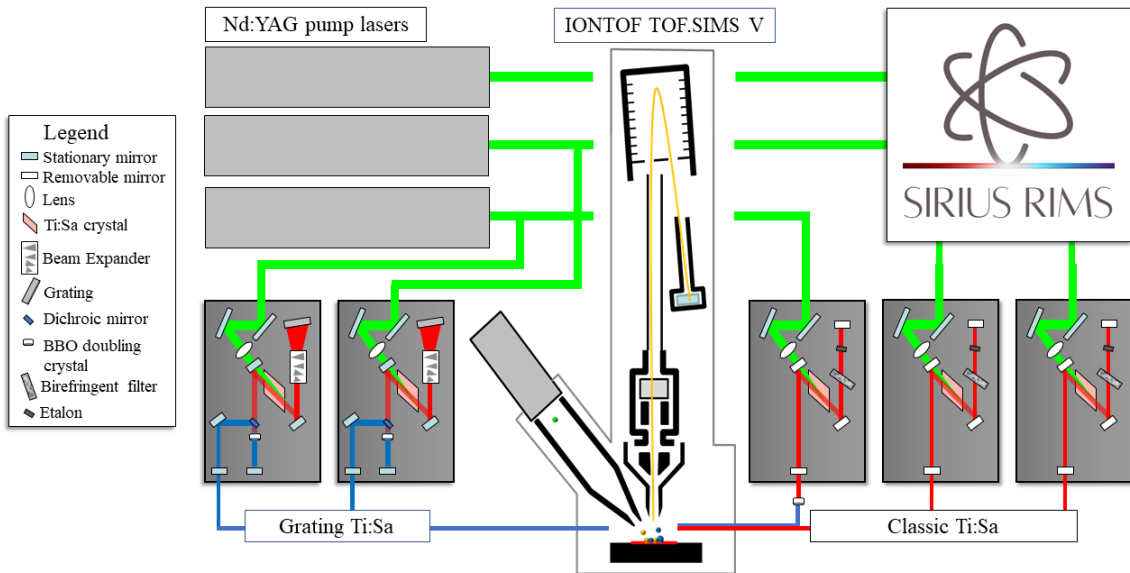


Figure 3.8: The SIRIUS RIMS instrument, wherein five lasers, either the two ‘grating’ (left) or the three ‘classic’ Ti:Sa lasers (right) are pumped by the frequency doubled Nd:YAG lasers, which are triggered by the ToF-SIMS (TOF.SIMS V by IONTOF GmbH).

RIMS analysis enabled by a combination of five Z-pinch 10 kHz Ti:Sa lasers. The full instrument set-up is illustrated in fig. 3.8, where the legend describes the individual laser components.

The ToF-SIMS uses a Bi⁺ ion liquid metal ion gun (LMIG) to sputter the first atomic layers of a sample, ionising a fraction of the resulting atoms and molecules, leaving a neutral fraction behind. Analysis of material is typically done in either ‘spectrometry’ or fast imaging’ mode, the former prioritizing mass resolution (quoted as up to 50 000 $\Delta m/m$ [197], though typically closer to 1000 in RIMS mode [167]) and the latter spatial resolution (quoted down to 70 nm [197], though $< 1 \mu\text{m}$ is more typical in RIMS mode [168]). The sample can be sputter-cleaned by a gas-cluster ion beam (GCIB) of argon clusters. Sputter cleaning can improve ion signal of a particle by an order of magnitude or more, and is the first step in particle analysis. Through extended use of the GCIB, depth-profiling can be made of a given sample, though this mode was not used in this work.

For RIMS analysis, a delayed extraction of 700 ns and positive bias of +500 V is required to suppress the generated secondary ions. A typical measurement therefore starts in SIMS mode by adjusting the ion optics for a 700 ns delay. A description of SIMS/RIMS optimization for hot particle analysis can be found in the appendix.

The SIMS cycle time is variable, though 100 μs is standard, and it goes to 200 μs with the use of the GCIB. The cycle must be set to 100 μs for RIMS mode to trigger the 10 kHz pump lasers. The three 532 nm Nd:YAG pump lasers (DM60-532, Photonics Industries) each have a maximum power of 50 W, which is attenuated and distributed such that each

Ti:Sa laser gets 13 to 15 W input power. The Ti:Sa design is from the LARISSA group of the Institute of Physics at the Johannes Gutenberg University Mainz. The laser frequency is measured by a wavemeter (WS6-600, High Finesse) with a precision of 600 MHz. The timing is controlled by the trigger signal of the ToF analyser, and the laser timings are overlapped with a digital delay pulse generator (DG465 Stanford Instruments).

RIMS analysis with SIRIUS either uses the set of classic lasers, or the set of grating lasers. The three classic Ti:Sa lasers run at the fundamental frequency and use birefringent filters with a Fabry–Pérot etalon to tune the wavelength, while the two grating lasers are internally frequency doubled. For the classic lasers, the wavelength range is determined by a mirror set of limited range, and fine-tuned by a birefringent filter and etalon. The remaining two Ti:Sa lasers are tuned via a grating affixed to a motor, and power stabilized by adjusting the angle of the beta-barium borate (BBO) crystal.

In RIMS, the ionised fraction is removed by an external bias at +500 V, after which the lasers hit the remaining neutral fraction. The target element is ionised, along with oxides and dioxides of U and some fission products. The ion gun is rastered over the sample to give a spatially resolved image of the intensity of each mass peak [54].

To measure a hot particle, the system is first optimised on a standard sample containing a dried droplet of mixed-oxide (MOX) fuel solution [167]. The laser position and timing are adjusted to give maximum signal, and the ToF-SIMS is adjusted for signal and mass resolution. The standard is measured to serve as the calibration baseline for fractionation in the Pu isotope composition [165]. The particle is measured, which requires the adjustment of ToF-SIMS parameters, but leaves the lasers unchanged. The mass spectrum is then analysed (SurfaceLab, IONTOF), and isotope ratios are determined. The final isotope ratios are adjusted by the fractionation measured on the standard sample, and age-corrected per isotope. It is possible to then move the lasers to a different two-step scheme and measure other elements.

3.2.2 LION

Livermore’s LION instrument, in contrast, has six 1 kHz grating-tuned Ti:Sa lasers, pumped by three Nd:YLFs (DM40-527, Photonics Industries International Inc.) and a custom ToF-SIMS, described in full by Stephan et al. [170]. In the configuration shown in fig. 3.9, three lasers are used for the Pu scheme, and one each for the U, Sr and Ba schemes (further discussed in the following section on scheme development). The timing is controlled through an oscilloscope and automation program [159]. The lasers can be grossly adjusted by the pump laser timings, and finely adjusted by the Pockel cells. In this way, the Pu and Ba lasers can arrive 400 ns later, separating the resonantly ionised elements in the mass spectrum by 1 m/z so that no overlap exists between ^{238}Pu , ^{238}U [159]. Non-resonant ionization still occurs in both steps, enhanced by the additional lasers for measurement of other elements.

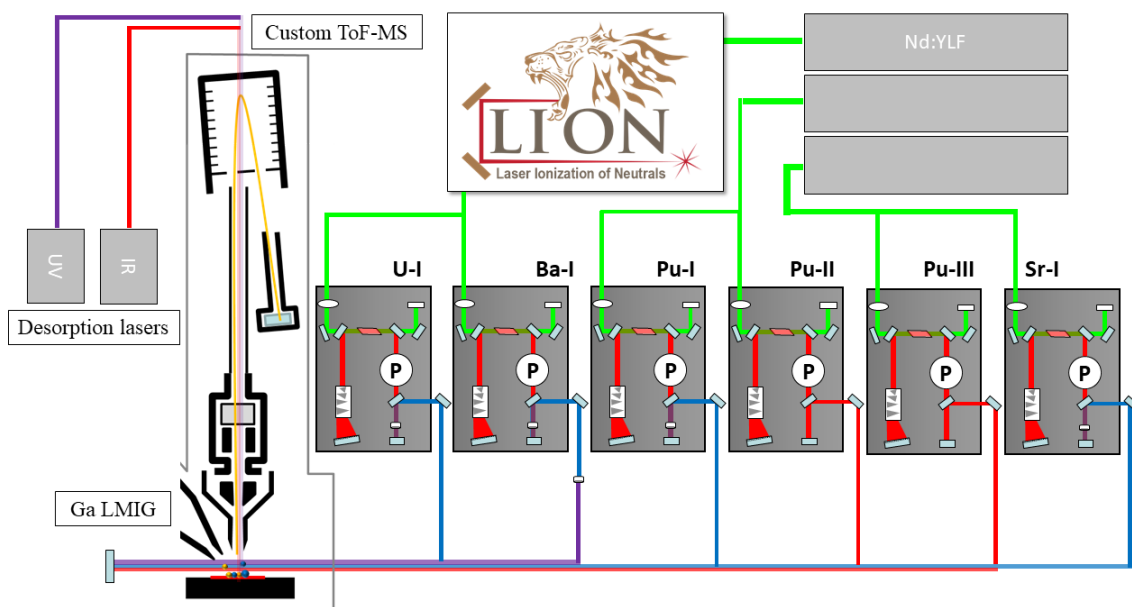


Figure 3.9: *The LION RIMS instrument as set up in May 2023 when CEZ hot particle measurements were conducted. Six possible lasers, shown here for the excitation schemes for U, Pu, Ba, and Sr are triggered by the ToF-SIMS at 1 kHz, with laser timings controlled initially by the input lasers, and finetuned by the Pockel cells. Surface analysis is achieved by either a Ga^+ LMIG, or by one of the desorption lasers: an IR or a UV laser.*

For the experiments conducted in this work, only the IR laser (Nd:YVO₄, Ekspla NL201 at 1064 nm) was used to desorb atoms and molecules from the surface, though other options include a UV laser and a Ga primary ion beam. The advantage of the laser desorption method is in the higher sensitivity achieved, in part for the lack of surface charging effects on the particle being analysed.

The desorption laser does, however, impart heat into the analyte, which changes as the measurement is ongoing, requiring manual adjustment of the laser power used (in the mW range). In the case of the hot particles, the heat was not well conducted through the particle, SEM glue, and tungsten needle, and resulted in the destruction and loss of several particles. The effect is shown in fig. 3.10, where cracks have formed on the particle surface, and glue has been removed from the left edge of the particle. It should be noted that other fragments of spent nuclear fuel, prepared with a focused ion beam (FIB) with platinum, were damaged this way [159].

One major advantage of the desorption laser is that in SIMS mode, the laser power can be set very low so as to only ionise elements with the lowest ionisation potential, namely the group 1 elements Cs and Rb. Similar to thermal ionisation mass spectrometry, the Cs and Rb can then be measured free of interference.

An optical image is used in the instrument, so that the particle can be centred. The laser

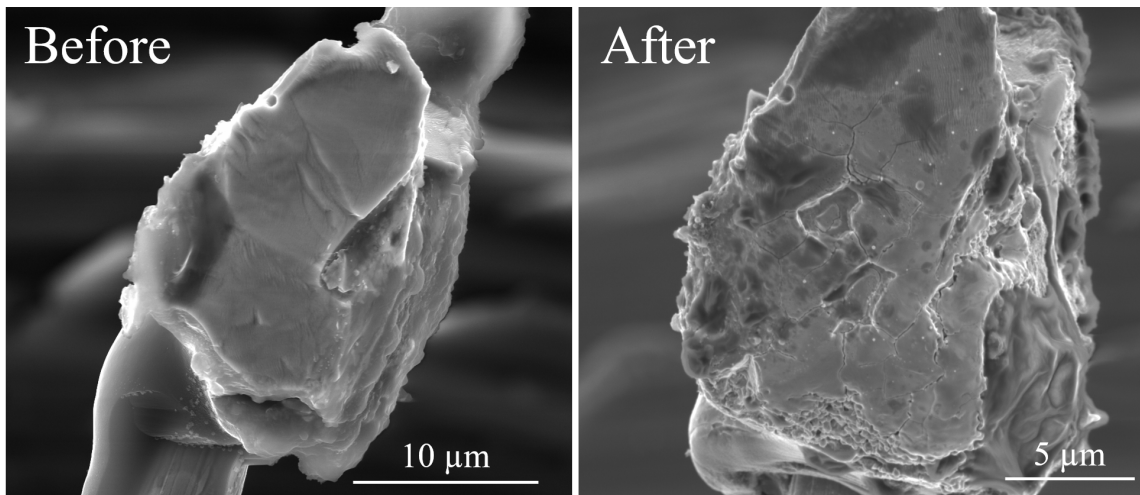


Figure 3.10: *SE imaging of particle CP036 before being measured in LION and after. In the first image, the particle had already been measured in SIRIUS, which did not show any visible changes in structure.*

beam is focused to ca. 3 μm . No spatially resolved information is captured from the ToF measurement, as the instrument is optimized for mass spectrometry.

In RIMS mode, the sample surface is kept at -2500 V to remove the ions, the neutrals get ionised, and then +3000 V is applied to accelerate them into the ToF-MS. Standards are measured first: a natural Ba and Sr mixed standard, a Rb standard, and spent fuel solution for U and Pu with known isotope ratios. The hot particle is then measured. Multiple measurements are taken until the counting statistics are satisfactory.

3.2.3 Iso-bar on 238

While most isotopes of Pu can be measured alongside other elements, ^{238}Pu cannot. For the reasons outlined in Chapter 2, non-resonant contributions are inescapable when dealing with blue light. Where the non-resonant element cannot be fully suppressed, two measurements must be taken. The principal method takes a resonant measurement, followed by a non-resonant measurement in near identical conditions, where the FES laser is offset by 0.1 nm. The resulting non-resonant spectrum serves as the background measurement of non-resonant U, with the difference at mass 238 showing plutonium, as illustrated in fig. 3.11.

^{238}Pu is the least abundant plutonium isotope in Chernobyl hot particles. The total non-resonant ^{238}U must be sufficiently suppressed to unequivocally register resonant ^{238}Pu counts. Meeting this condition is especially challenging in the blue-blue scheme, though it has been successfully demonstrated for particles where the composition and geometry is favourable to very low power measurements [168, 175]. The three-step scheme with only one blue step more consistently suppresses ^{238}U , as the high energy blue laser in the second step is replaced by low energy red lasers, which are less likely to produce non-resonant

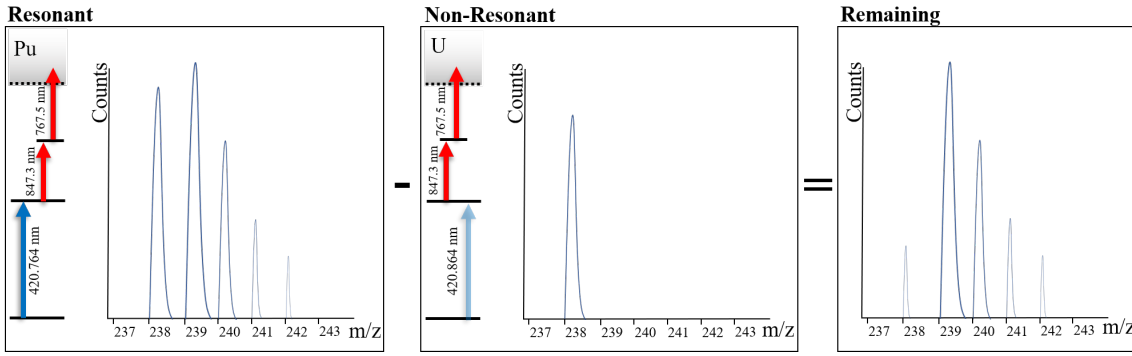


Figure 3.11: *Blinking method for determination of ^{238}Pu , whereby resonant Pu - non-resonant U = real Pu. The resonant scheme is a three-step scheme with resonant first step at 420.764 nm, tuned to maximise ^{238}Pu . The non-resonant step ionises only U, with a second laser at 420.784 nm. The subtraction of the two mass spectra allows for the isotope ratio analysis of $^{238}\text{Pu}/^{239}\text{Pu}$.*

^{238}U .

Securing identical conditions for the resonant and non-resonant measurement is an additional challenge, especially when sputtering efficiencies between elements can change over the course of measurement. Laser desorption is particularly variable, and a blinking method was developed to non-resonantly measure at alternating shots to minimize this time-dependent effect. It requires an additional laser to be used at half the repetition rate for the sole purpose of measuring the non-resonant signal. The additional laser means it has to be a dedicated set of measurements, referred to in this report as the Blink-238, in contrast to the multi-element study completed before. The resonant FES laser is tuned closer to the ^{238}Pu resonance, at 420.764 nm, to enhance the ^{238}Pu signal further, instead of the multi-element study in which it is set closer to the ^{240}Pu resonance at 420.766 nm. The off-resonant laser is set to 420.864 nm, as shown in fig. 3.11.

3.2.4 Analysis of mass spectra

In the SIRIUS instrument, a mass spectrum is dead-time corrected, calibrated and analysed in the SurfaceLab.7 software provided by IONTOF. The total area of the mass peak is calculated, and an area of the same peak width is chosen in the mass spectra to account for background ions. The LION instrument has custom software that achieves the same end results [198]. The background is subtracted from the peak to define the total counts. The isotope ratio x/y is then simply the ratio of the measured counts on two masses $\frac{N_x}{N_y}$. Errors propagate according to the Poisson counting error \sqrt{N} [199]. In the case of the $^{242}\text{Pu}/^{239}\text{Pu}$ ratio, $\frac{N_{242}}{N_{239}}$, this would propagate as

$$\left(\frac{N_{242}}{N_{239}}\right)_u = \frac{N_{242}}{N_{239}} \times \sqrt{\frac{1}{N_{242}} + \frac{1}{N_{239}}}. \quad (3.1)$$

The largest source of uncertainty in ultra-trace RIMS analysis is counting statistics. For an uncertainty of less than 10%, a minimum of 100 counts is required, which is not always achievable in a typical measurement day. Isotope fractionation within an instrument is on

the order of 0.01% [200], but isotope shifts from the ionisation scheme cause substantially more fractionation. In the above example of $^{242}\text{Pu}/^{239}\text{Pu}$, this is corrected for by measuring a standard with known isotopic composition. The measured ratio on the standard, M_{242} is compared to the known ratio R_{242} to obtain the correction factor C_{242} . As will be seen in the following chapter, the correction factor is depends on the laser power, isotope shift, and odd-even effects in the isotopes being measured.

Decay correction

Of all the nuclides measured, only ^{90}Sr , ^{137}Cs , ^{241}Pu have a short enough half-life whereby the change in activity needs to be accounted for. If Δt is the time since the Chernobyl accident, $t_{1/2}$ is the half-life of the respective nuclide, and N_M is the measured counts, the counts on the date of release N_C is

$$N_C = N_m \times e^{\ln(2) \times \frac{t_{1/2}}{\Delta t}}. \quad (3.2)$$

Decay correction of ^{241}Am is more complex. It increases with time, because ^{241}Pu decays into ^{241}Am . However, it is not possible to estimate the total ^{241}Pu to be constant over time, as some may have been separated in the years in the environment. The ^{241}Am data is therefore always presented on the day of the measurement.

Correction of natural isotopes

Environmental exposure can introduce natural ^{88}Sr , ^{137}Ba , and ^{138}Ba . The extent of contamination can be calculated using the non-fission isotopes of Sr and Ba. The two most abundant non-fission isotopes are used to estimate the natural fraction and averaged. In the example of Sr, the measured counts of ^{86}Sr and ^{87}Sr are purely environmental. The measured counts (N_{86} , N_{87}), can each estimate the environmental ^{88}Sr via the known natural ratios $R_{86} = ^{86}\text{Sr}/^{88}\text{Sr}$ and $R_{87} = ^{87}\text{Sr}/^{88}\text{Sr}$, as measured on an isotopic standard. The average of the estimates E_{88} is then the environmentally-derived ^{88}Sr . This can be expressed as

$$E_{88} = \frac{1}{2} \times \left(\frac{N_{86}}{R_{86}} + \frac{N_{87}}{R_{87}} \right). \quad (3.3)$$

The environmentally derived ^{88}Sr is then subtracted from the measured counts on $m/z = 88$, such that the $^{90}\text{Sr}/^{88}\text{Sr}$ ratio is

$$\frac{^{90}\text{Sr}}{^{88}\text{Sr}} = \frac{N_{90}}{N_{88} - E_{88}}, \quad (3.4)$$

where $N_{90,88}$ are the respective measured counts on each mass. Errors are propagated by the sum of squares of relative errors on each measurement. The same correction is used for ^{137}Ba and ^{138}Ba , using the purely natural ^{135}Ba and ^{136}Ba .

3.3 Summary

This chapter presented the methods utilized in this work for the sampling, isolation, and analysis of hot particles from Chernobyl and Fukushima. Soil, sediment, and moss samples were taken around ChNPP, while soil, sediment and fibre samples were taken around FDNPP. Before analysis is possible, hot particles must be isolated from the sample matrix. For both sampling locations, initial filtering was done by activity. The Chernobyl hot particles, being made mostly of U, are very dense, and can be separated by flotation, and identified through BSE imaging. The Fukushima particles are less abundant than the Chernobyl samples, both by the accident releasing fewer particles, and active decontamination efforts in the region. The Cs-MPs are mostly Si, which rules out separation by density. Autoradiography is therefore the preferred identification method, followed by gamma spectrometry of isolated fractions.

Once identified, a particle can be secured onto a tungsten needle for further analysis. The subject of this work is the non-destructive RIMS method on the SIRIUS and LION instruments. Eight particles were measured in both instruments, which differ in their repetition rate, ToF-MS instrument size, and laser design. The SIRIUS instrument uses two grating-Ti:Sa frequency doubled lasers to switch between two-step ionisation schemes, and three fixed Ti:Sa lasers for schemes requiring steps in the fundamental. The LION instrument uses six fixed Ti:Sa lasers simultaneously, with time delays between lasers to separate isobars. The Blink-238 method, which alternates resonant and non-resonant Pu measurements, is used for the analysis of ^{238}Pu . The alternation allows for in-situ correction of the overabundant non-resonant ^{238}U , which cannot be fully suppressed in laser ionisation.

Chapter 4

Advances in RIMS Capabilities

Theoretically, RIMS analysis is applicable to any element for which there is an efficient resonant scheme. The schemes available are determined by their ease of use. Where new investigations into isotope ratios are desired, they must be tested in the individual instrument. In the following chapter, new schemes are investigated on SIRIUS, combined with imaging capabilities of the TOF.SIMS V instrument. The choice of scheme is discussed, weighing the accessibility of the scheme and saturation power required.

To selectively measure a given element, multiple factors must be considered. To start, the transition wavelengths must be accessible to the available laser systems. Second, the transition must be saturated within the power output of said laser system, in the geometry required by the mass spectrometer. The isotope shift across all relevant isotopes must be within range of the laser bandwidth, and considered against interferences from overlapping elements. This section discusses the measurement of elements in this work, presenting, where relevant and novel, the isotope shifts and saturation curves measured with the SIRIUS instrument. The capabilities of the laser systems will be introduced, whereupon the elements will be discussed in order of their atomic mass.

4.1 Ti:Sa range

With a maximal tuning range of 660 - 1050 nm [201], the Ti:Sa crystal is well suited to a wide range of ionisation schemes. In fig. 4.1, the wavelength ranges are shown for the two Ti:Sa laser systems used in the SIRIUS instrument. In the classic laser design operating in the fundamental frequency, the mirrors inside the laser cavity determine the range of output frequency possible, as shown in fig. 4.1a. Further selectivity is achieved by narrowing the wavelength through a Lyot filter that consists of three birefringent crystal plates. It is further narrowed by a Fabry-Perot etalon. Frequency doubling and tripling can be added internal or external to the cavity, though this is not used in this work. Once aligned, the stability of these lasers is high, shown by the stability in power across wavelengths in 4.1a.

In fig. 4.1a, two red schemes are shown, the scheme for Cs (which uses mirror set combination SP2-OC2 and SP4) and the red component of the scheme for Pu (which

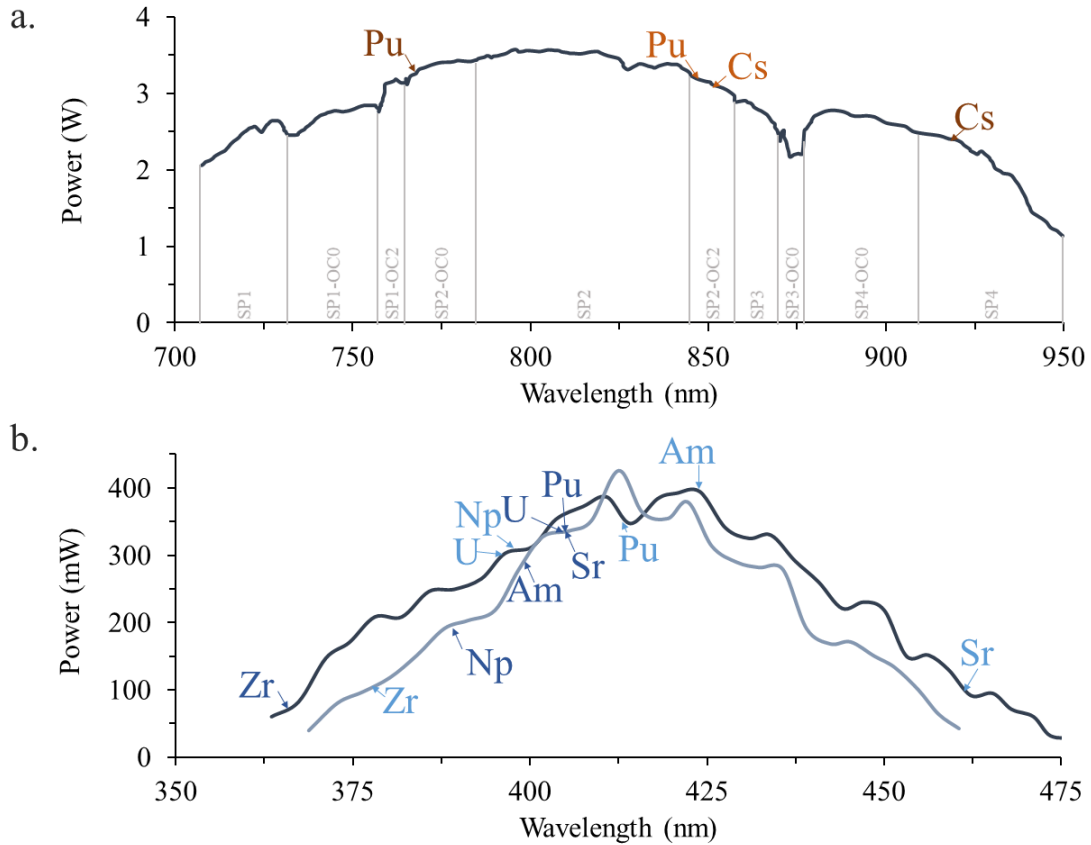


Figure 4.1: Output power in Z-cavity Ti:Sa range in the SIRIUS instrument with excitation steps marked at the corresponding wavelength (see fig. 2.4). a. Fundamental lasers, requiring different mirror sets (SP, OC) for different wavelengths. Adapted from Franzmann [162]. b. Frequency doubled grating-lasers, where the grating angle is shifted to to correct wavelength. Adapted from Raiwa [101].

uses SP1-OC2 and SP2-OC2). To change from one scheme to the next, the SP2-OC2 mirror set could remain the same, but the SP4 mirrors would have to change completely to SP1-OC2. For the experienced laser operator this may take a matter of minutes, but for the unfortunate operator who loses alignment, this may take multiple days.

The grating lasers, however, offer more flexibility in switching between wavelengths shown in fig. 4.1b. This is done by adjusting the angle of the grating, and adjusting the doubling crystal angle for maximum power output. There is no need for additional alignment, as it can be done automatically through LabView software [101]. The output power is substantially lower than in the fundamental range, which may cause difficulties in achieving saturation power in the far edges of the frequency range, such as in the Zr scheme. The total range can be extended by adjusting input power and cavity alignment. As seen in fig. 4.1b, two lasers nominally pumped at the same power and tuned by the same person, show slight differences in range and maximum power.

The lasers at LION operate similarly to the fundamental lasers at SIRIUS, as they require manual mirror changes to access a broad range of wavelengths. They can be frequency doubled or tripled, internally or externally as needed. It is not a Z-form cavity, but does

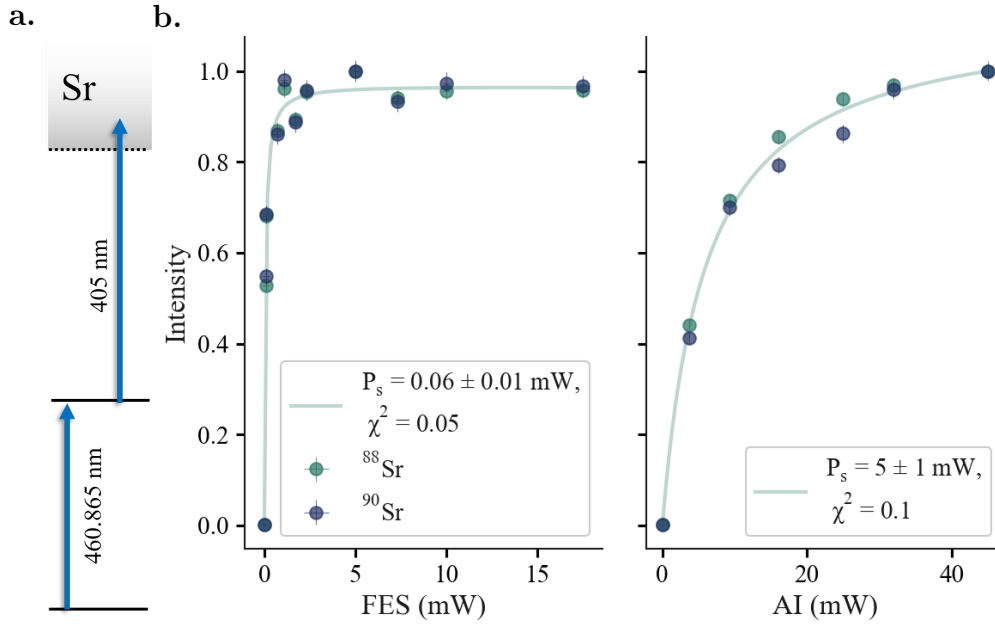


Figure 4.2: *a.* ionisation scheme for Sr based on work by Zhao et al. [203]. *b.* Saturation curves for the FES and AI of $^{88,90}\text{Sr}$, normalised to maximum counts. Fitted for the FES and AI of most abundant ^{88}Sr . Each measurement was performed on particle RW001, for 300 s.

use a grating as one end mirror [170]. While the SIRIUS lasers are pumped at 10 kHz with a Nd:YAG laser, the LION lasers are pumped at 1 kHz with Nd:YLF lasers, and use Pockel cells to further control the laser timings. This means that the SIRIUS lasers' timing is controlled by the pump lasers, whereas the LION lasers are controlled individually. The input power of the pump lasers has also been shown to be a way of fine-controlling the laser timings without the need for additional Pockel cells [202].

Each laser system is controlled by active feedback systems to stabilize wavelength and timing over long measurement times [162, 101, 170]. Changes in temperature, both externally in the lab and internal to the crystal, are the main sources of instability as thermal lensing becomes an issue. Directly cooling the Ti:Sa crystal is essential, but additional temperature controls around the lasers have also proven effective.

4.2 Sr

Nuclear material found in the environment will contain the fissionogenic Sr isotopes ^{88}Sr and ^{90}Sr . To assess a scheme for the measurement of nuclear material, it should then be tested on nuclear material, which includes all relevant nuclides and potentially interfering nuclides. The particle RW001, notably named by Hamann et al. as “Bob”, is one such sample [167]. A scheme found in the literature, as shown in fig. 4.2a, must be tested in the RIMS instrument. Saturation curves are required to assess the minimum laser power in each step to achieve an efficient resonant signal. A wavelength scan is then required to assess isotope

shifts, hyperfine effects, and interfering signals from other nuclides. At the saturation power P_s , you achieve 50% of the maximum achievable signal. Higher powers will also increase non-resonant signals, and result in broadening of the transition. A balance is then made based on increased signal from the target element, and non-resonant signals elsewhere.

In fig. 4.2b, we see each isotope is fully saturated in the FES and AI, described as

$$I = I_m \left(\frac{P/P_s}{1 + P/P_s} \right), \quad (4.1)$$

where I is the intensity, I_m is the maximum intensity ($=1$), P is the power in mW, and P_s is the saturation power. A saturation power is then found at an extremely low 0.06 mW in the FES, and at 6 mW for the AI. Such a highly efficient scheme reduces the need for higher powers, reducing power broadening of the laser and non-resonant signal from other nuclides and their oxides.

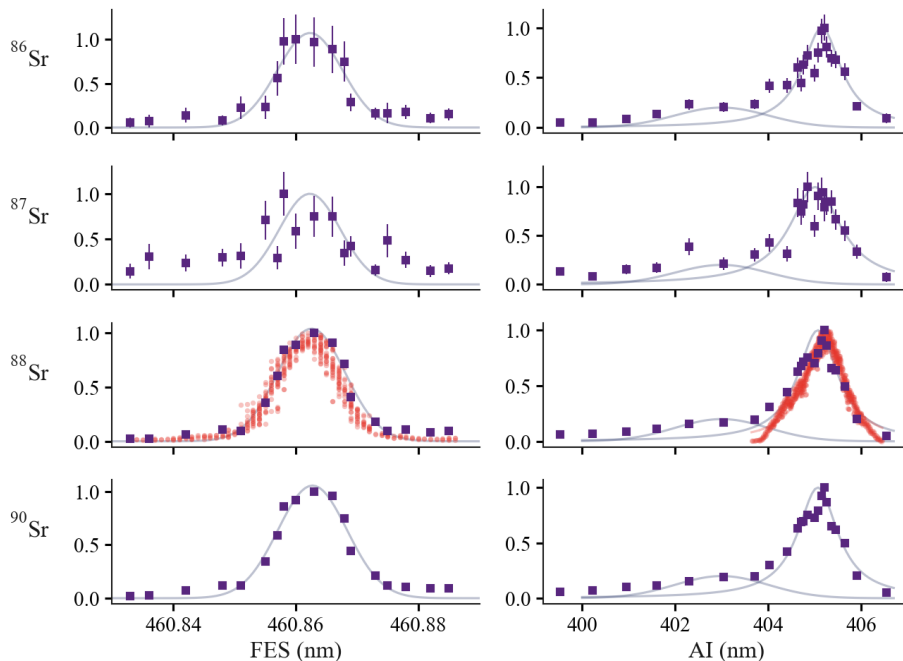


Figure 4.3: Wavelength scan over Sr resonance for the FES and AI of $^{86,87,88,90}\text{Sr}$, with literature data for ^{88}Sr in red from Zhao et al [203]. Each measurement was of 300 s, and normalized to the maximum counts.

The environmental origins of RW001 are evident in the presence of the natural and non-fissionogenic $^{86,87}\text{Sr}$, respectively forming 9.9% and 7.0% of natural Sr, with 82.6% ^{88}Sr forming the majority. The wavelength scans for the FES and AI shown in fig. 4.3 show a narrow transition in the FES, and extremely broad transition in the AI. Through the natural isotopes, it can therefore be estimated that $11 \pm 2\%$ of the Sr in this sample is of natural origin, meaning the natural isotopes are two orders of magnitude below $^{88,90}\text{Sr}$. ^{86}Sr is clear in both FES and AI scans, however the ^{87}Sr FES scan indicates interference may be seen in the spectrum. With the exceptionally low counting statistics at the edge of the AI (5 counts per measurement), it is likely that ^{87}Rb , present in both fissionogenic

and environmental forms in the sample, forms a small background signal due to insufficient suppression. In the AI scan it is clear that such interference is less significant with improved counting statistics.

Through a gaussian fit optimised through least squares fitting, the transition centres and linewidth can be calculated. In the FES, the centre can be found at 460.8625 ± 0.002 , with a FWHM of 0.0055 ± 0.001 . These results agree with the work done by Zhao et al., and confirms that the results of ^{88}Sr also apply to fissionogenic ^{90}Sr [203].

The AI is the broadest transition of the elements investigated in this work. In the measurements by Zhao et al., its centre is reported at 405.200 nm with an FWHM = 0.93 nm, fitted by a Lorentzian rather than a Gaussian fit. A Lorentzian would only be expected in a case without broadening, which would be rare in the SIRIUS instrument, as it is not optimized for high resolution spectroscopy. It is likely that it is a coincidental fit, with the observed subpeaks in the Zhao data suggesting there are multiple overlapping peaks. The measured data shows the main peak to be at 405.07 ± 0.03 nm and FWHM of 1.05 ± 0.08 . The large asymmetry can partially be attributed to a wide Gaussian peak centred at ~ 403 nm with an FWHM ~ 1 nm. The subpeaks observed in the Zhao data were not replicated identically in SIRIUS, for which a more concentrated standard sample would be required for optimal counting statistics. A further spectroscopic investigation would be required with a far narrower laser linewidth to assess these transitions accurately. Importantly for RIMS measurements, this scheme is both efficient and does not overlap with Zr, allowing for interference-free assessment of fissionogenic and natural Sr ratios.

4.3 Zr

The Zr measured in CEZ particles is a mixture of natural Zr used in fuel cladding material, and the fission product Zr generated during reactor operation. In the particle K001, both fissionogenic and cladding Zr can be found, with ^{90}Zr being the most naturally abundant, and isobaric with ^{90}Sr . The scheme shown in fig. 4.4 is new for Zr [204], and works well on the CEZ particles. The FES is easily saturated above 0.5 mW, though the second step is to a Rydberg state rather than an AI state, and is only saturated at $90 \text{ mW} \pm 9 \text{ mW}$.

This estimate is limited in that 90 mW is the maximum laser output power at that wavelength. It is at the edge of the capabilities of the SIRIUS lasers (see fig. 4.1b), even with optimisation of the laser cavity. A saturation power higher than 90 mW is therefore likely. As a further consequence, this high saturation power limits the ability to perform a wavelength scan, as to maintain that power around this extremely small wavelength was insufficiently stable for consistent measurement. Compared to other schemes, this saturation power is extremely high, raising concern of non-resonant ionisation of isobaric ^{90}Sr . However, as no ^{88}Sr was observed in the spectrum, it can be concluded that there is no non-resonant ^{90}Sr .

In fig. 4.5, we see the isotopes of Zr in the FES scan only. Reactor-derived Zr contains the

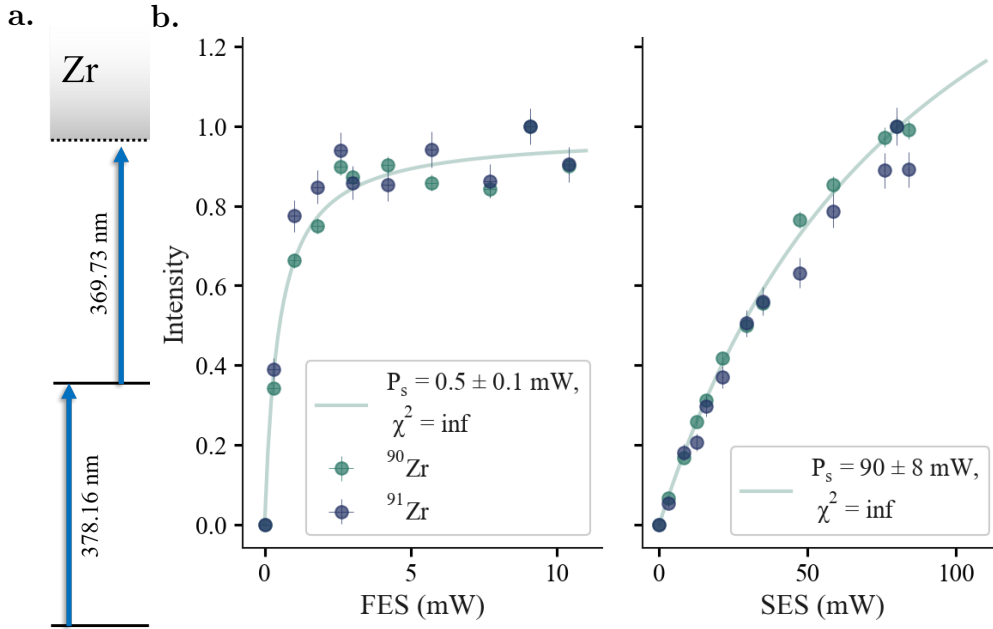


Figure 4.4: *a.* ionisation scheme for Zr based on the scheme by Raiwa et al. [204]. *b.* Saturation curves for $^{90,91}\text{Zr}$, normalised to maximum counts. Fitted for the FES and SES of ^{90}Zr . Each measurement was performed on particle K001 for 100 s.

long-lived isotope ^{93}Zr (half-life 1.6×10^6 years), which is not found in natural Zr. It is an odd isotope, with the same $+5/2$ nuclear spin as the only other odd isotope ^{91}Zr . The FES scan in fig. 4.5 shows no isotope shift, with the centre at 378.1606 ± 0.002 and FWHM of 0.0026 ± 0.001 . The counts are significantly lower for ^{93}Zr , reflecting the relative intensity of the cladding against the fission products.

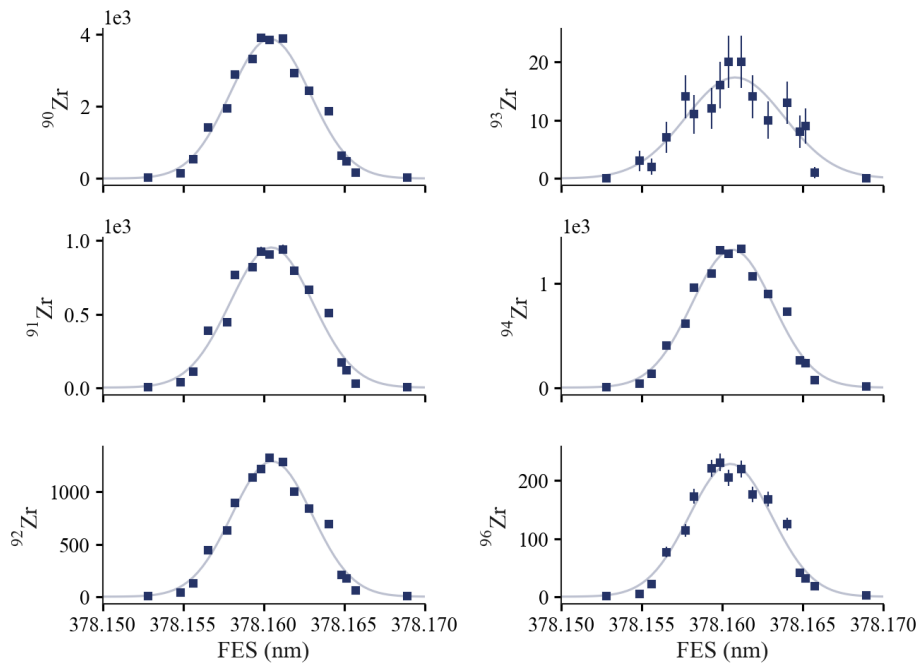


Figure 4.5: Wavelength scan over Zr resonance for the FES for $^{90,91,92,93,94,96}\text{Zr}$.

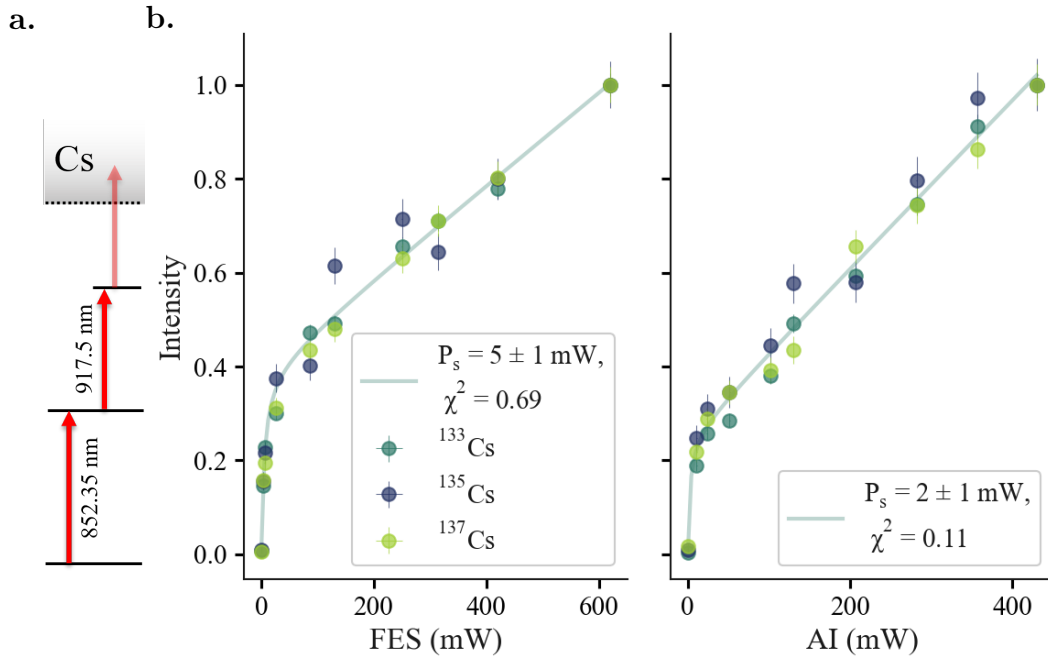


Figure 4.6: *a.* ionisation scheme for Cs based on work by Sakamoto et al. [138]. *b.* Saturation curves for $^{133,135,137}\text{Cs}$, normalised to maximum counts. Fitted for the FES and SES of the most abundant ^{133}Cs . Each measurement was performed on particle K001 for 200 s.

A normalization is not applied here, to show the relative abundance of the isotopes. All natural isotopes of Zr are also fissionogenic, produced at roughly the same fission yields. Only ^{93}Zr is purely fissionogenic, and is of the lowest abundance in this particle, indicating most of the Zr is of natural origin. As will be shown in the following chapter, this isotope can be used to spatially separate natural from fissionogenic Zr.

4.4 Cs

With the low ionisation potential of Cs, shown in fig. 4.6, work by Sakamoto et al. demonstrates a scheme that uses only two red lasers [138]. It is, however, not an entirely resonant scheme. It relies on multi-photon absorption from either the FES or SES laser to excite Cs atoms beyond the ionisation potential. This results in a scheme that cannot be fully saturated, with signal increasing linearly with power after the nominal saturation point, as seen in fig. 4.6.

In contrast to the saturation formula previously used, eq. 4.1, a modified relation must be used of the form

$$I = I_m \left(\frac{P/P_s}{1 + P/P_s} + b \times P \right), \quad (4.2)$$

with the additional term $b \times P$, a linear component after nominal saturation is reached. This results in a nominal saturation power of $5 \pm 1 \text{ mW}$ in the FES, and $20 \pm 8 \text{ mW}$ in the

SES, but a doubling of the signal can be achieved at powers over 100 mW. Heating of the sample can interfere with its measurement, potentially leading to chemical changes. Laser powers below 200 mW for both lasers are therefore recommended as providing sufficient power for RIMS measurement.

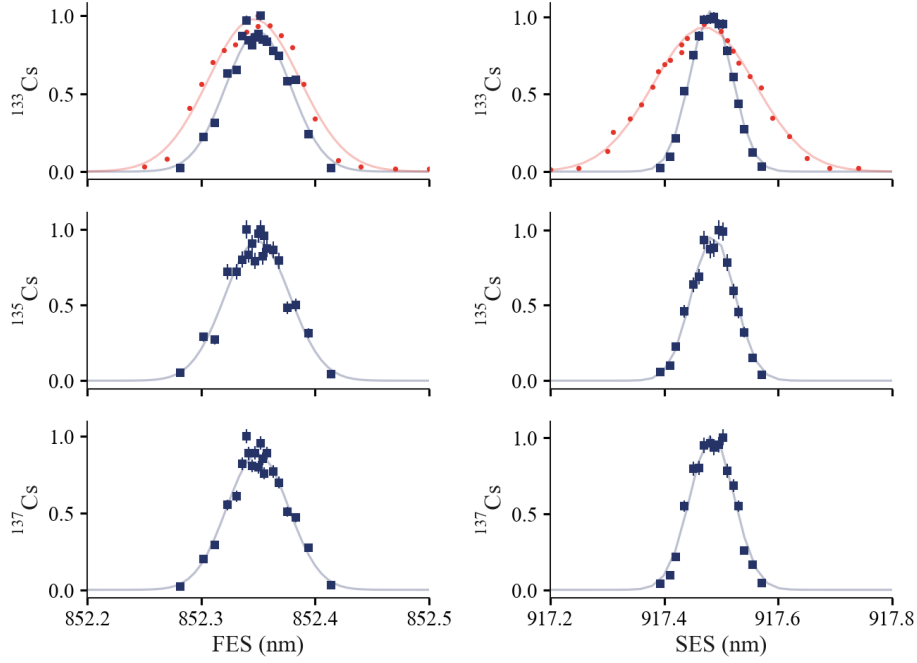


Figure 4.7: Wavelength scan over Cs resonance measured on particle RW001 for the FES and SES for $^{133,135,137}\text{Cs}$, with literature data for ^{133}Cs in red from Sakamoto et al [138].

The work of Sakamoto et al. focused only on the natural Cs isotope ^{133}Cs . In fig. 4.7, all Cs isotopes found in spent fuel are shown, measured on the CEZ particle RW001. No isotope shift is observed in either excitation step, with the FES centred at 852.350 ± 0.001 with an FWHM of 0.029 ± 0.001 nm, and the SES centred at 917.484 ± 0.002 with an FWHM of 0.038 ± 0.001 nm, where the uncertainties reflect the errors in the Gaussian fit.

In comparison to the Sakamoto data, the centre is the same in the FES: 852.347 ± 0.002 nm, but shifted in the SES: 917.470 ± 0.002 nm. More notable is the significant broadening of the linewidth, with an FES FWHM of 0.040 ± 0.001 nm and 0.089 ± 0.001 nm in the SES. The linewidths of the lasers are comparable (0.01 - 0.03 nm [138, 161]), so it is likely that higher powers were used in the Sakamoto measurements resulting in power broadening. However, Sakamoto et al. used 3 and 0.2 $\mu\text{J}/\text{pulse}$, equivalent to 2 and 30 mW at 10 kHz, which is lower than the 150 mW used in SIRIUS. The focus of the laser beam, or interaction volume with the cloud of neutrals, could be smaller in the Kogakuin instrument. Regardless, the transition width does not affect the ability to measure Cs with RIMS, as it affects neither the isotopic fractionation, nor the resonant ionisation of interfering isobars.

4.5 Np

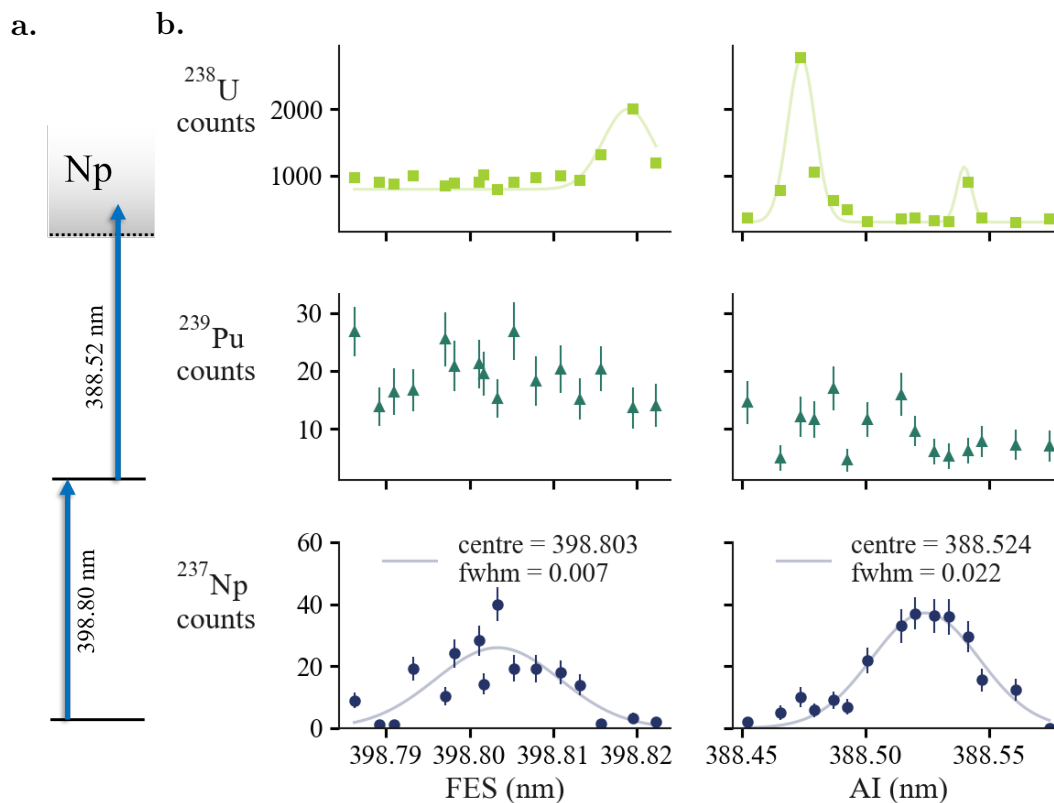


Figure 4.8: *a.* ionisation scheme for Np used for wavelength scan based on work by Kaja et al. [205]. *b.* Wavelength scan over Np resonance measuring counts for ^{238}U , ^{239}Pu , and ^{237}Np , over 200s measurement time normalised to non-resonant UO. A Gaussian fit is plotted with the centre and FWHM for ^{237}Np .

Neptunium derived from a reactor is composed of only one very long-lived alpha-emitting isotope, ^{237}Np (half-life 2.14×10^6 years), and two short-lived isotopes ^{238}Np and ^{239}Np (half-lives 2.1 days and 2.4 days respectively). Isotope ratio analysis for nuclear forensics purposes is therefore insubstantial. However, the (spatially resolved) identification of ^{237}Np in a given sample, derived as activation product of ^{236}U , or decay product of ^{241}Am , could potentially be of use in determining chemical behaviour of nuclear materials over long time scales.

In other fields, RIMS can facilitate analysis in multi-element matrices. In spectroscopic work by Kaja et al. on the exotic isotopes of Np [205], scheme development is limited in time by the fast decay of its isotopes. In this case, a scheme was developed on a Np sample that contained ^{237}Np in combination with ^{239}Np generated in the TRIGA reactor in Mainz from a ^{238}U target. While the sample was chemically separated to contain only Np, ^{239}Pu will be rapidly produced by decay. In the scheme development, it was noticed that ^{239}Pu was producing a substantial interference on ^{239}Np . To study this effect further, a multi-element sample would be required. Spent fuel contains all the necessary elements with which to measure this. In future beamline measurements that use depleted uranium

as the target material, ^{238}U and ^{239}Np may be significant sources of interference [205].

The RW001 particle was therefore used to conduct an analysis of nine different potential schemes. The strongest of these schemes was investigated, using an additional etalon to further narrow the laser linewidth of one of the lasers. The FES and AI step were scanned with the aim of revealing the resonances of ^{239}Pu and ^{238}U , which necessitated the use of a more narrow laser. In fig. 4.8, the centre for the ^{237}Np FES was fit with a Gaussian to be 398.803 ± 0.007 , with a broader AI step of 388.524 ± 0.022 . The ^{238}U shows narrow resonances at 398.819 ± 0.005 nm in the FES scan, and two resonances at 388.473 ± 0.018 nm and 388.54 ± 0.003 nm in the AI scan. There is a broad and inefficient resonance of ^{239}Pu throughout the range of the Np FES, but this drops off in the AI with wavelengths beyond 388.52 nm.

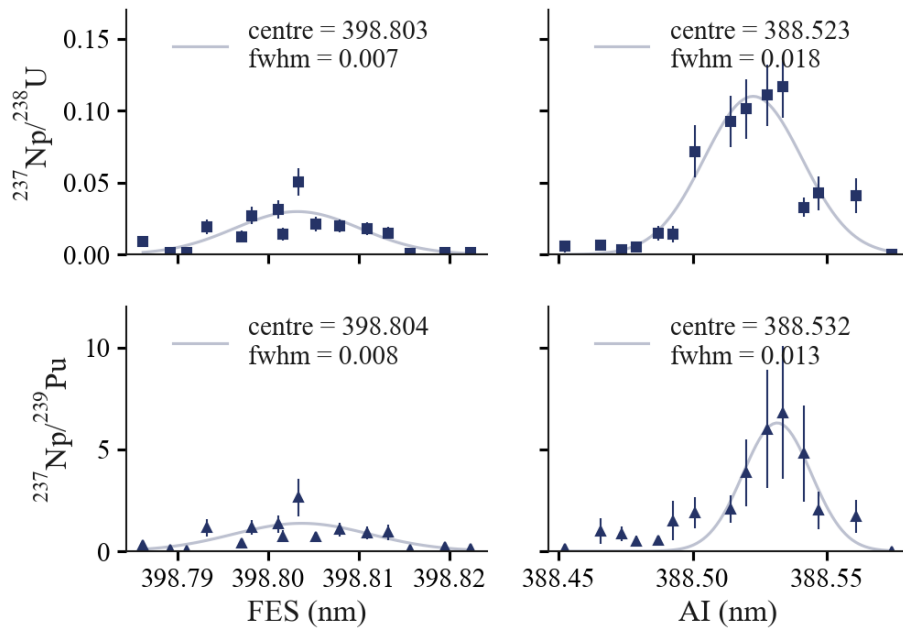


Figure 4.9: Ratios of $^{237}\text{Np}/^{238}\text{U}$ and $^{237}\text{Np}/^{239}\text{Pu}$. Conditions for the scans were as follows: FES (1 mW, 13 mW AI at 388.523 ± 0.001 nm) and AI (13 mW, 1 mW FES at 398.802 ± 0.001 nm).

It is clear from the results in fig. 4.8 that both ^{238}U and ^{239}Pu are not fully suppressed, even at low powers (1 mW for the FES and 13 mW for the AI). The ^{239}Pu signal is constant within error in the FES, and drops off with increasing AI wavelength. This raises the question of whether the ideal wavelength should be increased in the AI to more fully suppress ^{239}Pu , and whether this is limited by the ^{238}U resonance at 388.54.

The relative ^{237}Np signal is then shown in fig. 4.9. The ratio between $^{237}\text{Np}/^{239}\text{Pu}/^{238}\text{U}$ in RBMK spent fuel is on the order of $1/1 \times 10^2 / 1 \times 10^5$ according to literature data [46]. The measured ratio between $^{237}\text{Np}/^{238}\text{U}$ ranges from 1×10^{-3} at the U resonances to 1×10^{-1} at the Np resonance in the AI. A maximal suppression of ^{238}U on the order of 1×10^{-4} is in line with previous investigations on two-step ionisation [175]. While not a lot is to be

gained by shifting the FES, changes in the AI do. An optimal ratio between $^{237}\text{Np}/^{239}\text{Pu}$ can be found at the outer edge of the Np AI resonance, at 388.532 nm. This is however to the disadvantage of $^{237}\text{Np}/^{238}\text{U}$, which is centred at 388.523 nm, a shift of 0.12 nm.

The narrowband laser's effect can be seen most evidently in the relative signal of Np. While the absolute count-rate is not significantly higher in the SES scan for Np, it is significantly lower for both U and Pu. By using the narrowband in the AI, the neighbouring resonances of U and Pu are further suppressed. It is not useful in the FES, as no neighbouring resonance is avoided. Further enhancement of the Np signal, which may be relevant in nuclear forensics applications, can be achieved by increasing the laser power. While this will increase the Pu and U signals, for the analysis of ^{237}Np alone, which has no interfering isobars, this is recommended.

4.6 Pu

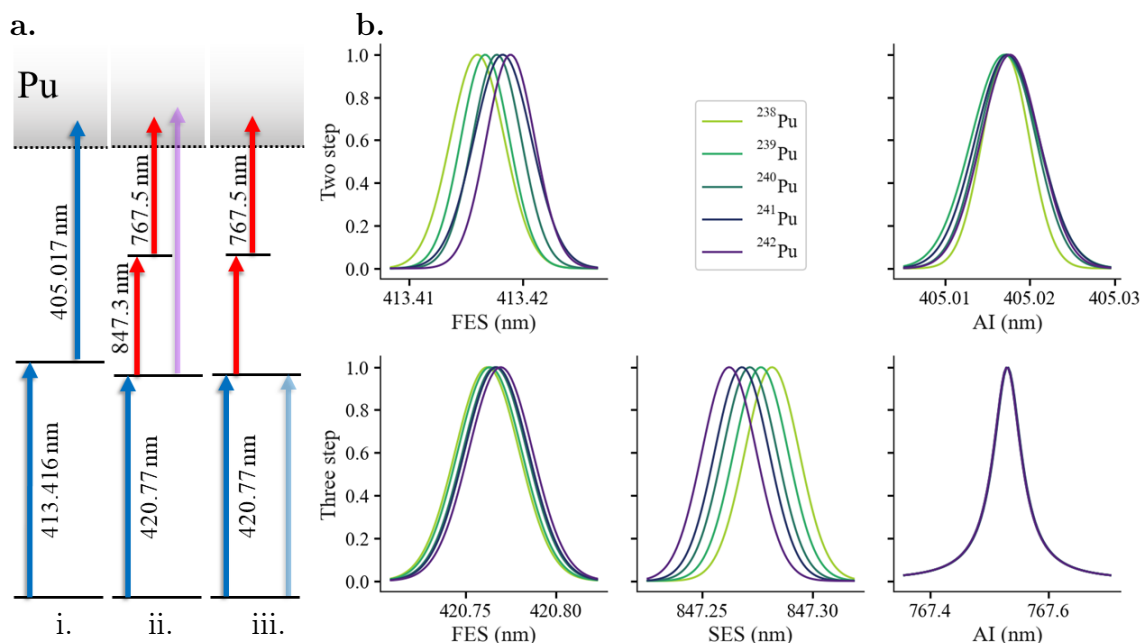


Figure 4.10: *a. ionisation schemes used for Pu in this work, as described in [169] i. SIRIUS, ii. LION multi-element, iii. LION Blink-238. b. Wavelength scans for the two and three-step schemes, modeled based on transition centres and widths for $^{238-242}\text{Pu}$ reported by Raiwa and Grüning respectively [168, 183].*

The analysis of Pu in environmental samples is one of the most important applications of RIMS and has been extensively studied [168, 164, 159, 183, 167, 161]. Depending on the analytical requirements, a variety of efficient schemes are available (see table 2.1). Two of these schemes form the basis of the plutonium measurements in this work, are shown in fig. 4.10a. Notably different from the schemes so far discussed is the clear isotope shift observed in plutonium. The influence of the isotope shift on the measurement depends both on the scheme and laser used, and is demonstrated in fig. 4.10b. The two step scheme shows a

distinct isotope shift in the FES, and a minimal shift in the AI. The three-step scheme has a less strong isotope shift in the FES, but is strong in the SES and non-existent in the AI. The laser bandwidth influences how strong the influence is: a large bandwidth can cover the full isotope shift, while narrow bandwidths do not, resulting in isotope fractionation in the mass spectrum.

The transition linewidth depends on the lifetime of the state as well as the power of the laser used to excite it. As seen in the Cs excitation (fig. 4.6), this can vary from instrument to instrument. The isotope shift is clearly a substantial factor in both the two and three-step schemes, which will fractionate the Pu isotopes in mass spectrometry. In practice, standards of known isotopic composition are used to measure the fractionation and account for it in analysis of unknown samples. Results in fig. 4.11 show how fractionation is affected by different application of Pu schemes.

The SIRIUS measurements used the first scheme shown in fig 4.10a.i. By using a higher powered laser, the transition linewidth increases. The results of this widening can be seen in fig. 4.11, where the low power laser produces ratios that are further away from the known ratios, based on a Pu MOX sample. The LION measurements used the three-step schemes. In the multi-element measurement (light green), an additional laser used for Ba analysis also contributed to the ionisation of Pu as seen in fig 4.10a.ii. The standard used for these measurements was a MOX fuel sample, containing both U and Pu, and this is evident in the complete obfuscation of $^{238}\text{Pu}/^{239}\text{Pu}$ ratio. This is improved in the Blink-238 method, which corrects for the non-resonant ^{238}U .

Overall, it is more important to measure the deviation from the known standard than to have an excitation scheme that most closely replicates the known standard. This is due to the fractionation within the mass spectrometer, or drifting of the lasers from day to day measurement as seen in fig. 4.11. The standard deviation for each isotope measurement is lowest for the Blink-238 method in LION, where $^{240-242}\text{Pu}/^{239}\text{Pu}$ has a standard deviation of 2 to 3%. In both the LION multi-element and SIRIUS high power measurements, the ratios are closer to the known values, but with standard deviations between 4% in $^{242}\text{Pu}/^{239}\text{Pu}$, to 53% in $^{241}\text{Pu}/^{239}\text{Pu}$ for the SIRIUS high power measurements. And yet, as will be seen in further results, the results obtained with both LION and SIRIUS remain comparable across instruments and time.

4.7 Ba, Am, U, and selective desorption of Rb, Cs

Four more elements were studied in this work. In the multi-element analysis of CEZ particles with LION, Ba was studied simultaneously with Pu. The scheme used is shown in fig. 4.12a, showing the first UV step, requiring the generation of a frequency tripled laser [170]. This non-resonant scheme is then further enhanced by the first step of the Pu scheme. The resulting work showed a significant enhancement ($\sim 95\%$) of the odd isotopes $^{135,137}\text{Ba}/^{138}\text{Ba}$ with respect to the natural ratios in the Ba standard sample. Technically this is a suppression of the even isotopes, and is dependent on the polarization of the lasers

[167, 177]. A scheme that doesn't require frequency tripling would be preferred, though such a schemes in the blue [206], measured in SIRIUS, insufficiently suppressed Cs isotopes.

In the analysis of spent nuclear fuel, U will always form the majority of the sample, dominantly found in the form UO_x . The oxide form has a significantly lower ionisation potential than the elemental form, leading to its non-resonant excitation by lasers of all wavelengths, as illustrated in fig. 4.12b. As proposed by Raiwa, the non-resonant UO^+ can consistently and accurately be used in isotope ratio analysis in CEZ particles. During the LION measurements, a resonant first step was used, enhanced by the first step used in Sr excitation (see fig 4.2a).

Resonant ionisation of Am has been thoroughly discussed in previous work [168, 166, 207, 159] and will only be briefly summarised here. An isotope shift is seen between $^{241,243}\text{Am}$, though by setting the lasers in between the resonances this effect does not result in fractionation in the mass spectrum [101]. It has a low saturation power, and is particularly efficient compared to other schemes, allowing for the detection of ultra-trace ^{242m}Am [165].

The laser desorption method in LION imparts heat into the sample. At very low powers, this heating can ionise group 1 alkali metals preferentially over other elements. In this manner, Rb and Cs were analysed in CEZ particles in SIMS rather than RIMS mode, and showed no significant fractionation between the isotopes.

While many other elements can be measured, (see [208, 163, 164] for schemes across the

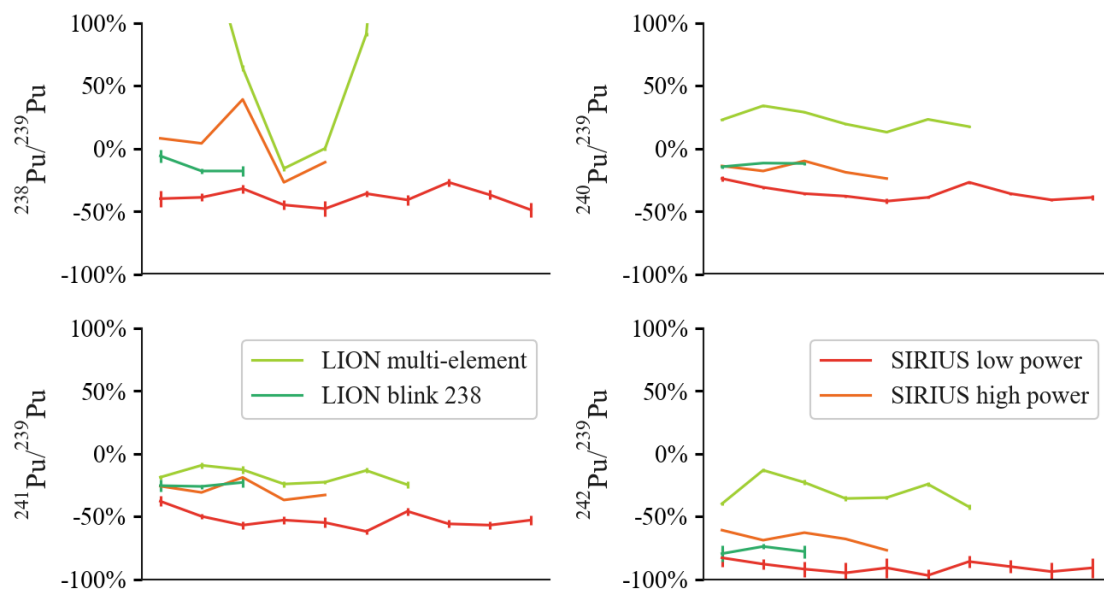


Figure 4.11: Isotope fractionation plutonium as a percentage deviation from the known standard. The LION measurements (green) use broad bandwidth lasers while SIRIUS (red) use narrow bandwidth lasers.

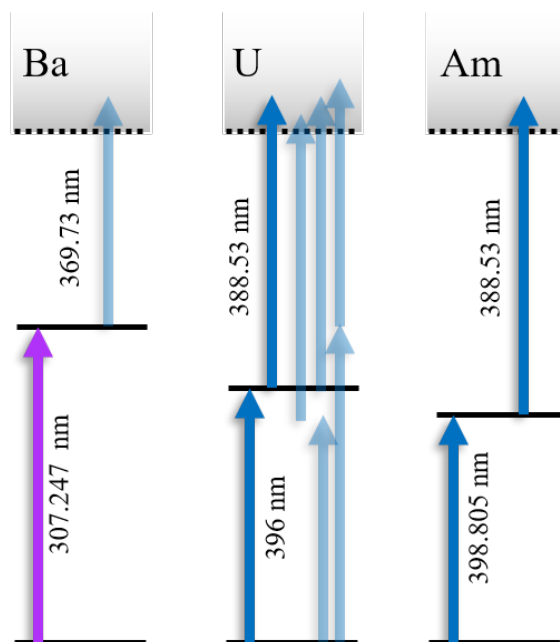


Figure 4.12: *Partially resonant schemes for U and Ba, used in multi-element analysis at LION, and additionally resonant Am scheme used in SIRIUS.*

periodic table), each scheme must be tested on the individual RIMS instrument. The exact centre of a given transition may shift from one instrument to the next, as in the Sr example. The width of the transition is dependent on the atomic state of the transition, but more importantly on the broadening of the laser linewidth and power. The selectivity and suppression of non-resonant isobars at low powers must be weighed against the lower count-rate. With these parameters in mind, the analysis of isotope ratios can open up in any relevant direction, in the analysis of nuclear materials, star grains, meteorites, and elsewhere.

4.8 Summary

In this chapter, the capabilities and advances in RIMS have been presented. Through the use and optimisation of ionisation schemes, relevant isotopes of unique elements can be investigated. Each element presents unique challenges in the isotope shift, odd-even effect, saturation power, efficiency and accessibility of the scheme. Once optimised to the RIMS instrument, they can then be used for isotope ratio analysis with a mass spectrometry focus, or in imaging to analyse the spatial distribution of different elements and isotopes.

For mass spectrometry, Sr, Zr, and Cs can be readily analysed in the SIRIUS instrument without significant interference. For Np and Pu, the resonant and non-resonant ionisation of U and Pu must be considered depending on the aims of analysis. The remaining chapters will concentrate on the isotope ratio analysis of many particles, and the resulting impact that has on their structure and degradation in the environment.

Chapter 5

RIMS for Forensics

In the development of RIMS techniques, a common goal has been its application to nuclear forensics [153, 157, 155, 161, 167, 168]. The aim in nuclear forensics is to ascertain the most likely origin of the nuclear material by its physical, chemical, elemental and isotopic composition. The use of RIMS allows for a nearly non-destructive assessment of a microparticle's composition, which can then be compared to known libraries, or isotopic fingerprints associated with specific applications.

5.1 Actinide isotopic fingerprint

The primary sources for isotopic analysis in nuclear forensics are U and Pu. A set of 8 particles sampled in the CEZ will be discussed in this section, previously shown in fig. 3.2. We work on the assumption that they are spent fuel particles from the Chornobyl RBMK-type reactor, released during the accident in 1986. In contrast to the case when particles were first discovered in Sweden days after the Chornobyl accident, there are no short-lived radionuclides left in these particles. In this chapter, we shall consider the particles independent of their sampling location, for the purposes of demonstrating the use of isotope ratio analysis to determine particle origin.

The first order of inquiry is to determine the general category of nuclear material that is being analysed: weapons material, fresh fuel, irradiated/spent fuel, natural uranium, and depleted uranium. Of particular concern is the identification of weapons material, categorised by the very high ratios (> 0.9) of $^{235}\text{U}/^{238}\text{U}$ or very low ratios (< 0.1) of $^{240}\text{Pu}/^{239}\text{Pu}$. As shown in figure 5.2, the eight particles measured are clearly not weapons material as $^{235}\text{U}/^{238}\text{U} < 0.015$.

In fig. 5.1 we see the comparison between two Soviet reactor-types, the WWER and RBMK. Each of the eight particles measured in SIRIUS and LION show agreement in the $^{235}\text{U}/^{238}\text{U}$ and $^{242}\text{Pu}/^{239}\text{Pu}$ ratios, and seven of these particles closely align with the RBMK type. The particles are shown in fig. 3.2, which shows the one outlier in this measurement: B010, seen here in orange. It contains no Pu, and has an exceptionally low $^{235}\text{U}/^{238}\text{U}$ ratio.

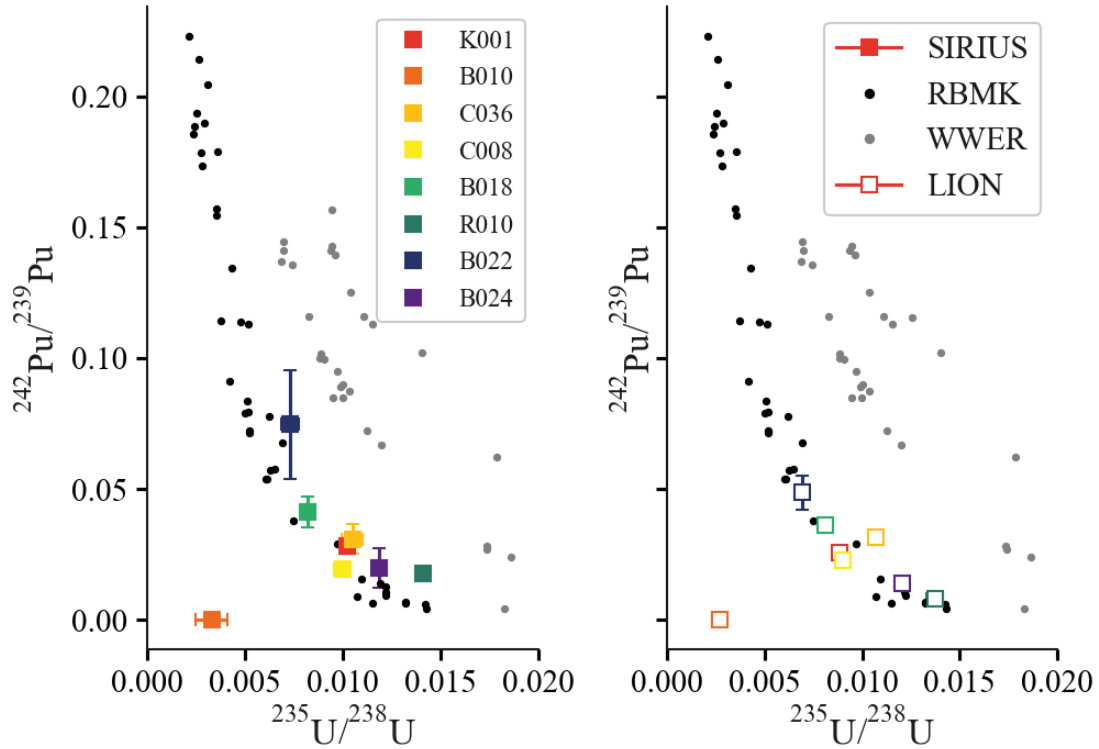


Figure 5.1: *Four-isotope plot showing $^{235}\text{U}/^{238}\text{U}$ vs $^{242}\text{Pu}/^{239}\text{Pu}$. Particles (square) measured in SIRIUS (filled squares) and LION (open squares), where each individual particle is shown in a separate colour. Black and grey dots are the literature data isotope ratios measured in spent fuel rods of a variety of initial enrichments and operating times from RBMK-type (black) and WWER-type (grey) reactors by Makarova et al. [46].*

The Makarova dataset of the two reactor types comprises samples taken from different points in the fuel rod, from varying reactors, with varying initial fuel compositions, for varying reactor operating times. This provides a rich dataset with which to compare different reactor conditions. These conditions each impact the production of isotopes. As seen in fig. 5.1, the accumulation of $^{242}\text{Pu}/^{239}\text{Pu}$ with burnup is accelerated in RBMKs with respect to WWERs.

The accumulation of neutron captured ^{236}U with fuel burnup is considered in fig. 5.2. Here, there is more spread in the data between the LION and SIRIUS measurements, with the SIRIUS data aligning more closely to an expected linear trend. The statistical variation in the measurement data between the instruments will be discussed in further detail in section 5.4. The comparison between $^{236}\text{U}/^{238}\text{U}$ ratios in RBMK and WWER reactor is predominantly based on the initial enrichments used in the respective reactor types, as shown in trends of the Makarova data [46].

In Chapter 1, the production pathways of the actinides were discussed in thermal reactors. With reference to fig. 1.1, we can algebraically describe the ratio between ^{235}U and ^{236}U with fuel burnup. Fresh fuel is an enrichment of the $^{235}\text{U}/^{238}\text{U}$ isotope ratio from 0.007 to

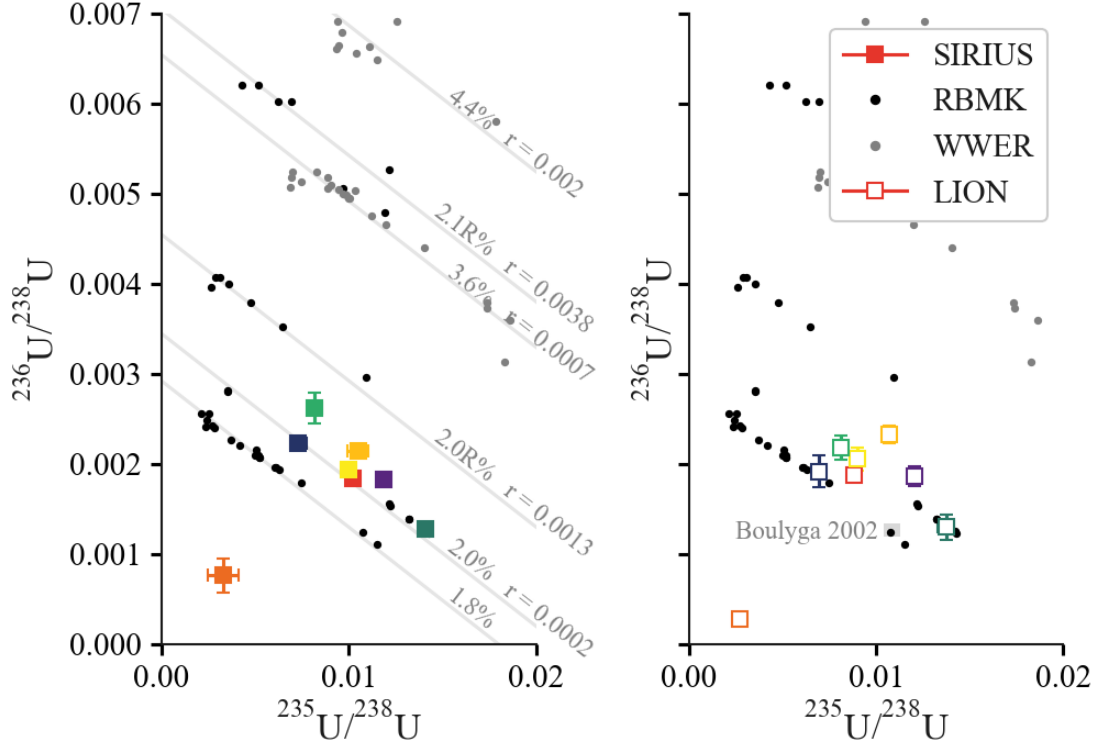


Figure 5.2: Three-isotope plot showing $^{235}\text{U}/^{238}\text{U}$ vs $^{236}\text{U}/^{238}\text{U}$. Particles (square) measured in SIRIUS (filled squares) and LION (open squares), where each individual particle is shown in a separate colour. Black and grey dots are the literature data isotope ratios measured in spent fuel rods of a variety of initial enrichments and operating times from RBMK-type (black) and WWER-type (grey) reactors by Makarova et al. [46]. The algebraic relation of initial enrichment (%) and ^{236}U recycling ($r = ^{236}\text{U}/^{238}\text{U}$ at initial enrichment, see text). The grey box is the range of ratios measured in CEZ soil by Boulyga et al. [100].

>0.018 , and should contain effectively no ^{236}U ($< 10^{-7}\%$ in U ore [43]). The production of ^{236}U can therefore be expressed as a linear relation to the $^{235}\text{U}/^{238}\text{U}$ ratio based on the initial enrichment ie , and the fraction of neutron capture $\sigma(n, \gamma)$ to fission $\sigma(n, f)$, described as

$$\frac{^{236}\text{U}}{^{238}\text{U}} = \frac{\sigma(n, \gamma)}{\sigma(n, f)} \left(ie - \frac{^{235}\text{U}}{^{238}\text{U}} \right), \quad (5.1)$$

where $\frac{\sigma(n, \gamma)}{\sigma(n, f)} = \frac{95}{586} = 0.16$ assuming purely thermal fission according to the cross-sections in the JEFF-3.3 library [7]. The $\sigma(n, \gamma)$ of ^{236}U is only 5 b, and is therefore insignificant in this algebraic simplification. In fig. 5.2, we can see that this linear relation holds very well for the 1.8% enriched RBMK fuel in the Makarova dataset. Makarova notes that certain fuel rods are composed of recycled fuel (noted 2.0%R and 2.1%R in fig. 5.2), meaning the $^{236}\text{U}/^{238}\text{U} > 0$ at the start of irradiation. This would add a linear offset to the previous equation in the form of r , such that

$$\frac{^{236}\text{U}}{^{238}\text{U}} = \frac{\sigma(n, \gamma)}{\sigma(n, f)} \left(ie - \frac{^{235}\text{U}}{^{238}\text{U}} \right) + r. \quad (5.2)$$

In fig. 5.2, it is clear that fuels noted as containing recycled fuel have a high r component, 0.0013 in the 2.0%R fuel, and 0.0038 in the 2.1%R fuel, which aligns with the 0.135 and 0.38% initial ^{236}U content reported by Makarova et al. [46]. What is remarkable is that the other fuels, the 2.0% RBMK fuel, and 3.6% and 4.4% WWER fuel cannot be described without an r component (0.0002, 0.0007, and 0.002 respectively). This suggests that (partial) recycling of fuel, potentially remixed with freshly enriched fuel, would have been common in Soviet reactors. In RBMK reactors in particular, fuel rods were replaced ‘online’ without the need for reactor shutdown. Particles measured from the ChNPP reactor, reported to be enriched at 2% will show a range of $^{236}\text{U}/^{238}\text{U}$, deriving both from the variation in burnup across the reactor, and the potential influence of (low-concentrated) recycled fuel.

It is evident in the CEZ particles that this is the case, with a spread in data around 2.0% enrichment. The soil data from Boulyga et al. predicts a very small range of isotope ratios in $^{235}\text{U}/^{238}\text{U}$ and $^{236}\text{U}/^{238}\text{U}$. This is due to the effects of averaging in the soil, which are not seen in individual particles. Forensically, we can say that the CEZ particles match the expected enrichment of 2.0%, and are not significantly recycled. The exception is B010, which has a $^{235}\text{U}/^{238}\text{U}$ ratio of 0.003, and a $^{236}\text{U}/^{238}\text{U}$ ratio 0.0003. The low $^{235}\text{U}/^{238}\text{U}$ indicates it is likely depleted U, a waste product of enrichment that has a $^{235}\text{U}/^{238}\text{U} < 0.007$, and typically contains no fission or activation products, such as Pu. However, the presence of the ^{236}U , confirmed by both SIRIUS and LION, indicates that this may again derive from a recycling process, where some spent fuel is re-enriched alongside natural U.

5.2 Strontium chronometry

Further forensics work has been proposed on the isotopes of Sr [66]. With a known $^{90}\text{Sr}/^{88}\text{Sr}$ isotope ratio from the fission yields, the measured ratio is then only subject to the ^{90}Sr half-life of 28.91 years, while the fissionogenic ^{88}Sr is stable. As described in Chapter 1, the contribution of thermal ^{239}Pu fission on the $^{90}\text{Sr}/^{88}\text{Sr}$ isotope ratio is minimal. The main source of uncertainty is in the nuclear libraries. For thermal ^{235}U fission, the $^{90}\text{Sr}/^{88}\text{Sr}$ isotope ratio ranges from 1.60 to 1.64 [7]. This range, confirmed by modelling described in the next chapter, then forms the upper and lower limit expected from a release on April 26th 1986. This must be decay corrected to a common date to compare with the measured particles, chosen as December 1st 2023. In fig. 5.3, grey bands mark the expected ratios for releases in April in the years 1966, 1976, 1982, 1986 and 1996 for comparison.

From the results in fig. 5.3, it is clear that concluding a definite release date is not possible, both in the uncertainty of the fission yield ratio, and in the spread of the measured data. Rather, the particles can clearly be grouped to a defined irradiation period. The oldest particles in this analysis appear to be from 1982. The spread in age may reflect different irradiation times of the fuel in the reactor. In this case it is most likely a function of uncertainty deriving from the correction of the naturally derived ^{88}Sr , as described in Chapter 3.

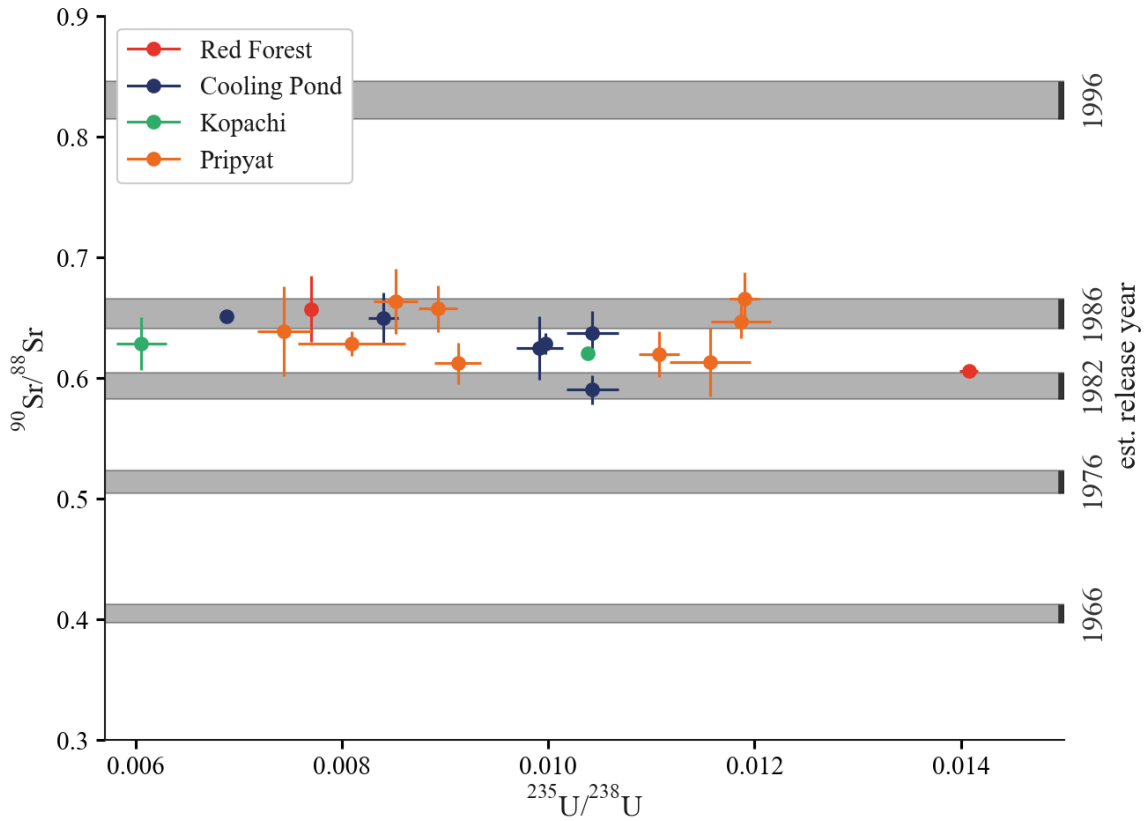


Figure 5.3: Four-isotope plot comparing the $^{90}\text{Sr}/^{88}\text{Sr}$ and $^{235}\text{U}/^{238}\text{U}$ in the CEZ particles, with calculations of estimated release on April 26th in 1966, 1976, 1982, 1986, 1996. The particles are coloured by their sampling location (see map in fig. 3.1). All $^{90}\text{Sr}/^{88}\text{Sr}$ data decay corrected to December 1st 2023.

It is worth considering the particles in the context of their sampling location. The location is not correlated with either the particle burnup or the measured $^{90}\text{Sr}/^{88}\text{Sr}$ ratios. We saw with the actinide ratios that a sample set could be tied to a reactor type, but here we see that this collection of particles truly belongs together. Outliers can be checked against this reference to count them in, or out, of this era. In the final chapter, we will investigate the ways in which environmental Sr interferes with fissionogenic Sr through particle imaging.

5.3 Zirconium cladding

Evidence of a reactor meltdown will not be found in the actinide isotope ratios. However, the fission products form an interesting interface with the natural world, as fissionogenic nuclides can mix with natural nuclides, which can be investigated through RIMS imaging in the SIRIUS instrument. RBMK type reactor fuel is clad in a Zr alloy, whose isotopes have low neutron absorption cross sections (see fig. 5.4). During the accident in Chernobyl, the fuel core melted, and parts of it fused with the cladding, which was then ejected into the environment in the explosions [4]. A handful of such particles have been found, of which K001 is the largest (see fig. 3.2).

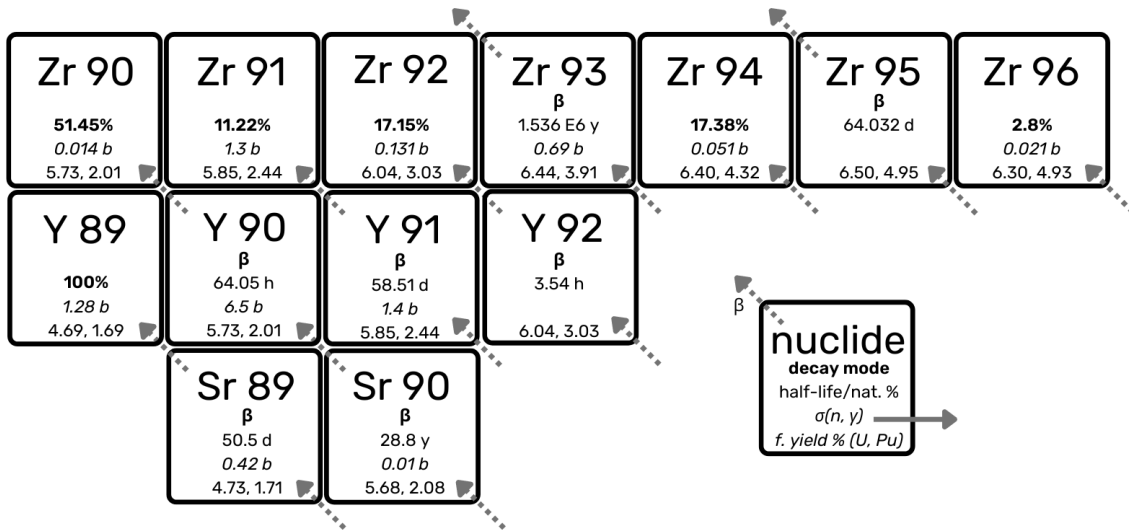


Figure 5.4: Production pathways of Zr isotopes, data from the JEFF-3.3 library [7].

As shown in fig. 5.4, there are five natural isotopes of Zr, all of which are also produced during fission. There are two radioactive isotopes, ^{93}Zr and ^{95}Zr , of which only ^{93}Zr has a sufficiently long half-life to be measurable in the CEZ hot particles. The isobar on ^{90}Zr and ^{90}Sr is fully suppressed in RIMS analysis, as measured by the lack of signal on mass 88.

As shown in fig. 5.5, RIMS imaging analysis presents an opportunity to separate the isotopes of Zr of natural and fissionogenic origin. In the top row, the non-resonant signals are shown, whereby UO^+ is most prevalent, and concentrated in the centre of the particle. The U^+ is similarly central, but the ZrO^+ shows a hollow triangle within the particle. This heterogeneity makes it peculiar, and is evidence of only partial fusing of the Zr cladding to the fuel, rather than full melting occurring.

The naturally occurring isotopes $^{90,91,92,94,96}\text{Zr}^+$ all follow the triangular pattern of ZrO^+ . The outlier is $^{93}\text{Zr}^+$, which follows the pattern of UO^+ and U^+ , showing that it is indeed a fissionogenic isotope. According to the fission yields, all the fissionogenic Zr isotopes should be of equal magnitude, indicating that fissionogenic Zr makes up roughly 1/8th of the total Zr.

The targeting of specific elements that are sensitive to chemical processes in a meltdown scenario shows great potential for forensic analysis. The majority of the particles do not contain a significant amount of cladding to be analysed in this way, however because of the previous isotope ratio analysis, we can tie the Zr-clad particles directly to the non-clad particles. The sequential and spatially resolved capabilities of the SIRIUS instrument make such analysis quickly accessible for further investigation.

5.4 Instrument comparison

In the case of nuclear forensics, it is imperative that the results obtained agree across different instruments. As previously shown in fig. 5.1, a general agreement can be found in the measurement of eight particles measured in both the SIRIUS and LION instruments that corresponds to literature data on RBMK type reactors. However there are singular discrepancies which are worth considering in more detail. The analysis of $^{241}\text{Pu}/^{239}\text{Pu}$ and $^{240}\text{Pu}/^{239}\text{Pu}$ ratios shows an interesting trend across the different measurement methods. In fig. 5.6, SIRIUS is compared to two measurement methods in LION, namely the multi-element measurement and the Blink-238 method.

The uncertainty is determined by the counting statistics. Where the count rate is low, as is the case in very small and morphologically complex particles, the uncertainty is particularly high. This is especially the case with particle BK022. The LION instrument achieves higher efficiency in its measurements, helped by the laser desorption method that

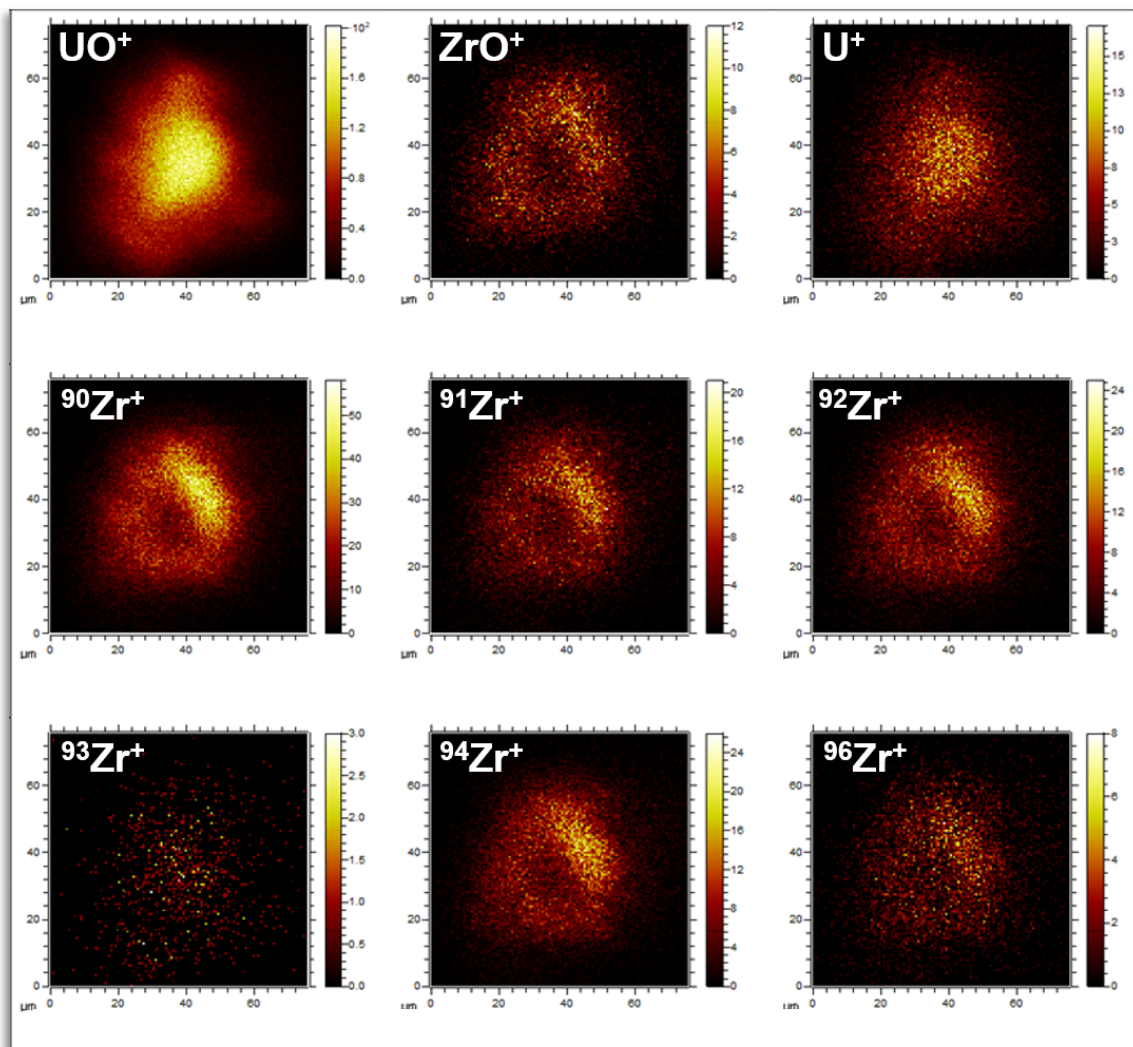


Figure 5.5: Resonant Zr RIMS analysis in SIRIUS on particle K001 (red in figures 5.1, 5.2, and 3.2). Top row: Imaging of non-resonant UO^+ , ZrO^+ , and U^+ . Middle and bottom row: Imaging of every zirconium isotope $^{90,91,92,93,94,96}\text{Zr}^+$.

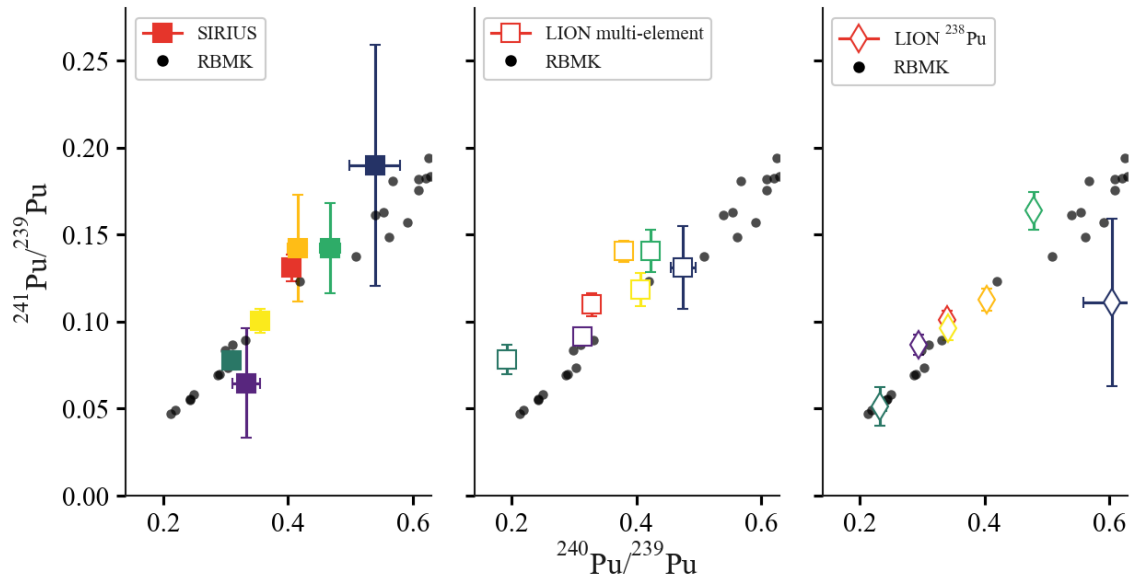


Figure 5.6: Comparison of results from SIRIUS, multi-element LION, and ^{238}Pu blinked LION for the ratios $^{241}\text{Pu}/^{239}\text{Pu}$ and $^{240}\text{Pu}/^{239}\text{Pu}$, with literature values for RBMKs [46]. All $^{241}\text{Pu}/^{239}\text{Pu}$ data is decay-corrected to the date of the Chornobyl accident, 26th April 1986. Each particle is represented by a unique colour.

removes more material from the particle surface.

From similar isotopic characteristics, it may be possible to assign particles to the same location within the reactor. For example, three particles in particular, the K001 (red), CP036 (orange), and CP008 (yellow) particles are very close together around $^{240}\text{Pu}/^{239}\text{Pu} = 0.4$ in fig. 5.6. From the SIRIUS measurements, one would conclude that K001 and CP036 are the same, but that CP008 is clearly separate. From the LION multi-element measurements, it would be concluded that each particle is distinct. From the LION Blink-238 measurements, the conclusion would be different again, where K001 and C008 are identical, and CP036 is distinct. Therefore, the results between the instruments agree sufficiently to say each particle is from the same reactor, but are insufficiently consistent to determine the exact location within the reactor.

Taken together, the results from fig. 5.7 demonstrate that the ratios of $^{241}\text{Pu}/^{239}\text{Pu}$, $^{242}\text{Pu}/^{239}\text{Pu}$ and $^{236}\text{U}/^{238}\text{U}$ do agree with each other within error. However, outliers are particularly found in $^{240}\text{Pu}/^{239}\text{Pu}$ and $^{235}\text{U}/^{238}\text{U}$ for the two Zr-bearing particles K001 and RW010. It was proposed that such deviations could be the result of these two particles being Zr-clad, which may have produced a non-resonant signal in the LION or SIRIUS analysis. Imaging can confirm or reject suspicions of interference in a given mass spectrum. The K001 particle, being heterogeneous on the surface, allowed for the testing of this hypothesis such that at the Zr cladding there should be a clear deviation from the measured isotope ratios in U and Pu.

Rather, as seen in fig. 5.8, no such deviation is observed, either in the U or Pu imaging.

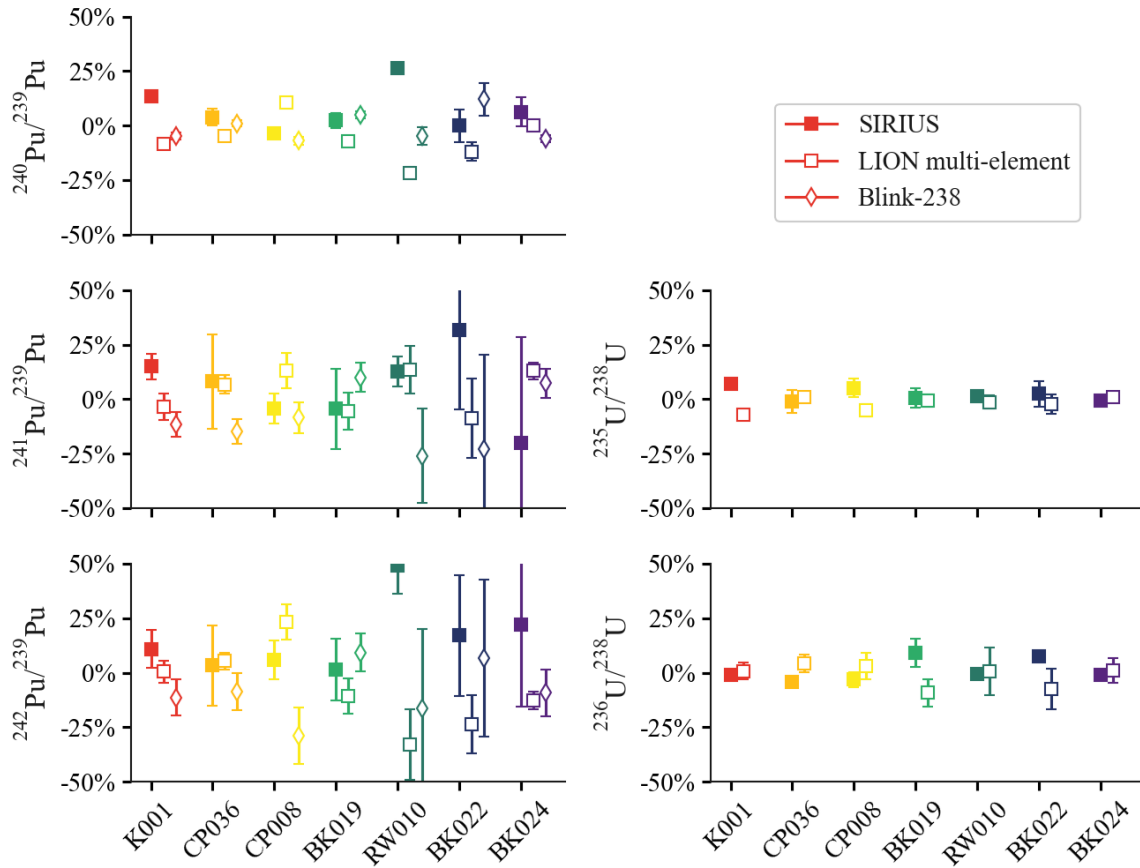


Figure 5.7: Percentage difference from the average isotope ratios, with 1σ error, as measured by all three methods.

If a significantly deviating ^{240}Pu were to be observed, it should, like either the ^{93}Zr in fig. 5.5, follow a distinct pattern around the particle. As such a pattern is not visually evident, regions of interest as seen in areas b1, b2, b3 (fig. 5.8b) were analysed for the isotope ratios, shown in 5.8c. Within these areas, no shift in isotope ratios is seen beyond error, and does not explain the LION measurements of $^{235}\text{U}/^{238}\text{U}$ and $^{240}\text{Pu}/^{239}\text{Pu}$. The source of the lower isotope ratios in the LION measurements was therefore not explained by the Zr cladding as pertained to the two-step excitation of Pu. It could however still be that the different laser schemes used in the LION measurements may have contributed to the suppression of the U and Pu isotope ratios.

5.5 Summary

In this chapter, an approach has been laid out for the forensic analysis of microscopic nuclear materials found in the environment solely using RIMS capabilities. It has shown that a positive identification of origin can be achieved, based on a collection of such particles. The actinide isotope ratios are key to the assessment of reactor-type, or in the case of a single particle, its composition of depleted uranium. It is curious that such a particle should be found in the sampling in the CEZ, though it demonstrates the powerful

capabilities of RIMS analysis.

The flexibility of the SIRIUS instrument in particular allows for more exploratory analysis of a particle, with an extended investigation into the fission products and RIMS imaging. It was shown that the fissionogenic Sr isotopes can be used to determine a time period of origin, dating the CEZ particles to an estimated irradiation period between 1982 and 1986. The Zr isotopes reveal in turn how the reactor meltdown caused a fusion of some particles to the Zr cladding around the fuel, which can be visually separated from fissionogenic Zr by spatially resolved imaging in SIRIUS.

For the future of RIMS analysis in the field of nuclear forensics, the comparison between instruments worldwide will need to establish global standards and methods. As shown by the measurements in LION and SIRIUS, general agreement on the origin and attribution of the particles is evident, even with high uncertainty in the measurements. However, apparent discrepancies that may be caused by interfering signals should be investigated further if RIMS is to serve as a ‘first pass’ method of forensic analysis.

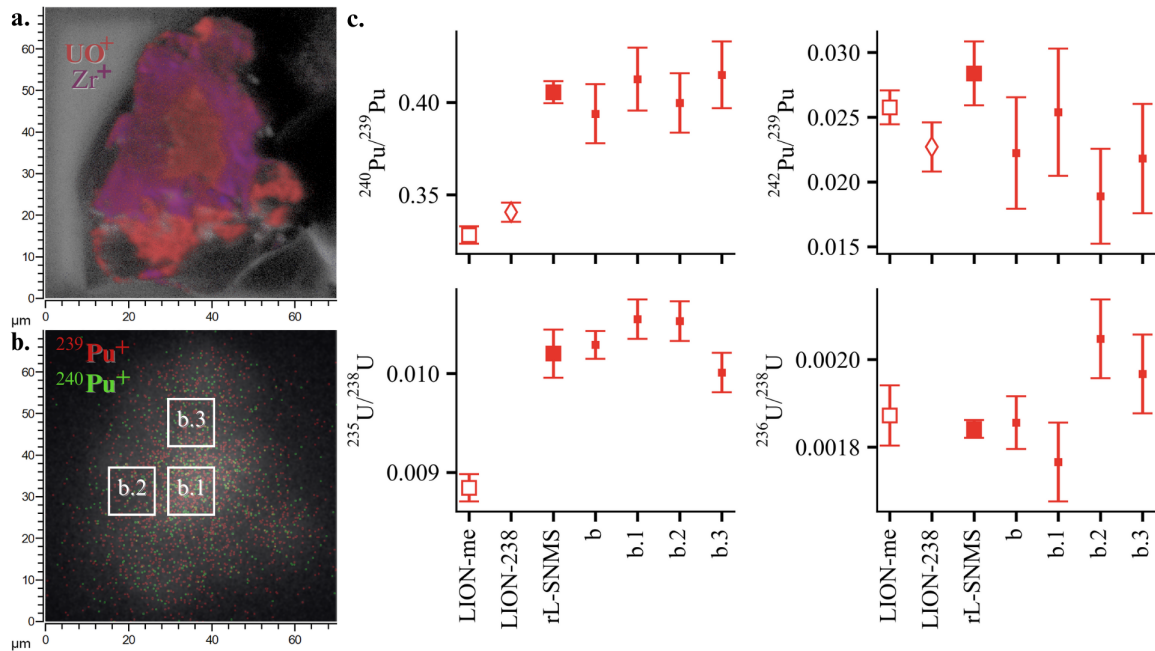


Figure 5.8: *a.* SIMS imaging on particle K001 showing UO and Zr distribution. *b.* Resonant Pu RIMS imaging on the same particle, showing distribution of ^{240}Pu , ^{239}Pu . *c.* Isotope ratios for $^{235,236}U/^{238}U$ and $^{240,242}Pu/^{239}Pu$ measured by SIRIUS and LION, with 1σ error.

Chapter 6

RIMS for Reactor Physics and Radioecology

As discussed in previous chapters, multi-element analysis requires a bespoke approach to each element. In the following sections the analysis of multiple elements is considered together, using multiple techniques to interpret the change in isotope ratios observed in this collection of particles. One can consider each particle on its own, influenced by its morphology, sampling location, and fuel burnup, but one must also consider all particles as a collection, indicative of the state of the RBMK reactor at the moment of the accident.

The following section compares the measured results in particles to modelling of the fuel composition in the RBMK reactor. Here, we consider how burnup and environmental exposure affect the isotope ratios in the CEZ particles. In the first section, the model is discussed with respect to the RBMK design, showing the effects of the fuel pin position in the assembly, and the effects of initial enrichment, reactor power, and moderator density. The following section looks more deeply into the consequences of particle exposure to the environment, and how this is reflected in the isotope ratios.

6.1 Experimental Results vs Reactor Model

In analysing the isotope ratio data in CEZ particles, one of the challenges is assessing the expected ratios. As we have seen in the previous section, the Makarova dataset is extremely useful, but limited in the range of data relevant to ChNPP. We must then look to a model to calculate how burnup affects the change in isotope ratios under various conditions. Here, we consider results from a reactor model developed by Ohm, based on the SCALE modules ORIGEN and TRITON developed by Oakridge National Laboratory [212]. These models have been designed for western-type BWR and PWRs, and so must be adapted for RBMKs with fuel enrichment in the range of 1.7 to 2.2%. The reactor design is shown in fig. 6.1. One benefit of a model is that one can use unrealistic inputs to assess the influence of different factors at extremes. The effects of recycled fuel and elevated initial ^{236}U is considered in the case of the 2.1% enrichment.

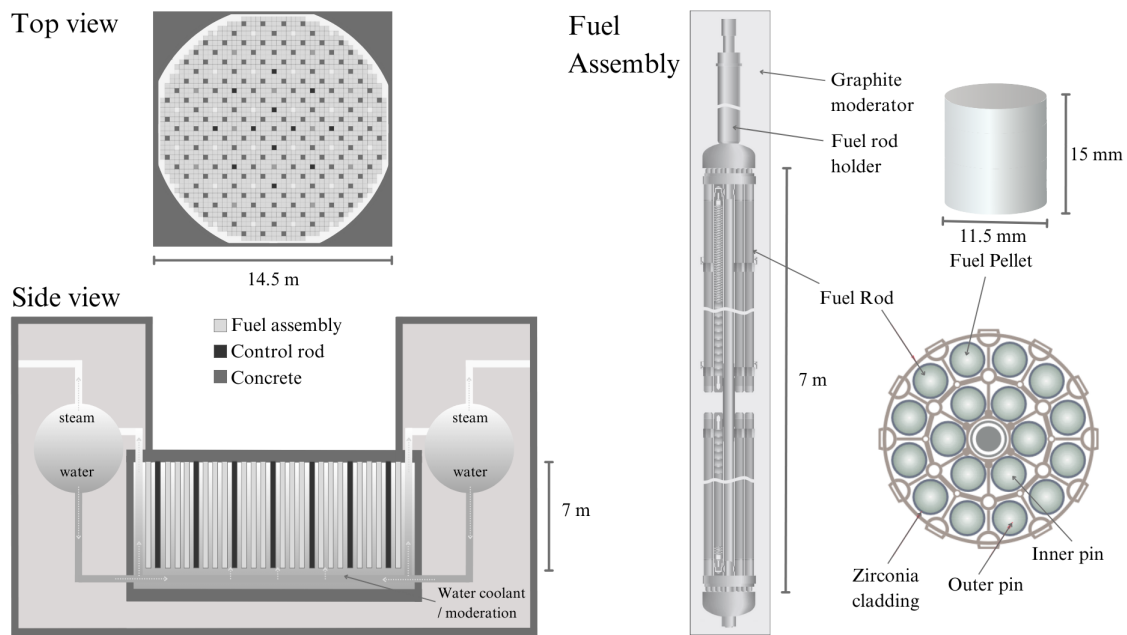


Figure 6.1: *Aspects of the RBMK design, not to scale. Top view: Each fuel assembly, control rods, and neutron sources are contained in square graphite tubes, arranged as seen in a circular construction. Individual fuel rods could be exchanged from the top. Side view: Water acts both as coolant and as secondary moderator. Steam drives turbines to generate electricity. Fuel assembly: The fuel rod holder is contained in the graphite tube, which holds 6 inner and 12 outer pins. Each rod is composed of fuel pellets, and is clad in a zirconia alloy. All figures adapted from Wikimedia Commons under Creative Commons and GNU licenses [209, 210, 211].*

The first aspect to note is that the reactor is large, with accessible fuel rods for exchange during reaction operation. The top of the reactor blew off during the accident at ChNPP, which is how the hot particles entered the environment [90]. From the top view, it is shown how the fuel assemblies are positioned amongst control rods and neutron sources. As has been shown so far, neutron flux, and the time-integrated neutron fluence, are the main drivers of isotope production. In modelling, changes in power effectively mean changes in flux.

From the side view, we see how the water coolant flows upwards. Water serves both as coolant and moderator, and as water turns to steam, its density decreases. At lower density, it moderates less and absorbs fewer neutrons. In the model, the moderator density is given as a fraction of that of water, from 0.75 at the bottom of the reactor to 0.15 at the top.

A fuel pellet's location affects the flux received: lowest at the outer edges near a control rod, highest in the centre surrounded by other fuel rods. In the model, one inner pin and one other pin in a fuel assembly are examined as shown in fig. 6.1, averaged over their entire length. The changes observed along the height of a fuel rod [46] are then approximated by changes in moderator density. The changes in reactor power from 13 to 20 MW approximate different flux conditions. Each burnup step of 0.5 GWd/tU is then

modelled up to 30 GWd/tU, meaning lower powers operate for longer to achieve the same total burnup. The results only show the isotope ratios from the first to third years. This range is an approximation of the effects of burnup across the reactor, as would be seen in the CEZ hot particles.

6.1.1 Actinides

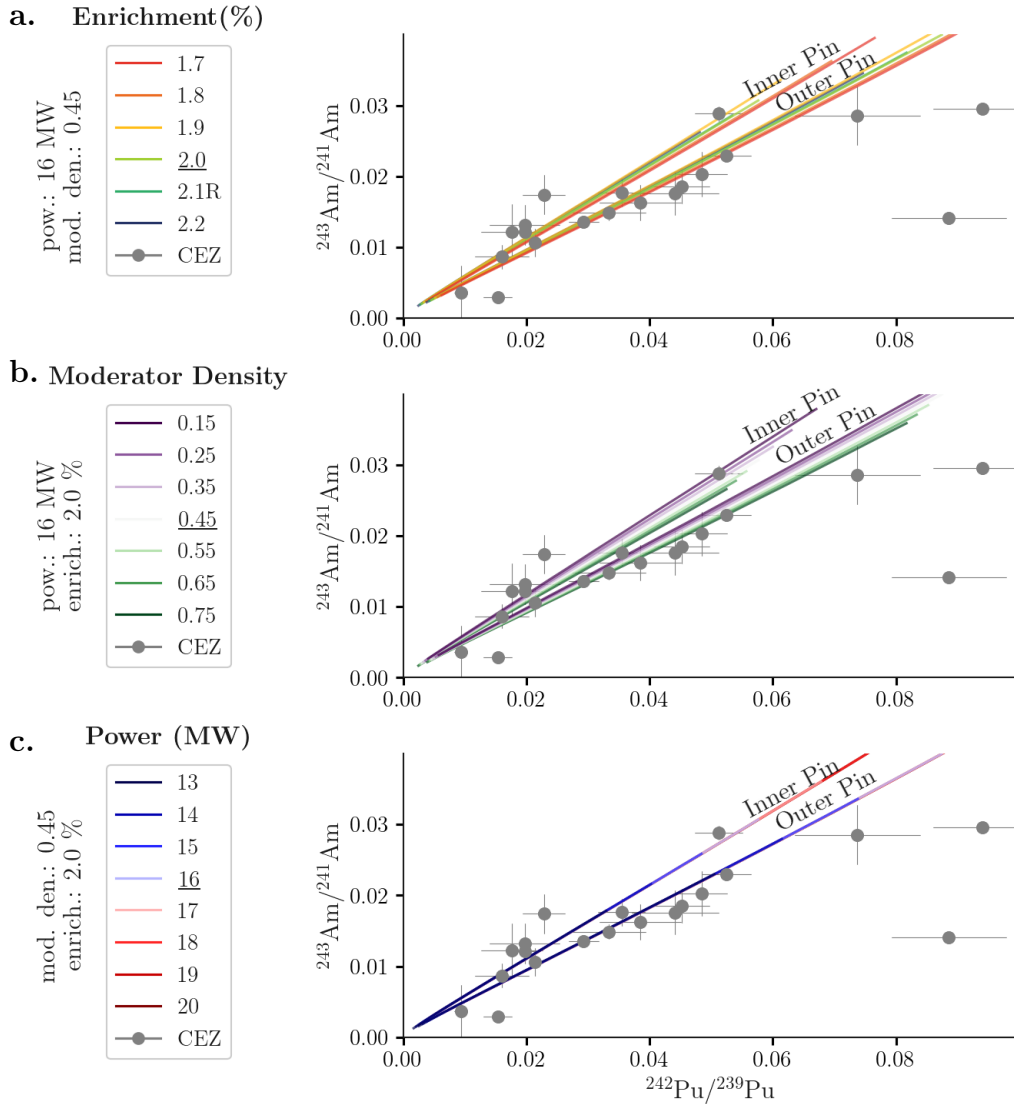


Figure 6.2: Four-isotope plot comparing the $^{242}\text{Pu}/^{239}\text{Pu}$ and $^{243}\text{Am}/^{241}\text{Am}$ in the CEZ particles compared to modelling results for RBMK type reactors under varying conditions. a. Varying enrichment from 1.7 to 2.2% at 16 MW and moderator density 0.45 (a.u.), for both and pin location within the fuel assembly [212]. b. Varying moderator density 0.15 to 0.75 at 16 MW power and enrichment 2.0%. c. Varying reactor power at 2.0% enrichment and 0.45 moderator density. Decay corrections are applied to the ^{241}Am modelling data to account for 36 years of ^{241}Pu decay. No corrections are applied to the measured ^{241}Am data as the initial ^{241}Pu concentration in the particles is not known.

One of the major assessments of Am and Pu is the ratio between $^{242}\text{Pu}/^{239}\text{Pu}$ and $^{243}\text{Am}/^{241}\text{Am}$, which targets the branching point at ^{241}Pu (see isotope production pathways in fig. 1.1). ^{241}Pu is affected by three competing processes. Its fission and neutron capture cross-sections are high, where $\frac{\sigma(n,\gamma)}{\sigma(n,f)} = \frac{370}{1010}$. Its beta-decay half-life is also relatively short at 14.1 years. This is however long compared to reactor operating times. The ^{241}Am measured in particles is then mostly what has decayed outside the reactor, whereas ^{243}Am is produced in the reactor via ^{242}Pu capture to fast decaying ^{243}Pu (half-life 5 hours).

In fig. 6.2 we see three iterations of the same particle and model data, reflecting each of the four variables in the model: pin location, initial enrichment, moderator density, and power. $^{243}\text{Am}/^{241}\text{Am}$ increases as $^{242}\text{Pu}/^{239}\text{Pu}$ increases, as would be expected with increasing burnup. As all isotopes considered here derive from neutron capture on ^{238}U , there should be no substantial difference in the ratios based on initial enrichment. This is reflected in the top row of fig. 6.2, where all enrichments overlap and no distinction can be made. Similarly in the bottom row, the power makes no significant difference.

The main difference in the ratios is evident in the moderator density and pin position, seen clearly in the middle row of fig. 6.2. At low moderator density, production of ^{243}Am and ^{242}Pu is favoured. The pin position has a similar affect on the slope, with the inner pin favouring ^{243}Am production. The outer pin is less affected by moderator density, therefore has a lower slope.

The CEZ particles fit the outer pin data better than the inner pin, with two major outliers at the highest $^{242}\text{Pu}/^{239}\text{Pu}$. It could be suggested that the ^{243}Am is depleted for environmental reasons, where the fission-generated ^{243}Am has been leached out preferentially over ^{241}Am generated by post-accident decay of ^{241}Pu . If such leaching is occurring, these results indicate that it is of minor influence on the $^{243}\text{Am}/^{241}\text{Am}$ ratios observed in the CEZ particles, which are well described by modelling on aged reactor fuel.

In the following discussion we can then focus on the parameters that influence the ratios the most. In the previous chapter, notably in fig. 5.2, we discussed how $^{235}\text{U}/^{238}\text{U}$ vs $^{236}\text{U}/^{238}\text{U}$ measures burnup and fuel recycling. There, we looked at literature data and concluded that a linear relation could be algebraically determined via the thermal neutron capture/fission ratio of ^{235}U , the initial enrichment, and initial ^{236}U . This is reflected in fig. 6.3a, where the 2.1% model includes recycled fuel, which aligns roughly with the literature data for recycled 2.1% fuel (dark blue triangles). It is curious that the lowest enrichment in the literature, the orange triangles at 1.8%, align closer to the model 1.7% enrichment rather than 1.8%. This could reflect statistical uncertainty in the measurement data, or energy spectrum data in the model that affects the ratio of neutron capture to neutron fission.

As in fig. 6.2, the reactor power only affects the maximum burnup achieved, and so is not shown as a variable in fig. 6.3. The pin position makes no substantial difference to the $^{235}\text{U}/^{238}\text{U}$ vs $^{236}\text{U}/^{238}\text{U}$ relation and is also not shown. The moderator density does however make a slight difference to the slope of the relation, seen in fig. 6.3b where lower

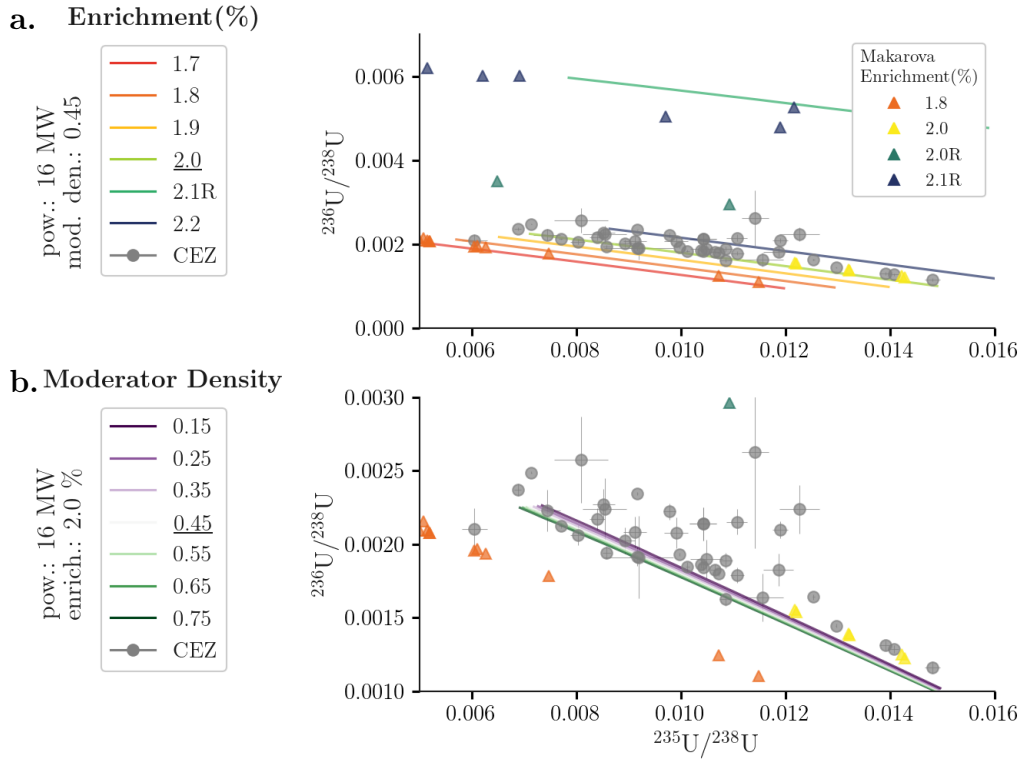


Figure 6.3: Three-isotope plot comparing the $^{235}\text{U}/^{238}\text{U}$ and $^{236}\text{U}/^{238}\text{U}$ in the CEZ particles compared to modelling results in the inner pin only [212] and literature data for RBMK type reactors [46]. a. Varying enrichment from 1.7 to 2.2%, with recycled fuel in 2.1%, at 16 MW and moderator density 0.45 (a.u.). b. Varying moderator density 0.15 to 0.75 at 16 MW power and enrichment 2.0%.

moderator density favours ^{236}U . As neutrons are less moderated and absorbed at low density, the slope suggests that neutron capture is enhanced, resulting in a higher $^{236}\text{U}/^{238}\text{U}$.

In fig. 6.3, the model isotope ratios clearly distinguish fuels of different initial enrichment, as also seen in the measured data by Makarova [46]. The CEZ particle results however are spread between 2.0 and 2.2%. While fuel mixing is possible, the accident reports for ChNPP only note 2.0% fuel [89]. The spread in data suggests that minor recycling could be a factor, however, not to the degree seen in the Makarova data for 2.0 or 2.1%. To investigate this further, we look at ^{238}Pu , which derives from neutron capture on ^{236}U .

In fig. 6.4a, the effects of fuel recycling are seen in both the model and Makarova data, where recycling leads to an increase in $^{238}\text{Pu}/^{239}\text{Pu}$. It is clear that ^{236}U recycling results in a higher $^{238}\text{Pu}/^{239}\text{Pu}$ ratio. In fig. 6.4b, it is shown that neutronics, in the form of low moderator density and inner pin position, also increase the relative proportion of ^{238}Pu . Thermal neutron capture is stronger for ^{235}U than for ^{238}U , while in the epithermal range (>0.025 eV) it is stronger for ^{238}U .

The measurement of ^{238}Pu , as noted in Chapters 2 and 3, is limited by the isobaric ^{238}U . The insufficient suppression of this isobar may therefore result in high $^{238}\text{Pu}/^{239}\text{Pu}$ ratios

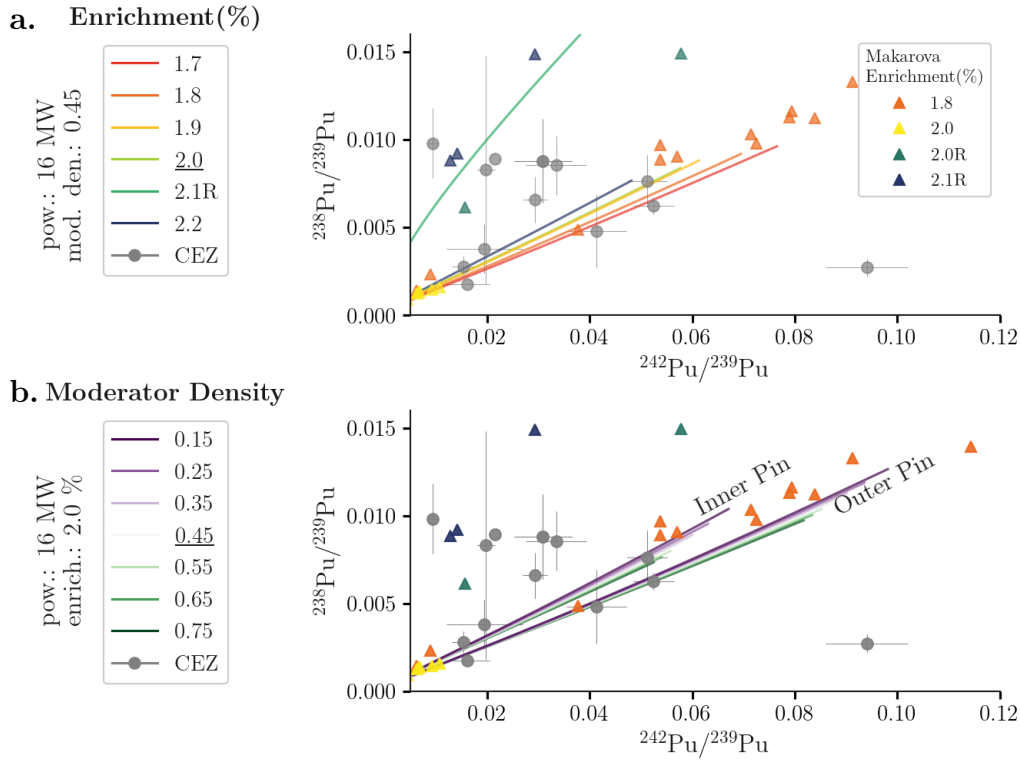


Figure 6.4: Three-isotope plot comparing the $^{242}\text{Pu}/^{239}\text{Pu}$ and $^{238}\text{Pu}/^{239}\text{Pu}$ in the CEZ particles to modelling results [212] and literature data for RBMK type reactors [46]. a. Varying enrichment from 1.7 to 2.2%, with recycled fuel in 2.1%, at 16 MW and moderator density 0.45 (a.u.) in the inner pin only. b. Varying moderator density 0.15 to 0.75 at 16 MW power and enrichment 2.0%, for inner and outer pins.

in the particles. Additionally, the ultra-trace concentration of ^{238}Pu in the particles result in high uncertainty, shown in the CEZ particle results in fig. 6.4. Just under half of the observed particles clearly align with the spread of results for 2.0% enriched fuel under different moderator conditions, seen in fig. 6.4b.

There is indication that some particles follow the recycled fuel trend, shown in fig. 6.4a. This is surprising considering the U results in fig. 6.3, where major recycling as in the 2.1% fuel case is not observed. Beyond low-level recycling, this indicates that the $^{238}\text{Pu}/^{239}\text{Pu}$ ratios are sensitive to further factors. Indeed, one outlying CEZ particle has exceptionally low ^{238}Pu and high ^{242}Pu , not explained by the model or literature data. These results point to the potential for strong local variations in ratios, caused for example by the skin effect, where the outer rim of a fuel pellet experiences drastically different neutronics from the centre [159].

The actinides have shown the ways in which a reactor model can effectively be used to predict the range of isotope ratios in a given reactor. It is a useful tool to investigate the influence of the neutron spectrum. The CEZ microparticles represent a large range of reactor conditions, that are sensitive to nuclear reactions on the micron scale. More edge cases may be shown in further modelling, for instance on a single fuel pellet to show the skin effect.

6.1.2 Fission Products

Literature data on fission product isotope ratios is scant, largely due to the challenges presented by the many isobaric nuclides, such as $^{135}\text{Cs}/^{135}\text{Ba}$, $^{137}\text{Cs}/^{137}\text{Ba}$, $^{87}\text{Rb}/^{87}\text{Sr}$, and $^{90}\text{Zr}/^{90}\text{Sr}$, as well as hydride and soil compound interference. Chemical separation procedures can remove such interferences [61], but must be tailored to the elements being separated. The chemical properties are also key to AMS measurements, which allow ultra-trace determination of $^{137}\text{Cs}/^{135}\text{Cs}$ because of the easy separation of Cs and Ba based on the electron affinity difference between the two elements [147]. This cannot simply be done with Sr isotope ratios, which require prior chemical separation [213].

For these reasons, when isotope ratios are available, they are not available in combination with actinide isotope ratios, or nuclear fuel burnup. In this application, models are essential to determine the range of possible ratios, and reactor parameters that affect them.

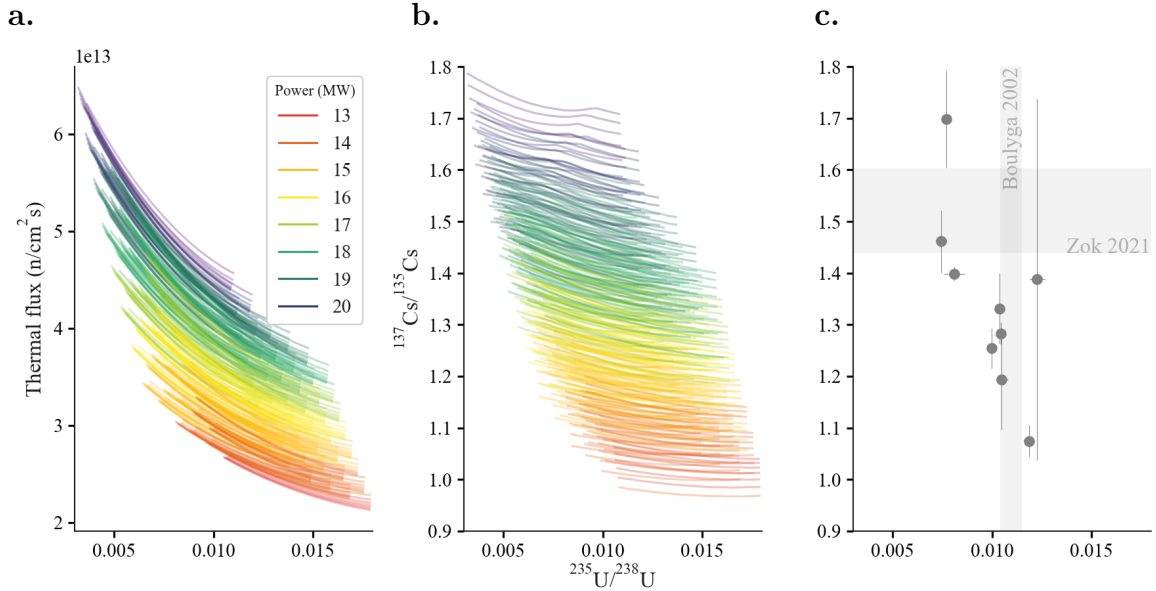


Figure 6.5: *a.* Flux variation as a function of the $^{235}\text{U}/^{238}\text{U}$ in the Ohm RBMK model, coloured by the average reactor power [212]. *b.* $^{137}\text{Cs}/^{135}\text{Cs}$ and $^{235}\text{U}/^{238}\text{U}$ in the Ohm RBMK model, coloured by the average reactor power [212]. *c.* The measured $^{137}\text{Cs}/^{135}\text{Cs}$ and $^{235}\text{U}/^{238}\text{U}$ ratios in the CEZ particles, grey bands marking the $^{137}\text{Cs}/^{135}\text{Cs}$ range measured in environmental samples in the CEZ samples by Zok et al. [61], and $^{235}\text{U}/^{238}\text{U}$ range in soil samples by Boulyga et al. [100]. All data decay corrected to December 1st 2023, assuming the model reactor stopped April 26th 1986.

The $^{137}\text{Cs}/^{135}\text{Cs}$ ratios in irradiated fuel are highly sensitive to the neutron flux in the reactor [58]. Higher flux leads to more burning of ^{135}Xe , increasing the $^{137}\text{Cs}/^{135}\text{Cs}$ ratio. In calculations by Robel et al., a linear relation between burnup and $^{137}\text{Cs}/^{135}\text{Cs}$ is observed when the flux is kept constant, valid at a steady state concentration of ^{135}Xe in a range of flux of between 10^{12} to 10^{15} n/cm²s) [58]. In the Ohm model, the reactor is kept constant at a certain power, requiring an increase in flux with burnup as shown in

fig. 6.5a. As such, the $^{137}\text{Cs}/^{135}\text{Cs}$ does not increase substantially with burnup as seen in fig. 6.5b. Rather, higher $^{137}\text{Cs}/^{135}\text{Cs}$ are a reflection of total flux experienced, or fluence, which correlates in the model to power.

In a real reactor, variations in both flux and power occur. This is reflected in the CEZ particle $^{137}\text{Cs}/^{135}\text{Cs}$ ratios, shown in fig. 6.5c as an increasing trend with burnup. As shown earlier in the actinides, the LION instrument has increased sensitivity through the desorption method. One particle (CP036) was measured in both SIRIUS and LION, at 1.30 ± 0.16 and 1.28 ± 0.02 respectively, showing that the Cs RIMS and desorption-SIMS agree within uncertainty. However, as shown by Okumura et al., heat-related Cs loss can occur in particles at temperatures over 100°C [214], and should be taken into consideration when measuring via the desorption laser.

The range in $^{137}\text{Cs}/^{135}\text{Cs}$ ratios observed in the CEZ particles is significant, giving the first indication of the range of flux found in the reactor. While generally increasing with burnup, two particles with highest burnup vary in $^{137}\text{Cs}/^{135}\text{Cs}$. From the reactor model, it could then be reasoned that these particles derived from different points in the reactor, experiencing different irradiation times at different fluxes. The highest fluxes (top left of fig. 6.5c) should derive from the centre, where the lowest fluxes (top left of fig. 6.5c) should derive from the outer edges.

The results measured in soil samples by Zok et al. [61] would suggest a range of high $^{137}\text{Cs}/^{135}\text{Cs}$ ratios indicative of high fluence. The fuel particles in contrast reflect a greater diversity of power and flux across the reactor, with far broader range. What is not measured in the Zok samples is the actinide ratios, though the average $^{235}\text{U}/^{238}\text{U}$ measured in CEZ soil by Boulyga was 0.0108 ± 0.003 [100]. A cluster of particles at this average burnup then suggests a far lower ratio of expected $^{137}\text{Cs}/^{135}\text{Cs}$ than found in bulk soils.

A number of factors could explain why bulk samples would be weighted towards high $^{137}\text{Cs}/^{135}\text{Cs}$ ratios. From a chemical vantage point, a distinction could be made between gaseous Cs released in the accident, which forms the majority of the contamination of the CEZ, and Cs trapped in the particles. As noted by Konings et al. [192], high burnup particles are more likely to release fission gases. This could mean that the gaseous Cs release during the accident is weighted towards high burnup $^{137}\text{Cs}/^{135}\text{Cs}$ ratios. Similarly, it was measured in CEZ particles by Poliakova et al. [142] that high burnup particles are more susceptible to degradation and dissolution. In this scenario, the high burnup Cs is more likely to have dissolved into the environment, whereas low burnup Cs remains trapped in solid fuel fragments.

Sampling bias must also be considered both in bulk samples and particle isolation. The particle isolation method in this work separates soil from fuel fragments by density and uranium content. Large and intact particles are favoured, and are chosen for a range of burnups rather than reflecting the total distribution of particle composition. Bulk samples are non-selective, though perhaps favouring high specific activity in soil to increase

concentration of ^{137}Cs . An analysis of how Cs may leach out of the particles is considered further in other work [64]. However, some indication of Cs retention can be analysed through Ba ratios in RIMS. The measured $^{137}\text{Ba}/^{138}\text{Ba}$ ratios in particles reflect the decay of ^{137}Cs , or lack thereof.

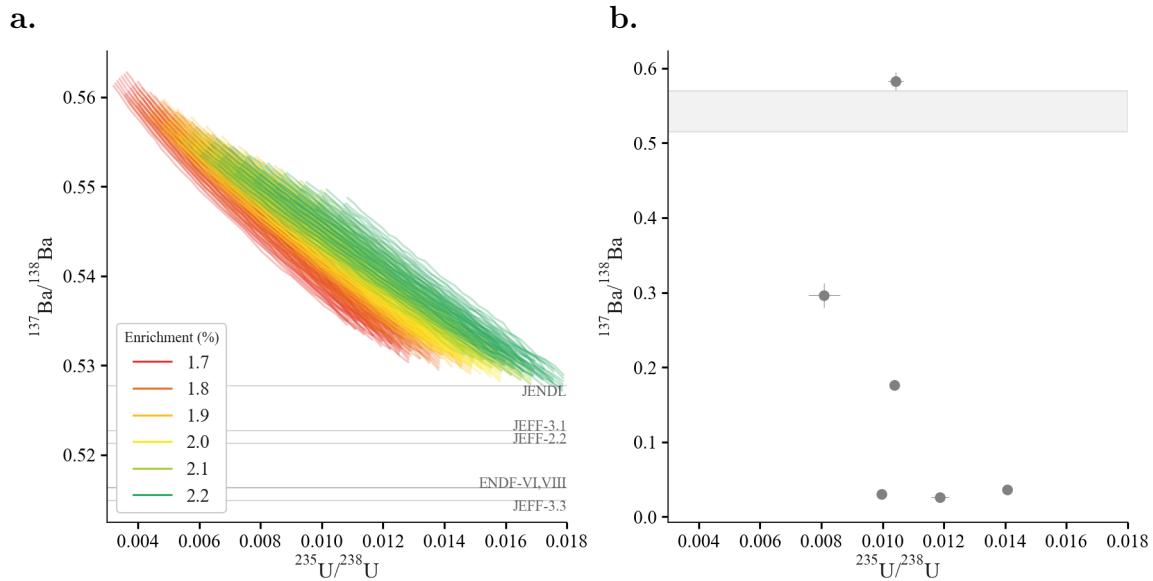


Figure 6.6: *Four-isotope plots of $^{137}\text{Ba}/^{138}\text{Ba}$ against $^{235}\text{U}/^{238}\text{U}$ a. Model simulation results for RBMK type reactors with variation of the initial enrichment [212], decay corrected to account for ^{137}Cs decay into ^{137}Ba from 26th April 1986 to 31st May 2022 when measurements were made of the CEZ particles. Nuclear data library [7] values for thermal ^{235}U fission yield ratio marked in grey, similarly decay-corrected. b. CEZ particles analysed in LION in May 2022, with the range of predicted ratios marked in grey.*

As discussed in Chapter 1, and demonstrated with the Sr chronometry in the previous chapter, fission yields can serve as useful estimates for expected isotope ratios in the fission products. Simplistically, fresh fuel only burns ^{235}U , and increasingly burns ^{239}Pu with higher burnup. The fission yields predict a ratio between ^{137}Cs and ^{138}Ba of 0.91 for ^{235}U and 1.08 for ^{239}Pu thermal fission in the ENDF-VI library (see section 1.4 for more detail). Over 36 years, ^{137}Cs will decay into ^{137}Ba . In fig. 6.6a, it is shown how different nuclear libraries predict the resulting $^{137}\text{Ba}/^{138}\text{Ba}$. This is the starting point at fresh fuel, with JEFF-3.3 predicting the lowest and JENDL predicting the highest ratio. The ^{239}Pu contribution to fission is determined by the neutron flux, which cannot be surmised algebraically. For that, we turn to Ohm’s model.

The results from the model in fig. 6.6a confirm that the variation in $^{137}\text{Ba}/^{138}\text{Ba}$ increases only slightly with burnup. The model is only as good as the nuclear data library it is based on (ENDF in this case), and so variation is likely. However, as shown in fig. 6.6b, the CEZ particles are not in the expected range. The majority of the particles have far too low a $^{137}\text{Ba}/^{138}\text{Ba}$ ratio. This leads to the conclusion that ^{137}Cs has escaped, and decayed into ^{137}Ba outside the particle matrix. The separation of Cs could be attributed to the accident or leaching into the environment. Evidence of the stability of each particle can be

further investigated by comparing other isotope ratios sensitive to the environment, such as $^{85}\text{Rb}/^{87}\text{Rb}$, and the gamma ratios of $^{241}\text{Am}/^{137}\text{Cs}$, and the natural contamination of the particles by $^{86,87,88}\text{Sr}$ and $^{135,136,137,138}\text{Ba}$.

6.2 Radioecology

The study of isotope ratios is generally limited to the effects of nuclear reactions, in controlled environments where the fuel pellets have come straight from the reactor and placed in storage [159]. In the rare case of nuclear material entering the environment, the study of radionuclides is described first by its chemistry, and secondly by the ecology of its environment. In this section, we consider the change in isotope ratios as a result of a particle's interaction with the environment.

6.2.1 Retention and loss

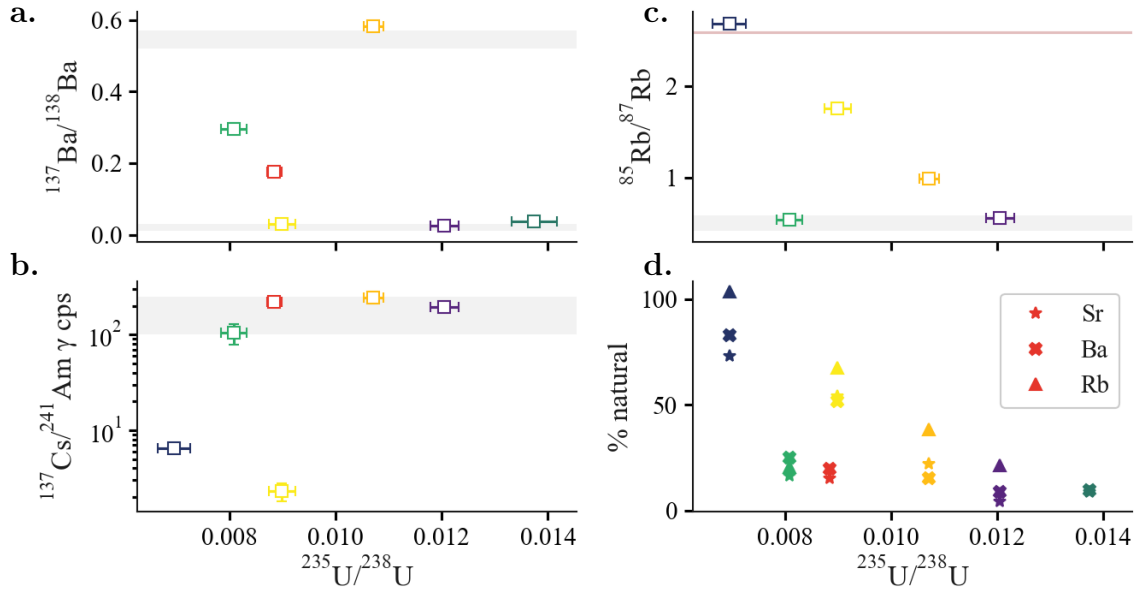


Figure 6.7: Ratios in relation to $^{235}\text{U}/^{238}\text{U}$. a. $^{137}\text{Ba}/^{138}\text{Ba}$, b. $^{137}\text{Cs}/^{241}\text{Am}$ gamma ratios (as measured in May 2022), c. $^{85}\text{Rb}/^{87}\text{Rb}$, d. Natural contamination of the particles as percentage of natural ratios in $^{85,87}\text{Rb}$, $^{86,87,88}\text{Sr}$, and $^{135,136,137,138}\text{Ba}$.

We can consider each individual particle via its characteristics in isotopic ratios, fig. 6.7 and its morphology in fig. 3.2. Not every particle could be measured in each ratio, such as B010 which was revealed by its $^{235}\text{U}/^{238}\text{U}$ ratios to be a depleted uranium particle [169], and therefore contains no fission products.

The $^{137}\text{Ba}/^{138}\text{Ba}$ ratios in fig. 6.7a will show the level of depletion of radiocesium from the particle, with the high grey band showing the range expected by modelling in fig. 6.6 for fully decayed ^{137}Cs after 36 years, and the lower grey band showing the $^{137}\text{Ba}/^{138}\text{Ba}$ range

directly out of the reactor. B022 is not shown because of low counting statistics. Of the CEZ particles, only C036 (light orange), with a mid-level $^{235}\text{U}/^{238}\text{U}$ ratio of 0.011, can be considered to have fully retained its Cs. The highest burnup particles B018 (green) and K001 (red) have partially retained the fissionogenic Cs. The remaining particles all show $^{137}\text{Ba}/^{138}\text{Ba}$ ratios at the level expected straight out of the reactor, with no substantial decay of ^{137}Cs .

The $^{137}\text{Cs}/^{241}\text{Am}$ gamma activity ratio is another measure of radiocesium depletion, as it relates to the activity of ^{241}Am , derived from decay of ^{241}Pu . In work by Leifermann et al., this ratio falls within 1×10^2 to 2.5×10^2 , where ratios orders of magnitude below that range are considered to have undergone Cs leaching [64]. In this interpretation, only the high burnup particles B022 (navy) and C008 (yellow) would be considered leached. While the $^{137}\text{Ba}/^{138}\text{Ba}$ might suggest there is no ^{137}Cs in B024 (violet), or R010 (teal), this is only true for R010, which did not have enough Cs to measure in gamma and is not shown in fig. 6.7b.

The $^{85}\text{Rb}/^{87}\text{Rb}$ ratios in fig. 6.7c cannot be corrected for naturally occurring Rb as was done in the cases of Sr and Ba, and particles K001 and R010 were not measured. The brown line shows the natural ratio of $^{85}\text{Rb}/^{87}\text{Rb}$, while the grey band shows the fissionogenic range as determined by the decay of ^{85m}Kr discussed previously. It is evident that the particles' surface is a mix of natural and fissionogenic Rb, being closer to natural Rb with higher burnup. The exception is particle B018, which is closest to fissionogenic origin.

In fig. 6.7d, the natural components of Sr, Ba and Rb together are considered. It is clear that each element exhibits the same general pattern, with higher burnup particles containing more nuclides of natural origin. The exceptions again are particles B018 and K001. This assessment is limited to the surface of the particle, though the question of whether environmentally derived nuclides penetrate the entire particle will be discussed in a different particle shown in fig. 6.8.

Individually, we can conclude a number of key characteristics in each particle from highest to lowest burnup. B022 collected from Pripyat, is highly porous, very small, and highly burned up. It contains the most environmentally derived nuclides, and suggests the Cs is substantially leached. B018, also from Pripyat, is more stable, though shows evidence of Cs leaching with respect to Ba, if not with respect to Am. It shows a remarkably low level of contamination with environmentally-derived stable nuclides, which may be related to its non-porous structure. K001 is a zirconium particle, collected from Kopachi (6 km southeast of Pripyat), with similar characteristics to B018 in burnup, Cs leaching, and natural contamination. C008 collected from the cooling pond, at medium burnup though with similar Cs leaching behaviour to B022 and is likewise highly porous.

C036, also from the cooling pond though not at all porous, is the most stable particle with no Cs leaching. It has natural contamination similar to B018 and K001 in terms of Sr and Ba, but has higher natural Rb contamination. B024 shows fractures on the particle surface,

commonly ascribed to high burnup structure [192]. It has contrasting leaching behaviour in Cs with respect to Ba and Am, and has very low contamination with natural nuclides. Finally, the only red forest particle (directly west of ChNPP) has the lowest burnup, no measurable Cs activity, reflected in a low $^{137}\text{Ba}/^{138}\text{Ba}$ ratio, and also low contamination with natural nuclides, with a surface smooth similar to C036.

The particles therefore exhibit a wide variety of attributes, for which particle origin is a poor predictor. Higher burnup particles appear to be more susceptible to environmental change, but this is hindered by a lack of porosity in the particles. Cs leaching does not appear to be uniform, and in fact may reflect different leaching mechanisms during the accident or in the environment.

6.2.2 Fissionogenic vs environmental nuclides

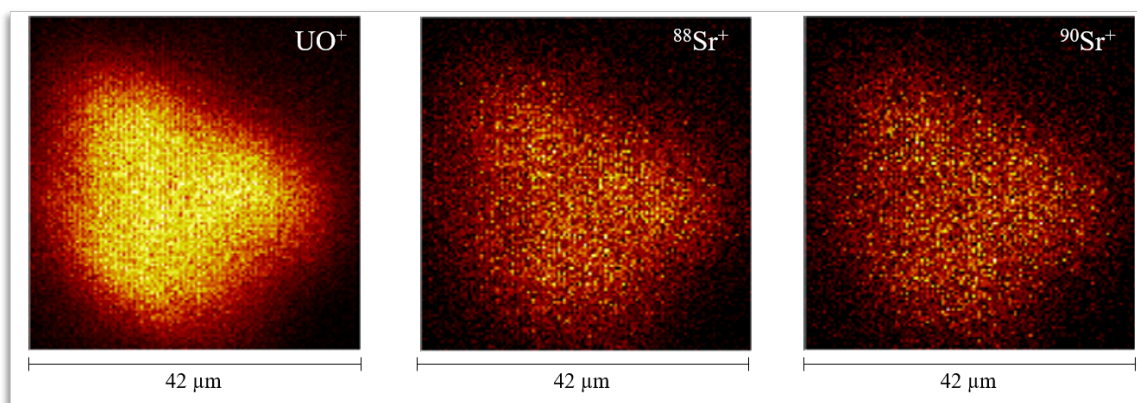


Figure 6.8: *Sr RIMS imaging in SIRIUS for non-resonant UO , ^{88}Sr (not corrected for environmental, ^{88}Sr) and ^{90}Sr in a bisected particle [190].*

Strontium poses a particularly interesting opportunity to investigate the relationship between nuclear material and the environment. Through fission, the Sr isotopes $^{88,90}\text{Sr}$ are produced alongside other fission products. The distribution of the fission products throughout nuclear fuel therefore depends on the distribution of the fissioning isotopes ^{235}U and ^{239}Pu , but also on migration of the fission products in gas form [192]. Strontium itself has a high melting point (1377 °C vs 671 °C in Cs), so migration is less likely than precursor elements Rb and Kr.

The natural abundance on Earth of Sr is comparable to Zr and Ba, and is higher than most transition metals [215]. Its chemical behaviour follows alkaline earth metals such as Ca, and can be readily found where Ca is rich, such as in chalk or bones. In CEZ particles, natural Sr isotopes $^{86,87,88}\text{Sr}$ can be found at ca. 10% of the total Sr measured. How the natural Sr gets incorporated into a nuclear fuel particle, and is influenced by its environment and particle structure (porosity, oxidation state), is not known.

In fig. 6.8, a CEZ particle was bisected by a gallium focused ion beam (FIB). A Sr RIMS measurement was performed on one half of the particle, and it was supposed that natural Sr should be concentrated at the edges of the particle, with more fissionogenic Sr in the centre. What is shown instead in fig. 6.8 is that the fissionogenic Sr isotopes show no significant spatial difference compared to natural Sr. This result indicates that, in this specific particle, natural Sr has penetrated the entirety of the particle in a homogeneous manner.

6.3 Summary

In this final chapter, the results of the isotope ratio analysis on hot particles has shown effects the of nuclear reactor operation and interaction with the environment. Comparison with models showed the influence of initial enrichment, reactor power, moderator density, fuel pin position, and fuel recycling. Initial enrichment influences the fission of ^{235}U , and production of ^{236}U and ^{238}Pu . Recycling of fuel leaves non-trace amounts of ^{236}U in fresh fuel, which increases both the relative contribution of ^{236}U and ^{238}Pu . Moderator density may also contribute to the mix of thermal and non-thermal fission, affecting the rate of isotope production, its influence is however minor in the isotope ratios.

Fuel position and reactor power have an influence on the neutron flux and total fluence experienced by the fuel. This affects particularly the $^{137}\text{Cs}/^{135}\text{Cs}$ isotope ratio, which is influenced by the neutron capture on ^{135}Xe . Flux can also favour one production path over the other, as seen $^{242}\text{Pu}/^{239}\text{Pu}$ and $^{243}\text{Am}/^{241}\text{Am}$. Flux has little effect on fission products with low $\sigma(n, \gamma)$, such as ^{137}Cs and ^{138}Ba . This stability with burnup allows for predictions of behaviour in the environment, which showed that most particles are leached to some extent of ^{137}Cs .

The chapter also showed the interaction of environmentally-derived isotopes with fissionogenic isotopes. All particles showed some interaction with the environment. Particle morphology is likely predictor of interaction, with porous and highly burned up particles being more susceptible. A cross-section of a particle showed that environmentally-derived nuclides could be found across the particle, suggesting it is not only a surface interaction.

Conclusions

In the literature, we have seen that isotope ratios have been used in a variety of ways to describe nuclear material in the environment. These are accessible through radiometric and mass spectrometric analyses. The $^{240}\text{Pu}/^{239}\text{Pu}$ ratio is key to identifying weapons-grade or weapons-derived Pu. The presence of heavier isotopes such as ^{242}Pu indicate reactor origin. The $^{242}\text{Pu}/^{239}\text{Pu}$ ratio is affected by the neutron spectrum and power of a reactor, producing an isotopic fingerprint unique to the reactor type. $^{235}\text{U}/^{238}\text{U}$ is an indication of the initial enrichment of a sample. As it relates to $^{236}\text{U}/^{238}\text{U}$, it can show burnup in the sample, and evidence of fuel recycling. The $^{137}\text{Cs}/^{135}\text{Cs}$ ratio is an indication of neutron flux, distinguishing between different reactors and their operating modes.

Mass spectrometric analysis typically requires chemical separation of the samples, which focuses on one or two isotope ratio measurements at a time, often in bulk samples only. Radiometric analysis such as the activity ratios of $^{137}\text{Cs}/^{90}\text{Sr}$ through gamma and beta spectrometry respectively can also measure burnup, as long as no chemical separation has occurred. When it has, it is reflected in this ratio. An environmentally insensitive measure of burnup is the gamma spectrometry of ratios of $^{137}\text{Cs}/^{134}\text{Cs}$. As with all spectrometric assessments, it is time sensitive, and limited at small sample volume.

RIMS instruments

For the analysis of hot particles, RIMS is a uniquely versatile technique, able to probe ultra-trace active and stable nuclides. This work built on the established capabilities for U, Pu, and Am analysis, showed the expansion of schemes for Rb, Sr, Zr, Cs, Ba, and Np. It delved further into the interpretation of actinide and fission product isotope ratios, and imaging capabilities on hot particles.

Two RIMS instruments were investigated, the SIRIUS instrument in Hannover, Germany, and the LION instrument in Livermore, USA. The LION instrument uses a laser desorption technique, which allows isobar-free analysis of alkali-metals in SIMS mode, which enables simultaneous analysis of Rb and Cs. The six lasers used at LION and flexible timing allow for simultaneous analysis of multiple elements in RIMS, with Ba and Pu arriving after Sr and U, shifting them out of possible isobaric interferences in the time-of-flight mass spectrum. The laser desorption method was however not ideally suited to CEZ hot particles mounted on tungsten needles with insulating glue, as it caused heat damage to the particles. The SIRIUS instrument's main advantages are in spatially resolved analysis,

and fast element-switching.

New excitation schemes for elements Sr, Zr, and Np were analysed in the SIRIUS instrument, in addition to already demonstrated U, Pu, and Am schemes. On a single particle, six elements can be non-destructively and sequentially probed, requiring only two lasers¹. Through wavelength scans and saturation curves, it was shown that Sr has a particularly broad autoionising state, and low saturation power. The Zr scheme is at the edge of the frequency range frequency-doubled Ti:Sa laser emission, and requires high saturation power in the second excitation step.

The Np scheme was shown to overlap with a minor resonance in Pu, and several minor resonances of U in the AI step. By adjusting the AI step, and using a narrow-band laser, the ratio of Np/Pu or Np/U can be improved as these resonances are avoided. Absolute suppression of non-resonant signal was not possible for U, even with the narrowband laser. This is likely due to the photodissociation of UO, caused by the frequency doubled blue lasers. This has consequences for the measurement of ²³⁸Pu in a resonant Pu RIMS measurement, for which the isobaric ²³⁸U can only be suppressed by up to four orders of magnitude. It was shown in the LION instrument that by blinking a resonant and non-resonant laser in a three step scheme, the non-resonant signal from the single blue laser can be corrected for in-situ, and the ²³⁸Pu/²³⁹Pu ratio effectively measured on CEZ particles.

A Cs RIMS scheme was tested in SIRIUS using two red steps. No saturation was achieved, meaning it is not an optimally efficient scheme. The limit of detection of ¹³⁷Cs via RIMS is estimated to be around 0.1 Bq, or 1×10^8 atoms based on the analysis of CEZ hot particles of known activity. With gamma spectrometry, the detection limit is an order of magnitude lower, as measured on a single 10 mBq particle by Macsik et al. [120]. In contrast to gamma spectrometry, particle morphology plays a major role in RIMS, where a higher activity particle may not result in better mass spectra. Only one spherical silicate particle was found in the Fukushima samples. It did not contain enough ¹³⁷Cs to be measured by gamma spectrometry or RIMS, though ¹³³Cs was identified.

RIMS imaging

Through RIMS imaging, isotopic heterogeneity can be investigated on the micrometre scale. In some CEZ hot particles, Zr-cladding was fused with the fuel during the accident, resulting in a heterogeneously distributed Zr on the micrometre scale. Zirconium isotopes are however also produced through fission, with the addition of non-naturally occurring ⁹³Zr and ⁹⁵Zr, of which only ⁹³Zr remains decades after the accident. It was shown through imaging that ⁹³Zr could be distinguished from the naturally occurring isotopes, correlated to U signal instead.

¹The most elements measured on one particle in one day to date is four: U, Pu, Am, Sr. Three elements (U, Sr, Am) can be measured in up to three particles. Unfavourable sample geometry, instability in the lasers, and equipment breakdown are the primary obstacles to rapid sample analysis. Careful planning is required for an efficient, thorough, and statistically significant analysis of hot particles

It is relevant to note that almost all isotopes are homogeneously distributed in hot particles. Isotopic changes in the actinides and fission products are known to occur on the skin of a fuel pellet which could result in heterogeneity on the micrometre scale to which the neutronics are sensitive, however this was not observed in any of the over 30 particles analysed in this work. As the Zr-fused particle is most likely to have derived from the fuel pellet edge, this particle was imaged for resonant Pu and U isotopes, and no significant changes were observed in isotope ratios across the particle.

Homogeneity was also observed in Sr isotopes, of which $^{88,90}\text{Sr}$ derive from fission, and $^{86,87,88}\text{Sr}$ derive from the natural environment. In a particle that was sliced in two by a focused ion beam, the cross-section showed no spatial separation between the fissionogenic Sr isotopes and the naturally derived isotopes. This suggests that the particle's interaction with the environment may not be limited to the edges of the particle, but could penetrate through. Similar analysis of other particles would show whether is true for all particles, or only those of a particular structure. Further, it should also consider whether and how Sr is entering and leaving the particles, which may be determined by the fissionogenic Zr isotope ratios, of which ^{90}Zr is a decay product of ^{90}Sr .

Isotope ratio analysis for forensics

RIMS analysis of a large number of CEZ hot particles has expanded the isotope ratios typically investigated in nuclear forensics and radioecology applications. Simultaneous analysis of $^{235}\text{U}/^{238}\text{U}$ and $^{242}\text{Pu}/^{239}\text{Pu}$ in both LION and SIRIUS shows that the CEZ particles match literature values for RBMK type reactors as opposed to WWER type reactors also present in the region. An exceptional particle was found that contained no ^{242}Pu , but rather depleted U, and showed evidence of irradiation exposure due to the presence of ^{236}U . The depleted uranium is likely from some form of shielding material present on the ChNPP site. Unusual particles such as these are likely to emerge when larger numbers of particles are analysed.

Expected ranges of these ratios can be found in the literature, though these studies have limited sample sizes and are reflective of bulk fuel samples on the order of grams rather than individual microparticles. Modelling is then used to predict a range of ratios at different burnups. The modelling shows the different influence of operating power, fuel pin location in the assembly, the moderator density, and initial enrichment. For $^{235,236}\text{U}/^{238}\text{U}$, these ranges are very narrow irrespective of power and moderator density.

The linear relation between the $^{235}\text{U}/^{238}\text{U}$ and $^{236}\text{U}/^{238}\text{U}$ isotope ratios is evident from the isotope production pathways. Initial enrichment is the main factor, which shows the CEZ particles to align with an initial enrichment between 1.9 and 2.2%, while reported initial enrichment for ChNPP is at 2.0%. Moderator density has only slight influence, whereas the most notable impact is from a non-zero $^{236}\text{U}/^{238}\text{U}$ ratio in fresh fuel, which results in a linear offset. This may be indicative of low-level fuel recycling, whereby the initial ^{236}U in

the fuel is non-zero from fuel recycling. This could account for the spread in isotope ratios seen in both the literature data and the CEZ particles.

The $^{238}\text{Pu}/^{239}\text{Pu}$ ratios corroborate this idea, with some particles exhibiting abnormally high ratios with respect to $^{242}\text{Pu}/^{239}\text{Pu}$. The production of ^{238}Pu derives from neutron capture on ^{236}U , while $^{239-242}\text{Pu}$ derive from ^{238}U . Other explanations could derive from microscopic changes in the neutronics of a fuel pellet, known as the skin effect. Further modelling and analysis work is needed on the scale of such effects, and whether this could result in the physical separation of U and Pu. Through the combination of RIMS and modelling, it becomes easier to investigate the outlying cases that may not be captured in a reactor model, and to explain the physical parameters that may cause them.

Analysis of the neutron fluence are found in the $^{137}\text{Cs}/^{135}\text{Cs}$ ratio. This ratio is highly sensitive to neutron flux, with lower ^{135}Cs production rates at higher flux due to activation of ^{135}Xe . During steady-state operation, this ratio should increase with burnup. This was found in the majority of particles measured, though significant variation was seen in particles of similar burnup suggesting different flux conditions within the same reactor.

The range in $^{137}\text{Cs}/^{135}\text{Cs}$ ratios measured in particles far exceeds that measured in bulk soil samples. This poses questions for the attribution of origin from isotope ratios in bulk samples, where averages may overlook such outliers. As the bulk sample ratios lean towards high burnup, it is probable that the high burnup sections of fuel contributed more towards the gaseous release of Cs during the accident. This may then also account for the relatively low burnup $^{235}\text{U}/^{238}\text{U}$ ratios measured in soil, which would derive only from particles rather than gas.

What the outliers have in common (when they aren't depleted uranium), is that they all share a $^{90}\text{Sr}/^{88}\text{Sr}$ ratio, associating them to one event. Through algebraic analysis, and confirmed by modelling, it was shown that this isotope ratio falls in a narrow range during reactor operation. Once removed from the reactor, it then serves as an environmentally independent chronometer. The particles fell in a range between 1982 and 1986, suggesting that multiple fuelling events took place and therefore a range of ages can be found in the reactor. The main sources of uncertainty are in the corrections required to account for environmentally-derived ^{88}Sr , and the range of fission yields quoted across the nuclear data libraries. Nonetheless, the use of the Sr chronometer presents a valuable marker of sample origin.

Isotope ratio analysis for radioecology

Hot particles are a unique form of contamination of the environment. One great difference between the Fukushima and Chernobyl accidents is that, in Fukushima, the release was almost exclusively gaseous, with some microparticles forming incorporated with that gas. The CEZ particles in contrast are chunks of nuclear material, far more numerous, large, and persistent in the environment. As such, the analysis of these particles

brings into question the assumptions of source term calculations. What is actually retained in fuel during an accident? Through isotope ratios, we can study the effects of nuclides leaching out of a particle, and the environmental nuclides adsorbing onto and into it.

The $^{241}\text{Pu}/^{239}\text{Pu}$ ratio is sensitive to time due to the decay of ^{241}Pu into ^{241}Am . The study of the $^{243}\text{Am}/^{241}\text{Am}$ then becomes a measure of environmental sensitivity, as ^{243}Am could become separated from the ^{241}Am parent ^{241}Pu . The possible leaching of one element over the other in the environment was tested by looking at the $^{241}\text{Am}/^{243}\text{Am}$ ratios. No significant separation was identified, as the particles mostly followed the linear trend with relation to $^{242}\text{Pu}/^{239}\text{Pu}$ as predicted by the model and literature values.

The loss of Cs in particles was measured through Ba RIMS and activity ratios between $^{137}\text{Cs}/^{241}\text{Am}$. It was shown in modelling that the $^{137}\text{Cs}/^{138}\text{Ba}$ ratio should remain in a narrow range with increased burnup in the reactor. Upon release, the ^{137}Cs should then decay into ^{137}Ba . The majority of particles measured in Ba RIMS were shown to be depleted in ^{137}Ba , suggesting leaching of Cs into the environment. Gamma activity ratios between $^{137}\text{Cs}/^{241}\text{Am}$ showed that leaching of Cs was not in all cases the same with respect to Am as for Ba. Significant Cs loss was attributed to particle morphology of high porosity, whereas Cs retention was associated with low porosity. More Ba RIMS could be done on CEZ particles with a more efficient and accessible scheme. Currently, only a frequency tripled, partially resonant scheme is available, which requires a dedicated laser setup not currently available in SIRIUS.

Evidence of the particles' interaction with the environment was shown by detection of naturally derived nuclides of the elements Ba, Rb, and Sr, found on all particles. The fraction of natural vs fissionogenic isotopes generally increased with burnup, though exceptions may again be due to particle morphology. For Ba and Sr it was shown that the non-fissionogenic isotopes seen in a mass spectrum could be used to account for environmentally-derived interference on fissionogenic isotopes. This was not the case for Rb, whose natural isotopes are also fissionogenic. Further work is needed to describe the exact interaction of particles with the environment, as described earlier in Sr RIMS imaging.

The retention of volatile gases within nuclear fuel, even during accident scenarios where they are assumed dissipate substantially, could be fruitfully explored through isotope ratio analysis. If measured free from environmental interference, the $^{87}\text{Rb}/^{85}\text{Rb}$ ratio could be indicative of the retention of noble gases, in this case ^{85}Kr in the particle, which are assumed in source term calculations to have entirely dissipated. Similarly, $^{137}\text{Cs}/^{135}\text{Cs}$ ratios could target the dissipation or retention of the ^{135}Xe .

The complexity of a nuclear reactor, especially one as colossal as the RBMK, can be viewed from so many different angles. Isotope ratios offer one way to distil the intricacies into a single value. By analysing multiple isotope ratios, in multiple elements, the complexity is opened back up again. Single microscopic particles could be quickly analysed for Pu to rule out any nefarious use. A single particle could show how metal and fuel fuse together

by mapping Zr. A collection of samples could be grouped by analysing Sr, show how flux changes the U, Pu, and Cs composition across a reactor, and show through Ba that Cs may have been lost to the environment.

Future Work

We have much still to learn from the Chernobyl samples, as they are a uniquely diverse sample set. These methods are, however, not limited to the CEZ, and in future work samples of different origins should be analysed. While no active Fukushima particles were found in this work, when they are found, isotopes beyond Cs can be measured, showing how other elements may have been captured in them. RIMS can also be applied to other contamination events, where multiple incidents from different sources over time can complicate the distribution of particles, as in Dounreay, Sellafield, and Mayak. As shown in this work, RIMS can group the particles by their origin and formation.

Its applications are not limited to severe nuclear accidents, but could be used in more routine analysis of material. In the decommissioning work at FDNPP, RIMS could offer diagnostic analysis of fuel recovered from the site. The effects of long-term storage conditions on waste materials could be investigated, showing its degradation in different conditions. They could be used to image ultra-trace elements, which would be particularly useful in mapping contaminants at the micro scale in biological samples.

In conclusion, RIMS is a uniquely versatile technique, relying on the universality of atomic structure to assess the nuclear history of a sample. In this effort, RIMS instruments around the world must work together to establish standards and share best practices. Through routine measurements and diverse applications, it can become an integral tool for ultra-trace elemental analysis, in nuclear material and other fields.

Bibliography

- [1] F. Belloni, J. Himbert, O. Marzocchi, and V. Romanello, “Investigating incorporation and distribution of radionuclides in trinitite,” *Journal of Environmental Radioactivity*, vol. 102, pp. 852–862, 2011.
- [2] L. Devell, H. Tovedal, U. Bergstrom, A. Appelgren, J. Chyssler, and L. Andersson, “Initial observations of fallout from the reactor accident at Chernobyl,” *Nature*, vol. 321, pp. 192–193, 1986.
- [3] K. Adachi, M. Kajino, Y. Zaizen, and Y. Igarashi, “Emission of spherical cesium-bearing particles from an early stage of the Fukushima nuclear accident,” *Scientific Reports*, vol. 3, 2013.
- [4] V. A. Kashparov, “Terrestrial, surface water and ground radioactive contamination, and remediation,” *Environmental Science and Pollution Research International*, pp. 21–30, 2003.
- [5] IAEA, “IAEA Statute,” 1956.
- [6] IAEA, “IAEA Safeguards Glossary 2001 edition,” 2001.
- [7] Nucleonica. <https://www.nucleonica.com/>.
- [8] K. Komura and M. Sakanoue, “Determination of $^{240}\text{Pu}/^{239}\text{Pu}$ ratio in environmental samples based on the measurement of Lx/a-ray activity ratio,” *Health Physics*, vol. 46, pp. 1213–1219, 1984.
- [9] B. Meyer, “The r-,s-, and p-processes in nucleosynthesis,” *Annual Review of Astronomy and Astrophysics*, vol. 32, pp. 153–190, 1994.
- [10] G. B. Dalrymple, “The age of the Earth in the twentieth century: A problem (mostly) solved,” *Geological Society Special Publication*, vol. 190, pp. 205–221, 2001.
- [11] D. M. Taylor, *Environmental plutonium creation of the universe to twenty-first century mankind*, vol. 1, pp. 1–14. Elsevier Science Ltd., 2001.
- [12] M. B. Chadwick, “Nuclear science for the Manhattan Project and comparison to today’s ENDF data,” *Nuclear Technology*, vol. 207, no. sup1, pp. S24–S61, 2021.
- [13] World Nuclear Association. <https://www.world-nuclear.org/information-library/nuclear-fuel-cycle/mining-of-uranium/world-uranium-mining-production.aspx>.

- [14] K. Mayer, M. Wallenius, and Z. Varga, “Nuclear forensic science: Correlating measurable material parameters to the history of nuclear material,” 2013.
- [15] G. T. Seaborg and M. L. Perlman, “Search for elements 94 and 93 in nature. Presence of 94-239 in pitchblende,” *J. Am. Chem. Soc.*, vol. 70, pp. 1571–1573, 1948.
- [16] K. M. Wilcken, T. T. Barrows, L. K. Fifield, S. G. Tims, and P. Steier, “AMS of natural ^{236}U and ^{239}Pu produced in uranium ores,” *Nuclear Instruments and Methods in Physics Research, Section B: Beam Interactions with Materials and Atoms*, vol. 259, pp. 727–732, 2007.
- [17] H. Becquerel, “On radioactivity, a new property of matter,” 1903.
- [18] O. Hahn and F. Strassman, “Über den Nachweis und das Verhalten der bei der Bestrahlung des Urans mittels Neutronen entstehenden Erdalkalimetalle,” *Naturwissenschaften*, vol. 1, pp. 11–15, 1939.
- [19] L. Meitner and O. R. Frisch, “Disintegration of uranium by neutrons: a new type of nuclear reaction,” *Nature*, vol. 143, pp. 239–240, 1939.
- [20] G. T. Seaborg, E. M. McMillan, and J. W. Kennedy, “Radioactive element 94 from deuterons on uranium,” *Phys. Rev.*, vol. 7 and 8, pp. 366–367, 1946.
- [21] A. Kudo, Y. Mahara, D. C. Santry, T. Suzuki, S. Miyahara, M. Sugahara, J. Zheng, and J.-P. Garrec, “Plutonium mass balance released from the Nagasaki A-bomb and the applicability for future environmental research,” *Appl. Radiat. Isot.*, vol. 46, pp. 1089–1098, 1995.
- [22] Y. Muramatsu, T. Hamilton, S. Uchida, K. Tagami, S. Yoshida, and W. Robison, “Measurement of $^{240}\text{Pu}/^{239}\text{Pu}$ isotopic ratios in soils from the Marshall Islands using ICP-MS,” *The Science of the Total Environment*, vol. 278, pp. 151–159, 2001.
- [23] J. N. Smith, K. M. Ellis, L. Polyak, G. Ivanov, S. L. Forman, and S. B. Moran, “Pu transport into the Arctic Ocean from underwater nuclear tests in Chernaya Bay, Novaya Zemlya,” *Continental Shelf Research*, vol. 20, pp. 255–279, 2000.
- [24] M. Yamamoto, A. Sakaguchi, S. Ochiai, T. Takada, K. Hamataka, T. Murakami, and S. Nagao, “Isotopic Pu, Am and Cm signatures in environmental samples contaminated by the Fukushima Dai-ichi Nuclear Power Plant accident,” *Journal of Environmental Radioactivity*, vol. 132, pp. 31–46, 2014.
- [25] J. Lachner, M. Christl, T. Bisinger, R. Michel, and H. A. Synal, “Isotopic signature of plutonium at Bikini atoll,” *Applied Radiation and Isotopes*, vol. 68, pp. 979–983, 2010.
- [26] J. H. Harley, “Plutonium in the environment - a review,” *Journal of Radiation Research*, vol. 21, pp. 83–104, 1980.
- [27] E. R. Sholkovitz, “The geochemistry of plutonium in fresh and marine water environments,” *Earth-Science Reviews*, vol. 19, pp. 95–161, 1983.

- [28] United States Department of Energy, “Environmental Measurements Laboratory Environmental Quarterly,” 1979.
- [29] C. Alewell, A. Pitois, K. Meusburger, M. Ketterer, and L. Mabit, “ $^{239+240}\text{Pu}$ from “contaminant” to soil erosion tracer: Where do we stand?,” *Earth-Science Reviews*, vol. 172, pp. 107–123, 2017.
- [30] F. Stäger, D. Zok, A. K. Schiller, B. Feng, and G. Steinhauser, “Disproportionately high contributions of 60 year old weapons- ^{137}Cs explain the persistence of radioactive contamination in Bavarian wild boars,” *Environmental Science and Technology*, vol. 57, pp. 13601–13611, 2023.
- [31] A. J. Parsons and I. D. Foster, “What can we learn about soil erosion from the use of ^{137}Cs ?,” *Earth-Science Reviews*, vol. 108, pp. 101–113, 2011.
- [32] M. M. Arienzo, J. R. McConnell, N. Chellman, A. S. Criscitiello, M. Curran, D. Fritzsche, S. Kipfstuhl, R. Mulvaney, M. Nolan, T. Opel, M. Sigl, and J. P. Steffensen, “A method for continuous ^{239}Pu determinations in Arctic and Antarctic ice cores,” *Environmental Science and Technology*, vol. 50, pp. 7066–7073, 7 2016.
- [33] L. Mabit, K. Meusburger, E. Fulajtar, and C. Alewell, “The usefulness of ^{137}Cs as a tracer for soil erosion assessment: A critical reply to Parsons and Foster (2011),” *Earth-Science Reviews*, vol. 127, pp. 300–307, 2013.
- [34] P. A. Chaboche, F. Pointurier, P. Sabatier, A. Foucher, T. Tiecher, J. P. Minella, M. Tassano, A. Hubert, S. Morera, S. Guédron, C. Ardois, B. Boulet, C. Cossonnet, P. Cabral, M. Cabrera, G. Chalar, and O. Evrard, “ $^{240}\text{Pu}/^{239}\text{Pu}$ signatures allow refining the chronology of radionuclide fallout in South America,” *Science of the Total Environment*, vol. 843, 2022.
- [35] E. Harrell and D. E. Hoffman, “Plutonium Mountain: Inside the 17-year mission to secure a dangerous legacy of Soviet nuclear testing,” 2013.
- [36] Y. Huang, S. G. Tims, M. B. Froehlich, S. Pan, L. K. Fifield, S. Pavetich, and D. Koll, “The $^{240}\text{Pu}/^{239}\text{Pu}$ atom ratio in Chinese soils,” *Science of the Total Environment*, vol. 678, pp. 603–610, 8 2019.
- [37] O. C. Lind, B. Salbu, K. Janssens, K. Proost, M. García-León, and R. García-Tenorio, “Characterization of U/Pu particles originating from the nuclear weapon accidents at Palomares, Spain, 1966 and Thule, Greenland, 1968,” *Science of the Total Environment*, vol. 376, pp. 294–305, 4 2007.
- [38] H. Yamana, T. Yamamoto, and H. Moriyama, *Isotopic ratio of Pu released from fuel cycle facilities-importance of radiochemically pure ^{236}Pu as a tracer*, vol. 1, pp. 31–46. Elsevier Sciences Ltd, 1 ed., 2001.
- [39] R. Pöllänen, M. E. Ketterer, S. Lehto, M. Hokkanen, T. K. Ikäheimonen, T. Siiskonen, M. Moring, M. P. R. Montero, and A. M. Sánchez, “Multi-technique characterization of a nuclearbomb particle from the Palomares accident,” *Journal of Environmental Radioactivity*, vol. 90, pp. 15–28, 2006.

- [40] D. H. Oughton, L. Skipperud, L. K. Fifield, R. G. Cresswell, B. Salbu, and P. Day, “Accelerator mass spectrometry measurement of $^{240}\text{Pu}/^{239}\text{Pu}$ isotope ratios in Novaya Zemlya and Kara Sea sediments,” *Applied Radiation and Isotopes*, vol. 61, pp. 249–253, 2004.
- [41] L. Skipperud, “Plutonium in the arctic marine environment—a short review.,” *TheScientificWorldJournal*, vol. 4, pp. 460–481, 2004.
- [42] D. Pittauerova, W. M. Kolb, J. C. Rosenstiel, and H. W. Fischer, “Radioactivity in Trinitite - a review and new measurements,” in *Third European IRPA Congress*, pp. 1–10, 2010.
- [43] G. A. Brennecka, L. E. Borg, I. D. Hutcheon, M. A. Sharp, and A. D. Anbar, “Natural variations in uranium isotope ratios of uranium ore concentrates: Understanding the $^{238}\text{U}/^{235}\text{U}$ fractionation mechanism,” *Earth and Planetary Science Letters*, vol. 291, pp. 228–233, 2010.
- [44] M. Ho, E. Obbard, P. A. Burr, and G. Yeoh, “A review on the development of nuclear power reactors,” vol. 160, pp. 459–466, Elsevier Ltd, 2019.
- [45] IAEA, “Advances in small modular reactor technology developments, A supplement to: IAEA advanced reactors information system (ARIS),” 2020.
- [46] T. P. Makarova, B. A. Bibichev, and V. D. Domkin, “Destructive analysis of the nuclide composition of spent fuel of WWER-440, WWER-1000, and RBMK-1000 reactors,” *Radiochemistry*, vol. 50, pp. 414–426, 2008.
- [47] I. Lantzou, C. Kouvalaki, and G. Nicolaou, “Plutonium fingerprinting in nuclear forensics of spent nuclear fuel,” *Progress in Nuclear Energy*, vol. 85, pp. 333–336, 2015.
- [48] M. Betti, G. Tamborini, and L. Koch, “Use of secondary ion mass spectrometry in nuclear forensic analysis for the characterization of plutonium and highly enriched uranium particles,” *Analytical Chemistry*, vol. 71, pp. 2616–2622, 1999.
- [49] M. Robel and M. J. Kristo, “Discrimination of source reactor type by multivariate statistical analysis of uranium and plutonium isotopic concentrations in unknown irradiated nuclear fuel material,” *Journal of Environmental Radioactivity*, vol. 99, pp. 1789–1797, 2008.
- [50] G. Nicolaou and S. R. Biegalski, “Discrimination of plutonium from thermal reactors in the frame of nuclear forensics,” *Journal of Radioanalytical and Nuclear Chemistry*, vol. 317, pp. 559–564, 2018.
- [51] G. L. Petit, G. Douysset, G. Ducros, P. Gross, P. Achim, M. Monfort, P. Raymond, Y. Pontillon, C. Jutier, X. Blanchard, T. Taffary, and C. Moulin, “Analysis of radionuclide releases from the Fukushima Dai-Ichi Nuclear Power Plant accident Part I,” *Pure and Applied Geophysics*, vol. 171, pp. 629–644, 2014.

- [52] W. Schulz, D. K. Gupta, B. Riebe, G. Steinhauser, and C. Walther, “Sorption of radiocesium on various soils,” *Applied Geochemistry*, vol. 101, pp. 103–108, 2019.
- [53] R. Querfeld, W. Schulz, J. Neubohn, and G. Steinhauser, “Anthropogenic radionuclides in water samples from the Chernobyl exclusion zone,” *Journal of Radioanalytical and Nuclear Chemistry*, vol. 318, pp. 423–428, 2018.
- [54] M. Mandel, L. Holtmann, M. Raiwa, A. Wunnenberg-Gust, B. Riebe, and C. Walther, “Imaging of I, Re and Tc plant uptake on the single-cell scale using SIMS and rL-SNMS,” *Journal of Hazardous Materials*, vol. 423, p. 127143, 2022.
- [55] B. Russell, I. W. Croudace, and P. E. Warwick, “Determination of ^{135}Cs and ^{137}Cs in environmental samples: A review,” *Analytica Chimica Acta*, vol. 890, pp. 7–20, 2015.
- [56] Oak Ridge National Laboratory. <https://www.ornl.gov/project/origen>.
- [57] Oak Ridge National Laboratory and Nucleonica. <https://www.nucleonica.com/Application/webKORIGEN/KorigenPlus.aspx>.
- [58] M. Robel, B. Isselhardt, E. Ramon, A. Hayes, A. Gaffney, L. Borg, R. Lindvall, A. Erickson, K. Carney, T. Battisti, A. Conant, B. Ade, H. Trelue, and C. Weber, “A composite position independent monitor of reactor fuel irradiation using Pu, Cs, and Ba isotope ratios,” *Journal of Environmental Radioactivity*, vol. 195, pp. 9–19, 2018.
- [59] Y. Satou, K. Sueki, K. Sasa, K. Adachi, and Y. Igarashi, “First successful isolation of radioactive particles from soil near the Fukushima Daiichi Nuclear Power Plant,” *Anthropocene*, vol. 14, pp. 71–76, 2016.
- [60] Z. Zhang, J. Igarashi, Y. Satou, K. Ninomiya, K. Sueki, and A. Shinohara, “Activity of ^{90}Sr in fallout particles collected in the difficult-to-return zone around the Fukushima Daiichi Nuclear Power Plant,” *Environmental Science and Technology*, vol. 53, pp. 5868–5876, 2019.
- [61] D. Zok, T. Blenke, S. Reinhard, S. Sprott, F. Kegler, L. Syrbe, R. Querfeld, Y. Takagai, V. Drozdov, I. Chyzhevskiy, S. Kirieiev, B. Schmidt, W. Adlassnig, G. Wallner, S. Dubchak, and G. Steinhauser, “Determination of characteristic vs anomalous $^{135}\text{Cs}/^{137}\text{Cs}$ isotopic ratios in radioactively contaminated environmental samples,” *Environmental Science and Technology*, vol. 55, pp. 4984–4991, 2021.
- [62] R. Plukiene, A. Plukis, D. Germanas, and V. Remeikis, “Numerical sensitivity study of irradiated nuclear fuel evolution in the RBMK reactor,” *Lithuanian Journal of Physics*, vol. 49, pp. 461–469, 2009.
- [63] S. Glasstone and P. J. Dolan, *The Effects of Nuclear Weapons. Third edition.* 1977.
- [64] L. Leifermann, M. Weiss, I. Chyzhevskiy, S. Dubchak, M. Raiwa, W. Schulz, G. Steinhauser, and C. Walther, *Localisation, Isolation and leaching of single hot particles from various environmental matrices in the vicinity of the Chernobyl Nuclear Powerplant*, vol. 357, pp. 1–18. Royal Chemistry Society, 2023.

- [65] A. W. McMahon, J. Toole, S. R. Jones, and J. Gray, “Investigation of a radioactive particle and a soil sample obtained from the Windscale area in 1956,” *Analyst*, vol. 119, pp. 991–995, 1994.
- [66] M. R. Savina, B. H. Isselhardt, D. Z. Shulaker, M. Robel, A. J. Conant, and B. J. Ade, “Simultaneous isotopic analysis of fission product Sr, Mo, and Ru in spent nuclear fuel particles by resonance ionization mass spectrometry,” *Scientific Reports*, vol. 13, 2023.
- [67] H. A. Perrett, B. S. Cooper, G. E. Edwards, K. T. Flanagan, C. M. Ricketts, S. Alsufyani, N. Dowd, and A. A. Shah, “Development of a photoionisation spectrometer for detection of atmospheric ^{85}Kr ,” vol. 1643, IOP Publishing Ltd, 2020.
- [68] J. Ole and R. B. Z. Erdsystemforschung, “Simulation of atmospheric krypton-85 transport to assess the detectability of clandestine nuclear reprocessing,” 2010.
- [69] L. Devell, S. Güntay, and D. Powers, “NEA/CSNI/R(95)24: The Chernobyl reactor accident source term: Development of a consensus view,” 1995.
- [70] C. D. Willett, S. R. Kimmig, W. S. Cassata, B. H. Isselhardt, M. Liezers, G. C. Eiden, and J. F. Wacker, “Fission gas measurements in spent fuel: Literature review,” 2020.
- [71] A. Smaizys, P. Poskas, E. Narkunas, and G. Bartkus, “Numerical modelling of radionuclide inventory for RBMK irradiated nuclear fuel,” *Nuclear Engineering and Design*, vol. 277, pp. 28–35, 2014.
- [72] World Nuclear Association. <https://world-nuclear.org/information-library/country-profiles/countries-a-f/china-nuclear-power.aspx>.
- [73] S. Jones, “Windscale and Kyshtym: a double anniversary,” *Journal of Environmental Radioactivity*, vol. 99, pp. 1–6, 2008.
- [74] A. D. Smith, S. R. Jones, J. Gray, and K. A. Mitchell, “A review of irradiated fuel particle releases from the Windscale Piles, 1950-1957,” *Journal of Radiological Protection*, vol. 27, pp. 115–145, 6 2007.
- [75] Dounreay Site Restoration Limited. <https://www.gov.uk/government/publications/radioactive-particles-in-the-environment-around-dounreay/dounreay-foreshore-particle-finds-2021>.
- [76] Scottish Environment Protection Agency, “Particles retrieval advisory group (Dounreay) 2012 report 2,” 2012.
- [77] Dounreay Particles Advisory Group and Scottish Environment Protection Agency, “Fourth report, november 2008,” 2008.
- [78] J. D. Harrison, T. P. Fell, A. W. Phipps, T. J. Smith, M. Ellender, G. J. Ham, A. Hodgson, and B. T. Wilkins, “RPD-RE-11-2005: Health implications of Dounreay fuel fragments: Estimates of doses and risks,” 2005.
- [79] P. J. Kershaw, K. S. Leonard, D. Mccubbin, and J. N. Aldridge, *Plutonium: the legacy of Sellafield*, vol. 1, pp. 306–328. Elsevier Science Ltd., 1 ed., 2001.

- [80] D. Ray, P. Leary, F. Livens, N. Gray, K. Morris, K. A. Law, A. J. Fuller, L. Abrahamsen-Mills, J. Howe, K. Tierney, G. Muir, and G. T. Law, “Controls on anthropogenic radionuclide distribution in the Sellafield-impacted Eastern Irish Sea,” *Science of the Total Environment*, vol. 743, 2020.
- [81] T. G. Hinton and J. E. Pinder, *A review of plutonium releases from the Savannah River Site, subsequent behavior within terrestrial and aquatic environments and resulting dose to humans*, vol. 1, pp. 413–435. Elsevier Science Ltd., 2001.
- [82] S. R. site, “Savannah River Site environmental report,” 2021.
- [83] Sellafield Limited. <https://www.gov.uk/government/publications/sellafield-ltd-annual-review-of-environmental-performance-202223/sellafield-ltd-annual-review-of-environmental-performance-202223>.
- [84] D. Oughton, P. Day, and K. Fifield, *Plutonium measurement using accelerator mass spectrometry: methodology and applications*, vol. 1, pp. 47–62. Elsevier Science Ltd., 2001.
- [85] B. V. Nikipelov, G. N. Romanov, L. A. Buldakov, N. S. Babaev, Y. B. Kholina, and E. I. Mikerin, “INFCIRC/368: Attachment official translation from Russian accident in the southern Urals on 29 september 1957,” 1989.
- [86] Strahlenschutzverordnung - StrlSchV. https://www.gesetze-im-internet.de/strlsv_2018/__64.html.
- [87] Bundesamt für Strahlenschutz. https://www.bfs.de/EN/topics/ion/radiation-protection/limit-values/limit-values_node.html.
- [88] V. Yoschenko, V. Kashparov, and T. Ohkubo, *Radioactive Contamination in Forest by the Accident of Fukushima Daiichi Nuclear Power Plant: Comparison with Chernobyl*, vol. 1, pp. 3–23. Springer Singapore, 1 ed., 2019.
- [89] U. D. of Energy, “NUREG-1250: Report on the accident at the Chernobyl Nuclear Power Station,” 1987.
- [90] *INSAG7: The Chernobyl Accident: Updating of INSAG-1*. No. 7 in INSAG Series, Vienna: INTERNATIONAL ATOMIC ENERGY AGENCY, 1992.
- [91] United Nations Scientific Committee on the Effects of Atomic Radiation, *Sources and effects of ionizing radiation: United Nations Scientific Committee on the Effects of Atomic Radiation: UNSCEAR 2000 report to the General Assembly, with scientific annexes*. United Nations, 2000.
- [92] V. Kashparov, S. Levchuk, M. Zhurba, V. Protsak, N. A. Beresford, and J. S. Chaplow, “Spatial radionuclide deposition data from the 60 km radial area around the Chernobyl Nuclear Power Plant: Results from a sampling survey in 1987,” *Earth System Science Data*, vol. 12, pp. 1861–1875, 2020.

- [93] M. D. Cort, G. Dubois, S. Fridman, M. Germenchuk, Y. Izrael, A. Janssens, A. Jones, G. Kelly, E. Kvasnikova, I. Matveencko, I. Nazarov, Y. Pokumeiko, V. Sitak, E. Stukin, L. Tabachny, Y. Tsaturov, and S. Avdyushin, *Atlas of caesium deposition on Europe after the Chernobyl accident*. Office for Official Publications of the European Communities 1998, 1998.
- [94] N. Evangeliou, T. Hamburger, N. Talerko, S. Zibtsev, Y. Bondar, A. Stohl, Y. Balkanski, T. A. Mousseau, and A. P. Møller, “Reconstructing the Chernobyl nuclear power plant (CNPP) accident 30 years after. A unique database of air concentration and deposition measurements over Europe,” *Environmental Pollution*, vol. 216, pp. 408–418, 2016.
- [95] S. Sadisavan and U. C. Mishra, “Radioactive fallout swipe from Chernobyl,” *Nature*, vol. 324, pp. 23–24, 1986.
- [96] P. G. Voilleque, *Radionuclide Source Terms*, pp. 1–728. Oxford University Press, 2008.
- [97] S. Guntay, D. A. Powers, and L. Devell, “NEA-CSNI-R–1995-24 The Chernobyl reactor accident source term: Development of a consensus view,” 1997.
- [98] P. A. M. Napoleau and A. Rudak, “Rapid method for estimating the mass and activity of nuclides in a RBMK core,” *Atomic Energy*, vol. 85, pp. 219–226, 1998.
- [99] V. P. Mironov, J. L. Matusevich, V. P. Kudrjashov, P. I. Ananich, V. V. Zhuravkov, S. F. Boulyga, and J. S. Becker, “Determination of uranium concentration and burn-up of irradiated reactor fuel in contaminated areas in Belarus using uranium isotopic ratios in soil samples,” *Radiochimica Acta*, vol. 93, pp. 781–784, 2005.
- [100] S. F. Boulyga and J. S. Becker, “Isotopic analysis of uranium and plutonium using ICP-MS and estimation of burn-up of spent uranium in contaminated environmental samples,” *Journal of Analytical Atomic Spectrometry*, vol. 17, pp. 1143–1147, 2002.
- [101] M. Raiwa, “Zerstörungsfreie Analyse von Kernbrennstoffpartikeln aus der Sperrzone Tschernobyls,” 2022.
- [102] M. López-Lora, G. Olszewski, E. Chamizo, P. Törnquist, H. Pettersson, and M. Eriksson, “Plutonium signatures in a dated sediment core as a tool to reveal nuclear sources in the Baltic Sea,” *Environmental Science and Technology*, vol. 57, pp. 1959–1969, 2023.
- [103] M. E. Ketterer, K. M. Hafer, and J. W. Mietelski, “Resolving Chernobyl vs. global fallout contributions in soils from Poland using plutonium atom ratios measured by inductively coupled plasma mass spectrometry,” *Journal of Environmental Radioactivity*, vol. 73, pp. 183–201, 2004.
- [104] T. Bisinger, S. Hippler, R. Michel, L. Wacker, and H. A. Synal, “Determination of plutonium from different sources in environmental samples using alpha-spectrometry and AMS,” *Nuclear Instruments and Methods in Physics Research, Section B: Beam Interactions with Materials and Atoms*, vol. 268, pp. 1269–1272, 2010.

- [105] P. Schubert and U. Behrend, “Investigations of radioactive particles from the Chernobyl fall-out hot particle Chernobyl,” *Radiochimica Acta*, vol. 41, pp. 149–155, 1987.
- [106] F. J. Sandalls, M. G. Segal, and N. Victorova, “Hot particles from Chernobyl: A review,” *J. Environ. Radioactivity*, vol. 18, pp. 5–22, 1993.
- [107] P. A. Vlasov, A. A. Shevchenko, S. V. Shashlov, Y. E. Kvacheva, R. I. Pogodin, A. M. Skryabin, and V. A. Kutkov, “Chernobyl hot particles in the lungs of personnel involved in the post-accident clean-up actions and of inhabitants of the contaminated Ukrainian and Belarus territories,” pp. 3–9, 1997.
- [108] E. Ansoborlo and J. Stather, “Review of the characterisation of hot particles released into the environment and pathways for intake of particles,” *Radiation Protection Dosimetry*, vol. 92, pp. 139–143, 2000.
- [109] B. Salbu, T. Krekling, D. H. Oughton, G. Ostby, V. A. Kashparov, T. L. Brand, and J. P. Day, “Hot particles in accidental releases from Chernobyl and Windscale nuclear installations,” *Analyst*, vol. 119, pp. 125–130, 1994.
- [110] V. A. Kashparov, Y. A. Ivanov, S. I. Zvarisch, V. P. Protsak, Y. V. Khomutinin, A. D. Kurepin, and E. M. Pazukhin, “Formation of hot particles during the Chernobyl nuclear power plant accident,” *Nuclear Technology*, vol. 114, pp. 246–252, 1996.
- [111] P. Achim, M. Monfort, G. L. Petit, P. Gross, G. Douysset, T. Taffary, X. Blanchard, and C. Moulin, “Analysis of radionuclide releases from the Fukushima Dai-ichi Nuclear Power Plant accident Part II,” *Pure and Applied Geophysics*, vol. 171, pp. 645–667, 2014.
- [112] S. Schneider, C. Walther, S. Bister, V. Schauer, M. Christl, H. A. Synal, K. Shozugawa, and G. Steinhauser, “Plutonium release from Fukushima Daiichi fosters the need for more detailed investigations,” *Scientific Reports*, vol. 3, 2013.
- [113] J. Zheng, K. Tagami, Y. Watanabe, S. Uchida, T. Aono, N. Ishii, S. Yoshida, Y. Kubota, S. Fuma, and S. Ihara, “Isotopic evidence of plutonium release into the environment from the Fukushima DNPP accident,” *Scientific Reports*, vol. 2, 2012.
- [114] J. M. Schwantes, C. R. Orton, and R. A. Clark, “Analysis of a nuclear accident: Fission and activation product releases from the Fukushima Daiichi nuclear facility as remote indicators of source identification, extent of release, and state of damaged spent nuclear fuel,” *Environmental Science and Technology*, vol. 46, pp. 8621–8627, 8 2012.
- [115] R. Ikehara, M. Suetake, T. Komiya, G. Furuki, A. Ochiai, S. Yamasaki, W. R. Bower, G. T. Law, T. Ohnuki, B. Grambow, R. C. Ewing, and S. Utsunomiya, “Novel method of quantifying radioactive cesium-rich microparticles (CsMPs) in the environment from the Fukushima Daiichi Nuclear Power Plant,” *Environmental Science and Technology*, vol. 52, pp. 6390–6398, 2018.

- [116] R. Ikehara, K. Morooka, M. Suetake, T. Komiya, E. Kurihara, M. Takehara, R. Takami, C. Kino, K. Horie, M. Takehara, S. Yamasaki, T. Ohnuki, G. T. Law, W. Bower, B. Grambow, R. C. Ewing, and S. Utsunomiya, “Abundance and distribution of radioactive cesium-rich microparticles released from the Fukushima Daiichi Nuclear Power Plant into the environment,” *Chemosphere*, vol. 241, 2020.
- [117] Y. Abe, Y. Iizawa, Y. Terada, K. Adachi, Y. Igarashi, and I. Nakai, “Detection of uranium and chemical state analysis of individual radioactive microparticles emitted from the Fukushima nuclear accident using multiple synchrotron radiation X-ray analyses,” *Analytical Chemistry*, vol. 86, pp. 8521–8525, 2014.
- [118] N. Yamaguchi, M. Mitome, A. H. Kotone, M. Asano, K. Adachi, and T. Kogure, “Internal structure of cesium-bearing radioactive microparticles released from Fukushima nuclear power plant,” *Scientific Reports*, vol. 6, 2016.
- [119] J. Imoto, A. Ochiai, G. Furuki, M. Suetake, R. Ikehara, K. Horie, M. Takehara, S. Yamasaki, K. Nanba, T. Ohnuki, G. T. Law, B. Grambow, R. C. Ewing, and S. Utsunomiya, “Isotopic signature and nano-texture of cesium-rich micro-particles: Release of uranium and fission products from the Fukushima Daiichi Nuclear Power Plant,” *Scientific Reports*, vol. 7, 2017.
- [120] Z. Macsik, L. A. Hudston, K. N. Wurth, D. Meininger, C. Jesinghaus, T. J. Tenner, B. E. Naes, M. Boswell, K. Shozugawa, S. P. LaMont, R. E. Steiner, and G. Steinhäuser, “Identification, isolation, and characterization of a novel type of Fukushima-derived microparticle,” *Journal of Radioanalytical and Nuclear Chemistry*, vol. 331, pp. 5333–5341, 2022.
- [121] K. Morooka, E. Kurihara, M. Takehara, R. Takami, K. Fueda, K. Horie, M. Takehara, S. Yamasaki, T. Ohnuki, B. Grambow, G. T. Law, J. W. Ang, W. R. Bower, J. Parker, R. C. Ewing, and S. Utsunomiya, “New highly radioactive particles derived from Fukushima Daiichi Reactor Unit 1: Properties and environmental impacts,” *Science of the Total Environment*, vol. 773, 2021.
- [122] E. Kurihara, M. Takehara, M. Suetake, R. Ikehara, T. Komiya, K. Morooka, R. Takami, S. Yamasaki, T. Ohnuki, K. Horie, M. Takehara, G. T. Law, W. Bower, J. F. W. Mosselmans, P. Warnicke, B. Grambow, R. C. Ewing, and S. Utsunomiya, “Particulate plutonium released from the Fukushima Daiichi meltdowns,” *Science of the Total Environment*, vol. 743, 2020.
- [123] C. T. Lee and K. A. Johannson, “Occupational exposures and IPF: When the dust unsettles,” *Thorax*, vol. 75, pp. 828–829, 2020.
- [124] by F. Cavariani and D. A. Pietro, “Incidence of silicosis among ceramic workers in central Italy,” *Scandinavian Journal of Work, Environment and Health*, vol. 21, pp. 58–62, 1995.
- [125] D. Poudel, M. Avtandilashvili, J. A. Klumpp, L. Bertelli, and S. Y. Tolmachev, “Modelling of long-term retention of high-fired plutonium oxide in the human

- respiratory tract: Importance of scar-tissue compartments,” *Journal of Radiological Protection*, vol. 41, pp. 940–961, 2021.
- [126] T. Azizova, M. Moseeva, E. Grigoryeva, G. Zhuntova, M. Bannikova, G. Sychugov, and E. Kazachkov, “Registry of plutonium-induced lung fibrosis in a Russian nuclear worker cohort,” *Health Physics*, vol. 118, pp. 185–192, 2020.
- [127] L. S. Newman, M. M. Mroz, and A. J. Ruttenber, “Lung fibrosis in plutonium workers,” *Radiation Research*, vol. 164, pp. 123–131, 2005.
- [128] Y. Matsuya, N. Hamada, Y. Yachi, Y. Satou, M. Ishikawa, H. Date, and T. Sato, “Inflammatory signaling and DNA damage responses after local exposure to an insoluble radioactive microparticle,” *Cancers*, vol. 14, pp. 1–15, 2022.
- [129] Dounreay Particles Advisory Group and Scottish Environment Protection Agency, “Dounreay particle advisory group third report,” 2006.
- [130] I. Byrnes, O. C. Lind, E. L. Hansen, K. Janssens, and B. Salbu, “Characterization of radioactive particles from the Dounreay nuclear reprocessing facility,” *Science of the Total Environment*, vol. 727, 2020.
- [131] B. C. Jaeschke, O. C. Lind, C. Bradshaw, and B. Salbu, “Retention of radioactive particles and associated effects in the filter-feeding marine mollusc *Mytilus edulis*,” *Science of the Total Environment*, vol. 502, pp. 1–7, 2015.
- [132] C. M. Fallon, W. R. Bower, I. C. Lyon, F. R. Livens, P. Thompson, M. Higginson, J. Collins, S. L. Heath, and G. T. Law, “Isotopic and compositional variations in single nuclear fuel pellet particles analyzed by nanoscale secondary ion mass spectrometry,” *ACS Omega*, vol. 5, pp. 296–303, 2020.
- [133] A. Diacre, P. Fichet, P. Sardini, J. Donnard, A.-L. Fauré, O. Marie, K. Shozugawa, M. Susset, M. Hori, and T. Tsutomu, “Comparison of techniques to localise U-bearing particles in environmental samples,” *Journal of Radioanalytical and Nuclear Chemistry*, vol. 331, pp. 1701–1714, 2022.
- [134] H. Saari, S. Luokkanen, M. Kulmala, S. Lehtinen, and T. Raunemaa, “Isolation and characterization of hot particles from Chernobyl fallout in southwestern Finland,” *Health Physics*, vol. 57, pp. 975–984, 1989.
- [135] B. Salbu, T. Krekling, and D. H. Oughton, “Characterisation of radioactive particles in the environment,” *Analyst*, vol. 123, pp. 843–849, 1998.
- [136] V. Zheltonozhsky, K. M. Uck, and M. Bondarkov, “Classification of hot particles from the Chernobyl accident and nuclear weapons detonations by non-destructive methods,” *Journal of Environmental Radioactivity*, vol. 57, pp. 151–166, 2001.
- [137] P. G. Appleby, G. Piliposyan, J. Weckström, and G. Piliposian, “Delayed inputs of hot ^{137}Cs and ^{241}Am particles from Chernobyl to sediments from three finnish lakes: implications for sediment dating,” *Journal of Paleolimnology*, vol. 69, pp. 293–303, 2023.

- [138] T. Sakamoto, M. Morita, K. Kanenari, H. Tomita, V. Sonnenschein, K. Saito, M. Ohashi, K. Kato, T. Iguchi, T. Kawai, T. Okumura, Y. Satou, and I. Wakaida, "Isotope-selective microscale imaging of radioactive Cs without isobaric interferences using sputtered neutral mass spectrometry with two-step resonant ionization employing newly-developed Ti:Sapphire lasers," *Analytical Sciences*, vol. 34, pp. 1265–1270, 2018.
- [139] M. Cook, B. Etschmann, R. Ram, K. Ignatyev, G. Gervinskas, S. D. Conradson, S. Cumberland, V. N. Wong, and J. Brugger, "The nature of Pu-bearing particles from the Maralinga nuclear testing site, Australia," *Scientific Reports*, vol. 11, 2021.
- [140] "Provenance of uranium particulate contained within Fukushima Daiichi Nuclear Power Plant Unit 1 ejecta material," *Nature Communications*, vol. 10, 2019.
- [141] O. N. Batuk, S. D. Conradson, O. N. Aleksandrova, H. Boukhalfa, B. E. Burakov, D. L. Clark, K. R. Czerwinski, A. R. Felmy, J. S. Lezama-Pacheco, S. N. Kalmykov, D. A. Moore, B. F. Myasoedov, D. T. Reed, D. D. Reilly, R. C. Roback, I. E. Vlasova, S. M. Webb, and M. P. Wilkerson, "Multiscale speciation of U and Pu at Chernobyl, Hanford, Los Alamos, McGuire AFB, Mayak, and Rocky Flats," *Environmental Science and Technology*, vol. 49, pp. 6474–6484, 2015.
- [142] T. Poliakova, M. Weiss, A. Trigub, V. Yapaskurt, M. Zheltonozhskaya, I. Vlasova, C. Walther, and S. Kalmykov, "Western Chernobyl trace uranium fuel "hot" particles: correlation of burnup and uranium oxidation state." 2023.
- [143] T. Poliakova, A. Krot, A. Trigub, I. Nevolin, A. Averin, V. Yapaskurt, I. Vlasova, P. Matveev, and S. Kalmykov, "Uranium oxides structural transformation in human body liquids," *Scientific Reports*, vol. 13, 2023.
- [144] L. Lakosi, J. Zsigrai, A. Kocsonya, T. C. Nguyen, H. Ramebäck, T. Parsons-Moss, N. Gharibyan, and K. Moody, "Gamma spectrometry in the ITWG CMX-4 exercise," *Journal of Radioanalytical and Nuclear Chemistry*, vol. 315, pp. 409–416, 2 2018.
- [145] J. H. Gross, *Mass Spectrometry: A Textbook*. Springer Berlin Heidelberg, 2011.
- [146] J. A. Entwistle, A. G. Flowers, G. Nageldinger, and J. C. Greenwood, "Identification and characterization of radioactive 'hot' particles in Chernobyl fallout-contaminated soils: the application of two novel approaches," *Mineralogical Magazine*, vol. 67, pp. 183–204, 2003.
- [147] M. Martschini, J. Lachner, K. Hain, M. Kern, O. Marchhart, J. Pitters, A. Priller, P. Steier, A. Wiederin, A. Wieser, and R. Golser, "5 years of ion-laser interaction mass spectrometry - Status and prospects of isobar suppression in AMS by lasers," *Radiocarbon*, vol. 64, pp. 555–568, 2022.
- [148] R. V. Ambartzumian and V. S. Letokhov, "Selective two-step (STS) photoionization of atoms and photodissociation of molecules by laser radiation," *Applied Optics*, vol. 11, pp. 354–358, 1972.

- [149] P. Campbell, I. D. Moore, and M. R. Pearson, "Laser spectroscopy for nuclear structure physics," *Progress in Particle and Nuclear Physics*, vol. 86, pp. 127–180, 2016.
- [150] M. Block, M. Laatiaoui, and S. Raeder, "Recent progress in laser spectroscopy of the actinides," *Progress in Particle and Nuclear Physics*, vol. 116, 2021.
- [151] F. Weber, C. E. Düllmann, V. Gadelshin, N. Kneip, S. Oberstedt, S. Raeder, J. Runke, C. Mokry, P. Thörle-Pospiech, D. Studer, N. Trautmann, and K. Wendt, "Probing the atomic structure of californium by resonance ionization spectroscopy," *Atoms*, vol. 10, 2022.
- [152] N. Kneip, F. Weber, M. A. Kaja, C. E. Düllmann, C. Mokry, S. Raeder, J. Runke, D. Studer, N. Trautmann, and K. Wendt, "Investigation of the atomic structure of curium and determination of its first ionization potential," *European Physical Journal D*, vol. 76, 2022.
- [153] K. Wendt, K. Blaum, B. A. Bushaw, C. Grüning, R. Horn, G. Huber, J. V. Kratz, P. Kunz, P. Müller, W. Nörtershäuser, M. Nunnemann, G. Passler, A. Schmitt, N. Trautmann, and A. Waldek, "Recent developments in and applications of resonance ionization mass spectrometry," *Fresenius Journal of Analytical Chemistry*, vol. 364, pp. 471–477, 1999.
- [154] B. H. Isselhardt, M. R. Savina, A. Kucher, S. D. Gates, K. B. Knight, and I. D. Hutcheon, "Improved precision and accuracy in quantifying plutonium isotope ratios by RIMS," *Journal of Radioanalytical and Nuclear Chemistry*, vol. 307, pp. 2487–2494, 2016.
- [155] M. R. Savina, R. G. Trappitsch, M. R. Savina, and R. Trappitsch, *Resonance ionization mass spectrometry (RIMS): Fundamentals and applications including secondary neutral mass spectrometry*. Wiley-VCH Verlag GmbH and Co. KGaA, 2020.
- [156] M. Franzmann, H. Bosco, C. Walther, and K. Wendt, "A new resonant Laser-SNMS system for environmental ultra-trace analysis: Installation and optimization," *International Journal of Mass Spectrometry*, vol. 423, pp. 27–32, 2017.
- [157] K. Wendt, N. Trautmann, and B. A. Bushaw, "Resonant laser ionization mass spectrometry: An alternative to AMS?," *Nuclear Instruments and Methods in Physics Research B*, vol. 172, pp. 162–169, 2000.
- [158] K. Wendt, G. K. Bhowmick, B. A. Bushaw, G. Herrmann, J. V. Kratz, J. Lantzsch, P. Müller, W. Nörtershäuser, E.-W. Otten, R. Schwalbach, U.-A. Seibert, N. Trautmann, and A. Waldek, "Rapid trace analysis of $^{89,90}\text{Sr}$ in environmental samples by collinear laser resonance ionization mass spectrometry," *Radiochimica Acta*, vol. 79, pp. 183–190, 1997.
- [159] M. R. Savina, B. H. Isselhardt, and R. Trappitsch, "Simultaneous isotopic analysis of U, Pu, and Am in spent nuclear fuel by resonance ionization mass spectrometry," *Analytical Chemistry*, vol. 93, pp. 9505–9512, 2021.

- [160] M. Morita, H. Tomita, R. Ohtake, K. Kanenari, A. Nakamura, K. Saito, T. Kawai, T. Okumura, V. Sonnenschein, and T. Sakamoto, “Development of a micro imaging system for element-selective analysis by coupling of focused ion beam and resonance ionization mass spectrometry,” *Nuclear Science and Technology*, vol. 5, pp. 179–182, 2018.
- [161] M. Franzmann, H. Bosco, L. Hamann, C. Walther, and K. Wendt, “Resonant laser-SNMS for spatially resolved and element selective ultra-trace analysis of radionuclides,” *Journal of Analytical Atomic Spectrometry*, vol. 33, pp. 730–737, 2018.
- [162] M. Franzmann, “A new tool for ultra-trace analysis of radionuclides-setup, optimization and characterization of the resonant Laser-SNMS system for IRS hannover,” 2018.
- [163] S. Raeder, N. Kneip, T. Reich, D. Studer, N. Trautmann, and K. Wendt, “Recent developments in resonance ionization mass spectrometry for ultra-trace analysis of actinide elements,” *Radiochimica Acta*, vol. 107, pp. 645–652, 7 2019.
- [164] N. Kneip, C. E. Düllmann, V. Gadelshin, R. Heinke, C. Mokry, S. Raeder, J. Runke, D. Studer, N. Trautmann, F. Weber, and K. Wendt, “Highly selective two-step laser ionization schemes for the analysis of actinide mixtures,” *Hyperfine Interactions*, vol. 241, 2020.
- [165] H. Bosco, M. Weiss, M. Raiwa, C. Walther, N. Kneip, and K. Wendt, “Influence of the hyperfine structure on plutonium in resonant laser-SNMS,” *Hyperfine Interactions*, vol. 241, 2020.
- [166] H. Bosco, “Ortsaufgelöste Analyse von Aktiniden mittels resonanter ToF-Laser-SNMS,” 2021.
- [167] H. Bosco, L. Hamann, N. Kneip, M. Raiwa, M. Weiss, K. Wendt, and C. Walther, “New horizons in microparticle forensics: Actinide imaging and detection of ^{238}Pu and ^{242m}Am in hot particles,” *Science Advances*, vol. 7, 2021.
- [168] M. Raiwa, S. Büchner, N. Kneip, M. Weiß, P. Hanemann, P. Fraatz, M. Heller, H. Bosco, F. Weber, K. Wendt, and C. Walther, “Actinide imaging in environmental hot particles from Chernobyl by rapid spatially resolved resonant laser secondary neutral mass spectrometry,” *Spectrochimica Acta - Part B Atomic Spectroscopy*, vol. 190, 2022.
- [169] D. van Eerten, M. Raiwa, P. Hanemann, L. Leifermann, T. Weissenborn, W. Schulz, M. Weiß, D. Z. Shulaker, P. Boone, D. Willingham, K. Thomas, B. Sammis, B. Isselhardt, M. Savina, and C. Walther, “Multi-element isotopic analysis of hot particles from Chornobyl,” *Journal of Hazardous Materials*, vol. 452, 2023.
- [170] T. Stephan, R. Trappitsch, A. M. Davis, M. J. Pellin, D. Rost, M. R. Savina, R. Yokochi, and N. Liu, “CHILI – the chicago instrument for laser ionization – a new tool for isotope measurements in cosmochemistry,” *International Journal of Mass Spectrometry*, vol. 407, pp. 1–15, 2016.

- [171] J. Warbinek, B. Andelić, M. Block, P. Chhetri, A. Claessens, R. Ferrer, F. Giacoppo, O. Kaleja, T. Kieck, E. Kim, M. Laatiaoui, J. Lantis, A. Mistry, D. Münzberg, S. Nothhelfer, S. Raeder, E. Rey-Herme, E. Rickert, J. Romans, E. Romero-Romero, M. Vandebrouck, P. V. Duppen, and T. Walther, “Advancing radiation-detected resonance ionization towards heavier elements and more exotic nuclides,” *Atoms*, vol. 10, 2022.
- [172] T. Stephan, R. Trappitsch, A. M. Davis, M. J. Pellin, D. Rost, M. R. Savina, M. Jadhav, C. H. Kelly, F. Gyngard, P. Hoppe, and N. Dauphas, “Strontium and barium isotopes in presolar silicon carbide grains measured with CHILI—two types of X grains,” *Geochimica et Cosmochimica Acta*, vol. 221, pp. 109–126, 2018.
- [173] W. Demtröder, *Atoms, Molecules and Photons: An Introduction to Atomic-, Molecular- and Quantum Physics*. Graduate Texts in Physics, Berlin, Heidelberg: Springer Berlin Heidelberg, 2018.
- [174] B. H. Isselhardt, “Quantifying uranium isotope ratios using resonance ionization mass spectrometry: The influence of laser parameters on relative ionization probability,” 2011.
- [175] P. Hanemann, S. Bister, M. Raiwa, S. Reinhard, D. van Eerten, and C. Walther, “Production and characterization of standard particles for rL-SNMS,” *Journal of Radioanalytical and Nuclear Chemistry*, vol. 331, pp. 5039–5045, 2022.
- [176] M. Savina. personal communication.
- [177] M. G. Payne, S. L. Allman, and J. E. Parks, “Effect of hyperfine structure on ionization efficiencies in stepwise ionization using broad bandwidth lasers,” *Spectrochimica Acta*, vol. 46, pp. 1439–1457, 1991.
- [178] H. Niki, K. Motoki, M. Yasui, Y. Horiuchi, S. Tokita, and Y. Izawa, “Selectivity and efficiency of laser isotope separation processes of gadolinium,” *Journal of Nuclear Science and Technology*, vol. 43, pp. 427–431, 2006.
- [179] P. Kunz, G. Huber, G. Passler, N. Trautmann, and K. Wendt, “Resonance ionization mass spectrometry (RIMS) with pulsed and CW-lasers on plutonium,” *Hyperfine Interactions*, vol. 162, pp. 159–166, 2005.
- [180] A. Voss, V. Sonnenschein, P. Campbell, B. Cheal, T. Kron, I. D. Moore, I. Pohjalainen, S. Raeder, N. Trautmann, and K. Wendt, “High-resolution laser spectroscopy of long-lived plutonium isotopes,” *Physical Review A*, vol. 95, 2017.
- [181] J. Blaise and J. F. Wyart, *Selected constants, energy levels and atomic spectra of actinides*, vol. 20. International Tables of Selected Constants, 1992.
- [182] S. Köhler, R. Deissenberger, K. Eberhardt, N. Erdmann, G. Herrmann, G. Huber, J. Kratz, M. Nunnemann, G. Passler, P. Rao, J. Riegel, N. Trautmann, and K. Wendt, “Determination of the first ionization potential of actinide elements by resonance ionization mass spectroscopy,” *Spectrochimica Acta Part B: Atomic Spectroscopy*, vol. 52, no. 6, pp. 717–726, 1997.

- [183] C. Grüning, G. Huber, P. Klopp, J. V. Kratz, P. Kunz, G. Passler, N. Trautmann, A. Waldek, and K. Wendt, “Resonance ionization mass spectrometry for ultratrace analysis of plutonium with a new solid state laser system,” *International Journal of Mass Spectrometry*, vol. 235, pp. 171–178, 2004.
- [184] A. Galindo-Uribarri, Y. Liu, E. Romero-Romero, and D. W. Stracener, “High efficiency laser resonance ionization of plutonium,” *Scientific Reports*, vol. 11, 12 2021.
- [185] Y. Zhao, M. Morita, and T. Sakamoto, “Accumulation of cesium in glue balls of spiders’ orb webs,” *Surface and Interface Analysis*, vol. 52, pp. 569–572, 2020.
- [186] W. Schulz, “Untersuchung radioaktiver Partikel mittels Sekundärionen-Flugzeit-Massenspektrometrie,” 2017.
- [187] W. Schulz, “Untersuchung des Migrationsverhaltens von Radionukliden in Umweltkompartimenten mit spektroskopischen und massenspektrometrischen Methoden,” 2020.
- [188] ESRI. <https://epsg.io/3857>.
- [189] M. Weiss, “Extraction and analysis of nuclear fuel fragments from the Chernobyl Exclusion Zone,” 2022.
- [190] L. Leifermann, “Extraktion und Speziationsanalytik von Brennstoffpartikeln aus der Chernobyl Exclusion Zone,” 2022.
- [191] T. Weissenborn, “Extraktion, Charakterisierung und sequentielles Auslaugen von einzelnen Kernbrennstoffpartikeln aus der Chernobyl Exclusion Zone,” 2022.
- [192] R. J. Konings, T. Wiss, and O. Beneš, “Predicting material release during a nuclear reactor accident,” *Nature Materials*, vol. 14, pp. 247–252, 2015.
- [193] L. Cui, Y. Taira, M. Matsuo, M. Orita, Y. Yamada, and N. Takamura, “Environmental remediation of the difficult-to-return zone in Tomioka town, Fukushima Prefecture,” *Scientific Reports*, vol. 10, 2020.
- [194] T. Parsons-Davis, K. Knight, M. Fitzgerald, G. Stone, L. Caldeira, C. Ramon, and M. Kristo, “Application of modern autoradiography to nuclear forensic analysis,” 2018.
- [195] Y. Wakiyama. personal communication.
- [196] G. E. H. L. Sciences. <https://www.dbi.udel.edu/wp-content/uploads/2017/07/Typhoon-FLA-9500-UserManual.pdf>.
- [197] IONTOF GmbH. <https://www.iontof.com/>.
- [198] R. Trappitsch. <https://github.com/RIMS-Code/RIMSEval>.
- [199] I. Hughes and P. Hase, *Measurements and their Uncertainties*. Oxford University Press, 2010.

- [200] I. C. W. Fitzsimons, B. Harte, and R. M. Clark, “SIMS stable isotope measurement: counting statistics and analytical precision,” *Minerological Magazine*, vol. 64, pp. 59–83, 2000.
- [201] EKSMA Optics. <https://eksmaoptics.com/nonlinear-and-laser-crystals/laser-crystals/ti-sapphire-crystals/>.
- [202] H. Tomita. personal communication.
- [203] Y. Zhao, T. Yoshida, Y. Ohmori, Y. Miyashita, M. Morita, T. Sakamoto, K. Kato, R. Terabayashi, V. Sonnenschein, H. Tomita, T. Kawai, T. Okumura, Y. Satou, M. Miyabe, and I. Wakaida, “Development of two-color resonant ionization sputtered neutral mass spectrometry and microarea imaging for Sr,” *Journal of Vacuum Science and Technology B, Nanotechnology and Microelectronics: Materials, Processing, Measurement, and Phenomena*, vol. 38, 2020.
- [204] M. Raiwa, “Zirconium analysis in microscopic spent nuclear fuel samples by resonance ionization mass spectrometry.” submitted, 2024.
- [205] M. Kaja, D. Studer, F. Berg, S. Berndt, C. E. Düllmann, N. Kneip, T. Reich, and K. Wendt, “Resonant laser ionization of neptunium within an electric field excitation schemes and ionization potential,” 2024.
- [206] R. Heine. personal communication.
- [207] M. Heller, “Entwicklung und Test eines Anregungsschemas für Am zur Spurenanalyse an Brennstoffpartikeln,” 2020.
- [208] Y. Kudryavtsev, R. Ferrer, M. Huyse, P. V. D. Bergh, P. V. Duppen, and L. Vermeeren, “Two-step laser ionization schemes for in-gas laser ionization and spectroscopy of radioactive isotopes,” *Review of Scientific Instruments*, vol. 85, 2014.
- [209] C. C. . Wikimedia. <https://creativecommons.org/licenses/by-sa/3.0/>.
- [210] G. Wikimedia. https://en.wikipedia.org/wiki/File:Rbmk_fuel_rods_holder.png.
- [211] C. C. Wikimedia. https://commons.wikimedia.org/wiki/File:RBMK_Reaktor_ChNPP-4.svg.
- [212] D. Ohm, “Berechnung isotopischer Fingerprints verschiedener Reaktortypen für die nukleare Forensik,” 2020.
- [213] M. Honda, M. Martschini, O. Marchhart, A. Priller, P. Steier, R. Golser, T. K. Sato, T. Kazuaki, and A. Sakaguch, “Novel ^{90}Sr analysis of environmental samples by Ion-Laser InterAction Mass Spectrometry,” *Analytical Methods*, vol. 14, pp. 2732–2738, 2022.
- [214] T. Okumura, N. Yamaguchi, T. Dohi, K. Iijima, and T. Kogure, “Loss of radioactivity in radiocesium-bearing microparticles emitted from the Fukushima Dai-ichi nuclear power plant by heating,” *Scientific Reports*, vol. 8, 2018.

- [215] J. Blaise and J. F. Wyart, *Abundance of elements in the earth's crust and in the sea*, pp. 14–17. CRC Handbook of Chemistry and Physics, 97 ed., 2016.

Appendix

A.1 ToF-SIMS/RIMS Settings SIRIUS

Most settings are set at the A grid, though the lens and VDP are unique to the particle. This is optimised in SIMS mode for the best ion signal and mass resolution. RIMS mode is then enabled by turning the external bias from 0 to 500 V to remove the ionised fraction, and increasing the X raster by 10 %. Settings are summarized in table A.1.

Analyser	Voltage (V)	Raster %	LMIG	Voltage (V)	Raster %
Extractor	1000		Focus	72.9 - 74	
Lens	2700 - 2900		X sensitivity		80 - 82
VDP	200 - 320		Y sensitivity		79 - 80
X		0.6	X raster		10.6 - 13.0
Y		13.8	Y raster		0 - 22
Lens	2700 - 2900				
External Bias	500				

Table A.1: Range of analyser and LMIG settings for RIMS analysis. Each particle requires optimised settings to maximize ion signal and mass resolution. Note that in SIMS mode the external bias is 0 V and the X raster is 10 % lower.

A.2 Mass spectra

Example mass spectra for two particles: CP025 in SIRIUS, and CP036 in LION.

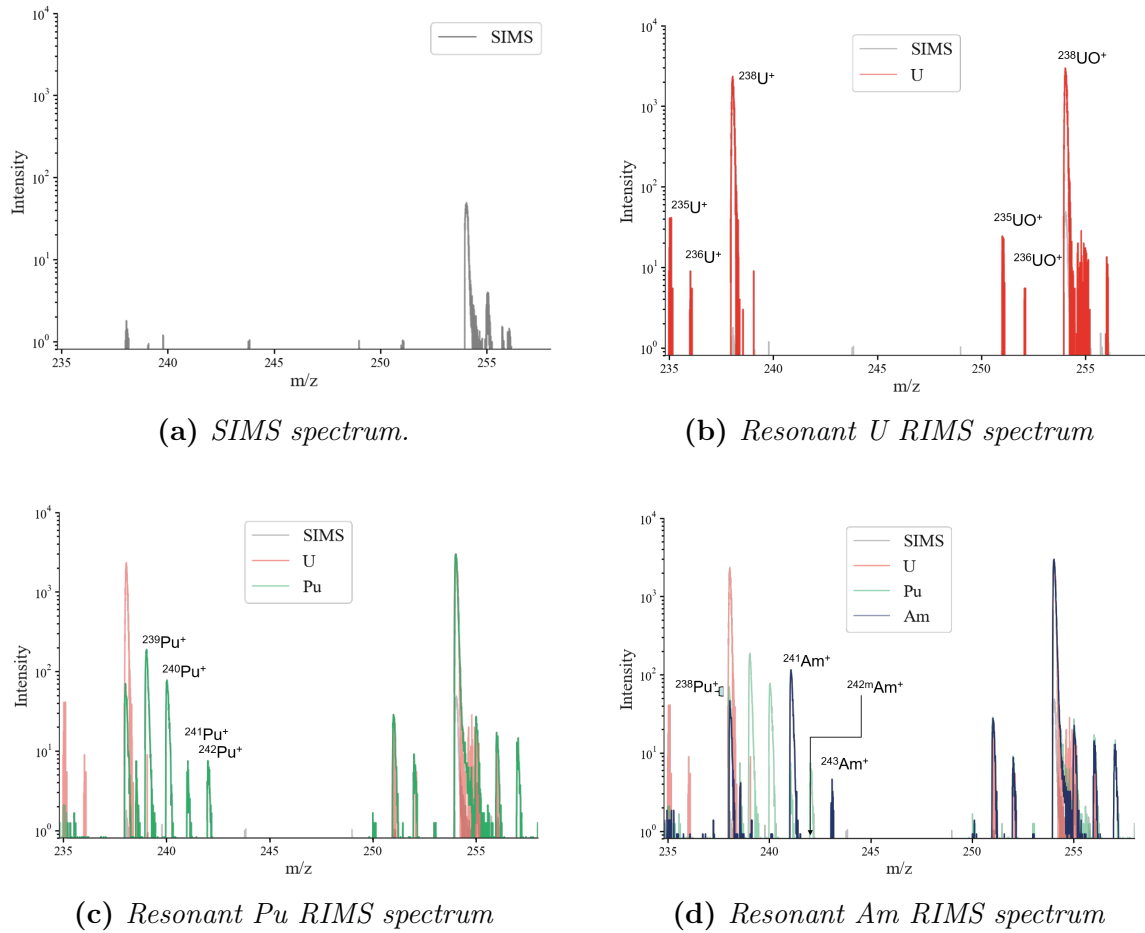
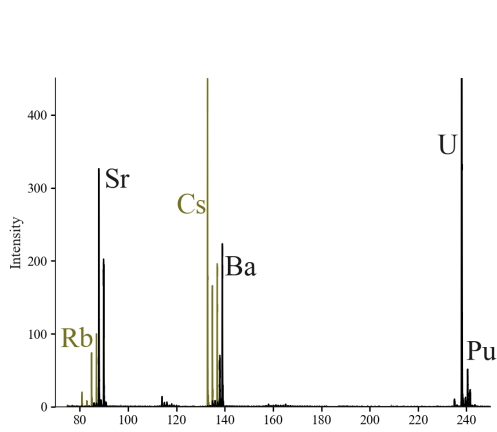
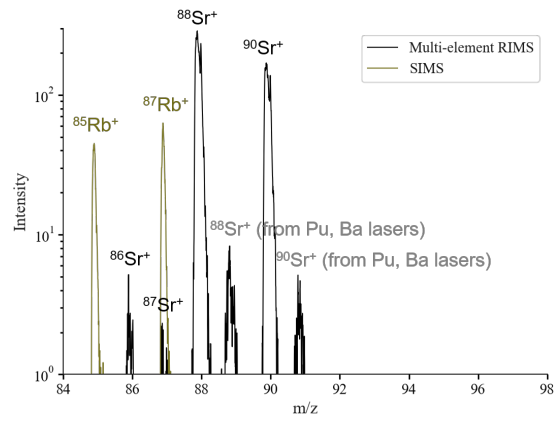


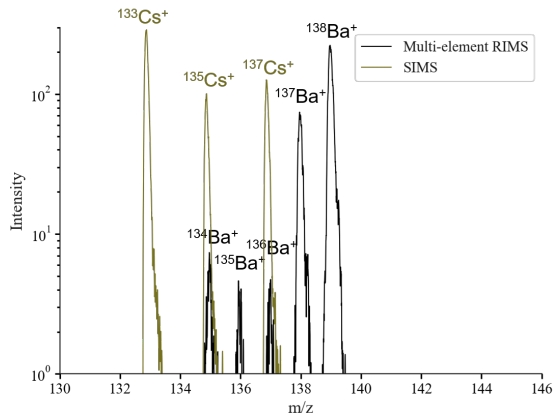
Figure A.1: *SIMS and RIMS spectra in the range 235 to 260 m/z for particle CP025 as sequentially measured in the SIRIUS instrument.*



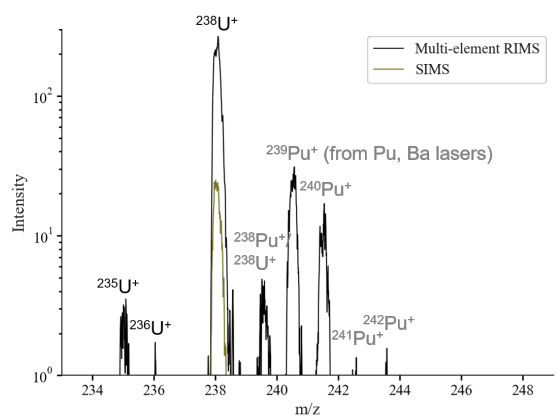
(a) Total spectrum with lineary intensity, overlaid with SIMS (green) and multi-element RIMS (black) in range 70 to 250 m/z.



(b) SIMS and RIMS spectra, showing the Rb in SIMS, resonant Sr on mass, and non-resonant Sr on the delayed lasers from Pu and Ba in the multi-element measurement.



(c) SIMS and RIMS spectra, showing the Cs in SIMS, resonant Ba by delayed lasers from Pu and Ba in the multi-element measurement.



(d) SIMS and RIMS spectra, showing ^{238}U in SIMS, resonant U on mass, resonant Pu by delayed lasers from Pu and Ba in the multi-element measurement.

Figure A.2: SIMS and RIMS spectra in the range for particle CP036 as measured in the LION instrument.

A.3 Particle Isotope Ratio Data

The following tables collate all the data on particles used in this work. Where measurement dates are known, they are included. The ratios and their respective uncertainties are given after corrections for background and isotope fractionation based on a standard (see Chapter 3 for full details).

Name	Loc	U234/U238	U235/U238	U236/U238	U234/U238 err	U235/U238 err	U236/U238 err
Amun-Ra	SL6.1	0.000166	0.010721	0.001800	0.000012	0.000018	0.000017
Ares	KOP-001	0.000154	0.010382	0.001861	0.000005	0.000044	0.000019
Barachiel	BK-010	0.000222	0.003153	0.000755	0.000099	0.000433	0.000161
Bellerophon	KOP-002	0.000191	0.008027	0.002062	0.000020	0.000135	0.000067
Bob	RW-001	0.000139	0.007703	0.002127	0.000005	0.000035	0.000018
Cate	CP-001	0.000173	0.010126	0.001846	0.000035	0.000035	0.000035
Dumah	BK-012	0.000207	0.009173	0.002346	0.000008	0.000004	0.000010
Gaia Spot 1	KOP-007	0.000179	0.010648	0.001827	0.000011	0.000090	0.000037
Gefion	CP-034	0.000282	0.008401	0.002171	0.000026	0.000148	0.000074
Heimdall	CP-036	0.000143	0.010427	0.002138	0.000024	0.000253	0.000113
Herakles	KOP-008	0.000164	0.009160	0.001918	0.000019	0.000145	0.000065
Ida	CP-007	0.000535	0.009198	0.001911	0.000161	0.000660	0.000287
James	CP-008	0.000212	0.009973	0.001931	0.000002	0.000002	0.000012
Jequin	BK-018	0.000190	0.007142	0.002487	0.000000	0.000005	0.000008
Johanna	BK-008	0.000187	0.010857	0.001626	0.000015	0.000117	0.000046
Jörmungandr	CP-026	0.000171	0.013914	0.001312	0.000012	0.000112	0.000035
Kerubiel	BK-019	0.000432	0.008092	0.002576	0.000117	0.000527	0.000295
Kronos	KOP-011	0.000184	0.009782	0.002222	0.000016	0.000119	0.000056
Loki	C037B	0.000356	0.008544	0.002241	0.000067	0.000420	0.000209
Lykos	KOP-012	0.000235	0.010426	0.001843	0.000003	0.000006	0.000022
Marie	RW-010	0.000169	0.014077	0.001287	0.000009	0.000087	0.000026
Daniel	BK-036	0.000313	0.012540	0.001641	0.000000	0.000020	0.000020
Mjoellnir	CP-025	0.000149	0.006883	0.002371	0.000010	0.000069	0.000040
Mopsimilian	BK-006	0.000154	0.014816	0.001161	0.000015	0.000145	0.000040
Nathaniel	BK-022	0.000352	0.007439	0.002231	0.000053	0.000257	0.000139
Njord	CP-035	0.000253	0.009916	0.002076	0.000034	0.000230	0.000103
Ophaniel	BK-023	0.000195	0.012972	0.001445	0.000014	0.000006	0.000012
Pahalia	BK-024	0.000283	0.011867	0.001827	0.000043	0.000288	0.000112
Thor	CP-033	0.000261	0.008585	0.001943	0.000058	0.000084	0.000045
Wormwood	BK-029	0.000374	0.008521	0.002271	0.000042	0.000212	0.000108
Hannibal	BK-039	0.000266	0.011077	0.002153	0.000028	0.000198	0.000085
Lailah	BK-020	0.000369	0.008933	0.002025	0.000042	0.000188	0.000091
Virtues	BK-028	0.000285	0.011904	0.002101	0.000024	0.000146	0.000058
Xatar	BK-030	0.000254	0.009123	0.002083	0.000037	0.000225	0.000106
Momos	KOP-013	0.000263	0.006052	0.002102	0.000039	0.000243	0.000142
Tennin	BK-027	0.000314	0.011569	0.001638	0.000049	0.000396	0.000164
Nereus	KOP-014	0.000169	0.012269	0.002238	0.000045	0.000388	0.000165
Eurybia	KOP-017	0.000231	0.010485	0.001900	0.000045	0.000307	0.000130

Table A.2: *Uranium isotope ratio data per particle.*

Name	Loc	Date (Am) measured	Am243/Am241	Am243/Am241 err
Amun-Ra	SL6.1			
Ares	KOP-001	29/04/2021	0.0136	0.0005
Barachiel	BK-010			
Bellerophon	KOP-002		0.0171	0.0009
Bob	RW-001		0.0229	0.0005
Cate	CP-001			
Dumah	BK-012		0.0141	0.0007
Gaia Spot 1	KOP-007		0.0145	0.0015
Gefion	CP-034	16/01/2023	0.0176	0.0019
Heimdall	CP-036			
Herakles	KOP-008		0.0122	0.0006
Ida	CP-007			
James	CP-008	21/05/2021	0.0122	0.0006
Jequin	BK-018		0.0296	0.0005
Johanna	BK-008		0.0082	0.0013
Jörmungandr	CP-026		0.0015	0.0008
Kerubiel	BK-019			
Kronos	KOP-011		0.0179	0.0008
Loki	C037B			
Lykos	KOP-012		0.0087	0.0005
Marie	RW-010	05/05/2021	0.0029	0.0004
Daniel	BK-036			
Mjoellnir	CP-025		0.0288	0.0010
Mopsimilian	BK-006			
Nathaniel	BK-022			
Njord	CP-035	16/01/2023	0.0174	0.0028
Ophaniel	BK-023		0.0036	0.0037
Pahalia	BK-024	17/02/2022		
Thor	CP-033		0.0148	0.0010
Wormwood	BK-029	13/01/2023	0.0203	0.0031
Hannibal	BK-039	17/01/2023	0.0163	0.0025
Lailah	BK-020	31/01/2023	0.0176	0.0031
Virtues	BK-028	31/01/2023	0.0132	0.0028
Xatar	BK-030	28/02/2023	0.0185	0.0024
Momos	KOP-013	28/02/2023	0.0286	0.0041
Tennin	BK-027	28/02/2023	0.0122	0.0039
Nereus	KOP-014	26/10/2023		
Eurybia	KOP-017	01/11/2023	0.0087	0.0017

Table A.3: *Am isotope ratio data per particle*

Name	Loc	Date (Pu) measured	Pu238/Pu239	Pu240/Pu239	Pu241/Pu239	Pu242/Pu239	Pu238/Pu239 err	Pu240/Pu239 err	Pu241/Pu239 err	Pu242/Pu239 err
Amun-Ra	SL6.1									
Ares	KOP-001	29/04/2021	0.007	0.406	0.034	0.029	0.0013	0.0060	0.0014	0.0025
Barachiel	BK-010									
Bellerophon	KOP-002									
Bob	RW-001	26/02/2021	0.006	0.586	0.050	0.052	0.0005	0.0125	0.0023	0.0040
Cate	CP-001									
Dumah	BK-012			0.567	0.049	0.089		0.0103	0.0029	0.0093
Gaia Spot 1	KOP-007									
Gefion	CP-034	12/01/2023		0.456	0.034	0.035		0.0192	0.0044	0.0038
Heimdall	CP-036	14/01/2022	0.009	0.414	0.038	0.031	0.0024	0.0156	0.0055	0.0056
Herakles	KOP-008									
Ida	CP-007			0.433	0.035	0.028		0.0188	0.0045	0.0045
James	CP-008	21/05/2021	0.008	0.357	0.026	0.020	0.0065	0.0055	0.0013	0.0017
Jequn	BK-018		0.003	0.670	0.054	0.094	0.0005	0.0134	0.0026	0.0080
Johanna	BK-008									
Jörmungandr	CP-026									
Kerubiel	BK-019	22/02/2022	0.005	0.469	0.038	0.041	0.0021	0.0158	0.0046	0.0059
Kronos	KOP-011									
Loki	C037B									
Lykos	KOP-012							0.0086	0.0019	0.0028
Marie	RW-010	05/05/2021	0.003	0.309	0.020	0.015	0.0006	0.0034	0.0010	0.0023
Daniel	BK-036			0.240	0.019	0.006		0.0103	0.0028	0.0013
Mjoellnir	CP-025		0.008	0.550	0.046	0.051	0.0015	0.0075	0.0021	0.0039
Mopsimilian	BK-006									
Nathaniel	BK-022	22/02/2022		0.637	0.049	0.072		0.0430	0.0123	0.0207
Njord	CP-035	12/01/2023		0.414	0.023	0.023		0.0195	0.0041	0.0034
Ophaniel	BK-023		0.010	0.273	0.017	0.009	0.0020	0.0039	0.0008	0.0011
Pahalia	BK-024	17/02/2022	0.004	0.334	0.017	0.019	0.0014	0.0223	0.0056	0.0074
Thor	CP-033		0.009	0.429	0.034	0.033	0.0017	0.0081	0.0023	0.0059
Wormwood	BK-029	12/01/2023		0.477	0.040	0.048		0.0182	0.0044	0.0042
Hannibal	BK-039	19/01/2023		0.434	0.040	0.038		0.0254	0.0066	0.0066
Lailah	BK-020	20/01/2023		0.483	0.043	0.044		0.0287	0.0076	0.0070
Virtues	BK-028	20/01/2023		0.385	0.034	0.020		0.0235	0.0074	0.0057
Xatar	BK-030	28/02/2023		0.477	0.045	0.045		0.0222	0.0051	0.0045
Momos	KOP-013	28/02/2023		0.564	0.047	0.074		0.0349	0.0087	0.0102
Tennin	BK-027	28/02/2023		0.337	0.023	0.018		0.0273	0.0072	0.0050
Nereus	KOP-014	26/10/2023		0.348	0.024	0.016		0.0285	0.0065	0.0044
Eurybia	KOP-017									

Table A.4: Pu isotope ratio data per particle

Name	Loc	Date (Sr) measured	90/88Sr	Sr90/Sr88 err	Date (Ba) measured	Ba137/Ba138	Ba137/Ba138 err	Date (Cs) measured	Cs133/Cs135	err_135	Cs133/Cs137	err_137	Cs137/Cs135	Cs137/Cs135 err
Amun-Ra	SL6.1													
Ares	KOP-001	24/05/2022	0.619	0.006	24/05/2022	0.196	0.017	01/11/2023	3.418	0.128	2.515	0.084	1.359	0.068
Barachiel	BK-010													
Bellerophon	KOP-002													
Bob	RW-001	28/11/2022	0.674	0.028				01/11/2023	4.312	0.182	2.487	0.085	1.734	0.094
Cate	CP-001													
Dumah	BK-012													
Gaia Spot 1	KOP-007													
Gefion	CP-034	16/01/2023	0.663	0.021										
Heimdall	CP-036	31/05/2022	0.612	0.012	31/05/2022	0.605	0.041	31/05/2022	3.165	0.037	2.382	0.025	1.329	0.021
Herakles	KOP-008							01/11/2023	3.129	0.282	2.361	0.192	1.325	0.161
Ida	CP-007													
James	CP-008	30/05/2022	0.626	0.005	30/05/2022	0.094	0.008							
Jequn	BK-018							30/05/2022	2.995	0.065	2.306	0.046	1.299	0.038
Johanna	BK-008													
Jörmungandr	CP-026													
Kerubiel	BK-019	25/05/2022	0.619	0.013	25/05/2022	0.509	0.069							
Kronos	KOP-011							25/05/2022	3.459	0.024	2.387	0.014	1.449	0.013
Loki	C037B													
Lykos	KOP-012													
Marie	RW-010	26/05/2022	0.610	0.009	26/05/2022	0.048	0.007							
Daniel	BK-036													
Mjoellnir	CP-025	01/03/2023	0.666	0.005										
Mopsimilian	BK-006													
Nathaniel	BK-022	23/05/2022	0.662	0.037	23/05/2022	0.310	0.110							
Njord	CP-035	16/01/2023	0.638	0.026				23/05/2022	7.626	0.232	5.036	0.128	1.514	0.060
Ophaniel	BK-023													
Pahalia	BK-024	17/05/2022	0.630	0.012	17/05/2022	0.034	0.004							
Thor	CP-033							17/05/2022	2.738	0.054	2.458	0.047	1.114	0.031
Wormwood	BK-029	16/01/2023	0.678	0.027				01/11/2023	1.906	0.416	2.259	0.522	0.844	0.268
Hannibal	BK-039	03/02/2023	0.631	0.019										
Lailah	BK-020	03/02/2023	0.670	0.019										
Virtues	BK-028	03/02/2023	0.678	0.021										
Xatar	BK-030	01/03/2023	0.626	0.017										
Momos	KOP-013	01/03/2023	0.643	0.022										
Tennin	BK-027	01/03/2023	0.627	0.028										
Nereus	KOP-014													
Eurybia	KOP-017							01/11/2023	3.33333333	0.5913797	2.352941176	0.4052766	1.41666667	0.350801279

Table A.5: Fission Product isotope ratio data per particle

Acknowledgements

Over the past three years, I have had the privilege to train and collaborate with exceptional researchers across the world from Europe to the U.S. to Japan. This work is the product of many collaborations, foremost the Laser Ionization and Spectroscopy of Actinides (LISA) project. This Marie Skłodowska-Curie Action (MSCA) Innovative Training Network (ITN) receives funding from the European Union's H2020 Framework Programme under grant agreement no. 861198. Part of this work was performed under the auspices of the U.S. Department of Energy by Lawrence Livermore National Laboratory under Contract DE-AC52-07NA27344, and was partially supported by the National Nuclear Security Agency Office of Defense Nuclear Nonproliferation Research and Development, LLNL-JRNL-844531. Additional funding was provided by the SOLARIS project of the German Federal Ministry of Education and Research (Bundesministerium für Bildung und Forschung), BMBF 2020+ 02NUK075A.

My deepest thanks goes to my supervisor Prof. Clemens Walther, for the support and guidance throughout this project.

At the IRS I would like to thank Bettina Weiler for her patience with all the absurd travel plans, and Jessica Hahne for help navigating the many forms. Special thanks to Stefan Bister, Sebastian Büchner, Ralf Groffmann, Frank Koepke, and Nurije Elezi for their technical support. Thanks to everyone at the IRS for their discussions on subject matter, Tobias Weissenborn, Laura Leifermann, David Ohm, Wolfgang Schulz, Martin Weiß, and Hauke Bosco for their learned wisdom, and everyone who listened to my ramblings and frustrations. This project would not have started without the work of Manuel Raiwa, and the ever-faithful CARO program. This project would never have finished without the comradery of Paul Hanemann.

Thanks to everyone in the LISA project, whose gatherings were endlessly fascinating and entertaining. To Thomas Cocolios, Isabelle Fontaine, and Bruce Marsh, thank you for bringing us all together. With the extreme events of this period of time, the pandemic, war in Ukraine, and tragic passing of Bruce, the community that formed around LISA will remain impactful. Additional thanks goes to Prof. Klaus Wendt and his group at Johannes Gutenberg University in Mainz for laser development and continued advice. The work of Magda Kaja and Mitzi Urquiza on Np schemes, and Nina Kneip on U, Pu and Am, is particularly thanked. Thanks also go to Mia Au for co-editing the LISA newsletter. To the team who planned the excursion to Chornobyl, Serigy Dubchak, Wolfgang Schulz,

Jessica Warbinek, Lauren Reed, Mitzi Urquiza, Miranda Nichols, Vaila Leask, and Fedor Ivandikov, thank you for all of your support, especially in the turn-around when it was cancelled.

At LLNL I would like to thank Mike Savina, Brett Isselhardt, and Ziva Shulaker for introducing me to LION, and the many hours dedicated to my 'giant' particles. Thanks go as well to David Willingham and Peter Boone for access to the SEM; Brian Sammis and Keenan Thomas for gamma spectroscopy; Mavrik Zavarin for arranging the secondment. Additional thanks to Becky and Hugh for hosting me in California. Thanks to my grandma for helping me get my driver's license, and being my all-round cheerleader.

At the IER in Fukushima, I would like to thank Prof. Kenji Nanba, Yoshifumi Wakiyama, and Satomi Sato for hosting me, Prof. Hirofumi Tsukada and Maksym Gusyev for the sampling trips and providing previous samples, Prof. Tsugiko Takase for SEM access, and Pierre-Alexis Chaboche for the coffee.

To everyone who took and provided samples in the past, I cannot thank you enough. To those who may provide samples in the future, know that they hold value for a long time. They allow us all to keep asking new questions, and revisit old questions with new techniques. It is so entirely worth the effort to get these handfuls of questionably radioactive dirt.

Special thanks go to my friends and family, especially my parents, who endured my spontaneous lectures with enthusiasm and always enquired after the wellbeing of the lasers.

And finally, to Joe, for everything.

CV, List of Publications

Curriculum Vitae

Education

2020 - 2024 *Doktorin der Naturwissenschaften, Dr. rer. nat.*, Leibniz Universität Hannover, Hannover, Germany

2015 - 2016 *Master of Physics, MPhys*, Durham University, United Kingdom

2011 - 2015 *VWO - Gymnasium*, The Hague, The Netherlands

Employment

2020 - 2024 *Wissenschaftlicher Mitarbeiterin*, Institut für Radioökologie und Strahlenschutz, Leibniz Universität Hannover, Hannover, Germany

2019 - 2020 *Intern*, International Atomic Energy Agency, Vienna, Austria

2018 *Trainee*, European Commission Joint Research Centre, Karlsruhe, Germany

2017 *Intern*, Organisation for the Prohibition of Chemical Weapons, The Hague, The Netherlands

Papers

[1] Paul Hanemann, Stefan Bister, Manuel Raiwa, Sandra Reinhard, Darcy van Eerten, Clemens Walther, “Production and characterization of standard particles for rL-SNMS”, *Journal of Radioanalytical and Nuclear Chemistry*, vol. 331, pp. 5039-5045, 2022.

[2] Darcy van Eerten, Manuel Raiwa, Paul Hanemann, Laura Leifermann, Tobias Weissenborn, Wolfgang Schulz, Martin Weiß, Danielle Ziva Shulaker, Peter Boone, David Willingham, Keenan Thomas, Brian Sammis, Brett Isselhardt, Mike Savina, and Clemens Walther, “Multi-element isotopic analysis of hot particles from Chernobyl”, *Journal of Hazardous Materials*, vol. 452, pp. 131338, 2023.

[3] Darcy van Eerten, David Ohm, Manuel Raiwa, Paul Hanemann, Laura Leifermann, Tobias Weissenborn, and Clemens Walther, “Isotope ratio analysis of partially spent fuel in RBMK type reactors - models and experiment”, *in preparation*, 2024.

Conference Talks

[1] ALLIANCE PhD Webinar, *Non-destructive mass spectrometry of single hot particles from the Chernobyl exclusion zone by resonant laser SNMS*, online, June 2021.

[2] Applied Nuclear Physics Conference, *Non-destructive mass spectrometry of single hot particles from the Chernobyl exclusion zone by resonant laser SNMS*, Prague, Czech

Republic, September 2021.

[3] Deutsche Physikalische Gesellschaft (DPG) Spring Meeting of the Atomic, Molecular, Quantum Optics and Photonics Section (SAMOP), *Multi-element isotopic analysis of hot particles from Chornobyl*, Hannover, Germany, March 2023.

[4] Laser Ionisation and Spectroscopy of Actinides, *Multi-element ultra-trace analysis of hot particles in the Chornobyl Exclusion Zone*, Leuven, Belgium, May 2023.

[5] Secondary Ionisation Mass Spectrometry (SIMS) Europe, *SIMS to RIMS: Element selective isotope analysis on hot particles from the Chornobyl Exclusion Zone*, Nottingham, UK, September 2023.

[6] Nuclear Forensics, *Multi-element isotope ratio analysis for nuclear material in the environment with resonance ionization mass spectrometry (RIMS)*, London, UK, October 2023.

[7] RIMS 2024 Workshop, *Spatially Resolved Multi-Element Analysis of Hot Particles in the SIRIUS RIMS instrument*, Fukushima, Japan, March 2024.

Training

[1] LISA Specialized Training - Nuclear chemical techniques and laser resonance Ionization laboratory training, Mainz, Germany, May 2021.

[2] Joliot Curie International School - The interplay between atomic electrons and the nucleus: traps, lasers and spectroscopy, **poster:** *Multi-element calibration standards for rL-SNMS measurement of environmental samples*, Saint-Pierre d'Oléron, France, October 2021.

[3] LISA Specialized Training - Advanced Techniques for the Production and Study of Actinides, Jyväskylä, Finland, October 2021.

[4] LISA Summer Schools - Nucleons to the Stars/Analysis of Structure of Complex Atoms, **poster:** *Multi-element isotopic analysis of hot particles from Chornobyl - Comparison of RIMS methods*, Caen, France, September 2022.

Secondments

[1] Lawrence Livermore National Laboratory, Chemical and Isotopic Signatures Group, March - June 2022.

[2] Fukushima University Institute for Environmental Radioactivity, March - May 2023.

Outreach

[1] International School Hannover, grades 9, 11 and 12, *Nuclear Physics - How a 9th grader ended up in a lab in Hannover*, Hannover, Germany, November 2021.

[2] @ch.ex.zo on instagram, an account explaining nuclear physics concepts in the context of the Chornobyl Exclusion Zone, March - June 2022.

[3] Invited talks: Manchester University and Dounreay Site Limited, *Chornobyl and Lasers - Resonance ionization mass spectrometry (RIMS) for isotopic analysis in environmental samples*, Manchester/Thurso, UK, August 2022.

[4] RIMS2024 Public Lecture, *Resonance Ionization Mass Spectrometry - Discovering the secrets hidden in radioactive specks of dust*, Fukushima, Japan, March 2024.

Declaration of Authorship

I hereby certify that I have written this dissertation independently. I certify that I have not used any sources other than those specified, that all statements taken literally or meaningfully from other works are identified as such, and that neither the whole nor parts of the submitted work are the subject of another examination procedure.

Einverständniserklärung

Hiermit versichere ich, dass ich die vorliegende Arbeit selbstständig verfasst habe. Ich versichere, dass ich keine anderen als die angegebenen Quellen benutzt und alle wörtlich oder sinngemäß aus anderen Werken übernommenen Aussagen als solche gekennzeichnet habe und dass die eingereichte Arbeit weder vollständig noch in wesentlichen Teilen Gegenstand eines anderen Prüfungsverfahrens gewesen ist.

28.02.2024, Hannover

A handwritten signature in black ink, consisting of several fluid, connected strokes. It starts with a small arrow-like shape on the left, followed by a series of loops and a long horizontal tail stroke on the right.